Propriétés des absorbants Lyman-alpha à grand décalage spectral

Céline Péroux

Céline Péroux. Propriétés des absorbants Lyman-alpha à grand décalage spectral. Astrophysics [astro-ph]. University of Cambridge, 2001. English. NNT : . tel-00003969

Properties of Lyman-α Absorbers at High-Redshift

CÉLINE PÉROUX

INSTITUTE OF ASTRONOMY
&
FITZWILLIAM COLLEGE

SEPTEMBER, 2001

A DISSERTATION SUBMITTED TO THE UNIVERSITY OF CAMBRIDGE
FOR THE DEGREE OF DOCTOR OF PHILOSOPHY

DECLARATION

This thesis, entitled *Properties of Lyman-α Absorbers at High-Redshift*, is submitted for the degree of Doctor of Philosophy at the University of Cambridge. The research described was performed in the Institute of Astronomy between October 1998 and September 2001. The work contained in this dissertation is original, except where explicit reference to the results of others is given. Parts of this work, which are indicated in the text, were performed in collaboration and some of the results have appeared or will appear in published form:

- **Céline Péroux**, Mike Irwin, Richard G. McMahon & Lisa J. Storrie-Lombardi, *The Evolution and Space Density of Damped Lyman-alpha Galaxies*, 2000, in proceedings of the Euroconference: "The Evolution of Galaxies. I - Observational Clues" ed. J.M. Vilchez, G. Stasinska and E. Perez.

- **Céline Péroux**, Lisa J. Storrie-Lombardi, Richard G. McMahon & Mike Irwin, *Absorption Systems in the Spectra of 66* $z \gtrsim 4$ *Quasars*, 2001, AJ, **121**, 1799.

- **Céline Péroux**, Richard G. McMahon, Mike Irwin & Lisa J. Storrie-Lombardi, *Cosmological Evolution of the Universe Neutral Gas Mass Measured by Quasar Absorption Sysems*, 2001, in the proceedings of the "Cosmic Evolution" conference, held at l'Institut d'Astrophysique de Paris, November 13-17, 2000.

- **Céline Péroux**, Richard G. McMahon, Lisa J. Storrie-Lombardi & Mike Irwin, *The Nature of High-Redshift Damped Ly-α Absorbers*, 2001, MNRAS, *submitted.*

- **Céline Péroux**, Mike Irwin, Richard G. McMahon & Lisa J. Storrie-Lombardi, *Statistical Properties of DLAs and sub-DLAs*, 2001, in proceedings of the "Chemical Enrichment of Intracluster and Intergalactic medium" Vulcano Workshop, ed. Francesca Matteucci.

The length of this work does not exceed 60,000 words.

Céline Péroux
Cambridge
September, 2001

SUMMARY

Properties of Lyman-α Absorbers at High-Redshift

Céline Péroux

In recent years, an extremely successful method to observationally study early stages of galaxy formation has been provided by the study of *quasar absorbers.* Quasar absorption lines are systems intercepting our line-of-sight to a given quasar and thus produce a feature in the quasar spectrum. **Damped Lyman-α systems** (hereafter DLAs) have N (H I) $> 2 \times 10^{20}$ atoms cm^{-2}, and were originally thought to be the precursors of present day disk galaxies but there is evidence that they may be dominated by gas-rich proto-dwarf galaxies representing the basic building blocks of hierarchical growth of structure. Since their detection is independent of their size, shape, and covering factor, they provide a unbiased method with which to study early galaxies. DLAs are a subset of **Lyman-limit Systems** (hereafter LLS) which have hydrogen column densities N (H I) $> 1.6 \times 10^{17}$ atoms cm^{-2}. At $z < 1$, they are probably associated with galactic halos. Finally, the **Lyman-α forest** is composed of many small column density systems ranging from N (H I) $= 10^{12}$ to 1.6×10^{17} atoms cm^{-2}.

This thesis presents a sample of 66 bright $z \gtrsim 4$ quasars observed with the 4 m Cerro Tololo Inter-American Observatory telescope and the 4.2 m William Hershel telescope. The first part of the study concentrates on the quasars themselves via the fitting of quasar continua and the measurement of continuum depression parameters characterising the mean absorption across the Lyman-α forest. The quasar spectra are then analysed to investigate the absorption systems they contain. This led to the discovery of 26 new DLAs, 34 LLS and many associated metal lines which enables the analysis of the evolution of the column density distribution, $f(N, z)$, and the total mass in high-column density neutral hydrogen quasar absorbers. The observed number of LLS per unit redshift is used to constrain $f(N, z)$ below the DLA limit in the range N(HI) $= 1.6 \times 10^{17}$ to 2×10^{20} atoms cm^{-2}. The joint analysis shows unambiguously that $f(N, z)$ deviates significantly from a single power law and that a Γ-law distribution of the form $f(N, z) = (f_*/N_*)(N/N_*)^{-\beta}\exp(-N/N_*)$ provides a better description of the observations. These results are further used to determine the amount of neutral gas contained in both DLAs and in systems with N(HI) $\geq 2 \times 10^{19}$ atoms cm^{-2} ("sub-DLAs"). In the redshift range 2 – 3, 85% of the *neutral H I + He II mass density* is in DLAs, however we find that at z>3.5 this fraction drops to 55% and that the remaining neutral gas mass lies in sub-DLAs. After correction of the observed mass in H I for this "missing" neutral gas the comoving mass density no longer shows any evidence for a decrease over the range z= 2 – 5. The change in the column density distribution supports a picture, where at z>3.5, we may be directly observing the *formation of high column density neutral hydrogen systems from lower column density units.* Finally, predictions on the redshift evolution of the sub-DLAs number density are presented. Preliminary results from measuring their incidence from archival UVES echelle data seem in good agreement with our predictions.

Contents

List of Figures

List of Tables

Chapter 1

Introduction

'Il n'y a pas de sentiment plus communément partagé, que de vouloir être différent des autres'
Jean-Paul Sartre

In this introductory Chapter, I recall historical developments in the discovery of both quasars (Section 1.1.1) and quasar absorbers (Section 1.1.2). In section 1.2, I describe the technique used to find the quasars which make up the sample studied in this thesis. I then detail the theory of absorption lines and Voigt profile fitting (Section 1.3.1) as well as the curve of growth (Section 1.3.2). In the last part, I define the scientific motivations for the project (Section 1.4.1) and emphasise the structure of the thesis (Section 1.4.2).

1.1 Scientific Background

1.1.1 Quasars: Cosmological Lighthouses

The *Third Cambridge (3C) Catalogue* prepared in the early 1960s, listed radio sources of which 10 were extremely small in size (less than 1 arcsec). At the same time, Hazard et al. (1963) developed a new method, using lunar occultation, to accurately determine the position of radio sources and hence allow for optical follow-up of these compact objects. This enabled Schmidt (1963) to take a spectrum of 3C 273, which showed a star-like object lying at the unexpectedly high (at the time) redshift of $z = 0.16$, implying a distance of ~ 1 Gpc and an optical luminosity $\sim 5 \times 10^{12}\,\mathrm{L}_{\odot}$. Other similar objects were subsequently observed and they became known as *quasi-stellar objects (QSO)* or *quasars.*

Such objects were (and still are) a challenge to theorists: how can so much energy come with such rapid variability out of such a compact region and be distributed over such a wide range of wavelengths (Figure 1)? Nowadays, there exists a "standard model" for quasars: an accreting black hole is the central engine from which relativistic

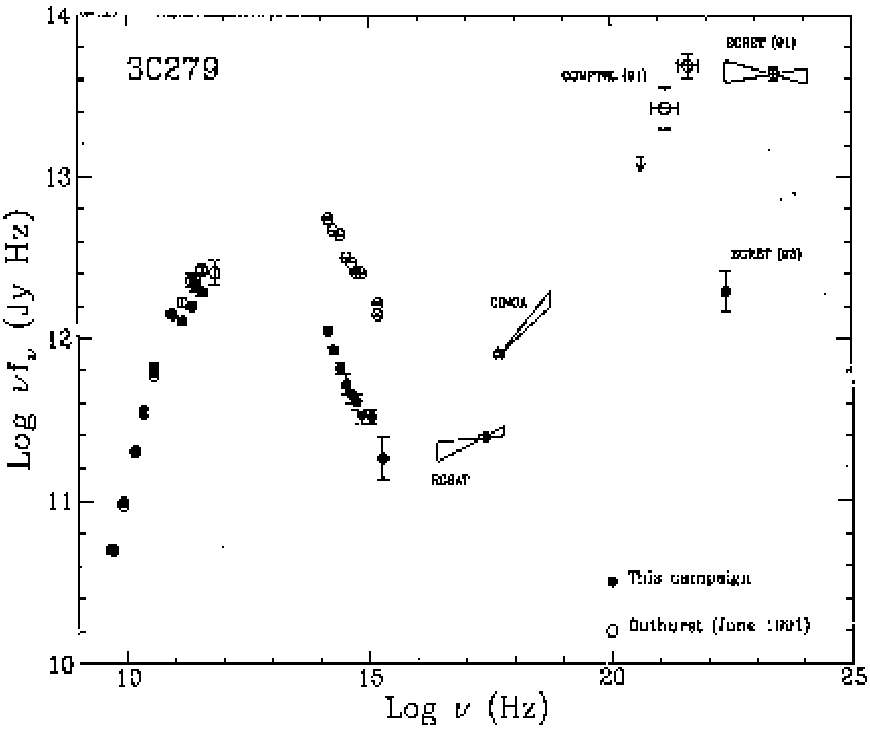

Fig. 1.— Continuum spectrum of the quasar 3C 279 from the radio to the γ-ray region (Maraschi et al., 1994).

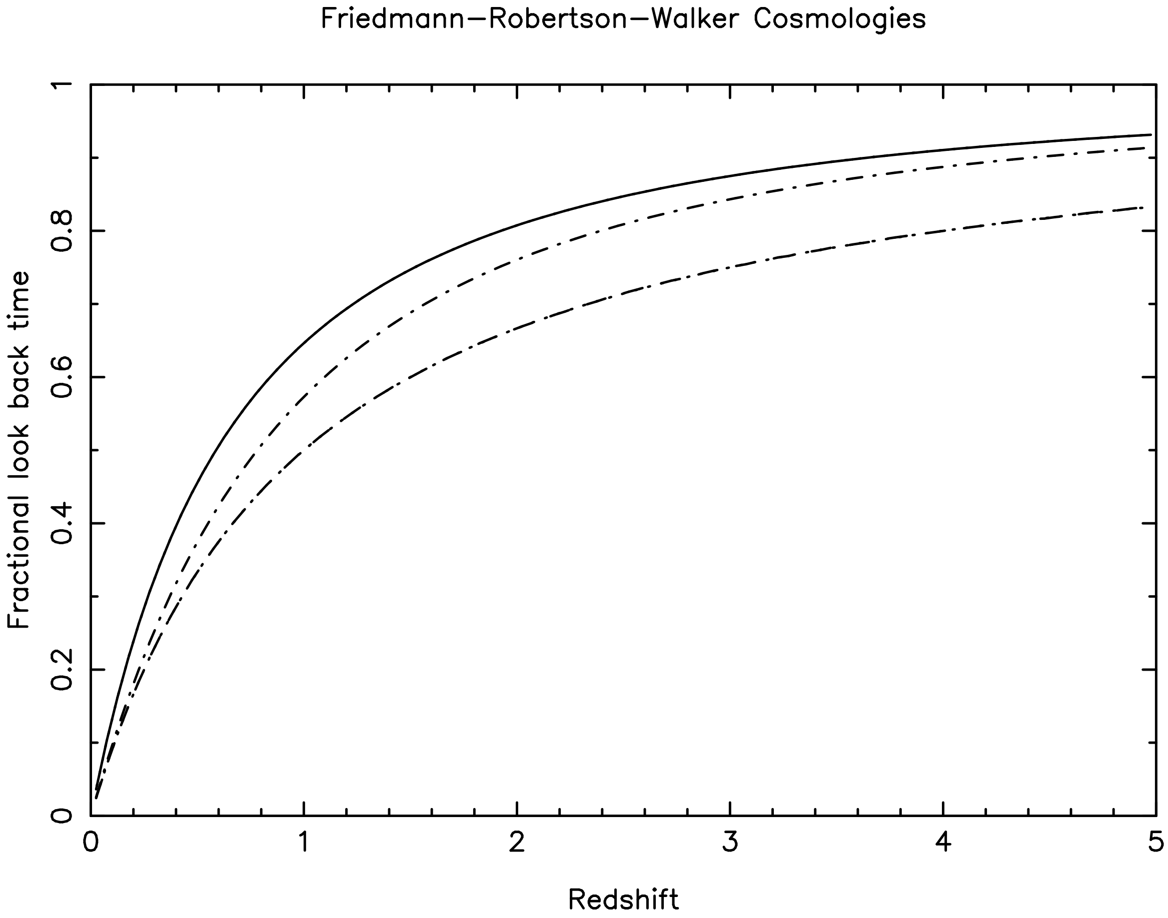

Fig. 2.— Fractional look-back time as a function of redshift. $\Omega_M = 1.0$, $\Omega_\Lambda = 0.0$ (solid line), $\Omega_M = 0.0$ and $\Omega_\Lambda = 0.0$ (dashed line) and $\Omega_M = 0.3$ and $\Omega_\Lambda = 0.7$ (dashed-dotted line).

beams arise surrounded by an accretion disc. In any case, the luminous, compact emission from quasars has made them ideal beacons from the early Universe. It is indeed because they are extremely luminous that quasars are among the youngest objects observed in the Universe. They have now been detected out to redshifts of $z > 5$. The current record holder is SDSS1030+0524 (Figure 10) at $z \sim 6.28$ (Fan et al., 2001b), a redshift which corresponds to a look-back time of over 90% of the age of the Universe (Figure 2).

1.1.2 Quasar Absorbers: Unrevealing the Structures of the Universe

In addition to being interesting objects in their own right, quasars allow for the detection of much fainter systems, observed in absorption in their spectra.

The nature of absorption lines was the object of much debate in the years following their discovery (e.g. Pettini, 1998). A currently accepted hypothesis states that the lines are *intervening* and arise in cosmologically distributed gas between the background quasar and the observer. This implies that the observed redshift is cosmological, due to the expansion of the Universe. However, since the density of lines as a function of redshift is observed to increase, this implies that the cross-section of the absorbers were higher in the past. Earlier hypotheses suggested that the absorption line systems represent material *ejected* from the quasar itself. The redshift would then be kinematic and represent a Doppler shift from the ejected material. This would imply a large ejection velocity requiring a vast amount of energy and also a mechanism to confine the ejecta to narrow velocity dispersions, two conflicting requirements difficult to achieve. At present, the commonly accepted picture favours the intervening hypothesis thanks to three main arguments:

1. Sargent et al. (1980) analysed the first homogeneous sample of Lyα forest lines in six quasars. They show that neither the line density nor the equivalent width distribution vary from quasar to quasar, or with redshift, along a given line-of-sight. They also found no clustering on all scales from 300 to 30, 000 km s^{-1}. This lack of any correlation between line properties and ejection velocity is extremely difficult to explain with an ejection model.

2. Boksenberg & Sargent (1978) observed, in emission, the galaxy NGC 3067 responsible for the Ca II absorption in the spectrum of the quasar 3C 232, well outside the extent of the galaxy. This was the first evidence that it is the extended gaseous halo of the galaxy which is responsible for that absorption line observed in the quasar spectrum. Similarly, more recent work (e.g. Steidel et al., 1995) show that candidate galaxies are associated with almost all of the low redshift MgII systems.

3. Shaver & Robertson (1983) discovered common absorption systems in the spectra of quasar pairs providing indisputable evidence in favour of the intervening hypothesis. In addition, such observations give an extra dimension to the study of quasar absorbers by providing fundamental information on the physical size of the

> absorbers (Wolfe et al., 1993; Petitjean et al., 1998). The observation of quasar pairs, or groups of quasars with small angular separations on the sky, indicates that the characteristic size of the absorbers is larger than the projected separation of the lines of sight. At present, the number of suitable groups of quasars is too small to provide detailed constraints on the structure of Lyα complexes. However, despite this, Ly-α absorbers provide a powerful way to study the correlation of baryonic matter at high redshift and hence a unique chance to study how galaxy formation is related to the distribution and dynamics of the underlying matter field.

This plus other evidence has lead to the standard picture of quasar absorbers as systems along the line-of-sight between the observer and a luminous background quasar. A cartoon representation of this phenomenon is shown on Figure 3.

1.2 Finding High-Redshift Quasars

Any survey for quasar absorbers starts with a survey for quasars. I have *not* been directly involved in the search for the high-redshift quasars which make up the sample presented in this thesis, but for completeness and later reference, this section describes the methodology used to find the quasar sample. Most of the quasars presented in this thesis have been optically selected which, because of reddening effects, means that we may potentially miss the most dusty intervening objects or alternatively those which contain more absorbers along their line-of-sight. Ellison et al. (2001c) have recently undertaken observations of radio-selected quasars with the aim of pin-pointing the effect of dust on quasar absorber surveys. In addition Pei & Fall (1995) have used self-consistent closed-box/inflow-outflow galactic models to show that the fraction of missing DLAs due to dust at $z = 3$ ranges from 23% to 38%. The following sections briefly describe the methods used to find the quasar sample. Storrie-Lombardi et al. (2001) provides more details on finding the APM quasars and Fan et al. (1999); Warren et al. (1991); Kennefick et al. (1995a); Storrie-Lombardi et al. (1996c); Zickgraf et al. (1997); Kennefick et al. (1995b); Henry et al. (1994); Hook (prep); Hall et al. (1996) give more information on the discovery of the remaining quasars.

1.2.1 The 2^{nd} APM Quasar Sample

Reviews on various techniques used to find quasars are described in Hook (1994); Kembhavi & Narlikar (1999). The APM quasars were found using a multicolour technique which is the high-redshift ($z > 2.2$) counterpart to the Ultra-Violet excess (UVX) method (Sandage 1965). Irwin et al. (1991) developed the so-called "BRX" method where they made use of the fact that for $z > 3.9$ quasars, the region of the spectrum absorbed by neutral hydrogen is redshifted to the B band. A majority of quasars with such redshifts have $B - R$, colours that are extremly red and different from the colours of normal stars. At $z > 4.2$, the quasars lie so far from the stellar positions

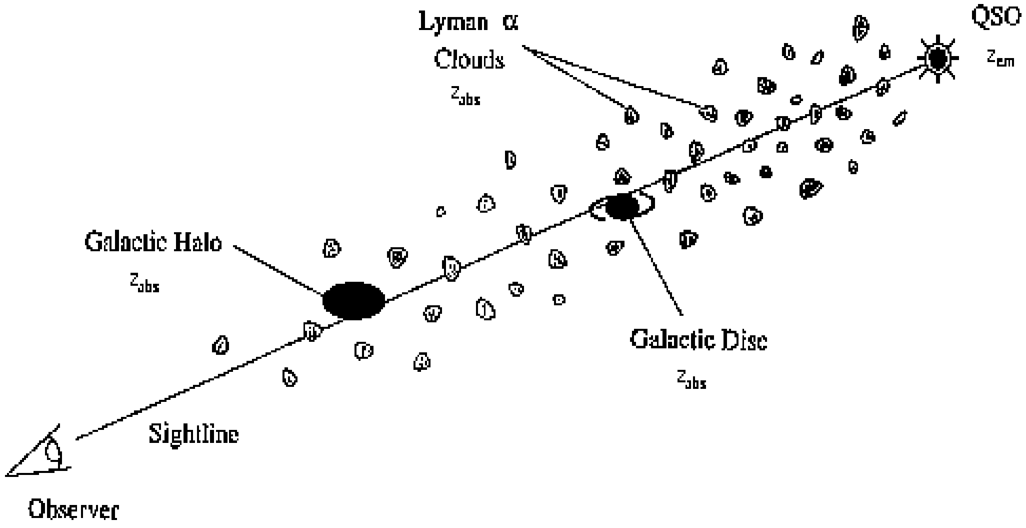

Fig. 3.— This cartoon illustrates a quasar sight line along which various objects give rise to absorption features in the spectrum of the background quasar (reproduced from Pettini, 1998, and kindly provided by Phil Outram).

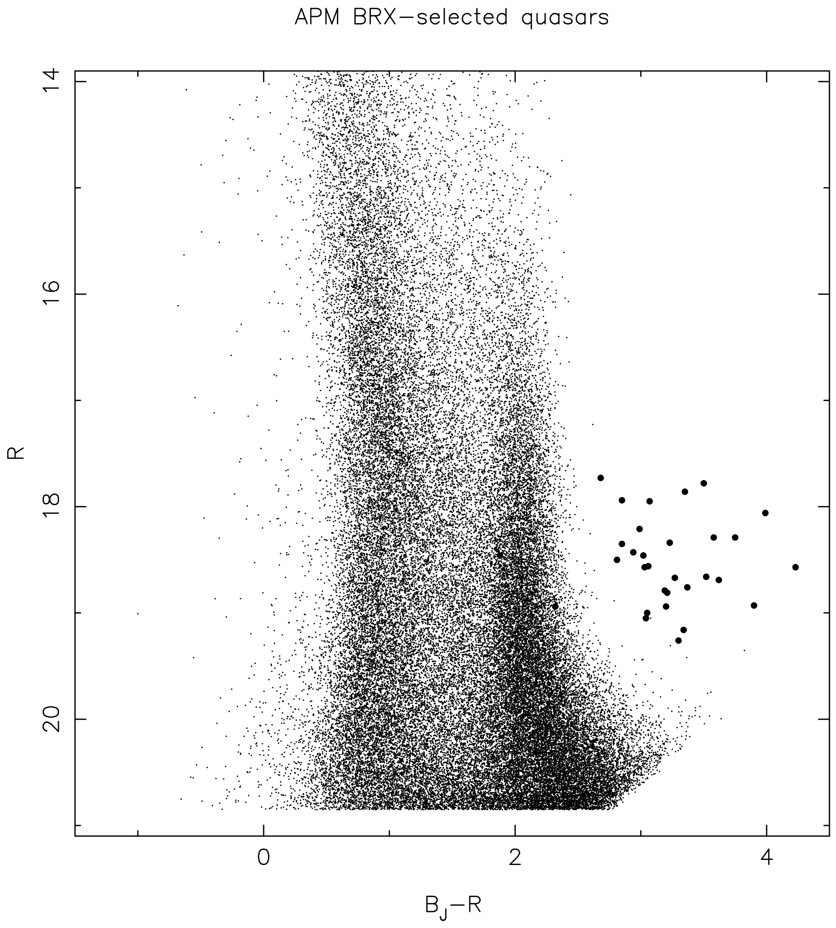

Fig. 4.— A $B_j - R$ colour-magnitude diagram for a typical high latitude UKST field used in the APM survey. Every detected B_J,R matched pair of objects classified as stellar on the R plate is plotted as small dot. Overlaid as filled circles are the complete southern sample of BRX-selected quasars (Storrie-Lombardi et al., 2001).

in the colour-colour diagram that selection in the single colour $B - R$ is sufficient to identify them with high probability. Figure 4 shows a B_j,R colour-magnitude diagram for a typical high latitude UKST field. Every detected B_j,R matched pair of objects classified as stellar on the R plate is plotted as a small dot. Overlaid as filled circles are the complete southern sample of BRX-selected quasars which form the 2^{nd} part of the APM quasar survey (Storrie-Lombardi et al., 1996c, 2001). Of the roughly 250,000 paired objects on each high latitude UKST field, two-thirds are classified as stellar on the R plate and roughly 50,000 of these are brighter than R = 19 – 19.5, the range for the R magnitude limit of the survey. The red boundary for BRX candidate selection was set to approximately B_j–R = 2.5 to 3 to follow the red extremity of the stellar locus. The effects of colour selection on sample completeness have been thoroughly investigated over the past few years (Warren et al., 1994; Storrie-Lombardi et al., 1996c; Kennefick et al., 1995a).

The plates came from the generic southern sky survey material taken by the UK Schmidt telescope (UKST) and were measured and analysed at the Automated Plate Measuring [1] (APM) facility in Cambridge. The total area of Southern high latitude sky surveyed is roughly 8000 square degrees from a total of 328 UKST fields. Low resolution ($\gtrsim$ 10 Å) spectra were then obtained to identify the quasars, primarily at the Las Campanas Observatory (Storrie-Lombardi et al., 2001). This technique was used to find 26 of the quasars which make up the sample presented in this thesis, the remaining APM discovered quasars were observed using the INT and WHT. The quasars discovered as part of the APM surveys are labelled "BR" or "BRI" accordingly.

1.2.2 Other High-Redshift Quasars

Thirty-two of the other quasars making up our 66 $z \gtrsim 4$ sample are from the Second Palomar Observatory Sky Survey. Kennefick et al. (1995a,b)[2] carried out a multicolour survey with the aim of determining the space density of bright quasars ($M_B < -27$) at $z > 4$. The quasars discovered as part of the Second Palomar Observatory Sky Survey are labelled "PSS".

Four of the quasars presented in this thesis are part of the Sloan Sky Digital Survey (SDSS) which makes use of the dedicated Apache Point 3.5m telescope. The survey is a joint project of The University of Chicago, Fermilab, the Institute for Advanced Study, the Japan Participation Group, The Johns Hopkins University, the Max-Planck-Institute for Astronomy (MPIA), the Max-Planck-Institute for Astrophysics (MPA), New Mexico State University, Princeton University, the United States Naval Observatory, and the University of Washington. It aims to map in detail one-quarter of the entire sky, determining the positions and absolute brightnesses of more than 100 million objects. The quasars found are often faint and thus not the most appropriate for absorber searches with 4m class telescope.

---

[1] http://www.ast.cam.ac.uk/~mike/apmcat/

[2] http://www.astro.caltech.edu/~george/z4.quasars

Of the four remaining quasars, one is radio-selected from the Parkes-MIT-NRAO survey and is labelled "PMN" (Hook, prep) and one is X-ray selected and labelled "RX" (Henry et al., 1994). The two last objects are optically selected by Warren et al. (1991) and by Hall et al. (1996) as part of the Deep Multicolor Survey (DMS). All the quasars making up the sample studied in this thesis are listed in Table 2.2.1.

1.3 Theory of Quasar Absorbers

1.3.1 Classification of Quasar Absorbers

Quasar absorption features can be ordered into categories having different characteristics as illustrated on the typical quasar spectrum shown in Figure 5:

I) $z_{abs} < z_{em}$

For absorption systems with wavelength (z_{abs}) below the quasar Lyα emission line (z_{em}), Lynds (1970) suggested that the absorption lines were caused by Lyα transitions. This was later confirmed by two arguments: firstly, the presence of the Lyman-β line, when observable (Baldwin et al., 1974; Oemler & Lynds, 1975), and secondly because the number density of absorbers blueward of the quasar emission line is much greater than redward. Since their detection is independent of their luminosity and morphology, these absorbers provide a unbiased method with which to study early galaxies.

In a few cases, the Lyα absorption line is observed at $z_{abs} > z_{em}$. The observed corresponding velocity rarely exceeds 2 000 km s^{-1} in good agreement with theoretical predictions (Loeb & Eisenstein, 1995), although quasar redshift measurements are sometimes subject to systematic offsets. The projected velocity of these clouds is directed *towards* the quasar itself. It is most probably associated with gas falling into the black hole potential well although more detailed studies of this problem are required to achieve a better understanding of this phenomenon.

Lyα absorbers are sub-divided into three classes according to their column density, the number of hydrogen atoms per unit area along the line-of-sight between the observer and the quasar (commonly expressed in atoms cm^{-2}). Therefore a low column density cloud could either be a small cloud with high density or a large cloud with low density. They thus probe media spanning the range from voids through to halos and disks of both dwarf and normal (proto)galaxies.

1. **Damped Lyman-α systems** (hereafter DLAs) have N(HI) $> 2 \times 10^{20}$ atoms cm^{-2}. This definition is somewhat artificial since damped wings appear for lower column densities (N(H I) $> 10^{19}$ cm^{-2}; see next Section and Figure 13). This threshold had been introduced because these lines are characteristic of local galactic disks (Wolfe et al., 1986). Also at the time, damped Lyα surveys were performed

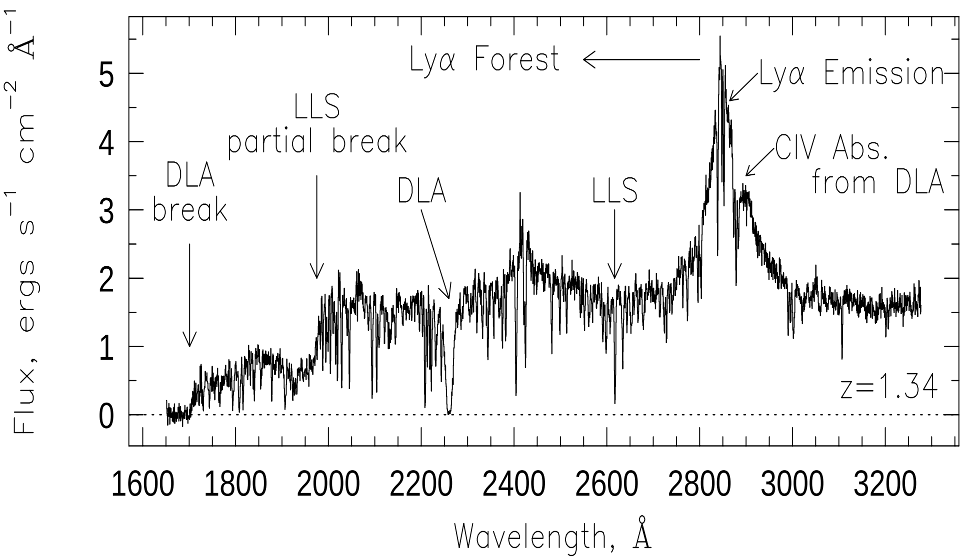

Fig. 5.— Typical spectrum of a quasar, showing the quasar continuum, emission lines, and the absorption lines produced by galaxies and intergalactic material that lie between the quasar and the observer. This spectrum of the $z = 1.34$ quasar PKS0454 + 039 was obtained with the Faint Object Spectrograph on the Hubble Space Telescope. The emission lines at ∼ 2400 Å and ∼ 2850 Å are Lyman-α and Lyman-β. The two strongest absorbers, due to galaxies, are a Damped Lyman-α Absorber at $z = 0.86$ and a Lyman Limit System at $z = 1.15$ (Charlton & Churchill, 2000).

at low resolution and this treshold made them relatively unambiguous to pick out. The equivalent width is $w_{\rm obs}(z \sim 2.5) > 17.5$ Å for $N(\text{H I}) > 10^{20}$ cm^{-2}. The probability that such a strong absorption feature is the result of blending is small. It is clear that this definition may introduce a systematic bias in the discussion of the nature of these DLAs and the work presented in this thesis generalises the definition in order to compare the properties of systems with $10^{19} <$ N(HI) $< 2 \times 10^{20}$ and N(HI) $> 2 \times 10^{20}$.

DLAs were originally thought to be the precursors of present day L_* disk galaxies, but there is growing evidence that they may instead be dominated by gas-rich proto-dwarf galaxies representing the basic building blocks of hierarchical growth of structure. Hypotheses for the morphology of DLAs range from large disk systems (Prochaska & Wolfe, 1998), to low surface brightness galaxies (Jimenez et al., 1999; Bowen et al., 2001; O'Neil, 2001) and dwarf galaxies (Matteucci et al., 1997). The Milky Way itself is detected in the spectrum of the low-redshift quasar 3C 273 (Figure 6). At low redshift, some of the galaxies that are responsible for the DLA absorption can be directly identified (Le Brun et al., 1997; Fynbo et al., 1999). These galaxies are a heterogeneous population: they are not just the most luminous galaxies, but include dwarf and low surface brightness galaxies, and there are many cases where no galaxy has been identified to sensitive detection limits. The size of one DLA, observed in PKS0458–020, has been measured from 21 cm absorption observations (see Figure 7) and is found to be greater that $8h^{-1}$ kpc (Briggs et al., 1989).

The kinematic structure of the absorption profiles of neutral and low ionisation species is consistent with the rotation of a thick disk (Prochaska & Wolfe, 1997), so it is possible that these are the $z = 3$ progenitors of normal spiral galaxies. However, this signature is not unique. It could also be the consequence of directed infall in an hierarchical structure formation scenario (Ledoux et al., 1998). Although the exact nature of the quasar HI absorbers is not known, they form a sample of systems unbiased as regards luminosity, specific morphology, or emission line strength, thus enabling studies of metallicity and HI evolution over a large redshift range.

For N(HI) $> 10^{19}$ atoms cm^{-2}, the optical depth at the Lyman limit is not necessarily large enough for the interior to be *self-shielded* from the external radiation field and thus might not be predominantly neutral HI gas. The correction for the ionising fraction is so far unknown and prevents reliable metallicity measurements and estimates of the total hydrogen content in these systems. Nevertheless, these quasar absorption lines are a powerful diagnostic tool for investigating the chemical composition of high redshift galaxies.

Fe abundance is often used to measure stellar metallicities and it would be convenient to use the same indicator in DLAs in order to allow for direct comparison. Fe II lines are usually present in large numbers in quasar spectra and have the

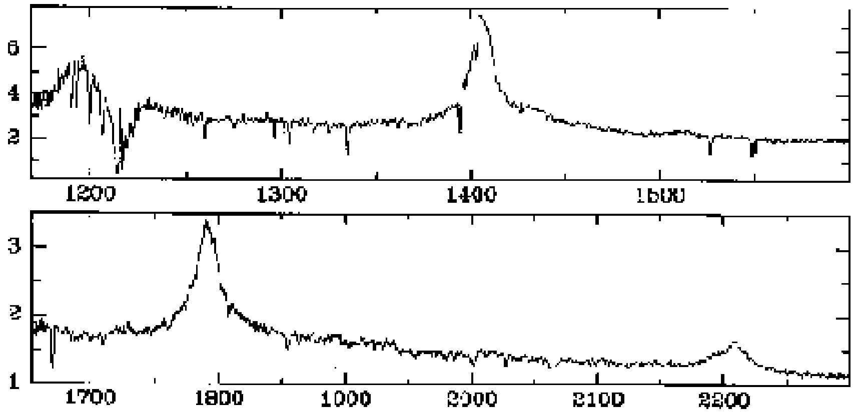

Fig. 6.— 3C 273 spectrum showing Lyα 1216Å absorption line due to the Milky Way. This illustrates the common nature of high column density intervening absorbers (Bahcall et al., 1991).

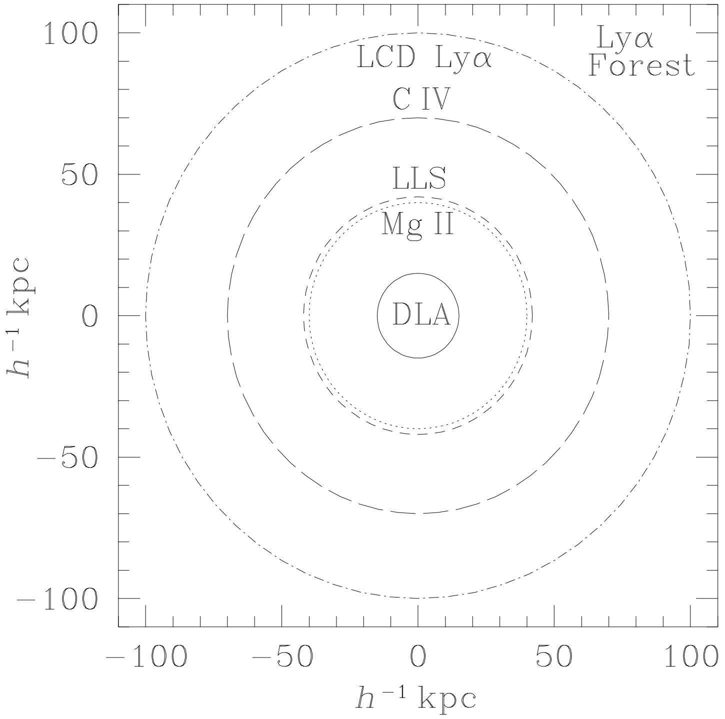

Fig. 7.— Quasar absorbers cross-sections showing the impact parameters at which various absorption features might arise in a typical galaxy (reproduced from Steidel, 1993, and kindly provided by Andy Bunker).

advantage that they exhibit a range of rest wavelengths and so are often detected (Savaglio & et al., 2000). However, the problem with studying metal abundances is the complication of dust depletion, the process by which particles are removed from the gas phase via condensation onto grains. Although the abundances of Zn and Fe track each other closely down to metallicities of $\lesssim 0.01Z_\odot$ (where $Z_\odot$ refers to the solar abundance) in Galactic stars, in the local inter-stellar medium an overabundance of Zn relative to Fe is often observed. This is due to differential depletion onto grains, such that whilst Fe is usually heavily depleted, very little Zn is seen to be incorporated into dust (Pettini et al., 1997). For these reasons, Zn (as well as Cr) are usually adopted as the metallicity indicator of choice for quasar absorbers metal abundances. It therefore follows that the relative abundances of [Zn/Cr] and [Zn/Fe] will provide an estimate of the fractions of these refractory elements which are missing from the gas-phase. Such studies show that at $z_{abs} > 1.5$, DLAs are generally metal poor, typically 1/10 of solar, with small amounts of dust depletion. These low abundances seem to persist for all redshifts observed, with no sign of metallicity evolution when column density weighted Zn abundances are considered.

DLA star formation histories can thus be derived from metal studies. α-elements (O, Si, S, Ar) are believed to be produced in Type II supernovae (SN II) after a relatively short lifetime of $\sim 10^7$ years. Most of the Fe-peak elements (Fe, Zn) come from the longer-lived ($\sim 10^9$ years) progenitors of Type Ia supernovae (SN Ia). The different lifetimes of supernovae progenitors means that an over-abundance of α is observed relative to Fe at low [Fe/H]. More recently, molecules have also been observed in DLAs. Measuring molecules at high-redshift is important because they dominate the cooling function of neutral metal-poor gas. Petitjean et al. (2000) have detected molecular hydrogen (H_2) in 11 absorbers and use these data to deduce that most of the DLA systems arise in warm and diffuse neutral gas. These measurements allow investigation of the processes of dust formation as well as cooling and photodissociation from the first stars (Levshakov et al., 2000).

2. **Lyman-limit Systems** (hereafter LLS) have hydrogen column densities N(HI) $> 1.6 \times 10^{17}$ atoms cm^{-2} and are optically thick at the Lyman limit due to the HI photo-ionisation:

$$H^o + \gamma \rightarrow H^+ + e^- \tag{1.1}$$

where the photon energy, 13.6 eV, corresponds to 912 Å rest wavelength. These absorbers are easily identifiable by their distinctive break signature in the quasar spectrum (see Figure 5). The optical depth, τ, is expressed as follows:

$$\tau = N(HI) \times \sigma \tag{1.2}$$

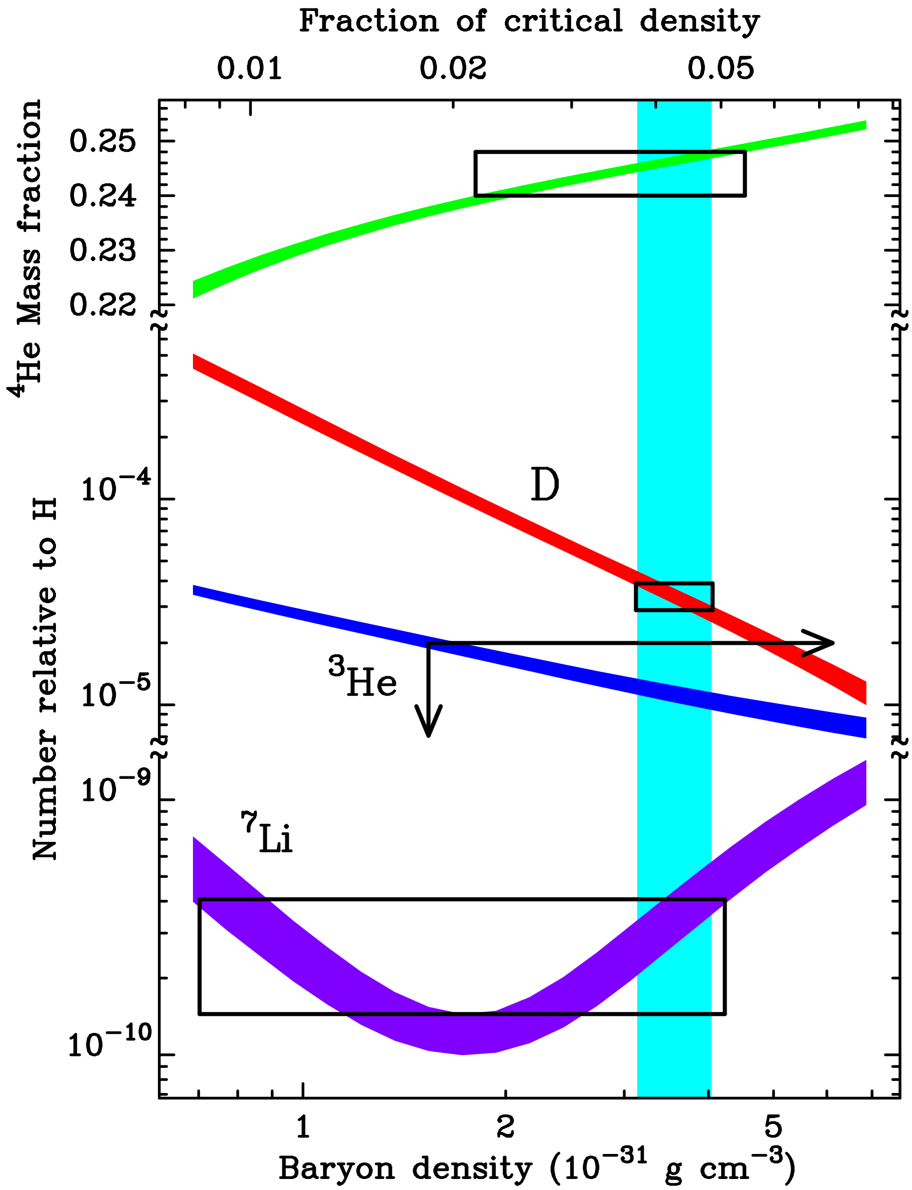

Fig. 8.— Abundances expected for the light nuclei ^{4}He, D, ^{3}He and ^{7}Li (top to bottom) calculated in standard Big Bang Nucleosynthesis. The 95% confidence intervals are shown by the vertical widths of the abundance predictions. The horizontal scale is expressed in units of the baryon density or critical density for a Hubble constant of 65 kms^{-1} Mpc^{-1} (Tytler et al., 2000).

where σ is the HI photo-ionisation cross-section 6.8×10^{-18} cm^{-2}. For $\tau_{912} = 1$ (optically thick), N(HI) has to be $= 1.6 \times 10^{17}$ atoms cm^{-2}. The optical depth below 912 Å is proportional to $\tau_{912}(\lambda/912)^3$. For example, if a LLS lies at $z = 3$ with a column density N(HI) $= 10^{18}$ atoms cm^{-2}, the continuum reaches zero ($\tau_{912} = 6$) at 3648 Å and the flux only recovers at around 2000 Å ($\tau = 1$). The detection of these systems is thus fairly easy, even in medium resolution spectra.

"Grey" LLS have optical depth $\tau < 1$ and thus produce a partial break in the quasar spectrum. Because of their relatively small column density, they provide some of the best candidates for measurement of the primordial abundance of deuterium (see Figure 8 and Molaro et al., 1999; Levshakov et al., 2000; O'Meara et al., 2001, and references herein). The first synthesis of light elements (D, He and Li) took place in the early Universe and heavier elements have then been produced through stellar nucleosynthesis. High-resolution observations of quasar absorbers can be used to determine the primordial abundances of elements formed in the Big Bang, which provides a fundamental tool for testing the Big Bang theory and a unique measure of the baryonic density of the Universe, $\Omega_b h^2$. Note that it has been demonstrated recently (D'Odorico et al., 2001; Pettini & Bowen, 2001) that DLAs and sub-DLAs can also be used for D measurements. Pettini & Bowen (2001) computed the weighted mean of the 6 D measurements currently available at high-redshift and found:

$$D/H = (2.2 \pm 0.2) \times 10^{-5} \tag{1.3}$$

The ionisation state of LLSs can be constrained by measuring the column density of the same ion in different ionising states (i.e. Fe^{+} and Fe $^{++}$) and comparing the CLOUDY software package (Prochaska, 1999). In addition, LLS provide information on the ionising photons of the intergalactic medium. The exact nature of LLS is not known but, at $z < 1$, they are probably associated with galactic halos (Steidel et al., 1994).

3. Finally, the **Lyman-α Forest** is composed of many low column density systems ranging from N(HI) $= 10^{12}$ to 1.6×10^{17} atoms cm^{-2}. It is currently believed that the absorption in the Lyα forest is caused not by individual, confined clouds, but by a gradually varying density field characterized by overdense sheets and filaments and extensive, underdense voids which evolve with time (Carswell & Rees, 1987), as shown in Figure 9. Rauch (1998) provides an excellent review of our current knowledge of the Lyα forest.

   The observation of multiple lines of sight has been sucessful in determining the size of the Lyα clouds (see §1.1.2). In particular, D'Odorico et al. (1998) analysed all the data available at the time and concluded that Lyα forest clouds have a typical size of $\sim 350h_{100}^{-1}$ kpc for a spherical geometry or to $\sim 400h_{100}^{-1}$ kpc for a disc

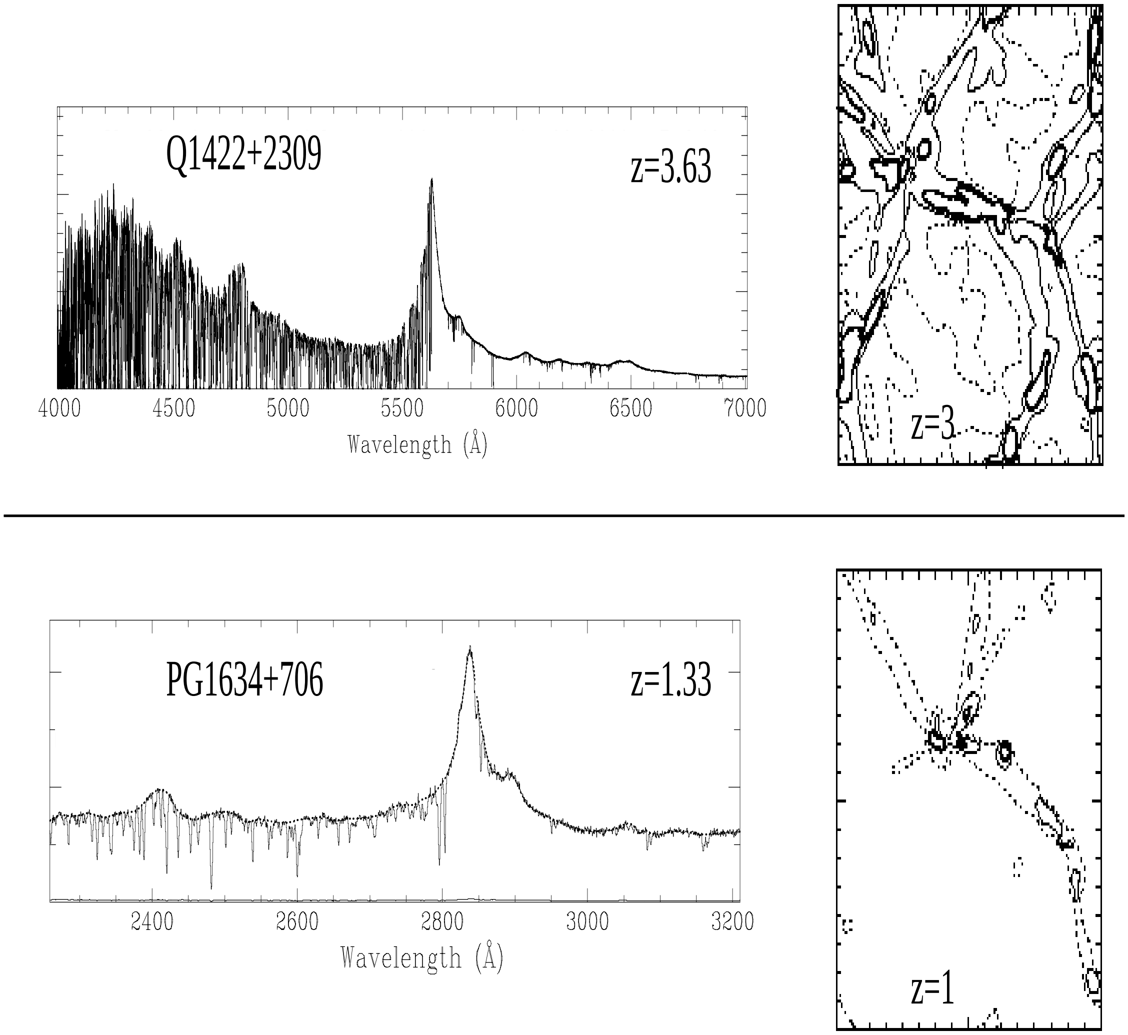

Fig. 9.— Illustration of structure evolution of intergalactic gas from high to low redshift. The upper spectrum of a $z = 3.6$ quasar is a Keck/HIRES observation, while the lower spectrum is a FOS/HST observations of a $z = 1.3$ quasar. Higher redshift quasars show a much thicker forest of Lyman-α lines. Slices through N–body/hydrodynamic simulation results at the two epochs $z = 3$ and $z = 1$ are shown in the right–hand panels. Three contour levels are shown: $10^{11} cm^{-2}$ (dotted lines), $10^{12} cm^{-2}$ (solid lines) and $10^{13} cm^{-2}$ (thick solid lines) (Charlton & Churchill, 2000).

geometry. Line of sight clustering distribution analysis is also possible with a two-point correlation function. There are several contradictory results in the literature but the consensus is for weak clustering on small scales, with little evidence for correlations over larger ($\Delta v > 300$ km s^{-1}) scales.

At first, the Lyα forest was thought to contain pristine material, but traces of metals were detected later on (Meyer & York, 1987). Ellison et al. (2000), have used two different methods to detect CIV in the forest: in the first approach, a high signal-to-noise ratio stacked spectrum produced by combining the data of two quasars leads to no detection of significant metals and in the second approach, measurements of individual pixel optical depths show that there are indeed CIV lines in the Lyα forest. This work illustrates the difficulties encountered in detecting metals in the Lyα forest. These observations make possible the study of chemical enrichment in the inter-galactic medium and hence the epoch at which the first generations of stars formed and then distributed their metals into the surrounding environment (Ferrara et al., 2000).

Gunn-Peterson Effect

Observing the Lyα forest at high-redshifts gives us direct indications of the ionisation state of the early Universe. We see some continuum blueward of the quasar's Lyα emission contrary to what one would expect from a neutral medium (Gunn & Peterson, 1965). This indicates that the inter-galactic medium (IGM) is predominantly ionised hydrogen even in the highest-redshift quasars, although recent observations at $z \sim 6$ show the absence of flux in the forest over a large region (Figure 10 Becker et al., 2001; Djorgovski et al., 2001). Since the high energy photons required to fully ionise helium are much rarer than those capable of re-ionising hydrogen, a Gunn-Peterson He trough is predicted to be present at lower wavelength than the corresponding H feature (Outram, 1999). Gunn-Peterson absorption has been detected for the He II Lyα ($\lambda_{rest} = 303.7822$ Å) at $z \sim 3$ (Jakobsen et al., 1994; Reimers et al., 1997). Similarly, if we were to observe the spectrum of a quasar before the re-ionisation of the Universe, the flux blueward of the quasar emission is expected to be almost fully absorbed leading to the so-called "Lyman-α prairie" (Loeb, 1999).

Proximity Effect

Another observational characteristic of the Lyα forest is the decreasing line density at the immedidate vicinity of the quasar first discovered by Carswell et al. (1982). This is probably due to the quasar Lyman continuum radiation boosting the metagalactic ionising field J_ν. Measurements of the so-called "proximity effect" have been used to infer the flux of the ionising background, $J_\nu \simeq 10^{-21}$ (Bajtlik et al., 1988; Williger et al., 1994). These measurements of J_ν suggest that known quasars alone cannot account for the ionising UV background seen, implying that other sources are required (Scott et al., 2000a,b).

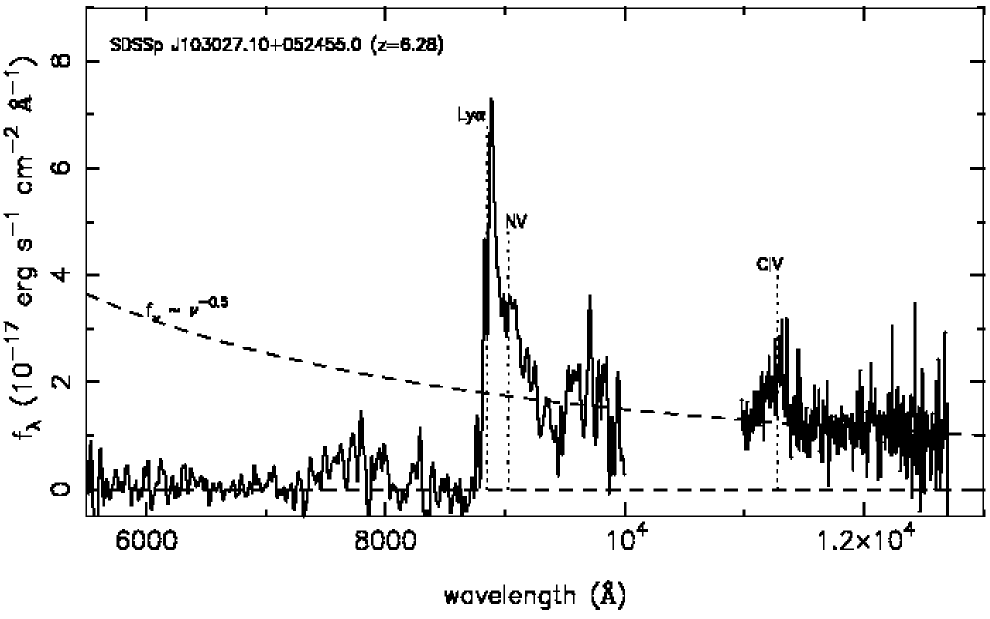

Fig. 10.— Optical and near-IR spectrum of SDSS 1030+0524, the highest-redshift ($z \sim 6.28$) quasar currently known discovered as part of the Sloan Digital Sky Survey (Fan et al., 2001b). A Keck spectrum of the object (Becker et al., 2001) shows the absence of flux over a large region, blueward of the lyman-α emission line. This suggests a possible first detection of the complete Gunn-Peterson effect (caused by neutral hydrogen in the intergalactic medium), but does not necessarily indicate that the quasar is observed prior to global re-ionisation.

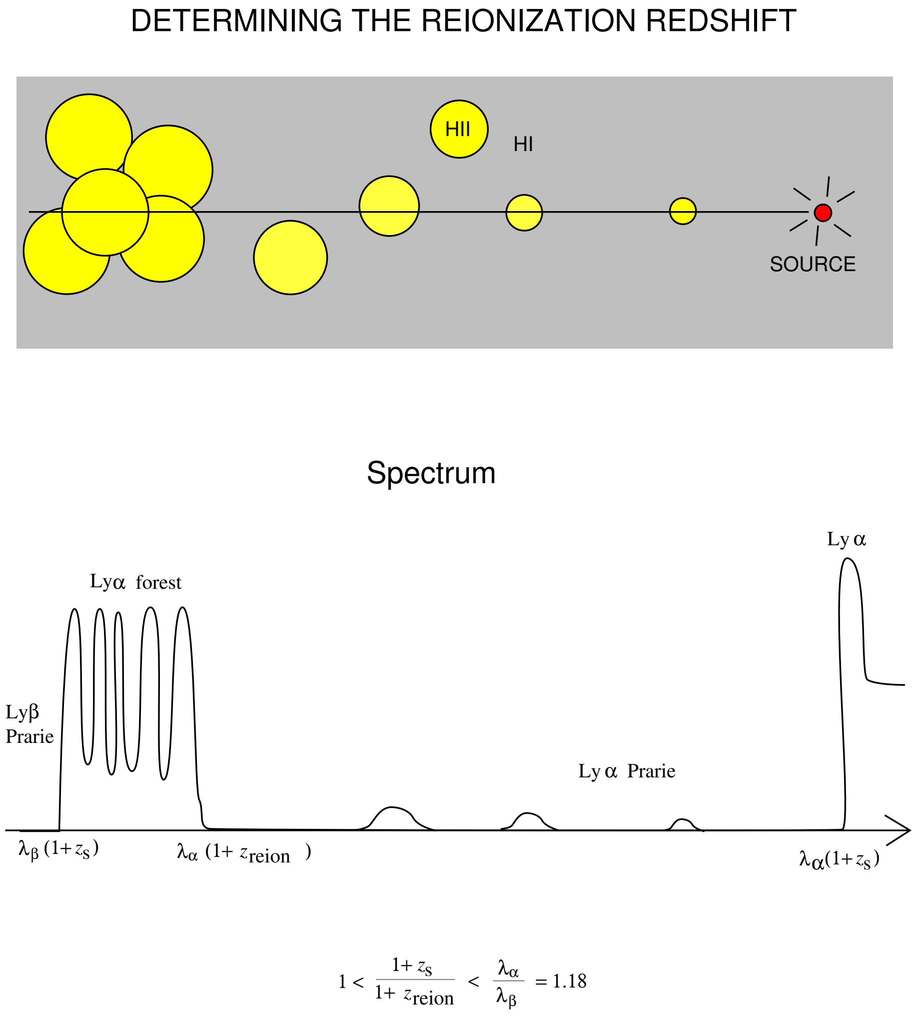

Fig. 11.— Expected quasar spectrum at z_{em} slightly above the redshift of the reionisation of the Universe. The "Lyα prairie" indicates the region where the Universe was still neutral (Loeb, 1999).

II) $z_{abs} > z_{em}$

Fewer absorption lines are observed at wavelengths longward of the quasar emission feature. These are not due to neutral hydrogen but are associated with metal systems. C, N, O, Si, Fe, Al, Mg, but also Ni, Zn, Cr, S and more recently Co (Ellison et al., 2001a) are detected. These are often multiple systems corresponding to different cloud components which can be resolved in high-resolution data. Magnesium II and Carbon IV are characteristic doublets and are easily detectable even in low resolution quasar spectra:

1. **CIV doublet (rest frame 1548 Å and 1551 Å):** Simulations have shown that the observed CIV kinematic structure and column densities can be well reproduced by merging of proto-galactic clumps (Haehnelt et al., 1996). Compact halos of hot gas with temperatures close to $\sim 10^5$ K seem to sucessfully account for the observed multi-component nature of the CIV absorbers. Based upon the number density of absorbers, dN/dz, which gives the average number of systems per unit redshift path, the sky-projected cross sections can be calculated for an assumed galaxy luminosity function. The CIV absorption-selected systems (to rest-frame detection sensitivity of 0.4 Å) are thus inferred to have a 70 kpc diameter (see Figure 7). The methods used to study the properties of CIV systems can be split into two different approaches. The first approach consists of observing CIV in high signal-to-noise ratio, high-resolution spectra and determining its column density down to log N(CIV) $\sim$ 11.5 atom cm^{-2}. This allows (i) detailed kinematics and temperature studies (Rauch et al., 1996) which shows that CIV components may be the building blocks of future normal galaxies; (ii) the determination of the low end of the CIV column density distribution (see Lyα forest section); (iii) the study of velocity structure within the halos (Petitjean & Bergeron, 1994; Crotts et al., 1997), but is limited to a few lines of sight. The second approach consists of studying a statistically significant sample of absorbers by constructing a large homogenous sample (Sargent et al., 1988; Steidel, 1990a). This method has proved successful at describing the number density and clustering properties of metals, but previous studies were restricted to the range $z \lesssim 3.5$ (Sargent et al., 1988) or were inhomogenous (Quashnock et al., 1996). The data presented in this thesis provide a sample of 80 CIV absorbers in the redshift range $3.0 < z < 4.5$ which could be used to study the characteristics and evolution of the galactic halos.

   Along with the CIV doublet, another very important transition is the CII line. The temperature of the Cosmological Background Radiation, T_{CMB} can also be measured using the abundance ratio of excited states of CII. This puts a direct constraint on the Big Bang, theory although only one measurement has been made so far: Srianand et al. (2000) have derived $6.0 < T_{CMB} < 14$ K at $z \sim 2.3$ when 9.1 K is expected in the Hot Big Bang cosmology.

2. **MgII doublet (rest frame 2796 Å and 2803 Å):** MgII systems are known to be associated with the extended gaseous envelopes of bright galaxies which

have been detected in emission at $z \sim 0.6$ (Bergeron & Boisse, 1991). The most extensive MgII surveys have been conducted by Lanzetta et al. (1987); Sargent et al. (1988); Petitjean & Bergeron (1990); Steidel & Sargent (1992); Churchill et al. (2000a,b). Using similar assumptions as in the previous paragraph (number density of absorbers and Schecter galaxy luminosity function), MgII systems are found to be 40 kpc in diameter (detection sensitivity of 0.3 Å) or 60 kpc (detection sensitivity of 0.02 Å). The MgII absorbing galaxies appear to be consistent with a normal 0.7 L_* Sb galaxy having a roughly constant star formation rate since z ~ 1. The data presented in this thesis provide a sample of 48 MgII absorbers in the redshift range $1.3 < z < 2.2$. An excellent review of our current knowledge on the topic of MgII absorbers compiled by Chris Churchill (1999) is available on-line at the following address: http://www.astro.psu.edu./users/cwc/qsogroup/mgii-over.html

III) $z_{abs} \sim z_{em}$

Associated systems are, by definition, at the same redshift as the quasar. They could be explained by (Petitjean, 1999):

- galaxies which are part of the quasar cluster
- gas from the galaxy within which the active galactic nuclei (AGN) is embedded
- gas ejected by the quasar itself

Because they are close to the quasar, these systems are often more ionised than other metal lines and have higher heavy element abundances (Petitjean et al., 1994).

IV) Broad Absorption Lines

Broad Absorption Lines (hereafter BALs) are observed in about 10% of all quasars (Weymann et al., 1991). They are characterised by troughs with outflow velocities up to 60,000 $\mathrm{km\,s^{-1}}$ blueward of the quasar emission redshift. They are often highly ionised and have high metallicities suggesting that BALs have are connected with the nuclear region of the quasar (the active galactic nuclei). Although *some* of these absorption lines may belong to external galaxies close in velocity space to the quasar, there is direct evidence from time-variability of the line strength (Hamann et al., 1995; Barlow et al., 1997; Vilkoviskij & Irwin, 2001) or partial coverage of the background source (Ganguly et al., 1999) that many of these lines are physically associated with the quasar. BALs have previously been thought not to occur in radio-loud quasars but recent discoveries by Becker et al. (2000) indicate that this is not always the case. This finding is problematic for simple unified models in which BAL quasars are a subset of quasars seen nearly edge-on and thus raises further questions about the nature of these objects.

1.3.2 Absorption Line Formation and Column Density Determination

Absorption Line Profile

The spectral flux intensity, $F(\nu)$, can be expressed in terms of the unabsorbed continuum intensity, $F_0(\nu)$, and the frequency ν:

$$F(\nu) = F_0(\nu) e^{-\tau(\nu)} \tag{1.4}$$

where $\tau(\nu)$, the optical depth, is expressed as a function of number density of atoms, n (or number of atoms per surface area, i.e. column density N) and cross-section $\sigma(\nu)$:

$$\tau(\nu) = \int_0^{+\infty} n\sigma(\nu) ds = N\sigma(\nu) \tag{1.5}$$

Two different processes lead to the line broadening that gives absorption features their characteristic profile:

Lorentzian Profile

Natural (damping) broadening of an absorption line is due to the intrinsic undertainty ΔE in the energy of the upper atomic level as expressed by the Uncertainty Principle: $\Delta E \Delta t \sim \hbar$. This leads to a Lorentz profile:

$$\sigma_L(\nu) = \left(\frac{\pi e^2}{m_e c}\right) f_{osc} \frac{\Gamma/4\pi^2}{(\nu - \nu_0)^2 + (\Gamma/4\pi)^2} \tag{1.6}$$

where m_e and e are the mass and charge of an electron respectively, c is the speed of light, f_{osc} is the transition oscillator strength, ν_0 is the central frequency and Γ is the total damping constant, i.e. the reciprocal of the mean lifetime of the upper energy state.

Gaussian Profile

Within the cloud that we are observing via quasar absorbers, the ions may have a characteristic radial velocity relative to the observer, resulting in a *Doppler-shift.* These internal motions can be characterised as a Gaussian velocity distribution:

$$P(v) = \frac{1}{b\sqrt{\pi}} e^{-(v/b)^2} \tag{1.7}$$

where the Doppler width, b, is determined by contributions from both thermal and turbulent motions within the absorbing cloud:

$$b = \sqrt{b^2_{thermal} + b^2_{turbulent}} = \sqrt{\frac{2kT}{m_{ion}} + b^2_{turbulent}} \tag{1.8}$$

where k is Boltzmann's constant.

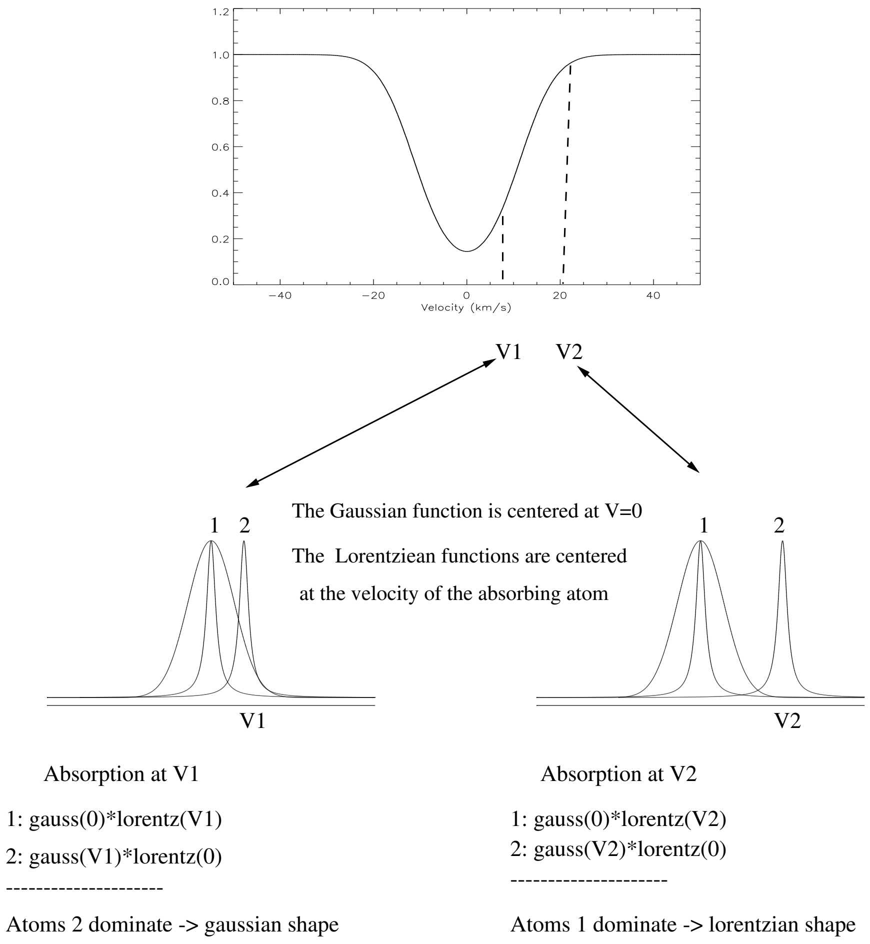

Fig. 12.— Formation of Voigt profiles from the convolution of Gaussian and Lorentzian functions. At V1, the Lorentzian function falls off more slowly at large ν than the Gaussian profile that describes Doppler broadening. It is thus the latter which dominates the absorption profile. However, at V2, the prominent damping wings completely dominate the outer parts of the line profile leading to a Lorentzian shape. This corresponds to very high column density absorbers, the so-called Damped Lyman-α systems (Petitjean et al., 1998).

Voigt Profile

Convolving the natural (Lorentz profile, see equation 1.6) and Doppler (Gauss profile, see equation 1.7) broadening produces a Voigt profile with an optical depth, τ:

$$\tau(\nu) = \frac{\sqrt{\pi}e^2}{m_e}\frac{Nf_{osc}}{b\nu}H(a,u) \tag{1.9}$$

where:

$$H(a,u) = \frac{a}{\pi}\int_{-\infty}^{+\infty}\frac{e^{-y^2}dy}{(u-y)^2+a^2} \tag{1.10}$$

and:

$$a = \frac{\Gamma}{4\pi\Delta\nu}; \qquad u = \frac{c(\nu-\nu_0)}{\nu_0 b}; \qquad y = v/b \tag{1.11}$$

The core of the Voigt function is thus Gaussian, while the extended wings of the profile are Lorentzian. This is illustrated by Figure 12: at V1, the Lorentzian function falls off more slowly at large ν than the Gaussian profile that describes Doppler broadening. It is thus the latter which dominates the absorption profile. However, at V2, the prominent damping wings completely dominate the outer parts of the line profile leading to a Lorentzian shape. This corresponds to very high column density absorbers, the so-called Damped Lyman-α systems.

The optical depth at the line centre is then given by:

$$\tau(\lambda_0) = \frac{\sqrt{\pi}e^2}{m_e c}\frac{Nf_{osc}\lambda_0}{b} = 1.497\times10^{-15}\frac{N(\mathrm{cm^{-2}})\mathrm{f_{osc}}\lambda_0(\mathrm{\AA})}{b(\mathrm{kms^{-1}})} \tag{1.12}$$

Absorption lines in quasar spectra are commonly fitted with theoretical Voigt profiles, although this section shows that this is based on the assumption that the velocity distribution of the atoms is described by a Gaussian function.

The Curve of Growth

At medium spectral resolution, it is not always possible to fit a Voigt profile to the absorption feature. In that case, we make use of the *curve of growth* which relates the equivalent width of the absorbers with its column density N (the equivalent width is traditionally used although measuring the Full Width Half Maximum, FWHM, of the line would be more appropriate as it is less dependent upon the continuum position). In general, the equivalent width of an absorption line, $W(\lambda)$, is defined as:

$$W_{obs}(\lambda) = \int\frac{F_0-F(\lambda)}{F_0}d\lambda_{obs} = \int(1-e^{-\tau(\lambda)})d\lambda_{obs} \tag{1.13}$$

where the observed equivalent width is:

$$W_{obs}(\lambda) = W_{rest}(\lambda)\times(1+z_{abs}) \tag{1.14}$$

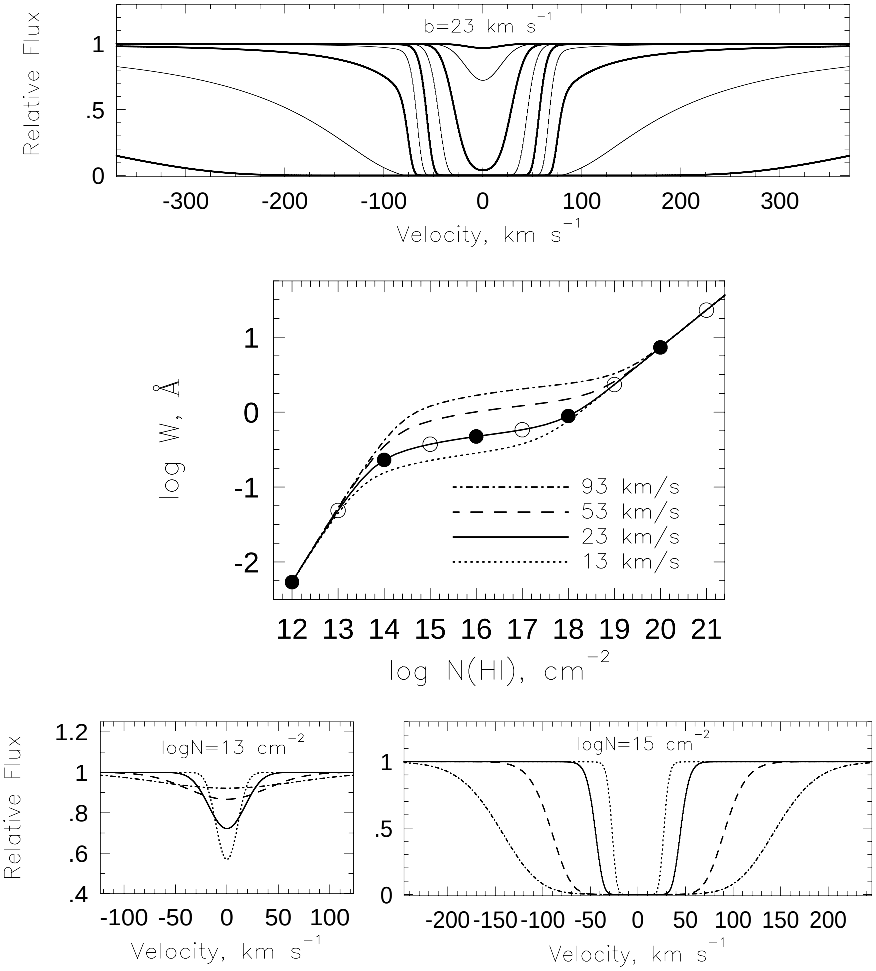

Fig. 13.— Illustration of the different regimes of the curve of growth. The middle panel shows the curve of growth for the HI Lyman-α transition, relating the equivalent width, $W(\lambda)$, of the absorption profile its column density, N(HI). The different curves represent four different values of the Doppler parameter: b = 13, 23, 53, and 93 $\mathrm{km\,s^{-1}}$. The upper panel shows absorption profiles with Doppler parameter $b = 23$ $\mathrm{km\,s^{-1}}$ for the series of neutral hydrogen column densities N(HI) = 10^{12} – 10^{20} atoms cm^{-2}. The thick (thin) curves correspond to the filled (open) points on the $b = 23$ $\mathrm{km\,s^{-1}}$ curve of growth (middle panel), starting at N(HI) = 10^{12} atoms cm^{-2}. For N(HI) $< 10^{13}$ atoms cm^{-2}, known as the linear part of the curve of growth, the equivalent width does not depend on b. The lower left panel shows that, at fixed N(HI), the depth of the profile is smaller for large Doppler parameter, b, such that the equivalent width remains constant. On the flat part of the curve of growth, profiles are saturated and the equivalent width increases with b for constant N(HI). For N(HI) $\gtrsim 10^{19.5}$ atoms cm^{-2}, the profile develops damping wings, which dominate the equivalent width (the so-called *DLA* and *sub-DLA regimes*) and thus allows for reliable column density measurements (Charlton & Churchill, 2000).

The equivalent width of an absorption line is thus independent of the spectral resolution since it is an integral over λ. The HI Lyα curve of growth is shown in Figure 13. There are three distinct regimes:

1. **The Linear Part.** The lines in this regime are unsaturated and correspond to absorbers with small column densities (N(HI) $< 10^{13}$ atoms cm^{-2}). Because the feature is optically thin, the equivalenth width is not dependent on the Doppler parameter b:

$$N = 1.13 \times 10^{20} \frac{W(\lambda)}{\lambda_0^2 f_{osc}} \tag{1.15}$$

2. **The Flat Part.** The lines in this regime are saturated and dominated by the Doppler contribution (see Section 1.3.2 above). Their column density, N, depend on the Doppler parameter b at a given equivalenth width $W(\lambda)$:

$$W(\lambda) \sim \frac{2b\lambda_0}{c} \sqrt{\ln\left(\frac{\pi^{0.5} e^2 N \lambda_0 f_{osc}}{m_e c b}\right)} \tag{1.16}$$

   In order to reliably determine the column density of such absorption systems, higher-order Lyman series lines which have smaller oscillator strength, f, (and thus lie on the linear part of the curve of growth) are required.

3. **The Damping Part.** The lines in this regime are saturated and dominated by the Lorentzian damping wings (see Section 1.3.2 above). They correspond to high column densities (N(HI) $\gtrsim 10^{19}$ atoms cm^{-2}) and their equivalent width is proportional to the column density independently of b-value:

$$N(HI) = 1.88 \times 10^{18} \times W_0^2(\text{Å})\text{cm}^{-2}. \tag{1.17}$$

1.4 Scientific Motivation

1.4.1 Thesis Motivation

One of the fundamental phenomena still poorly understood in cosmology is the detailed process of the origin of structure formation. Significant theoretical progress has been recently achieved with the development of Smooth Particle Hydrodynamic and Semi-Analytical simulations. But observationally probing the early Universe is crucially dependent upon new methods to overcome the natural challenges of high-redshift (z$\sim$4) observations and upon the advancement of telescope-related technologies. In recent years, an extremely successful method to observationally study early stages of galaxy formation has been provided by the study of quasar absorbers.

The primary goal of our spectroscopic campaign has been to obtain a statistically significant number of high-redshift quasar absorbers to answer the questions raised by the apparent deficit of high column density systems in the early Universe (Storrie-Lombardi et al., 1996a; Storrie-Lombardi & Wolfe, 2000). In particular we aim to study in more detail the evolution with redshift of the column density distribution, number density, and comoving mass density of high column density HI absorption systems. The aim of our new survey for quasar absorbers is to better understand the high-redshift end of the mass density of neutral hydrogen by significantly improving the statistics at $z \gtrsim 3.5$. Several fundamental questions remain including: locating the epoch of DLA assembly; clarifying the relationship between Lyman limit systems and damped absorbers via a detailed study of the column density distribution of quasar absorbers and its evolution with redshift; and measuring the total amount of neutral hydrogen contained in quasar absorbers and studying how this varies with redshift. This thesis emphasizes the impact of our new survey on these issues.

1.4.2 Thesis Outline

This thesis is organised as follows. In Chapter 2, we provide the details of the set-up for each observational run, describe the data reduction and present the quasar spectra together with redshift and magnitude measurements. Chapter 3 presents continuum fitting and continuum depression measurements of all our quasar spectra. These measurements are then compared with the most recent simulations. The sample of Lyman-limit systems is introduced in Chapter 4 which also includes an analysis of their number density and column density distribution. Damped Ly-α absorbers are presented in Chapter 5 together with a study of their properties. Metal absorbers detected in the quasar spectra are also listed. The cosmological neutral gas mass evolution and implications of our results for theories of structure formation are detailed in Chapter 6. In Chapter 7, the conclusions of this thesis are summarised and a brief discussion of the extension of this work to on-going and future projects is given.

This work assumes $H_0 = 65\,\mathrm{km\,s^{-1}\,Mpc^{-1}}$, $\Omega_M = 0.3$ and $\Omega_\Lambda = 0.7$, although results in other cosmologies are also presented in order to enable comparison with previous works.

Chapter 2

The $z \gtrsim 4$ Quasar Sample

'La souffrance est dans la solitude qui l'accompagne'
André Malraux

This Chapter details the observations of the 66 $z \gtrsim 4$ quasar studied in this thesis which were undertaken in four different runs. All the observations were carried out during two observing runs at the 4.2 m William Herschel telescope (WHT) of the Isaac Newton Group of telescopes in the Canary Islands (Section 2.2.1) and two observing runs at the Blanco 4 m telescope at the Cerro Tololo Inter-American Observatory (CTIO) in Chile (Section 2.2.2). Section 2.3.1 gives details on the data reduction process and the reduced spectra are presented in Section 2.3.2. The redshift and magnitude of each object have been measured and are tabulated in Section 2.4.2 and 2.4.3, respectively. Section 2.5 gives details on individual quasar spectra.

2.1 Introduction

This chapter presents the high signal-to-noise, ~ 5 Å resolution (FWHM) spectra of 66 $z \gtrsim 4$ bright quasars obtained with the 4 m Cerro Tololo Inter-American Observatory and 4.2 m William Hershel telescopes [1]. The primary goal of these observations was to undertake a new survey for intervening absorption systems detected in the spectra of background quasars. We look for both Lyman-Limit Systems (column densities $N_{HI} \geq 1.6 \times 10^{17}$ atoms cm^{-2} - see Chapter 4) and Damped Lyα Systems (column densities $N_{HI} \geq 2 \times 10^{20}$ atoms cm^{-2} - see Chapter 5). Ten of the quasars presented here exhibit intrinsic broad absorption lines (BAL).

---

[1] This sample is based on observations obtained at the William Herschel Telescope which is operated on the island of La Palma by the Isaac Newton Group in the Spanish Observatorio del Roque de los Muchachos of the Instituto de Astrofisica de Canarias, on observations made at the Cerro Tololo Intra-American Observatory which is operated by the Association of Universities for Research in Astronomy, under a cooperative agreement with the National Science Foundation as part of the National Optical Astronomy Observatories and on data obtained at the W.M. Keck Observatory, which is operated as a scientific partnership among the California Institute of Technology, the University of California and the National Aeronautics and Space Administration. The Observatory was made possible by the generous financial support of the W.M. Keck Foundation.

Any survey for quasar absorbers begins with a search for bright quasars and so constitutes an ambitious observational program. We observed sixty-six $z \gtrsim 4$ quasars discovered by various groups (Fan et al., 1999; Warren et al., 1991; Kennefick et al., 1995a; Storrie-Lombardi et al., 1996c; Zickgraf et al., 1997; Kennefick et al., 1995b; Henry et al., 1994; Hook, prep; Hall et al., 1996) almost all of which have not been previously studied at such resolution ($\approx$ 5 Å) and signal-to-noise (ranging from 10–30). We obtained optical spectra at the 4.2 m William Herschel Telescope for the northern quasars and at the 4 m Cerro Tololo Inter-American Observatory for the southern objects. More information about $z \gtrsim 4$ quasars is available at the following URL: http://www.ast.cam.ac.uk/~quasars.

2.2 Observations

High signal-to-noise optical spectrophotometry was obtained covering approximately 3500 Å to 9000 Å, the exact range depending on which instrument was used for the observations. A journal of the observations is presented in Table 2.2.1.

2.2.1 WHT Runs

Thirty-one (including the misclassified z=1.90 quasar PSS J0052+2405) quasars were observed at the WHT during 1998 September 22-24 and 1999 March 18-19. The integration times were typically 1800 – 3600 seconds. We used the ISIS double-spectrograph which consists of two independent arms fed via a dichroic allowing for blue and red observations to be carried out simultaneously. Gratings with 158 lines mm^{-1} and a dichroic to split the light at ~5700 Å were used. This gives a dispersion of 2.89 Å pixel^{-1} in the red arm and 1.62 Å pixel^{-1} in the blue. The gratings were arranged so that the blue part of the spectrum was centered on 4500 Å while the red was centered on 7000 Å. On the blue arm a thinned coated English Electric Valve (EEV) 2048×4096 CCD with 13.5 μm pixels was used as detector. On the red arm a thinned coated Tektronix 1024×1024 CCD with 24 μm pixels was used. All the narrow-slit observations were taken with a slit width of 1.2 – 1.5 arcsec while the wide-slit observations were carried out with a slit width of 5 – 7 arcsec. Blind-offsetting from bright $\sim$ 15–17th magnitude stellar fiducials was used to position the quasars in the slit partly to save acquisition time and partly because the majority of the quasars were not visible using the blue sensitive TV acquisition system. Readout time was reduced by windowing the CCDs in the spatial direction.

Table 1: Journal of Observations

Quasar Name	Telescope	Observing Date	Exp. Time B/R^a (secs)	Wide Slit	Ref
PSS J0003+2730	WHT	1998 Sep 22	3600/3600	yes	1
BR J0006−6208	CTIO	1998 Oct 14	3600	yes	3
BR J0030−5129	CTIO	1998 Oct 15	3600	yes	3
PSS J0034+1639	WHT	1998 Sep 22	3600/3600	yes	1
SDSS J0035+0040	CTIO	1999 Oct 10	8100	yes	4
PSS J0052+2405	WHT	1998 Sep 23	3600/3600	yes	2
Q J0054−2742	CTIO	1999 Oct 12	2700	yes	5
PSS J0106+2601	WHT	1998 Sep 24	3600/3600	yes	1
PSS J0131+0633	CTIO	1999 Oct 12	3600	no	2
PSS J0133+0400	CTIO	1999 Oct 12	3600	no	2
PSS J0134+3307	WHT	1998 Sep 22	3600/3600	yes	1
PSS J0137+2837	WHT	1998 Sep 24	5200/3600	yes	1
PSS J0152+0735	WHT	1998 Sep 24	3600/3600	yes	1
PSS J0207+0940	CTIO	1999 Oct 12	3600	no	2
PSS J0209+0517	CTIO	1999 Oct 12	2400	no	2
SDSS J0211−0009	CTIO	1999 Oct 10	8100	no	4
BR J0234−1806	CTIO	1999 Oct 09	5400	yes	3
PSS J0248+1802	WHT	1998 Sep 22	3600/3600	yes	6
BR J0301−5537	CTIO	1998 Oct 16	3600	yes	3
BR J0307−4945	CTIO	1998 Oct 14	5400	yes	3
SDSS J0310−0014	CTIO	1999 Oct 9	9900	no	4
BR J0311−1722	CTIO	1999 Oct 11	3600	yes	3
PSS J0320+0208	CTIO	1999 Oct 12	3600	no	2
BR J0324−2918	CTIO	1999 Oct 11	3600	yes	3
BR J0334−1612	WHT	1998 Sep 23	2740/1650	no	3
SDSS J0338+0021	Keck	1999 Feb 17	3000/3600	no	4
BR J0355−3811	CTIO	1998 Oct 15	3600	yes	3
BR J0403−1703	WHT	1999 Sep 19	1800/1800	no	7
BR J0415−4357	CTIO	1998 Oct 16	5400	yes	3
BR J0419−5716	CTIO	1998 Oct 14	3600	yes	3
BR J0426−2202	CTIO	1999 Oct 11	3000	yes	3
PMN J0525−3343	CTIO	1998 Oct 15	3600	yes	3
BR J0529−3526	CTIO	1998 Oct 14	5400	yes	3
BR J0529−3552	CTIO	1998 Oct 15	3600	yes	3
BR J0714−6455	CTIO	1998 Oct 15	3600	yes	3
PSS J0747+4434	WHT	1998 Sep 22	1800/1800	no	1
RX J1028−0844	WHT	1999 Mar 19	2700/2700	yes	8
PSS J1048+4407	WHT	1999 Mar 19	2700/2700	yes	9
PSS J1057+4555	WHT	1999 Mar 19	1800/1800	yes	9
PSS J1159+1337	WHT	1999 Mar 18	2700/2700	yes	1
PSS J1253−0228	WHT	1999 Mar 18	2700/1800	yes	2
BR J1310−1740	WHT	1999 Mar 19	2700/2700	yes	3
BR J1330−2522	WHT	1999 Mar 19	2700/2700	yes	3
FIRST J1410+3409	WHT	1999 Sep 19	2700/2700	yes	1

PSS J1438+2538	WHT	1999 Mar 18	2700/2700	yes	9
PSS J1456+2007	WHT	1999 Mar 18	2700/2700	yes	1
BR J1603+0721	WHT	1999 Mar 19	2700/2700	yes	3
PSS J1618+4125	WHT	1999 Mar 19	2700/2700	yes	1
PSS J1633+1411	WHT	1999 Mar 19	1800/1800	yes	2
PSS J1646+5514	WHT	1998 Sep 23	3600/3600	yes	1
PSS J1721+3256	WHT	1998 Sep 24	1800/3600	yes	1
RX J1759+6638	WHT	99/98 Mar 19/Sep 23	6300/6300	yes	10
PSS J1802+5616	WHT	1999 Sep 14	1800	no	2
BR J2017−4019	CTIO	1998 Oct 14	3600	no	3
PSS J2122−0014	WHT	1998 Sep 22	3600/3600	no	1
BR J2131−4429	CTIO	1998 Oct 16	1800	no	3
PMN J2134−0419	CTIO	1999 Oct 12	5400	yes	11
PSS J2154+0335	WHT	1999 Sep 14	1800	no	2
PSS J2155+1358	CTIO	1999 Oct 10	3600	yes	2
BR J2216−6714	CTIO	1999 Oct 09	3600	yes	3
PSS J2241+1352	CTIO	1999 Oct 11	3600	yes	2
DMS B2247−0209	WHT	1998 Sep 24	5400/3600	yes	12
PSS J2315+0921	CTIO	1999 Oct 11	3600	yes	2
BR J2317−4345	CTIO	1998 Oct 14	3600	yes	3
BR J2328−4513	CTIO	1998 Oct 15	3600	yes	3
PSS J2344+0342	CTIO	1999 Oct 11	3600	yes	2
BR J2349−3712	CTIO	1999 Oct 09	3600	yes	3

[a] For the quasars observed at the WHT the B/R designations give the exposure times through the blue and red arms of the ISIS spectrograph.

Notes:

The quasar prefixes indication the following origin: BR = APM survey objects selected by B_J-R color excess; PSS = Second Palomar Sky Survey; PMN = Parkes-MIT-NRAO radio-selected objects; RX = X-ray selected; SDSS = Sloan Digital Sky Survey; and DMS = Deep Multicolor Survey.

References:

(1) Stern et al. 2000;
(2) G. Djorgovski's www page at http://www.astro.caltech.edu/~george/z4.qsos;
(3) Storrie-Lombardi et al. 2000;
(4) Fan et al. 1999;
(5) Warren, Hewett, & Osmer 1991;
(6) Kennefick et al. 1995a;
(7) Storrie-Lombardi et al. 1996a;
(8) Zickgraf et al. 1997;
(9) Kennefick et al. 1995b;
(10) Henry et al. 1994;
(11) Hook et al. in preparation;
(12) Hall et al. 1996

2.2.2 CTIO Runs

Thirty-five quasars were observed at CTIO during 1998 October 14 – 16, and 1999 October 9 – 12. The typical exposure time was 3600 seconds for the brighter objects (R$\sim$ 18–19th mag) but substantially longer times were used for the fainter Sloan Digital Sky Survey quasars. We used the R-C spectrograph with the 316 lines mm^{-1} grating, centered at 6050 Å and covering the range 3000Å–– 9100Å. This set-up resulted in a dispersion of 1.98 Å pixel^{-1}. The detector used was a Loral 3072 × 1024 CCD detector. The narrow and wide slit observations were taken with 1 – 1.5 arcsec and 5 arcsec widths, respectively. Because of the substantial wavelength coverage available with this set-up we used a WG345 blocking filter (with 50 % transmission at 3450 Å) to minimize the second order contamination from the standard stars above 7000 Å. The contamination is negligible for the quasars as most have no flux below 4500 Å but affects the standard stars that have substantial flux at 3500 Å. Appropriate measures, as discussed in the data reduction section, have been taken so that this set-up does not modify the flux calibration at the red end of the spectra. Using two instrumental set-ups in order to completely remove the second order contamination problem would have resulted in a 60–80 % increase in the required observing time.

2.2.3 Keck Observation

The observations of SDSS J0338+0022 were taken at the Keck Observatory with the Low Resolution Imaging Spectrometer (LRIS) on 10 February 1999 with a 1".0 wide slit and 400ℓ/mm grating blazed at 8500 Å (spectral resolution 8.1 Å), and on 17 February 1999 with a 1".5 wide slit, with both the 400ℓ/mm grating blazed at 8500 Å (spectral resolution 12.3 Å), and with the 300ℓ/mm grating blazed at 5000 Å (spectral resolution 17.3 Å). Seeing was 0".7 – 0".9 FWHM on the first night, and 0".7 – 1".0 on the second night; observations were made under dark, photometric conditions in each instance. A sequence of three exposures, shifted by $10''$ along the slit, was taken in each configuration with the position angle of the slit set to the parallactic angle for the middle exposure. This yielded net integrations of 3600 s (5542–9350 Å; 8.1 Å resolution; 1".0 slit), 3600 s (5799–9609 Å; 12.4 Å resolution; 1".5 slit), and 3000 s (3673–8708 Å; 17.3 Å resolution; 1".5 slit). A GG495 blocking filter was used to suppress second order blue light. More observational details are given in Songaila et al. (1999).

2.3 The Data

2.3.1 Data Reduction

The data reduction was undertaken using the IRAF [2] software package. Because

---

[2] IRAF is distributed by the National Optical Astronomy Observatories, which are operated by the Association of Universities for Research in Astronomy, Inc., under cooperative agreement with the National Science Foundation.

the bias frames for each nights observations were so similar, a master 'zero' frame for each run was created using the IMCOMBINE routine. The data were overscan-corrected, zero-corrected, and trimmed using CCDPROC. Similarly a single flat-field frame was produced by taking the median of the Tungsten flats. The overall background variation across this frame was removed to produce an image to correct for the pixel-to-pixel sensitivity variation of the data. The task APALL was used to extract 1-D multi-spectra from the 2-D frames. The routine estimates the sky level by model fitting over specified regions on either side of the spectrum and uses optimal extraction to process the spectra (Horne, 1986).

The WHT data were wavelength calibrated using CuAr and CuNe arcs and monitored using night sky lines. Figure 1 shows the wavelength calibrated sky lines in the red arm region. Arcs were taken at each object position for wavelength calibrating the CTIO data. We used solely the sky lines to wavelength calibrate the Keck data [3]. The spectra were flux calibrated using observations taken of spectrophotometric standards. B-stars free of strong features in the red were observed at similar airmass in order to remove the effects of atmospheric absorption in the red-arm WHT spectra and the CTIO spectra (e.g. O_2 A band at 7600 Å). The atmospheric absorption features seen in the B-star spectrum were isolated by interpolating between values on either side of the feature (see top panel of Figure 2). The original B-star spectrum was then divided by this atmospheric-free spectrum to create an atmospheric correction spectrum (see bottom panel of Figure 2). Finally the object spectra were divided by the scaled correction spectrum. In the case of ISIS data the red and blue ends of the spectra were then joined using SCOMBINE. In all cases if a wide-slit observation was made (see Table 2.2.1), it was used to correct the absolute flux levels for slit losses.

As mentioned in the paragraph above, the quasar spectra observed using the R-C spectrograph at CTIO suffered a gradual flux decrement in the red end calibration due to the inclusion of the second order flux from the standard stars. In order to correct for this effect, spectra of standard stars were taken with two different blocking filters (3450 Å and 5000 Å). The effect of the filter at wavelengths above 8000 Å could thus be determined and a correction applied accordingly to the quasar spectra. In addition a quasar previously observed with the ISIS double-spectrograph on WHT was reobserved at CTIO and corrected as explained above. Comparing the two spectra reveals no significant difference and provides a successful double check on the method. In any case the flux calibration of the red end of the spectra is relatively unimportant for the majority of the work undertaken here, namely the search of quasar absorbers blueward of the Ly-α emission.

2.3.2 Quasar Spectra

The resulting spectra have a continuum signal-to-noise ratio ranging from $\approx$

---

[3] see the following URL for more information: http://www.astro.caltech.edu/mirror/keck/realpublic/inst/lris/skylines.html

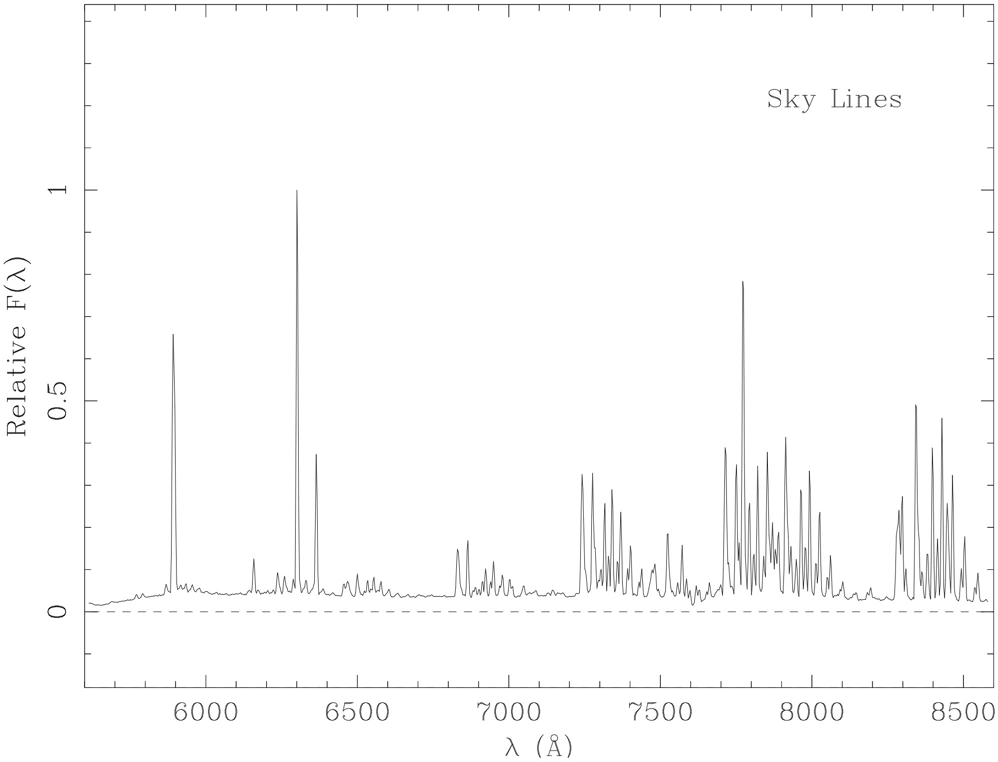

Fig. 1.— WHT/ISIS red arm spectrum showing the wavelength calibrated sky lines.

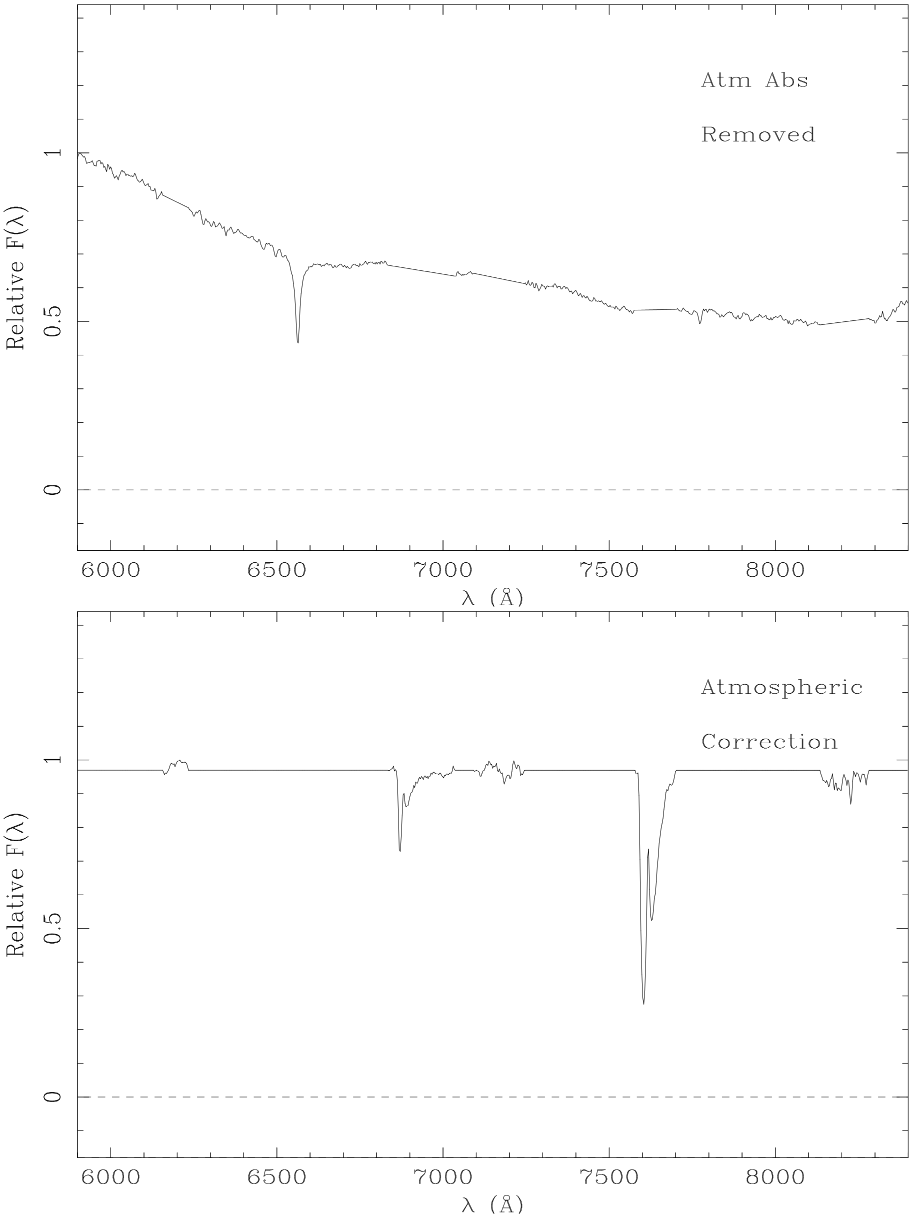

Fig. 2.— The top panel shows a B-star flux standard with atmospheric absorption features isolated by interpolating between values on either side of the feature. The bottom panel shows the atmospheric correction to applied to the quasar spectra.

10 – 30 per pixel at 7000 Å. The fluxed calibrated spectra in ergs $\mathrm{cm}^{-2}\ \mathrm{s}^{-1}\ \mathrm{Hz}^{-1}$ (i.e. F_ν) are shown in Figure 1 (normalised spectra detailing the LLS region are shown in Appendix A). Ten of the quasars presented here exhibit intrinsic broad absorption lines (BAL). The feature in all of the CTIO spectra at 8900 Å is due to bad columns in the CCD. In the 1999 run, the objects were moved along the slit between exposures so the effects of the bad columns were spread over a slightly wider region of the spectrum.

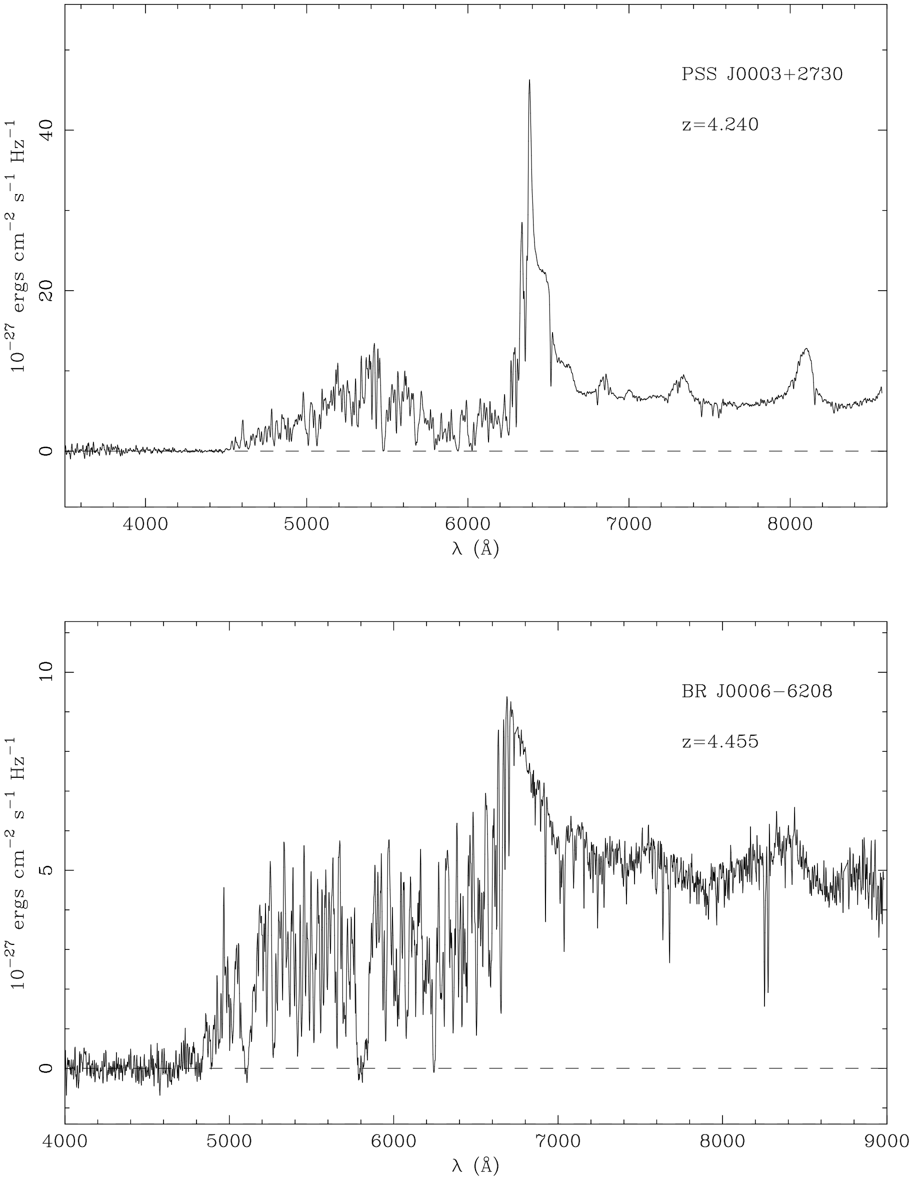

Fig. 3.— Fluxed spectra of all the observed quasars.

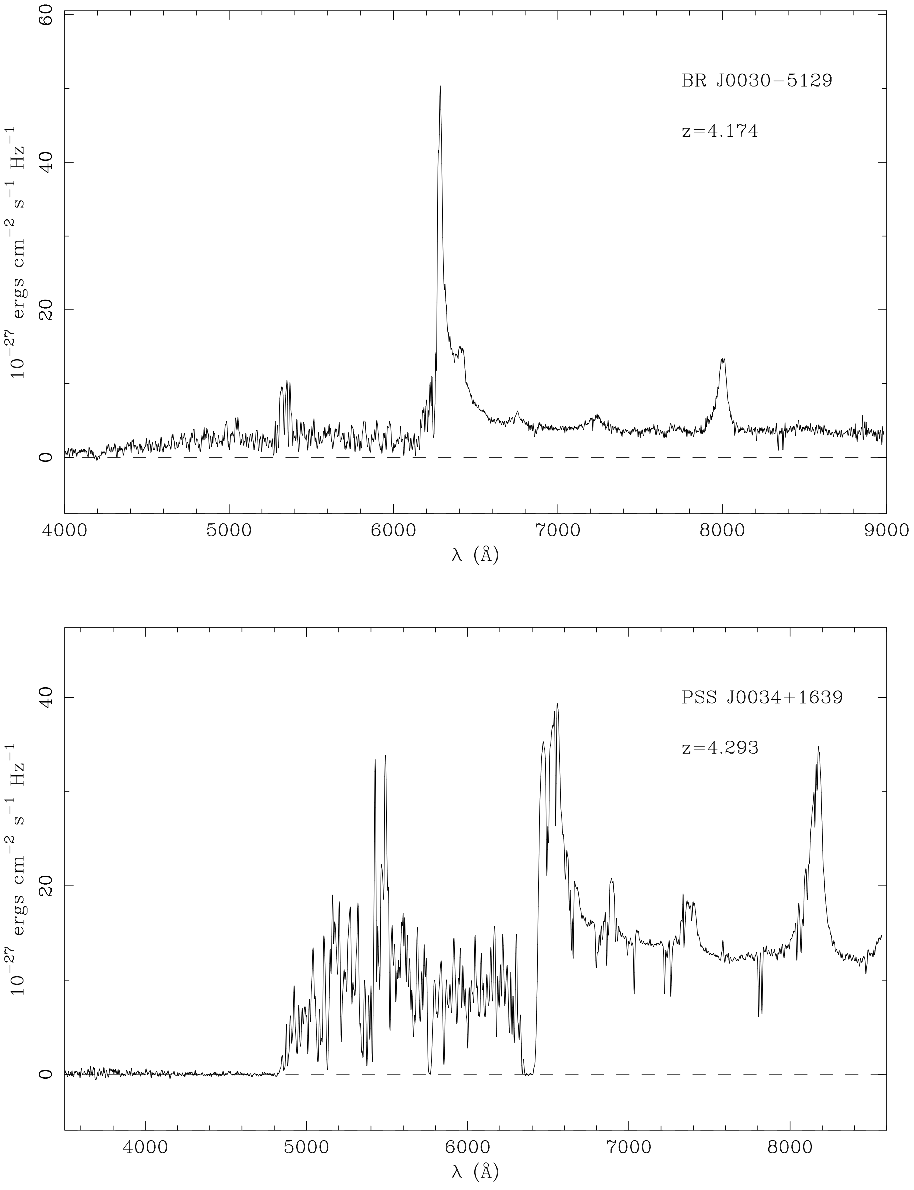

Fig. 3.— *continued*

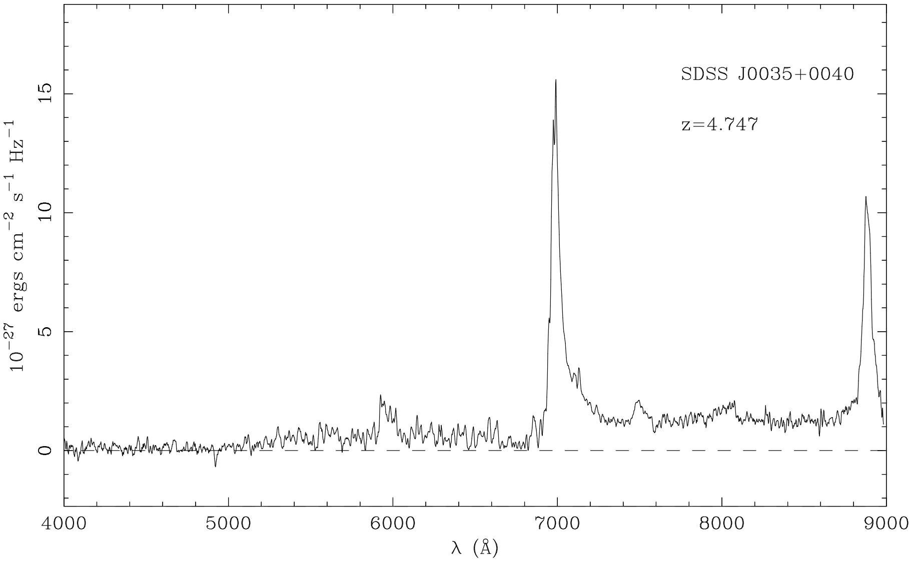

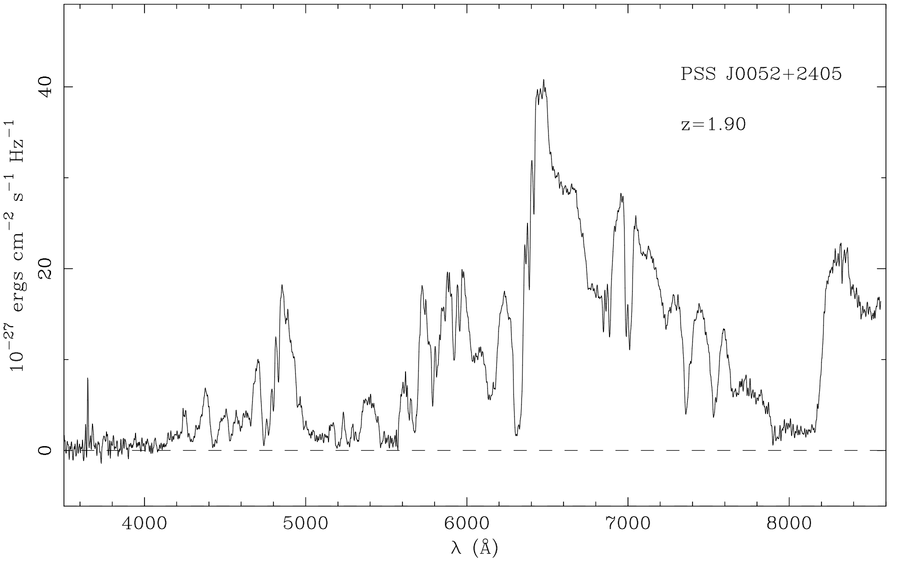

Fig. 3.— *continued*

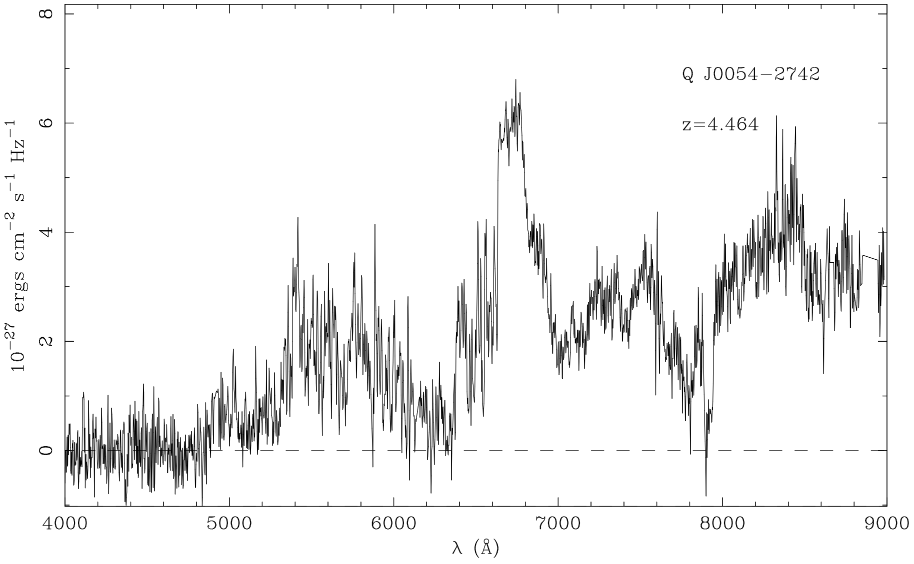

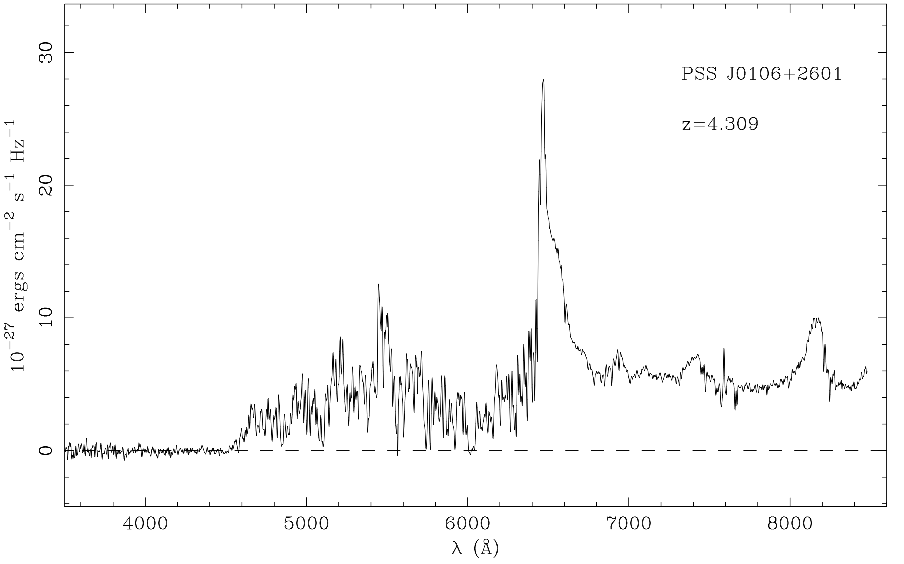

Fig. 3.— *continued*

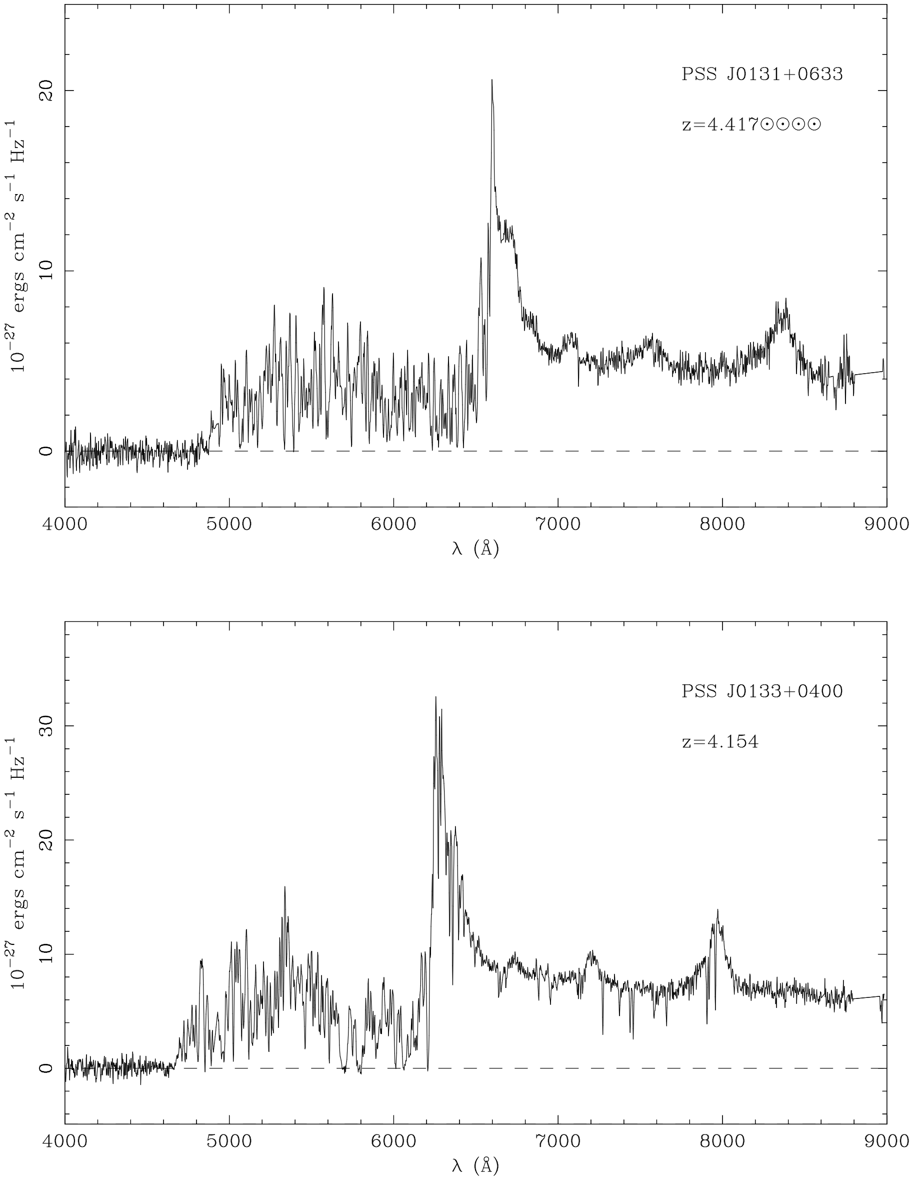

Fig. 3.— *continued*

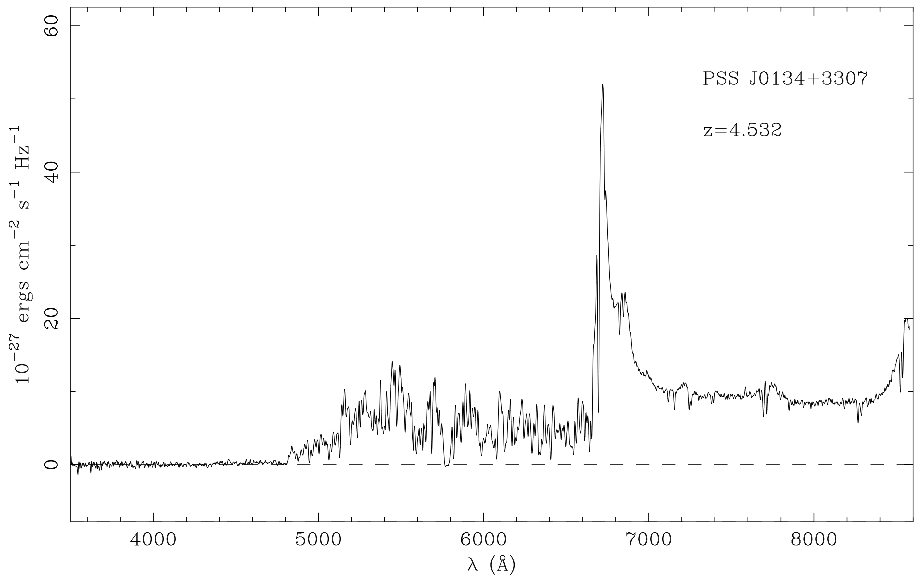

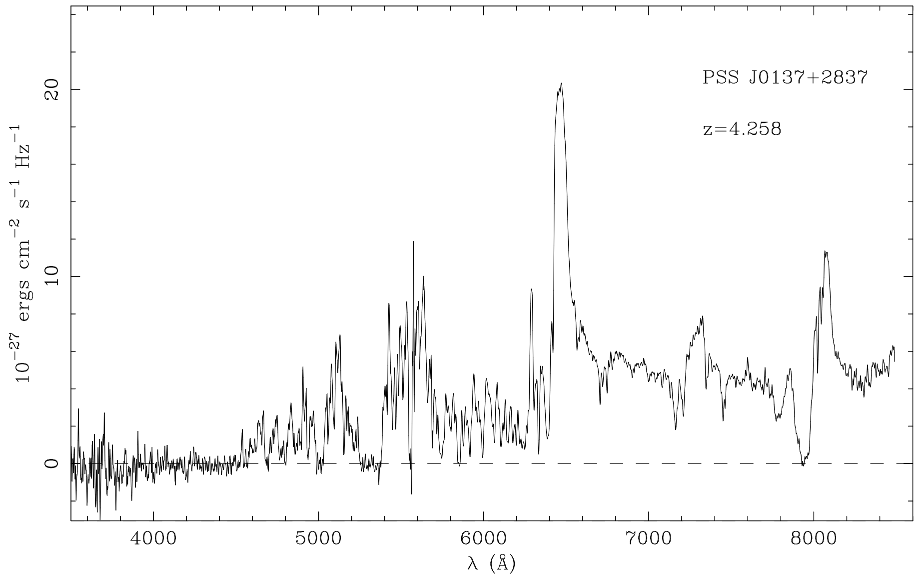

Fig. 3.— *continued*

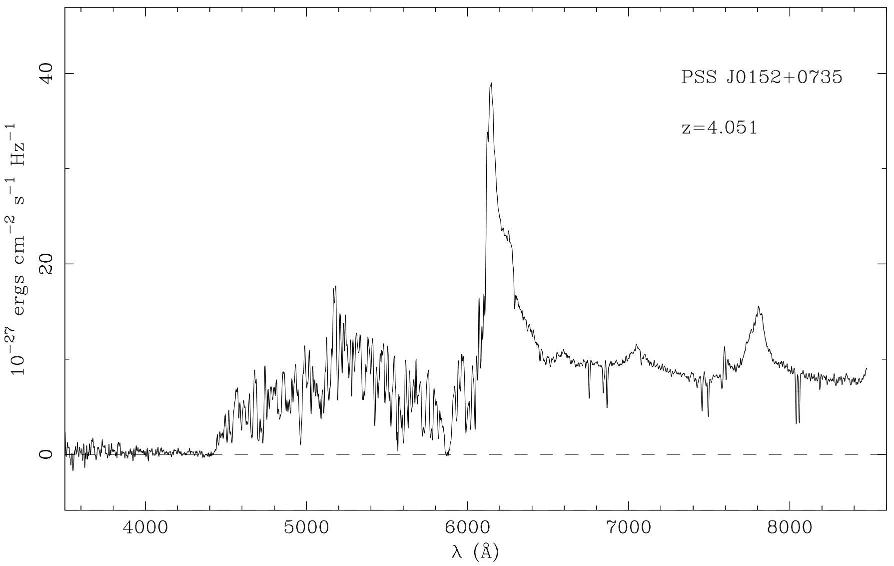

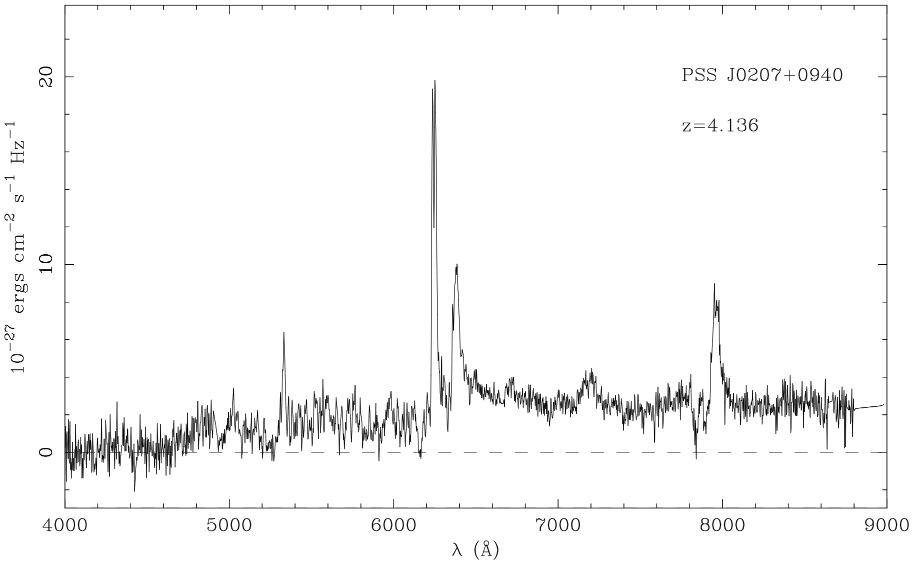

Fig. 3.— *continued*

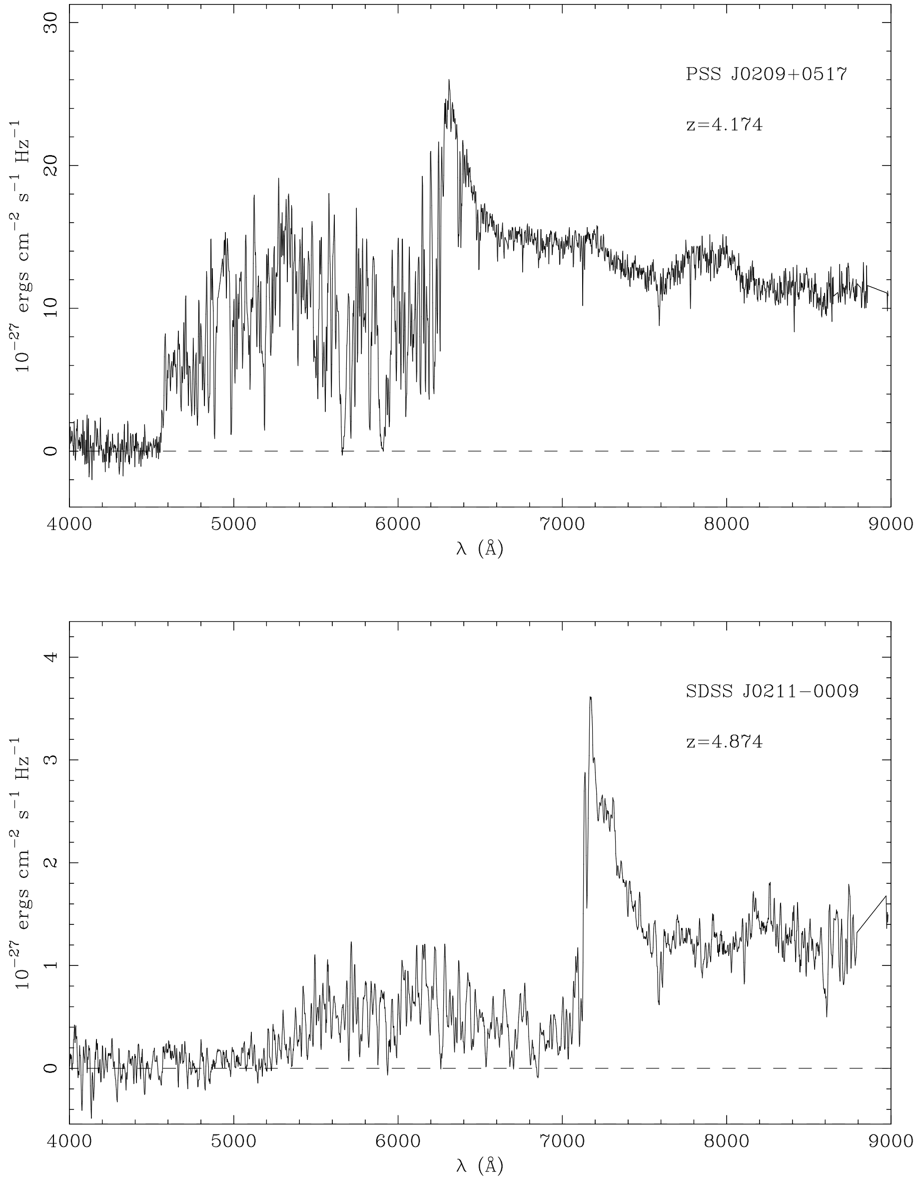

Fig. 3.— *continued*

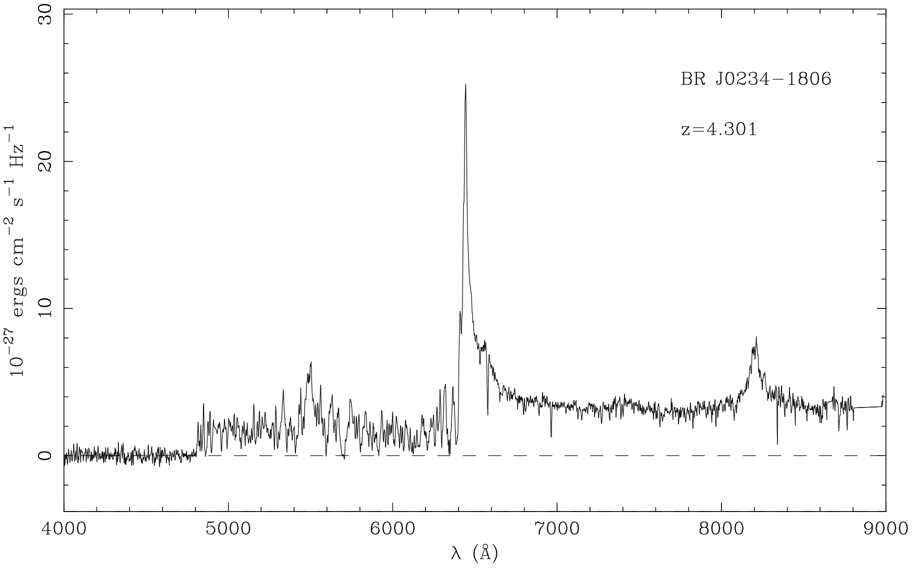

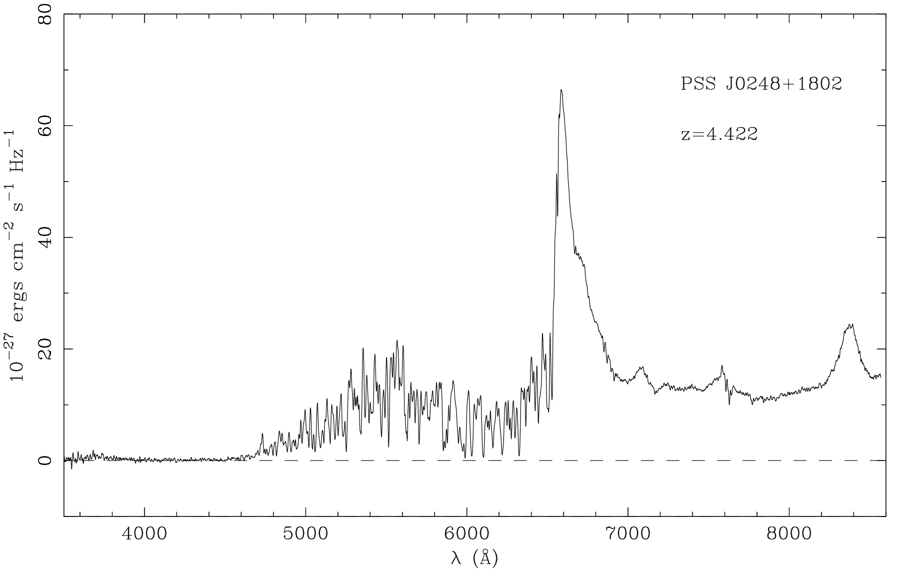

Fig. 3.— *continued*

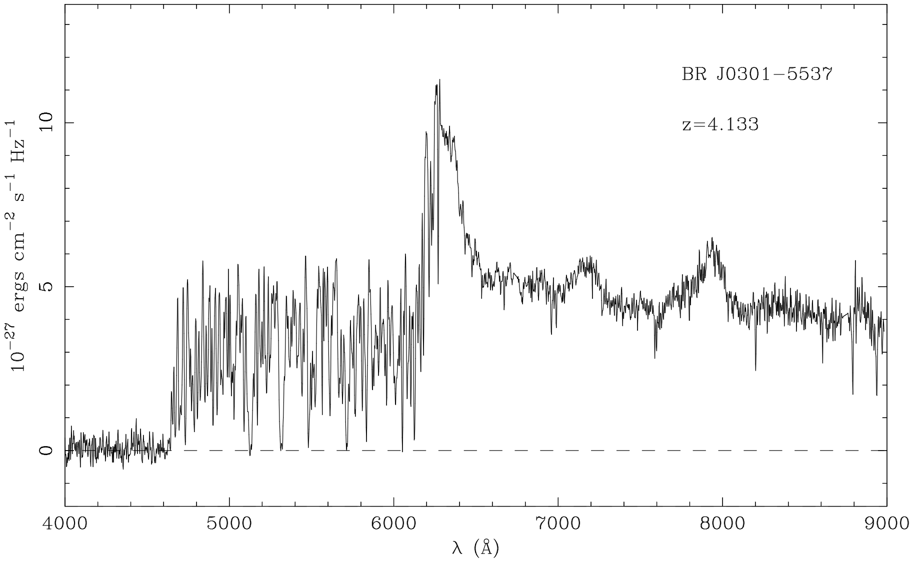

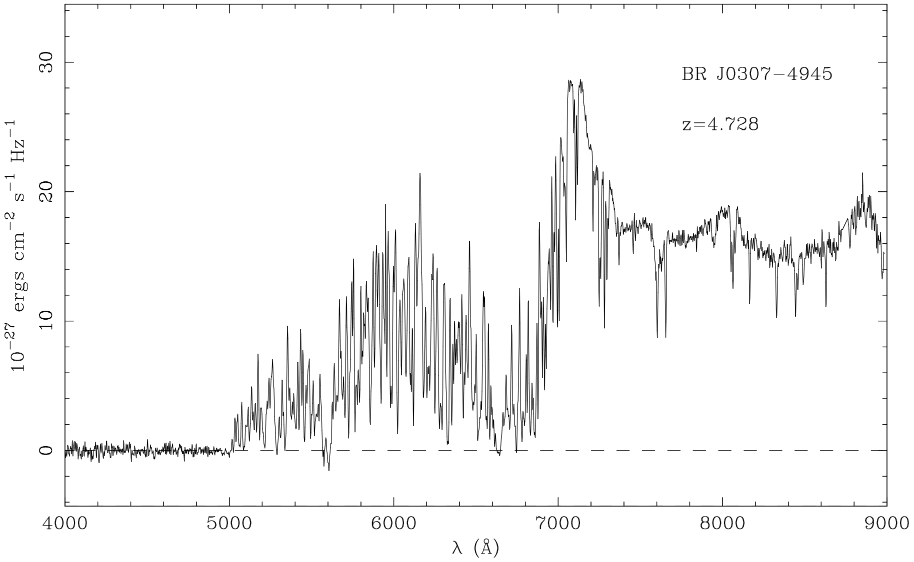

Fig. 3.— *continued*

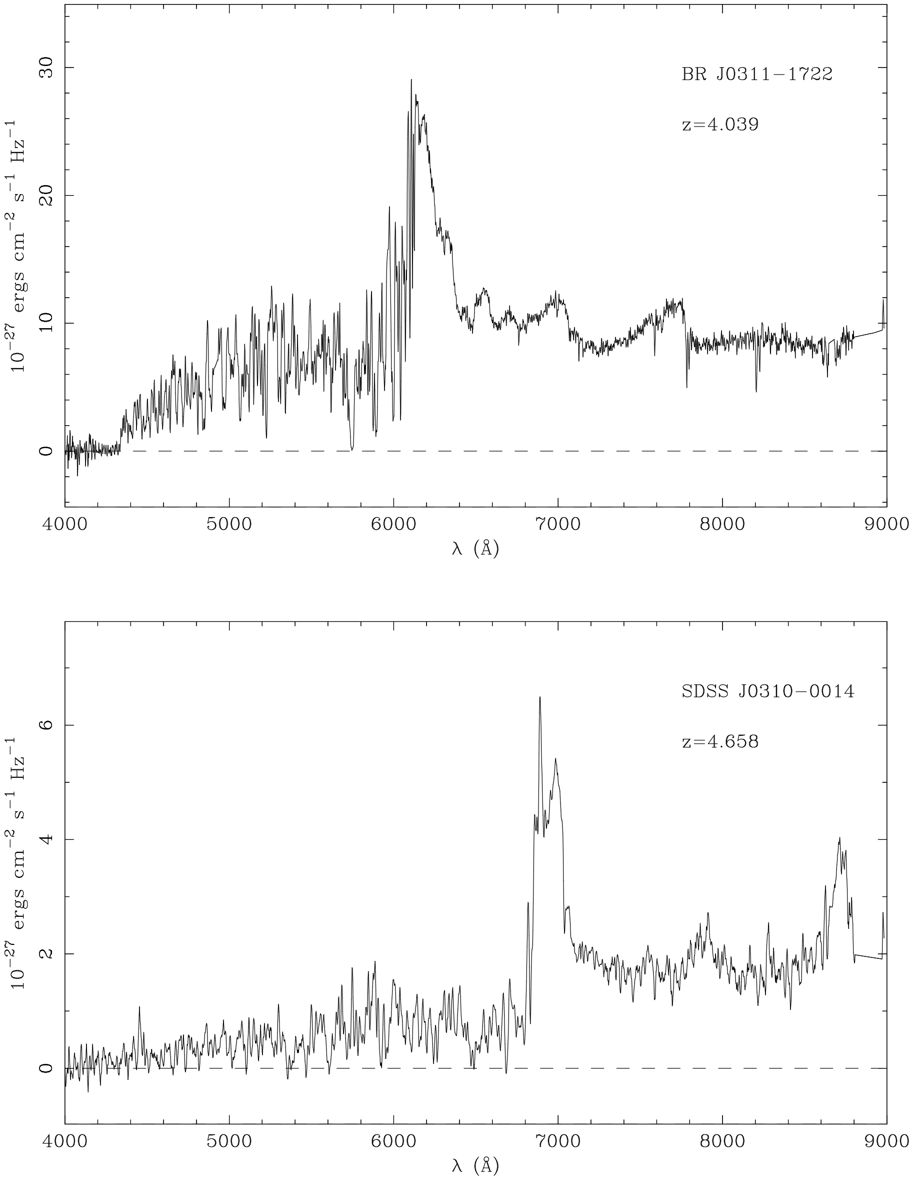

Fig. 3.— *continued*

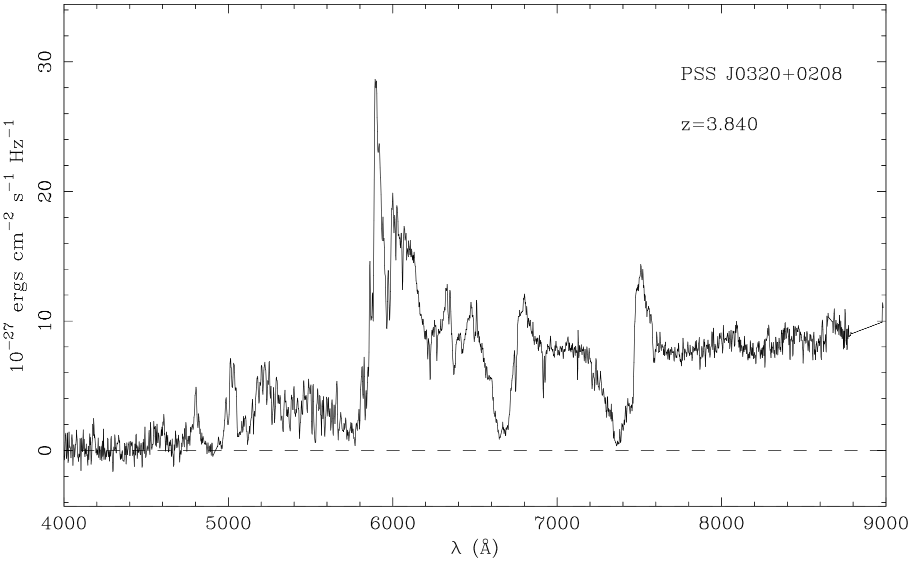

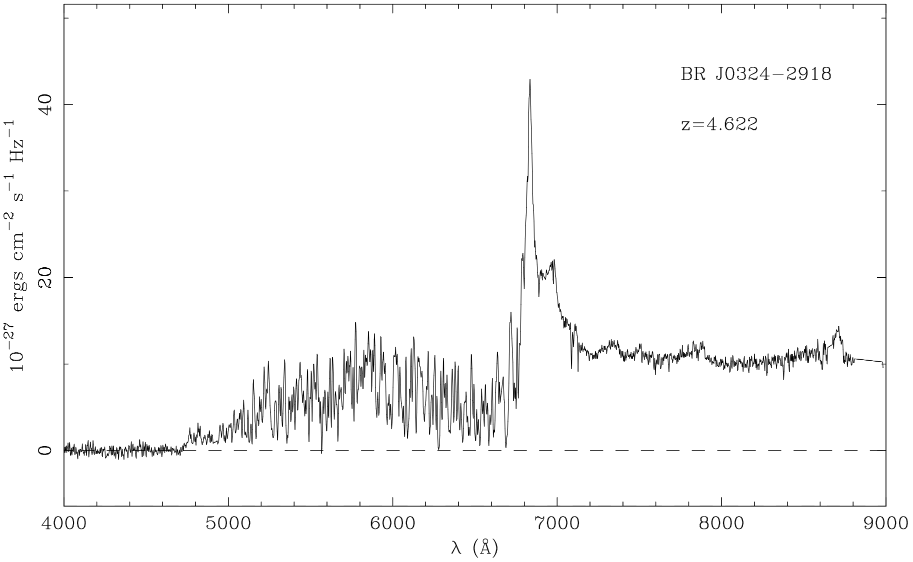

Fig. 3.— *continued*

2.4 Redshift and Magnitude Measurements

2.4.1 Redshift Measurements

In order to measure the redshifts, Gaussians were fit, if possible, to NV (rest wavelength 1240.13 Å), OI (1304.46 Å), SiIV + OIV] (1400.0 Å) and CIV (1549.1 Å) emission lines. The redshift for each line was determined from the central wavelength ($z = \lambda_{observed}/\lambda_{emitted} - 1$). Ly$\alpha$ (rest wavelength 1215.67 Å) is almost 50 % absorbed by the Lyα forest, so that the blue edge of the emission line has been used for redshift determination whenever possible. Some lines were impossible to fit and made the redshift determination difficult, especially in the case of the BALs. The redshift of each emission line, their average and the 1 σ error are shown in Table 2.4.1. This error is representative of the error in the fit, in wavelength calibration (estimated to be around 0.1 Å) and in the fact that the various species are coming from different physical regions of the quasar. In practice, this latter effect is probably the dominant source of differences in the emission line redshifts. In addition, we note that the redshifts derived from OI are generally higher than the ones derived from CIV emission line, an effect which is observed at $z_{em} \sim 1$ but seems to disappear at $z_{em} \sim 1$.

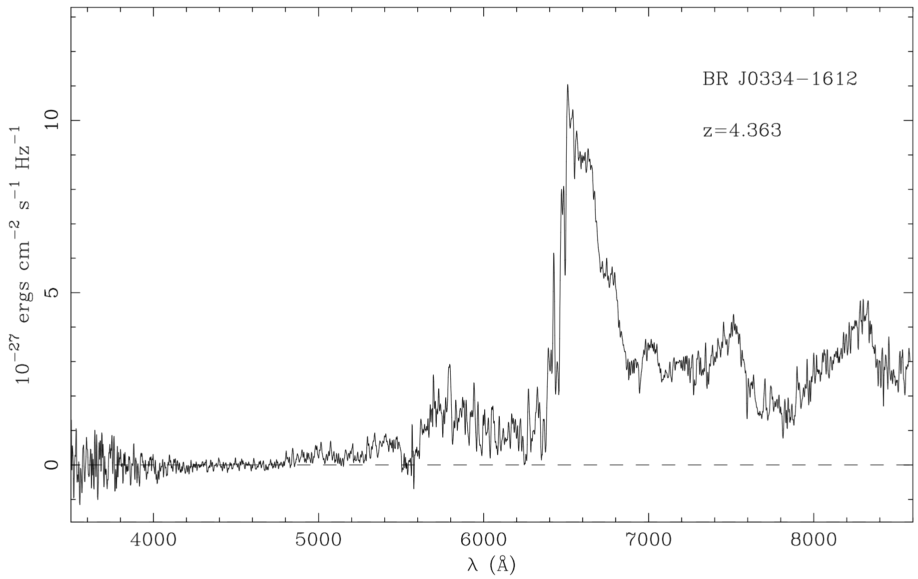

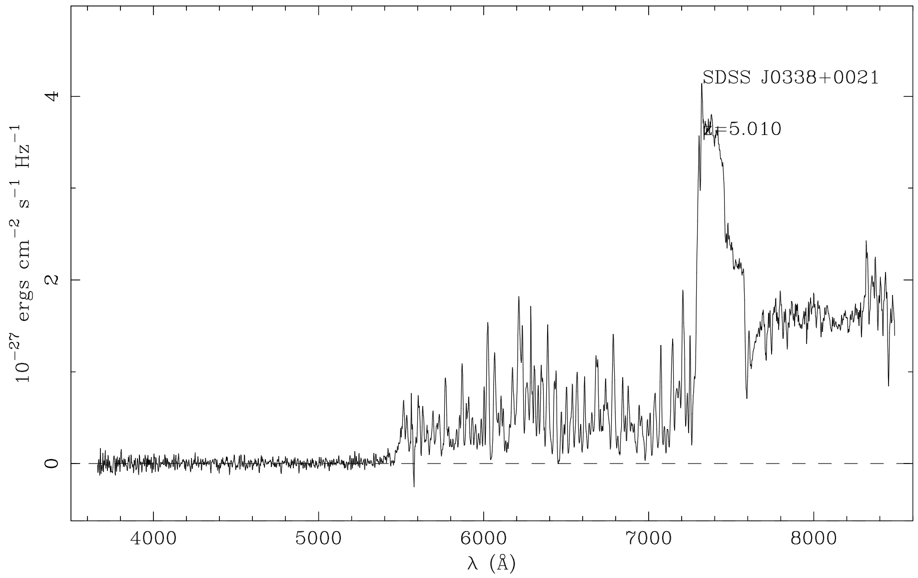

Fig. 3.— *continued*

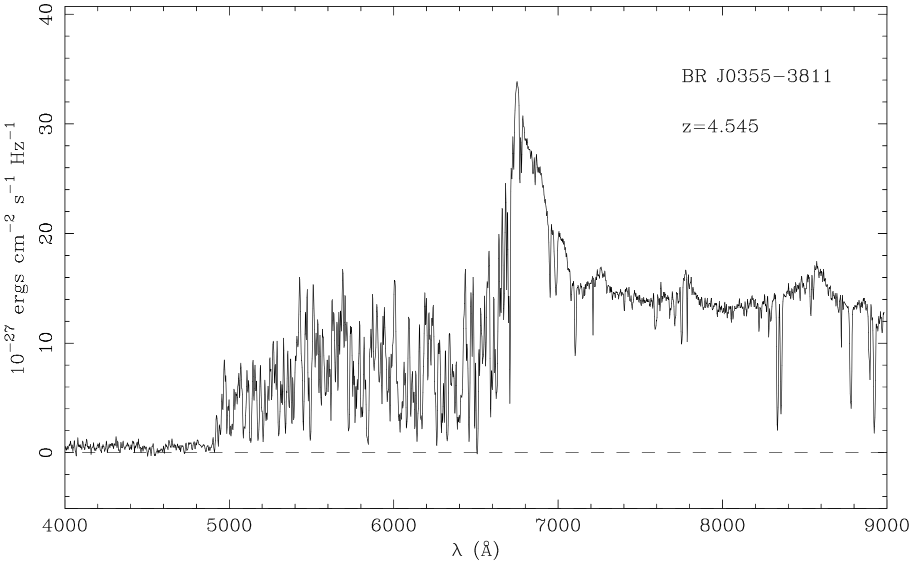

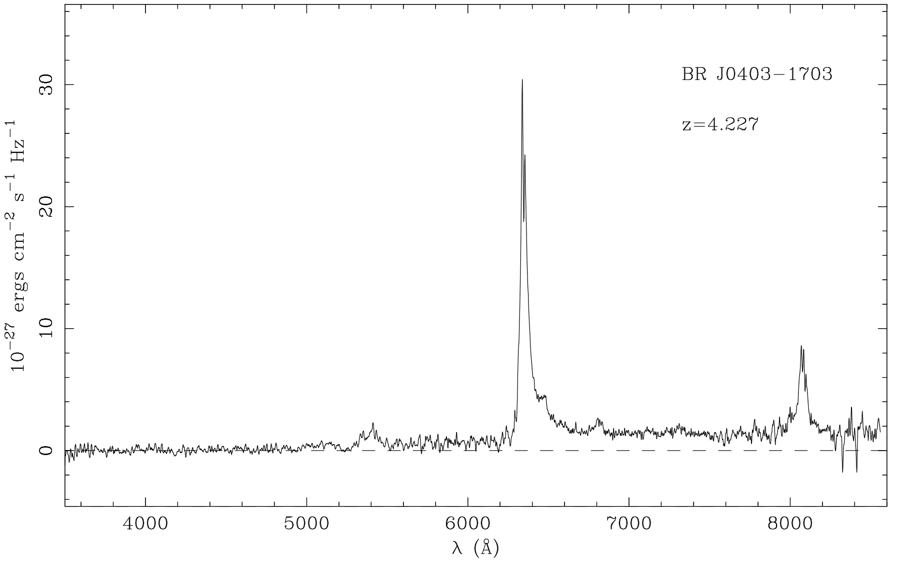

Fig. 3.— *continued*

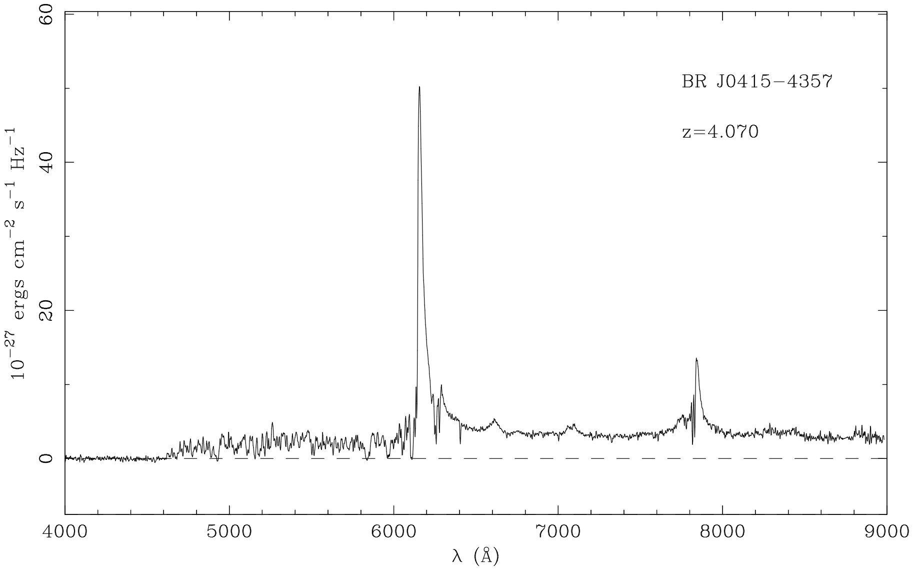

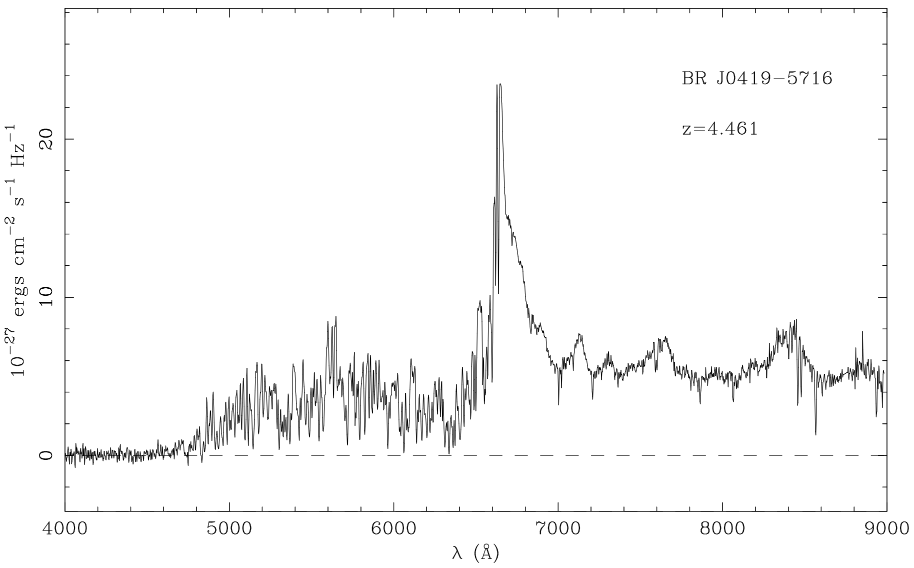

Fig. 3.— *continued*

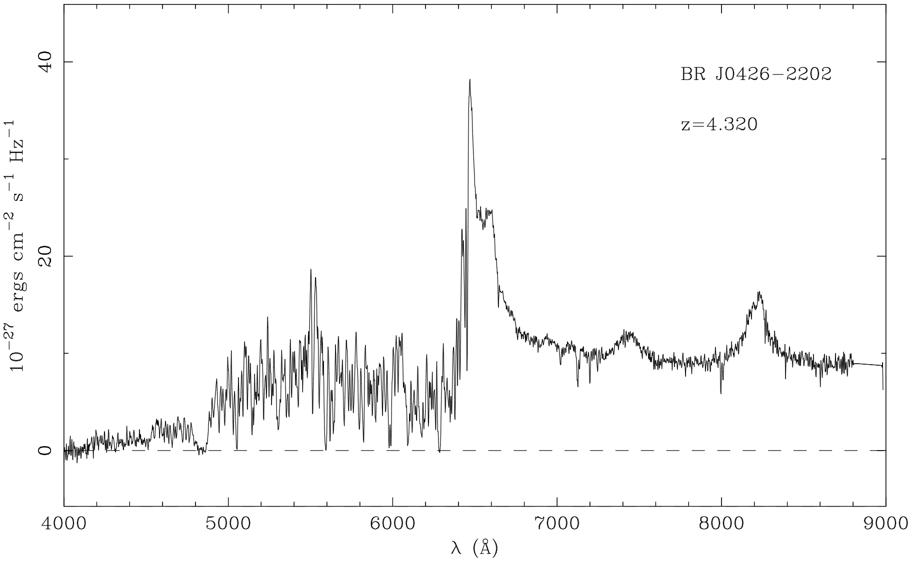

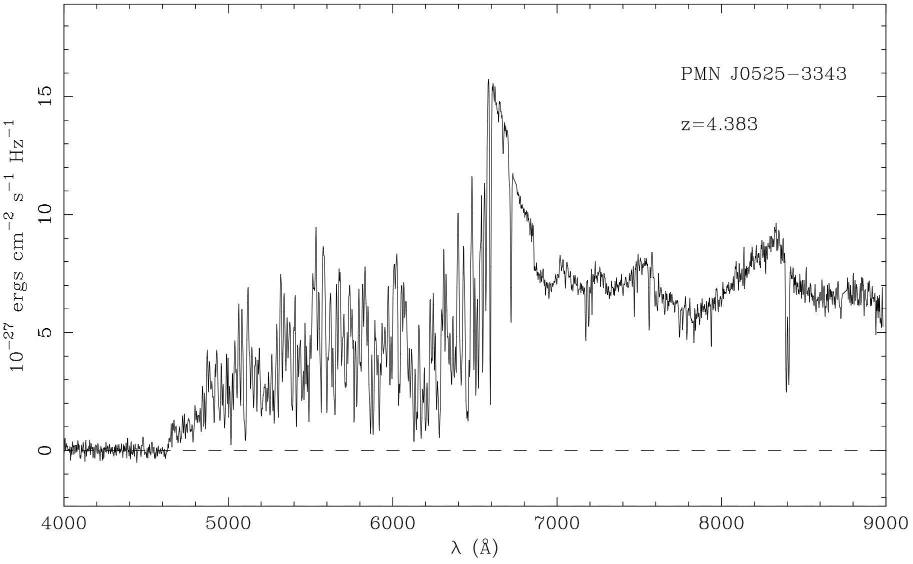

Fig. 3.— *continued*

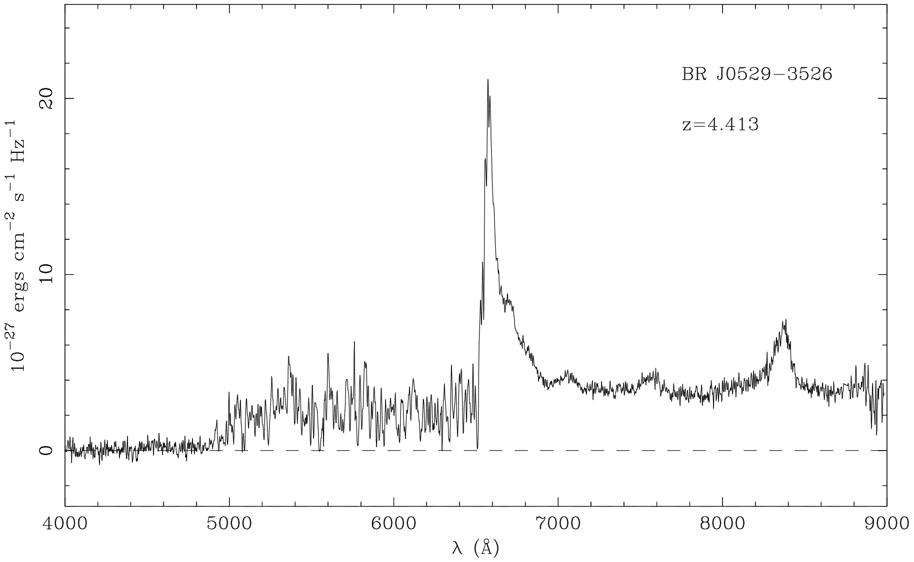

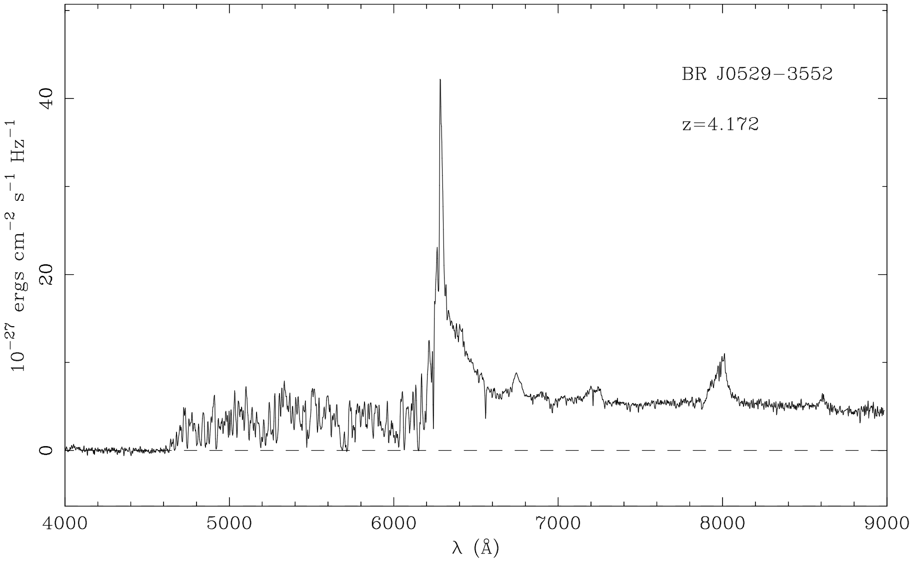

Fig. 3.— *continued*

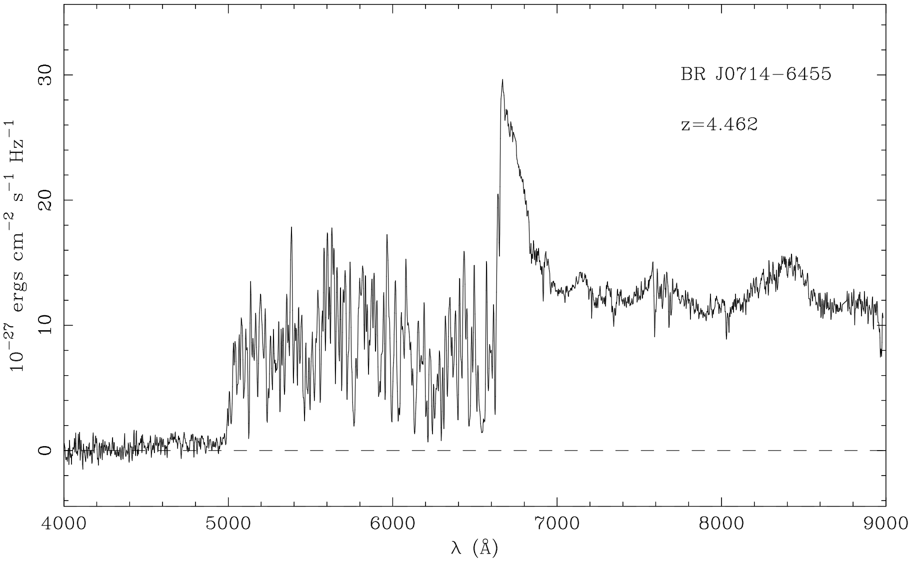

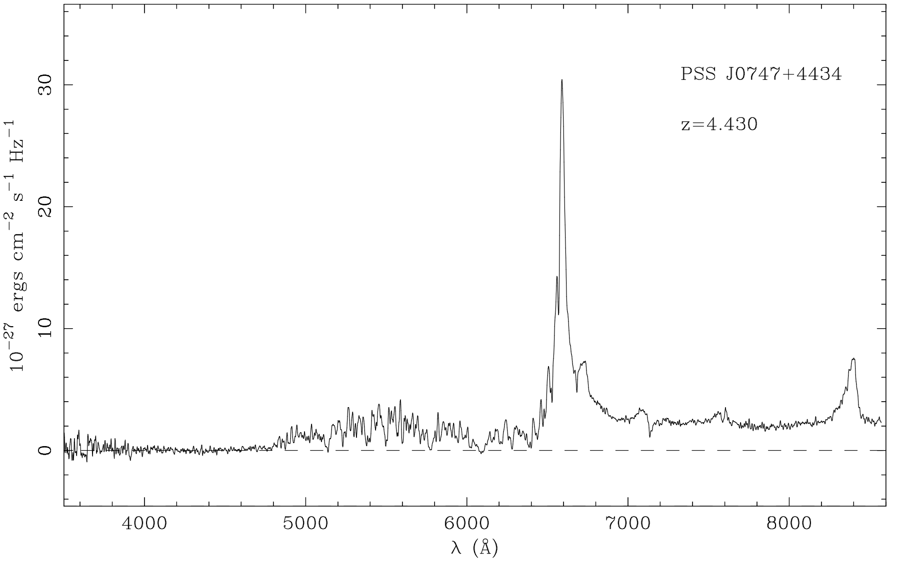

Fig. 3.— *continued*

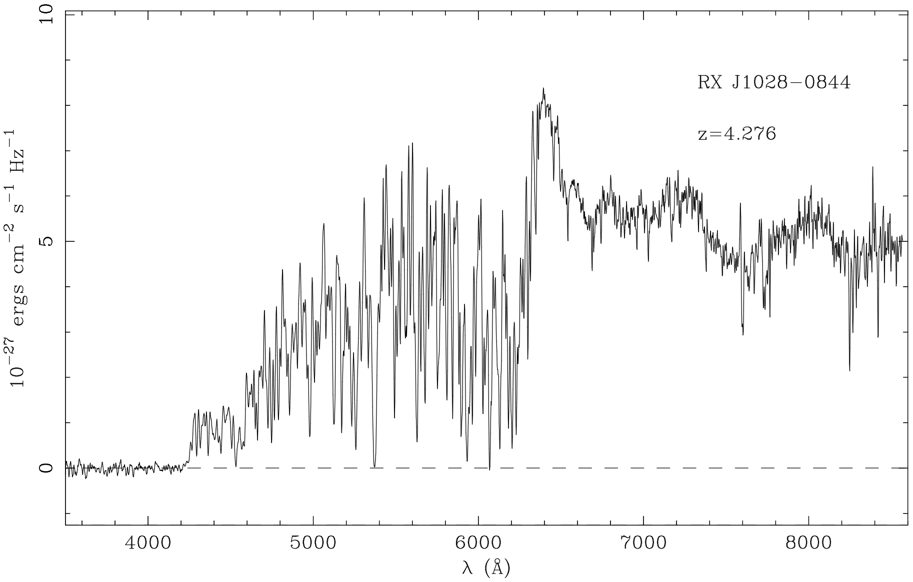

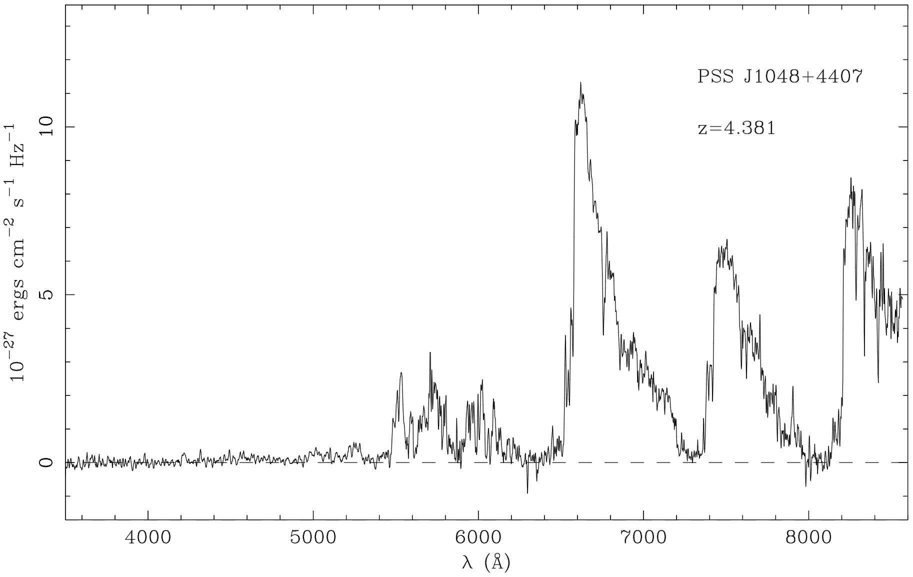

Fig. 3.— *continued*

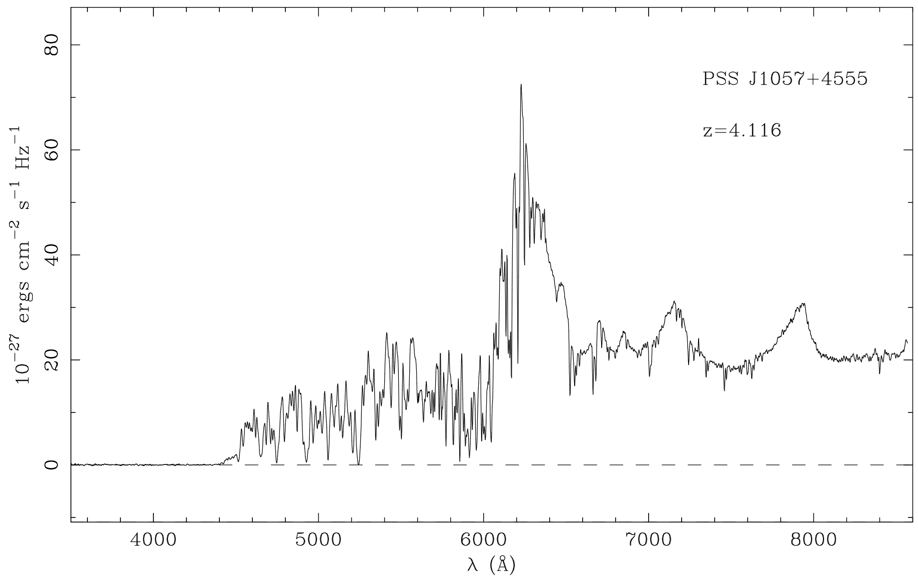

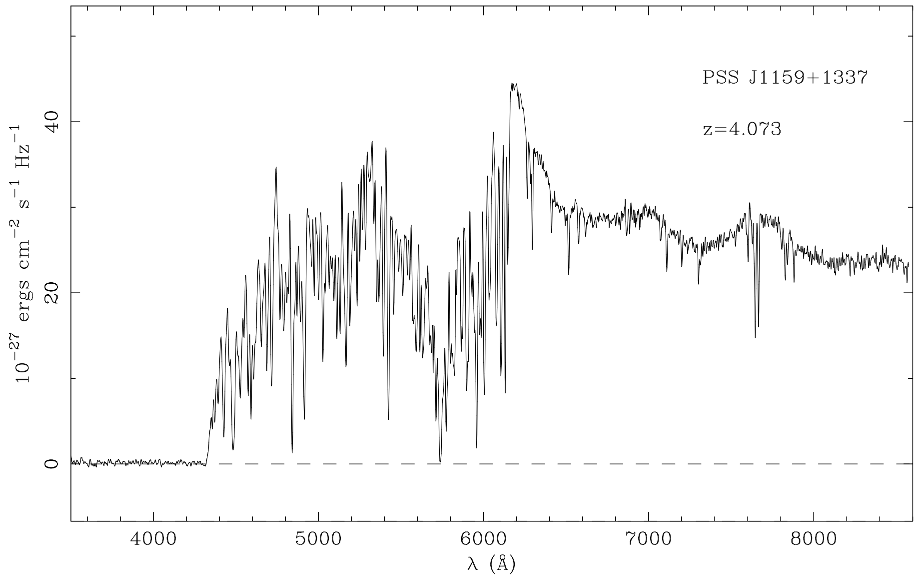

Fig. 3.— *continued*

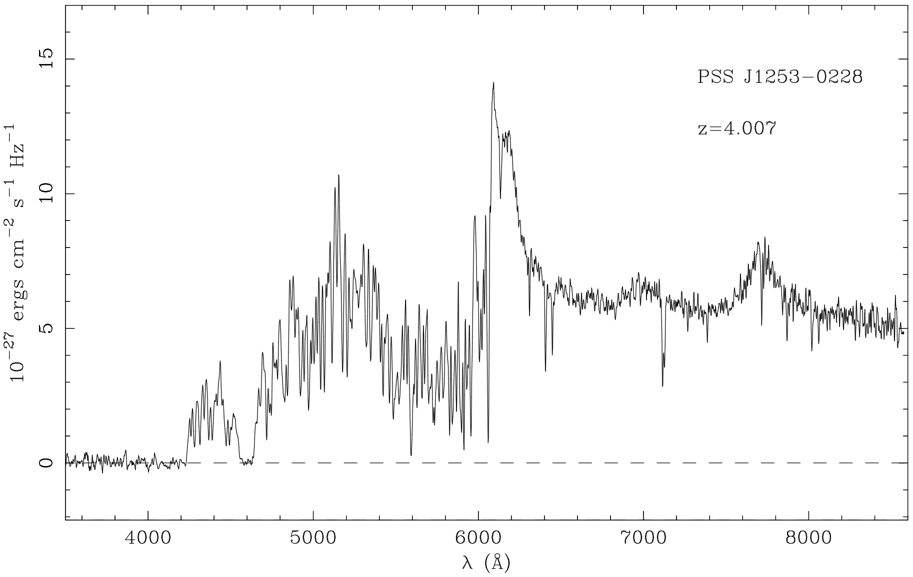

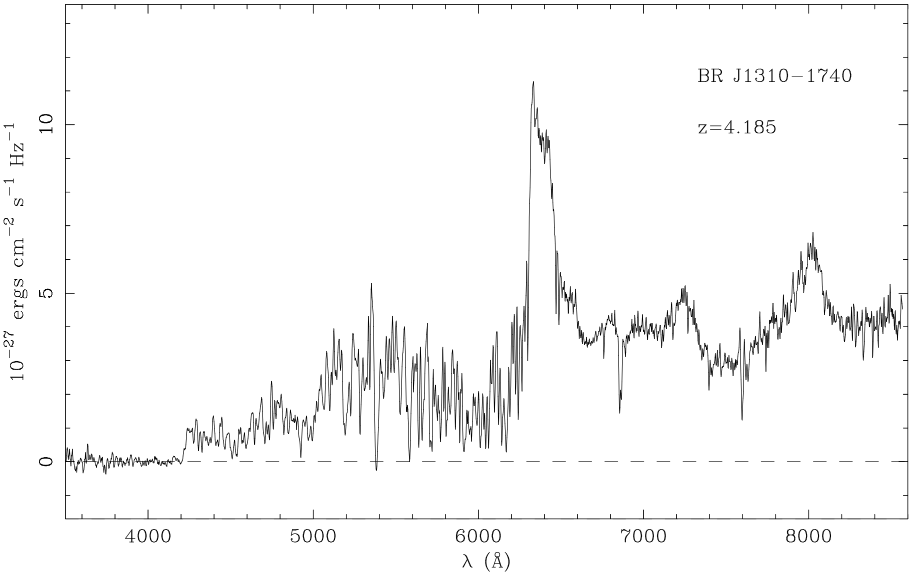

Fig. 3.— *continued*

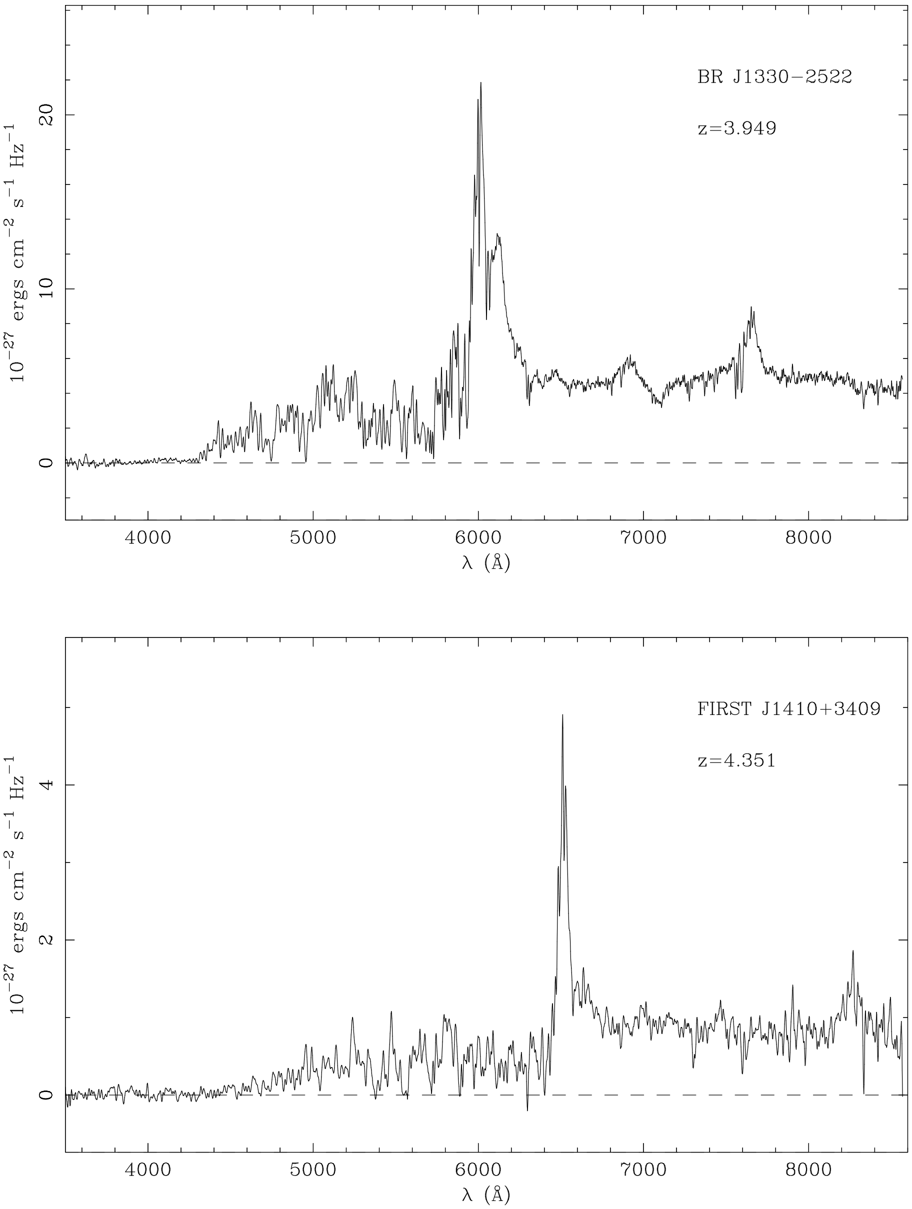

Fig. 3.— *continued*

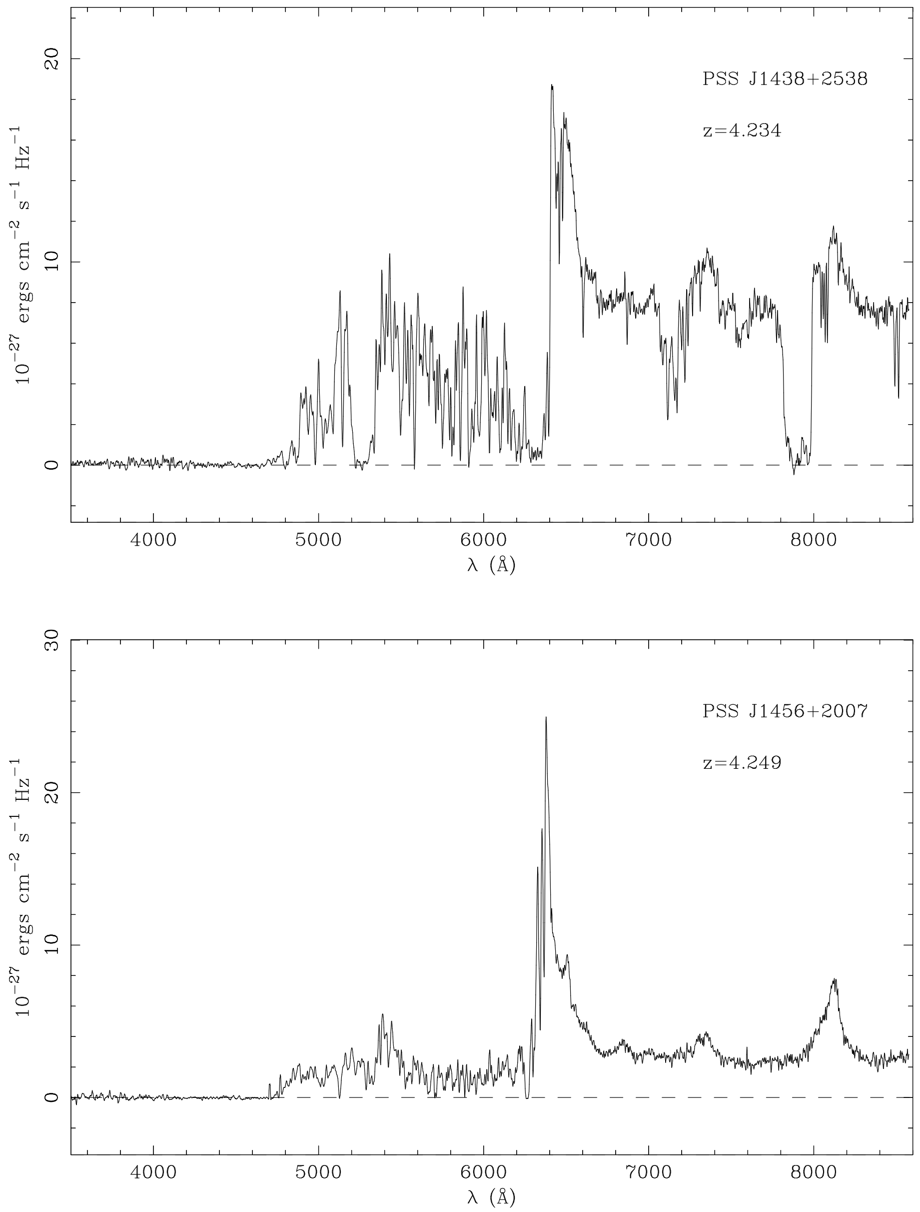

Fig. 3.— *continued*

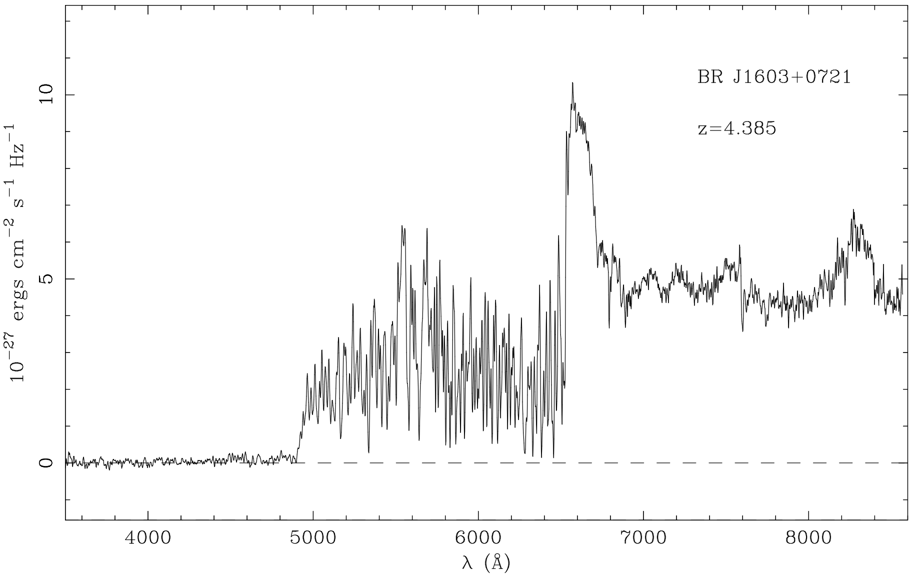

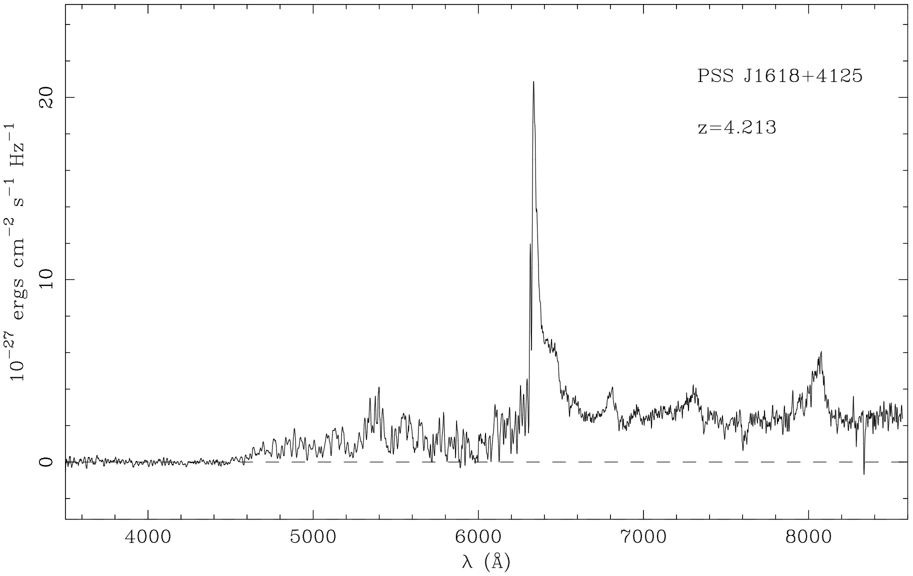

Fig. 3.— *continued*

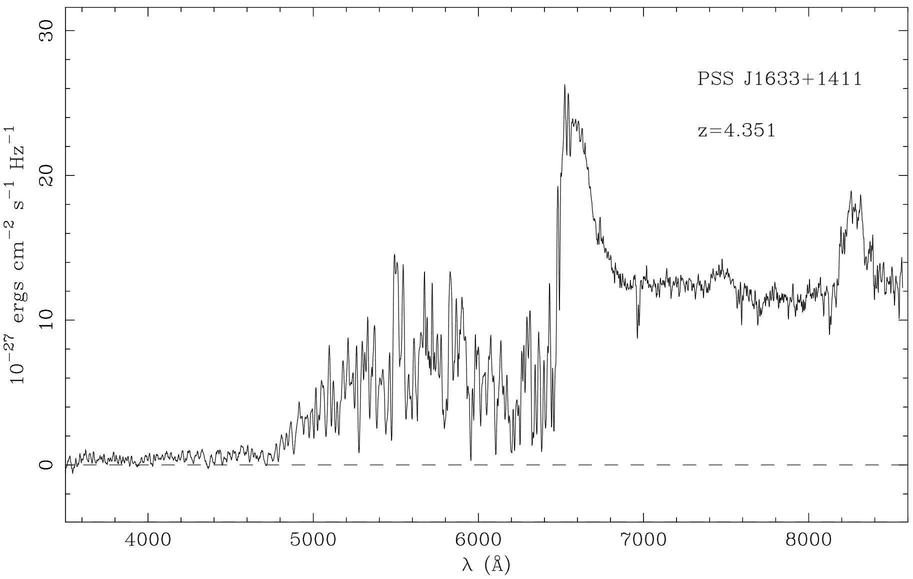

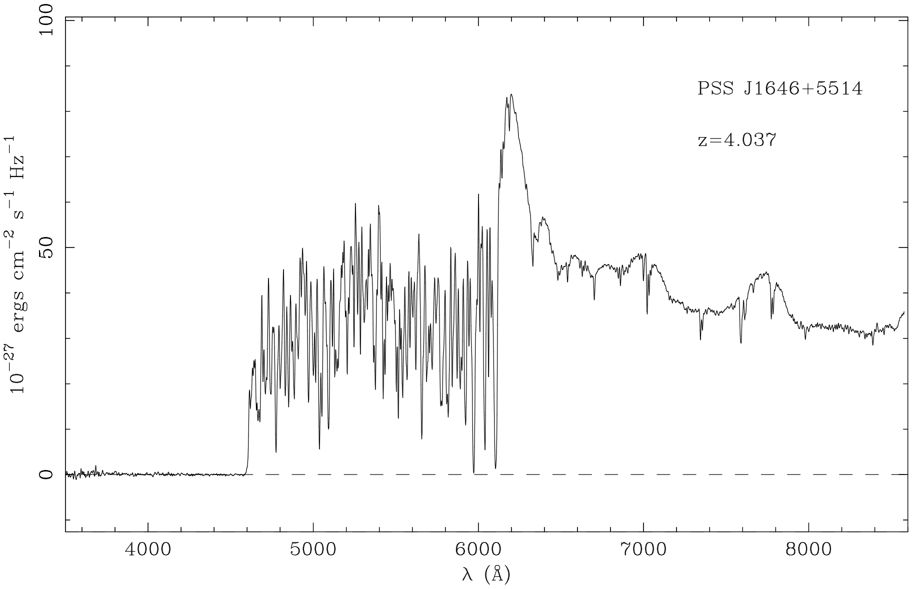

Fig. 3.— *continued*

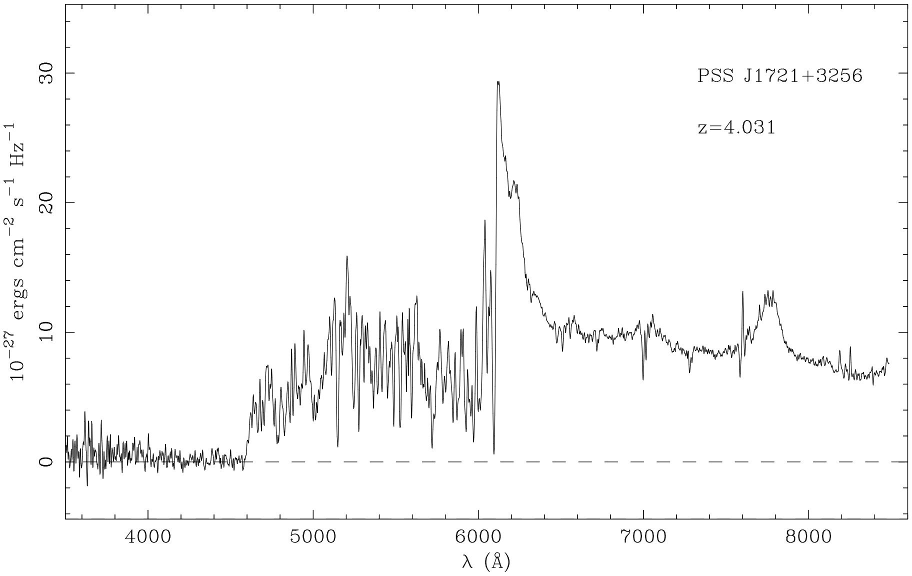

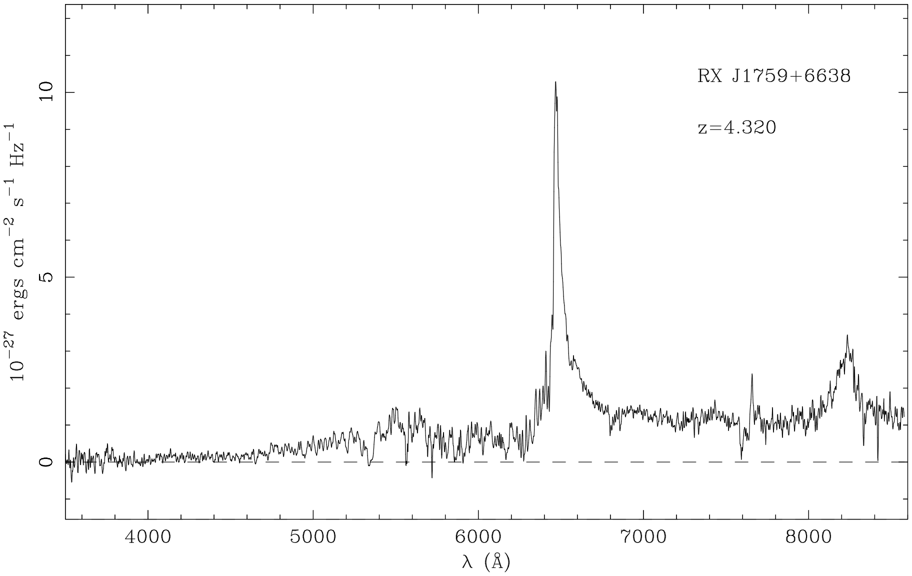

Fig. 3.— *continued*

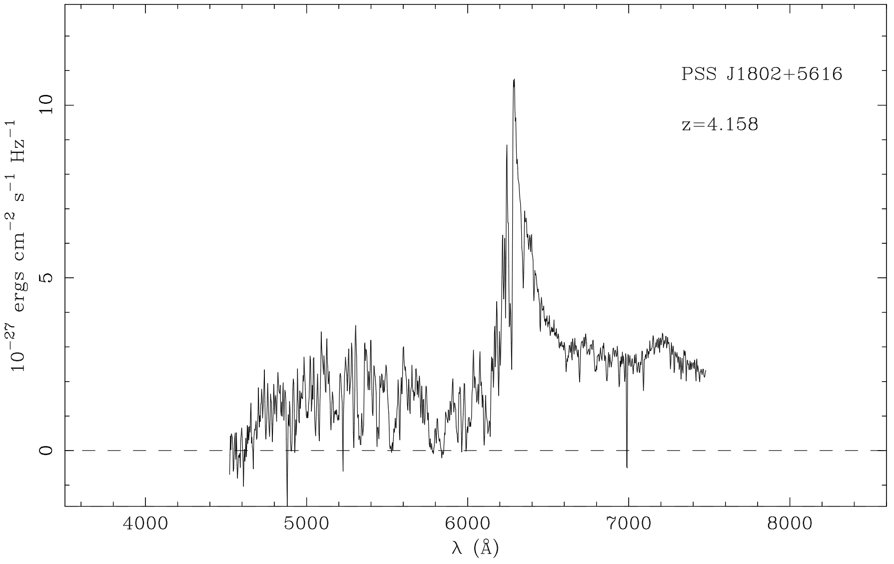

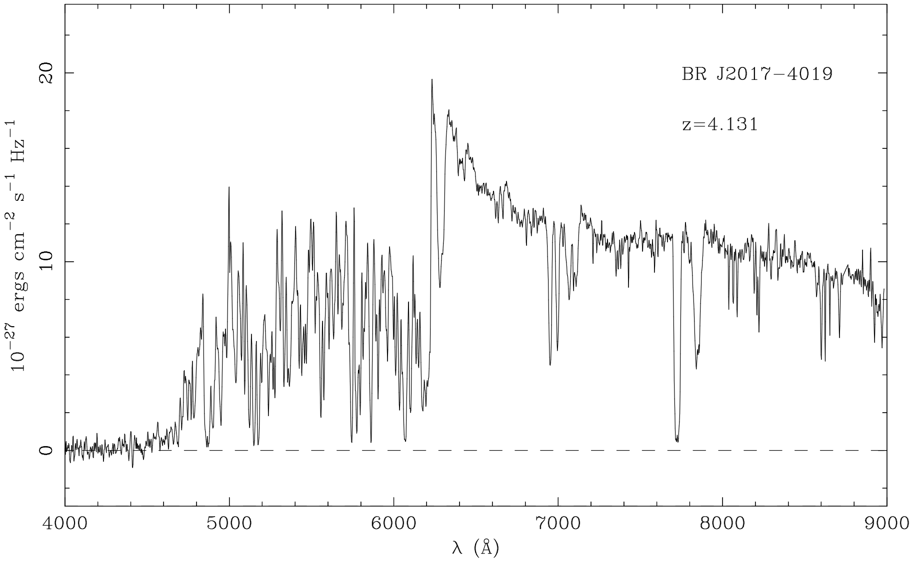

Fig. 3.— *continued*

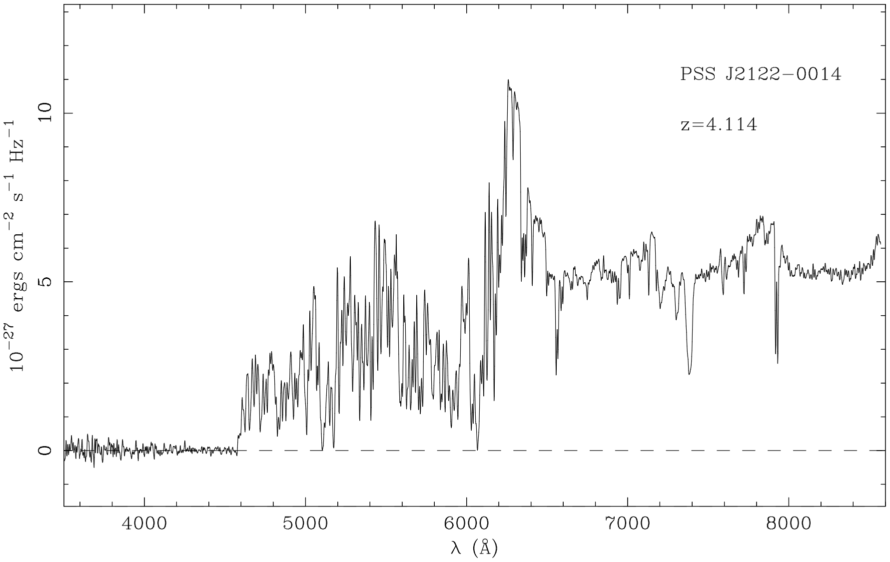

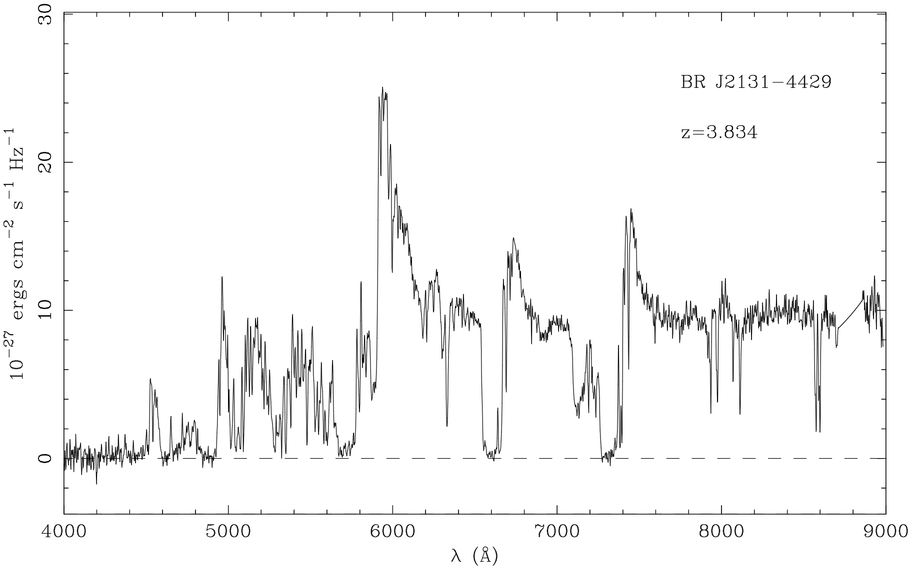

Fig. 3.— *continued*

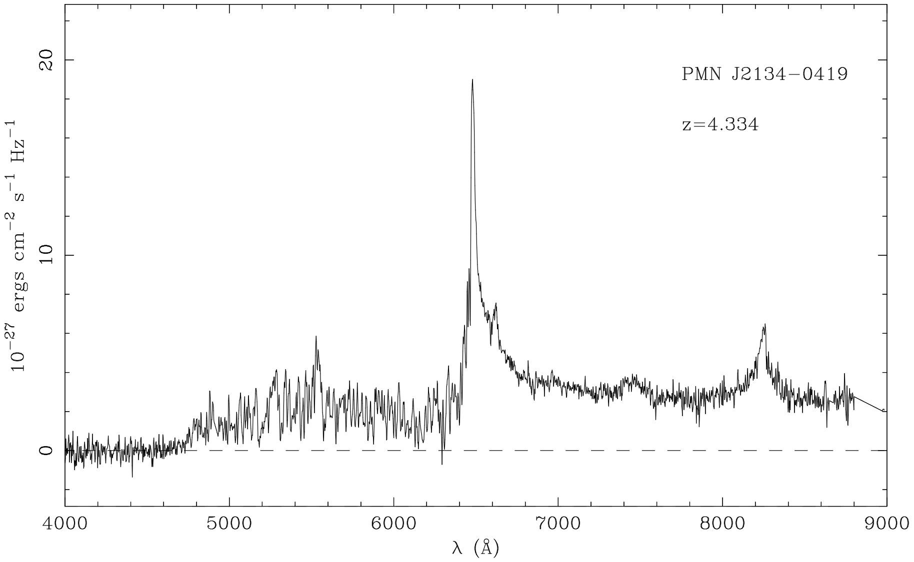

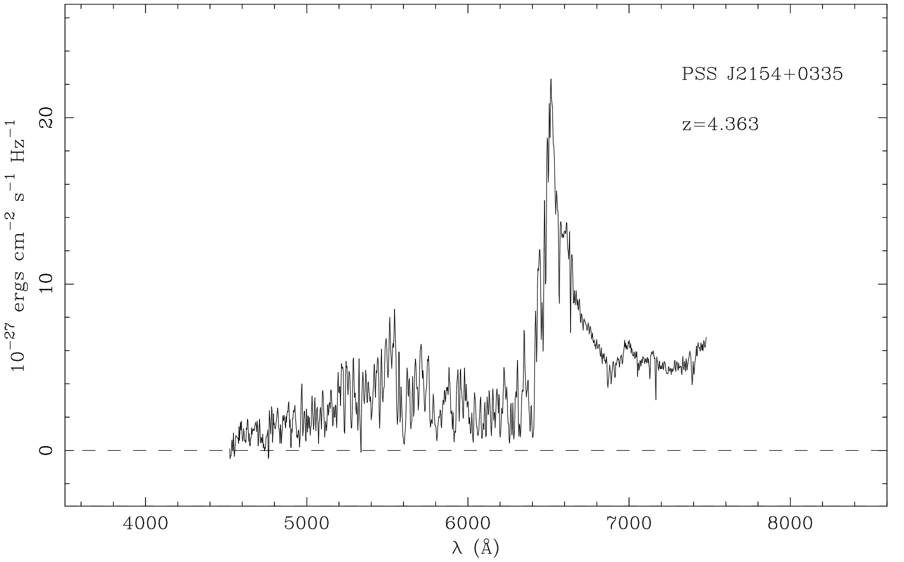

Fig. 3.— *continued*

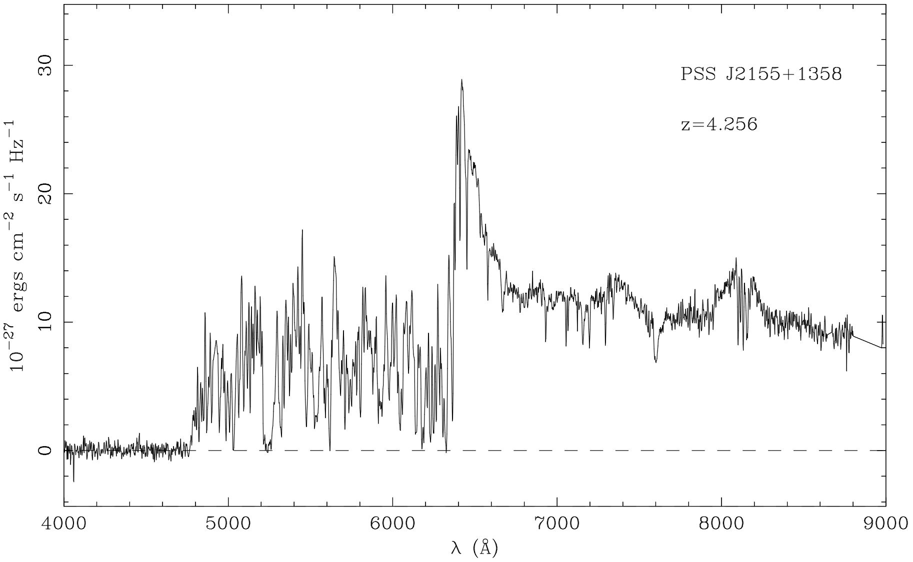

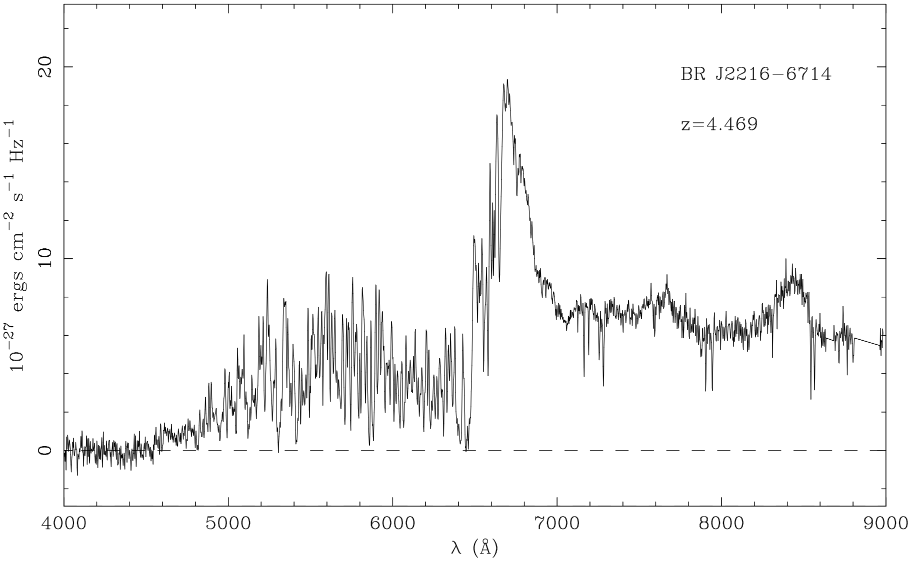

Fig. 3.— *continued*

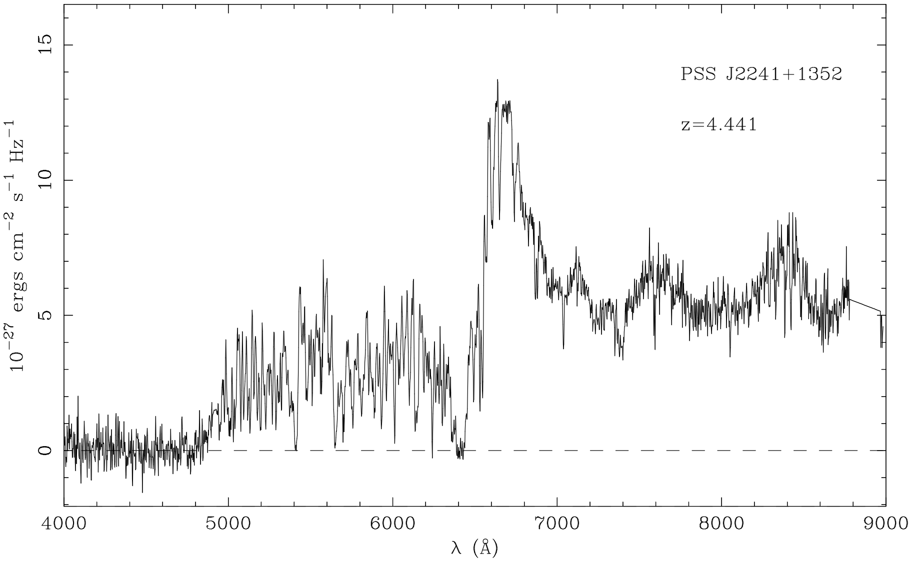

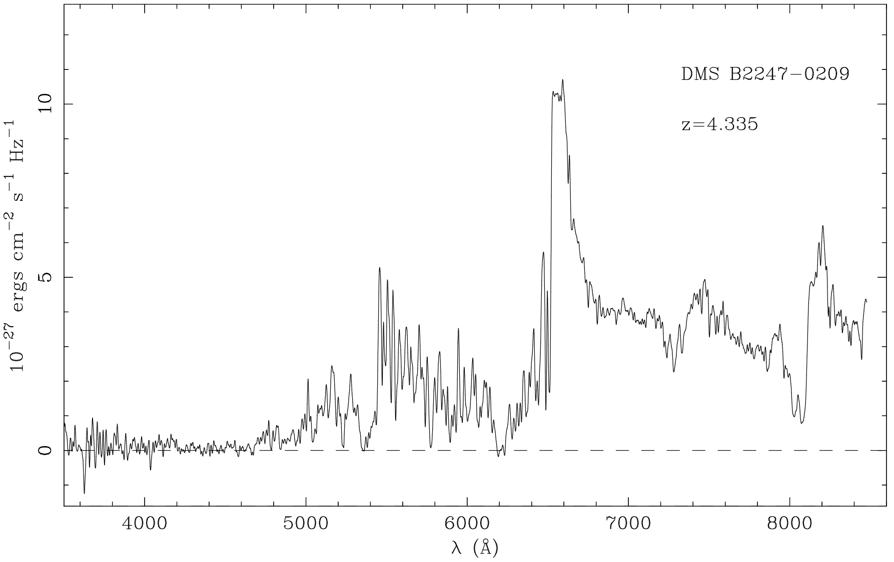

Fig. 3.— *continued*

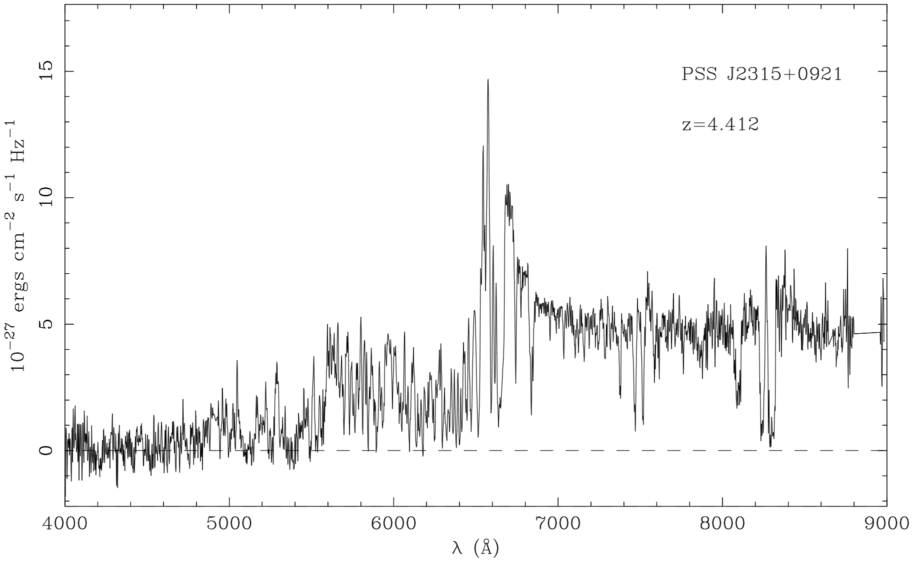

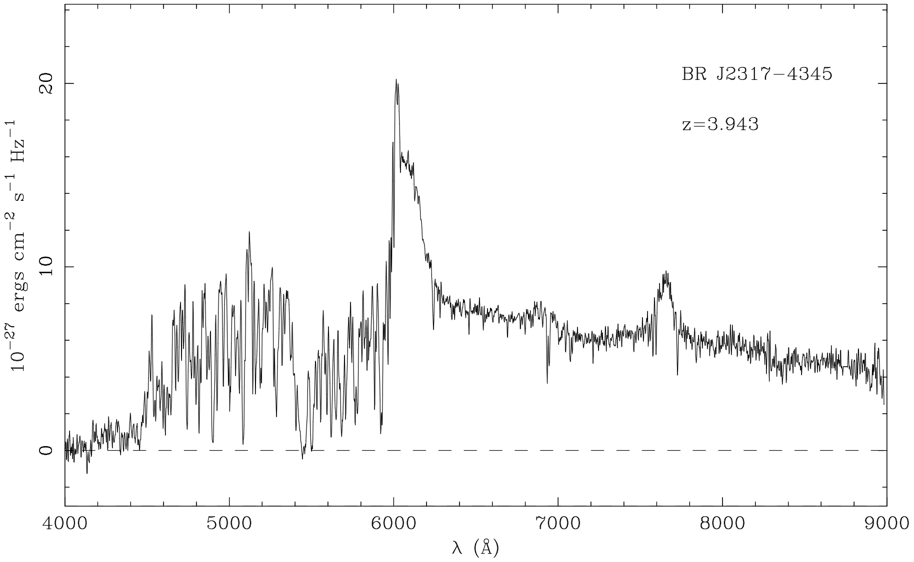

Fig. 3.— *continued*

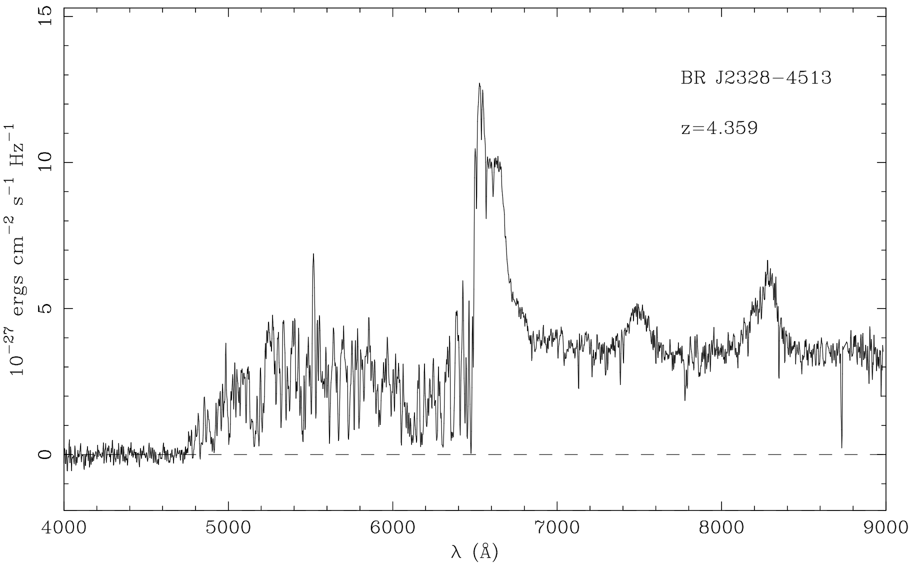

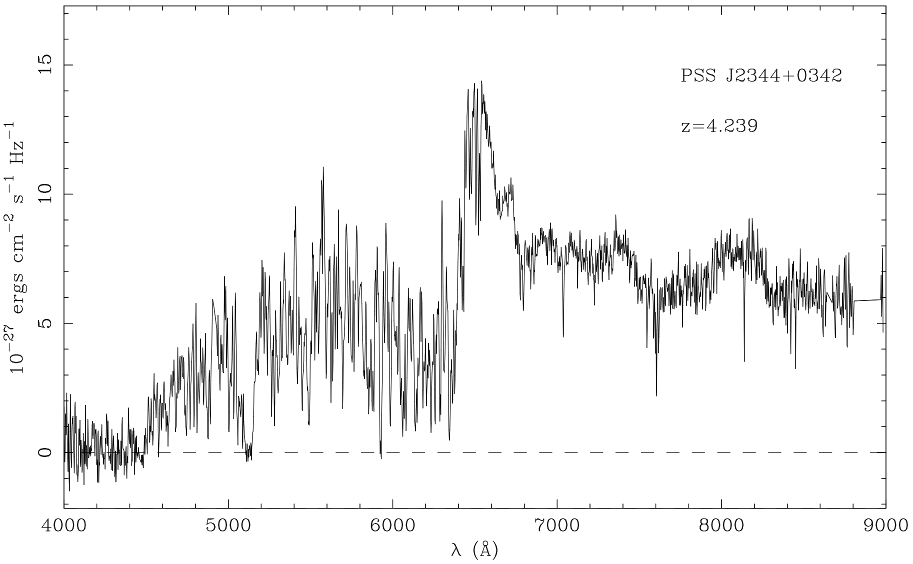

Fig. 3.— *continued*

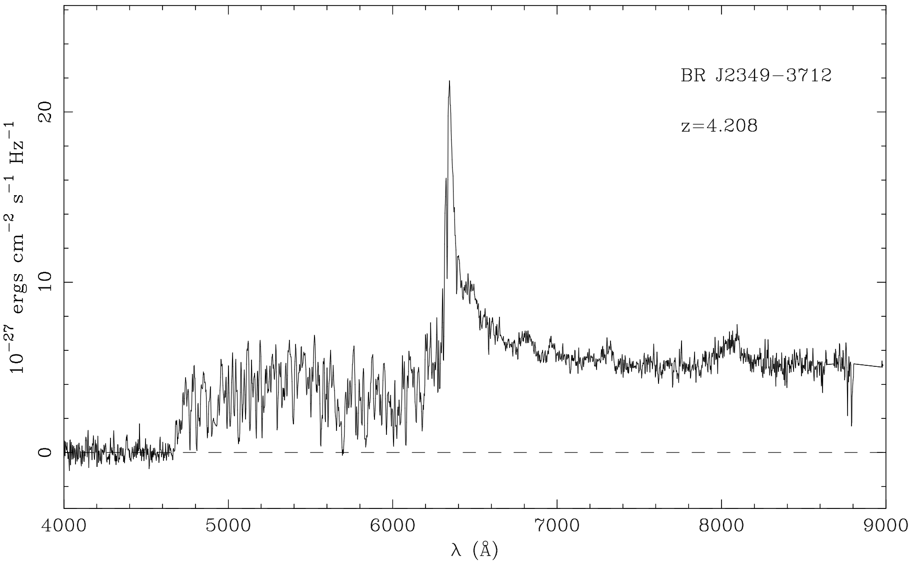

Fig. 3.— *continued*

Table 2: Quasar Redshift Measurements

Quasar	Lyα 1216Å	N V 1240Å	O I 1304Å	Si+O 1400Å	CIV 1549Å	Mean Redshift[a]	Note
PSS J0003+2730	4.255	4.205	4.261	4.248	4.233	4.240±0.022	
BR J0006−6208	4.505	...	4.471	...	4.388	4.455 ±.060	
BR J0030−5129	4.163	4.172	4.187	4.175	4.174	4.174 ±.009	
PSS J0034+1639	4.309	...	4.298	4.281	4.284	4.293 ±.013	
SDSS J0035+0040	4.737	...	4.758	...	4.746	4.747 ±.011	
PSS J0052+2405	...	...	...	...	...	1.90 ±0.05	BAL, [b]
Q J0054−2742	4.464	...	...	...	...	4.464 ±.005	BAL
PSS J0106+2601	4.323	...	4.332	4.303	4.276	4.309 ±.025	
PSS J0131+0633	4.431	...	4.430	4.405	4.402	4.417 ±.015	
PSS J0133+0400	4.142	...	4.172	4.156	4.148	4.154 ±.013	
PSS J0134+3307	4.524	4.534	4.538	4.530	...	4.532 ±.006	
PSS J0137+2837	4.297	...	...	...	4.220	4.258 ±.054	BAL
PSS J0152+0735	4.042	...	4.064	4.047	4.049	4.051 ±.010	
PSS J0207+0940	4.132	...	...	4.142	4.134	4.136 ±.005	BAL
PSS J0209+0517	4.174	...	...	...	...	4.174 ±.007	
SDSS J0211−0009	4.874	...	...	...	...	4.874 ±.036	
BR J0234−1806	4.296	...	...	...	4.307	4.301 ±.008	
PSS J0248+1802	4.403	...	4.440	4.428	4.418	4.422 ±.016	
BR J0301−5537	4.146	...	...	4.125	4.129	4.133 ±.011	
BR J0307−4945	...	...	...	4.738	4.717	4.728 ±.015	
SDSS J0310−0014	4.645	4.701	...	4.645	4.639	4.658 ±.029	
BR J0311−1722	4.049	4.083	4.025	4.000	...	4.039 ±.036	
PSS J0320+0208	3.850	...	...	3.837	3.833	3.840 ±.009	BAL
BR J0324−2918	4.609	4.627	4.630	4.615	4.629	4.622 ±.009	
BR J0334−1612	4.356	...	4.383	4.364	4.350	4.363 ±.014	
SDSS J0338+0021	5.010	...	...	...	...	5.010 ±.033	
BR J0355−3811	4.530	...	4.567	4.549	4.533	4.545 ±.017	
BR J0403−1703	4.220	4.231	4.232	...	4.227	4.227 ±.005	
BR J0415−4357	4.064	...	4.075	4.069	4.072	4.070 ±.005	
BR J0419−5716	4.473	...	4.472	4.453	4.445	4.461 ±.014	
BR J0426−2202	4.322	4.324	...	4.319	4.314	4.320 ±.005	
PMN J0525−3343	4.417	...	...	4.384	4.349	4.383 ±.034	
BR J0529−3526	4.411	...	4.419	4.414	4.407	4.413 ±.005	
BR J0529−3552	4.172	...	4.181	4.167	4.167	4.172 ±.006	
BR J0714−6455	4.483	...	4.486	4.456	4.422	4.462 ±.030	
PSS J0747+4434	4.424	4.434	4.442	4.423	4.427	4.430 ±.008	
RX J1028−0844	4.235	4.317	...	...	...	4.276 ±.058	
PSS J1048+4407	4.422	...	...	4.367	4.354	4.381 ±.036	BAL
PSS J1057+4555	4.125	...	...	4.114	4.109	4.116 ±.008	
PSS J1159+1337	4.073	...	...	...	...	4.073 ±.014	
PSS J1253−0228	4.007	...	...	4.027	3.988	4.007 ±.019	
BR J1310−1740	4.201	...	...	4.179	4.175	4.185 ±.014	

BR J1330−2522	3.950	3.935	3.961	3.946	3.951	3.949 ±.009	
FIRST J1410+3409	4.357	4.351	4.370	4.338	4.338	4.351 ±.014	
PSS J1438+2538	4.275	...	...	4.193	4.232	4.234 ±.041	BAL
PSS J1456+2007	4.251	4.255	4.251	4.247	4.242	4.249 ±.005	
BR J1603+0721	4.393	...	4.404	...	4.359	4.385 ±.024	
PSS J1618+4125	4.212	...	4.220	4.215	4.206	4.213 ±.006	
PSS J1633+1411	4.354	...	...	4.347	4.352	4.351 ±.004	
PSS J1646+5514	4.071	...	4.058	4.018	4.003	4.037 ±.032	
PSS J1721+3256	4.034	...	4.046	4.028	4.016	4.031 ±.012	
RX J1759+6638	4.321	4.321	...	4.318	4.318	4.320 ±.002	
PSS J1802+5616	4.171	...	...	4.146	...	4.158 ±.018	
BR J2017−4019	4.131	...	...	...	...	4.131 ±.013	BAL
PSS J2122−0014	4.156	...	...	4.105	4.080	4.114 ±.039	
BR J2131−4429	3.871	...	...	3.816	3.814	3.834 ±.032	BAL
PMN J2134−0419	4.330	4.344	...	4.331	4.330	4.334 ±.007	
PSS J2154+0335	4.360	...	4.367	...	...	4.363 ±.005	
PSS J2155+1358	4.285	...	...	4.269	4.216	4.256 ±.036	
BR J2216−6714	4.494	...	...	4.467	4.444	4.469 ±.025	
PSS J2241+1352	4.419	...	4.469	4.458	4.416	4.441 ±.027	
DMS B2247−0209	4.378	...	...	4.342	4.284	4.335 ±.048	BAL
PSS J2315+0921	4.412	...	...	...	...	4.412 ±.041	BAL
BR J2317−4345	3.949	...	...	3.931	3.950	3.943 ±.010	
BR J2328−4513	4.366	...	...	4.361	4.349	4.359 ±.009	
PSS J2344+0342	...	...	...	...	4.239	4.239 ±.052	
BR J2349−3712	4.221	4.169	4.231	...	4.211	4.208 ±.028	
median rest-frame composite spectrum	0.002		0.003	-0.001	-0.002	0.001	

[a] The error estimate is $\frac{\sigma}{\sqrt{n}}$.

[b] This object was originally in the PSS web page as a high redshift object. It has since been removed from that list. Our spectrum shows that it is a broad absorption line quasar at z=1.9.

Notes:

BAL: These quasars exhibit broad absorption line characteristics.

To provide an internal check on our redshift determinations we used the median composite spectrum of our quasar survey (Figure **??** of Chapter 3). Measuring the wavelength of the emission lines of the median composite spectrum provides an estimate of any systematic bias in the redshift measurements which in our case proves to be about z=±0.001 (see last row of Table 2.4.1) and allows any shift in quasar redshifts to be checked by cross-correlation.

2.4.2 Magnitude Measurements

Table 2.4.2 summarizes the photometric and spectroscopic magnitudes for each object. The photometric magnitudes were measured from the UKST and POSS1 plates scanned using the APM facility. The spectroscopic magnitudes are derived from the spectra themselves using the IRAF task CALCPHOT and the "R59" (OR) or "R63" (R) filter curves for the quasars magnitudes from the UKST survey and the "e" filter curve for quasar magnitudes from the POSS1 survey. These transmission curves are shown on Figure 5 overplotted on the z=4.172 BR J0529−3552 quasar spectrum.

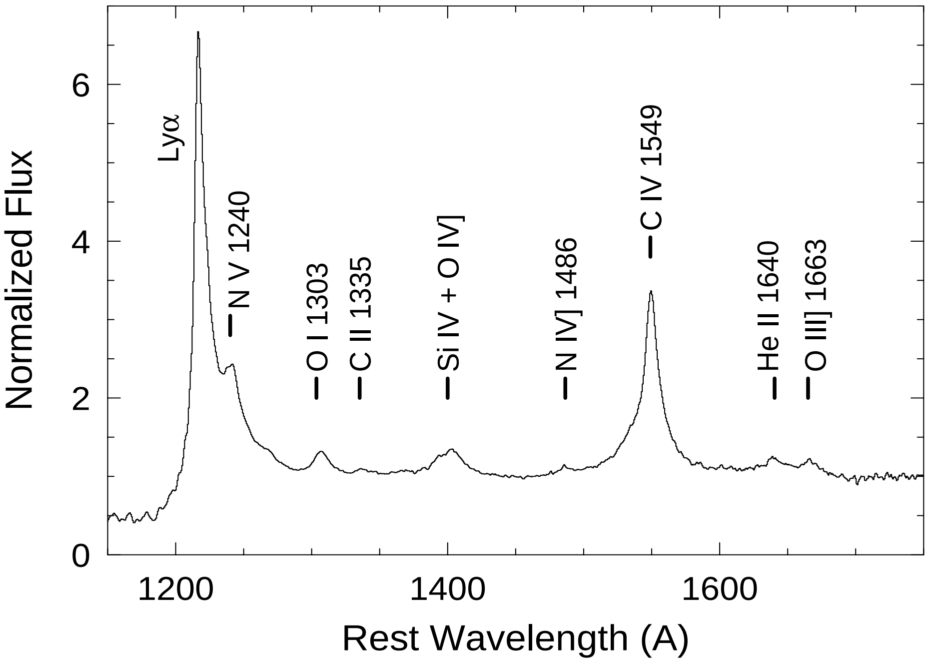

Fig. 4.— Normalised spectrum of a quasar, showing the main emission lines. Ly-α, NV, OI and CIV have been used whenever possible in order to determine the redshift of the quasars presented in this chapter (Shields et al., 1997).

Table 3: Quasar Magnitude Measurements

Quasars	R^a APM	R^b	Filter^c	Notes
PSS J0003+2730	18.3	17.8	e	
BR J0006−6208	18.3	19.2	R59	
BR J0030−5129	18.6	18.6	R59	
PSS J0034+1639	18.0	17.8	e	
SDSS J0035+0040	...	21.3	e	
PSS J0052+2405	17.4	17.4	e	BAL
Q J0054−2742	19.8	19.8	R59	BAL
PSS J0106+2601	18.5	18.3	e	
PSS J0131+0633	...	19.1	e	NC
PSS J0133+0400	18.3	18.0	e	NC
PSS J0134+3307	19.9	18.9	e	
PSS J0137+2837	18.3	18.6	e	BAL
PSS J0152+0735	18.7	18.0	e	
PSS J0207+0940	18.7	19.2	e	BAL, NC
PSS J0209+0517	17.8	17.8	e	NC
SDSS J0211−0009	...	21.5	e	NC
BR J0234−1806	18.8	19.2	R59	
PSS J0248+1802	17.7	17.6	e	
BR J0301−5537	19.0	18.9	R59	
BR J0307−4945	18.8	18.8	R59	
SDSS J0310−0014	20.7	21.0	R59	NC
BR J0311−1722	17.7	18.0	R59	
PSS J0320+0208	18.5	18.5	e	BAL, NC
BR J0324−2918	18.7	18.6	R59	
BR J0334−1612	17.9	19.2	R59	NC
SDSS J0338+0021	...	21.5	R63	NC
BR J0355−3811	17.9	18.2	R59	
BR J0403−1703	18.7	19.3	R63	NC
BR J0415−4357	18.8	18.9	R59	
BR J0419−5716	17.8	18.7	R59	
BR J0426−2202	17.9	18.0	R59	
PMN J0525−3343	18.4	18.7	R59	
BR J0529−3526	18.9	19.0	R59	
BR J0529−3552	18.3	18.5	R59	
BR J0714−6455	18.3	18.2	R59	
PSS J0747+4434	18.4	19.2	e	NC
RX J1028−0844	18.8	19.1	R59	
PSS J1048+4407	19.6	20.1	e	BAL
PSS J1057+4555	16.5	17.0	e	
PSS J1159+1337	17.1	17.1	e	
PSS J1253−0228	18.8	18.7	R59	
BR J1310−1740	19.5	19.2	R59	

BR J1330−2522	18.5	18.8	R59	
FIRST J1410+3409	19.9	20.7	e	
PSS J1438+2538	19.3	18.6	e	BAL
PSS J1456+2007	18.2	18.7	e	
BR J1603+0721	19.3	19.4	e	
PSS J1618+4125	18.5	19.0	e	
PSS J1633+1411	18.7	18.2	e	
PSS J1646+5514	17.1	16.5	e	
PSS J1721+3256	18.8	18.1	e	
RX J1759+6638	19.1	19.8	e	
PSS J1802+5616	18.3	19.2	e	NC
BR J2017−4019	18.6	18.2	R59	BAL, NC
PSS J2122−0014	20.3	19.0	R59	NC
BR J2131−4429	18.3	18.4	R59	BAL, NC
PMN J2134−0419	20.0	19.2	R59	
PSS J2154+0335	19.0	18.6	e	NC
PSS J2155+1358	18.0	17.9	e	
BR J2216−6714	18.6	18.6	R59	
PSS J2241+1352	19.1	19.3	e	
DMS B2247−0209	19.8	19.0	R63	BAL
PSS J2315+0921	19.2	19.5	e	BAL
BR J2317−4345	19.0	18.5	R59	
BR J2328−4513	19.2	19.1	R59	
PSS J2344+0342	18.2	18.6	e	
BR J2349−3712	18.7	18.7	R59	

[a] The R magnitude from the photographic plates as measured by the APM. If no magnitudes are specified in this column, the quasar is not detected on the APM plates. The uncertainties in these magnitudes are estimated to be ±0.25.

[b] The R magnitude measured from the spectra as described in the text. The uncertainties in these magnitudes are estimated to be ±0.1.

[c] R59 and R63 are UKST filters while e is the POSS1 filter.

Notes:
The NC in the notes column means that the spectrum has not been corrected for slit losses. The BAL designation means the quasar exhibits broad absorption lines.

The error on the spectroscopic measurements is estimated to be +/- 0.1 mag and the error on the APM R magnitude is +/-0.25 mag. The scatter between spectroscopic and APM magnitude measurements is illustrated by Figure 6 which on the one hand emphasizes the two different surveys and on the other hand shows the BAL objects and spectra not corrected for slit losts. Finally, Hook et al. (1994) have shown that optically selected quasars vary, which might explain in part the scatter observed in these plots.

2.5 Notes on Individual Objects

1. PSS J0003+2730 (z=4.240): This quasar has two weak Lyα absorbers at z=3.51 and 3.89. Neither has an estimated column density greater than $10^{20.3}$ atoms cm^{-2}, but metal lines associated with both absorbers have been detected.

2. BR J0006−6208 (z=4.455): This quasar has weak emission lines but a rich absorption spectrum. There are four candidate damped absorbers at z=2.97, 3.20, 3.78 and 4.14. The highest redshift is a weak candidate but the other three all have high estimated column densities. All the candidates have at least one associated metal absorption line. In addition, there is a MgII absorption system at z=1.958.

3. BR J0030−5129 (z=4.174): This quasar has one candidate damped absorber at z=2.45 with three associated FeII lines.

4. PSS J0034+1639 (z=4.293): This quasar has two damped Lyα candidate absorbers. The first is at z=3.75 and the estimated column density of log $N_{\rm HI}$ = 20.2 falls just below the formal definition of DLAs. Associated SiII and CIV metal lines are detected. The second damped system is at z=4.26 which is within 3000 km s^{-1} of the emission redshift of the quasar (z=4.293) so it will not be included as an intervening absorber in the statistical samples used in determining the neutral gas mass. However it is of interest because this is the first damped system detected at a redshift greater than 4 with a column density log $N_{\rm HI} > 21$. We estimate the column density for this system at log $N_{\rm HI}$ = 21.1 and detected associated metals lines of SiII, OI, CII, SiIV, CIV, and FeII in the range z=4.252-4.282.

5. SDSS J0035+0040 (z=4.747): We detect no damped Lyα candidates in this spectrum. This is one of the lower signal-to-noise spectra in our sample due to the faintness of the quasar (R=21.3) but we would have been able to detect a DLA with a column density log $N_{\rm HI} \geq 20.3$ over the redshift range $3.309 < z < 4.690$.

6. PSS J0052+2405 (z=1.90): This is a broad absorption lines quasar at z=1.9. We observed it because the coordinates were originally in the list of PSS $z > 4$ quasars available at their www site [4]. It has since been removed from that list.

---

[4] http://www.astro.caltech.edu/~george/z4.quasars

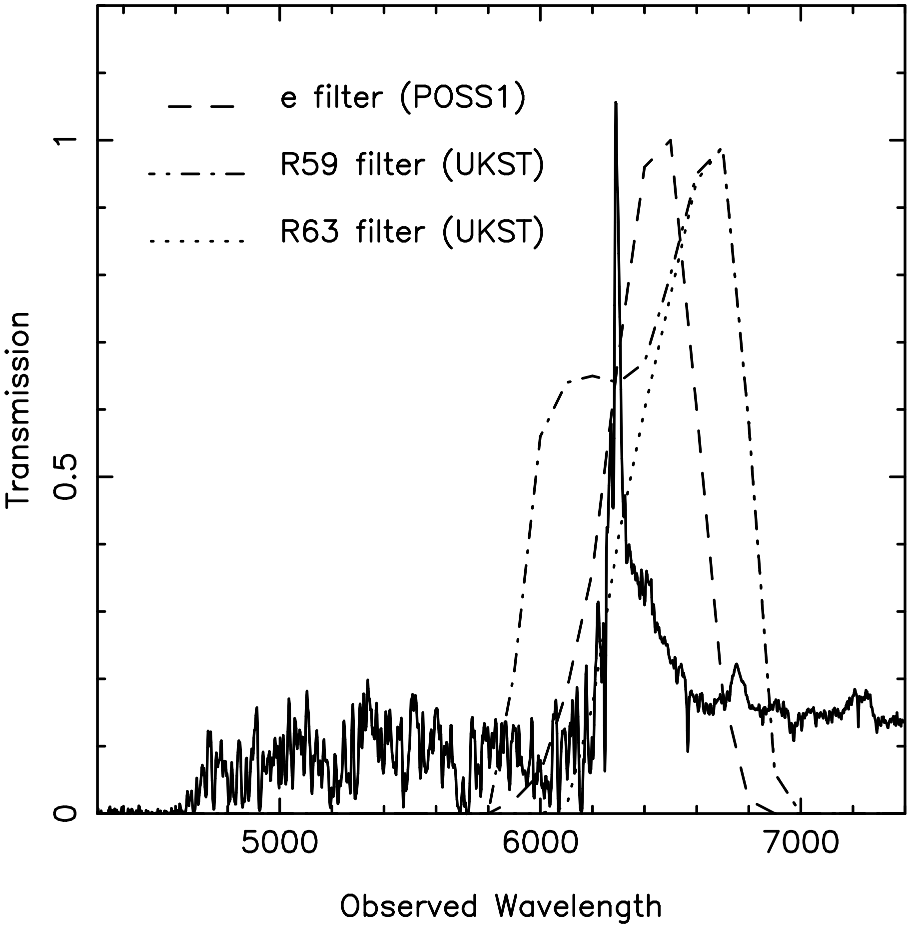

Fig. 5.— Filters used in various surveys. The R filters used for the photographic plates scanned with the APM facility are overplotted on the spectrum of z=4.172 BR J0529−3552. The "e" filter was used for the POSS1 survey and the "R59" (R) and "R63" (OR) were used for the UKST survey.

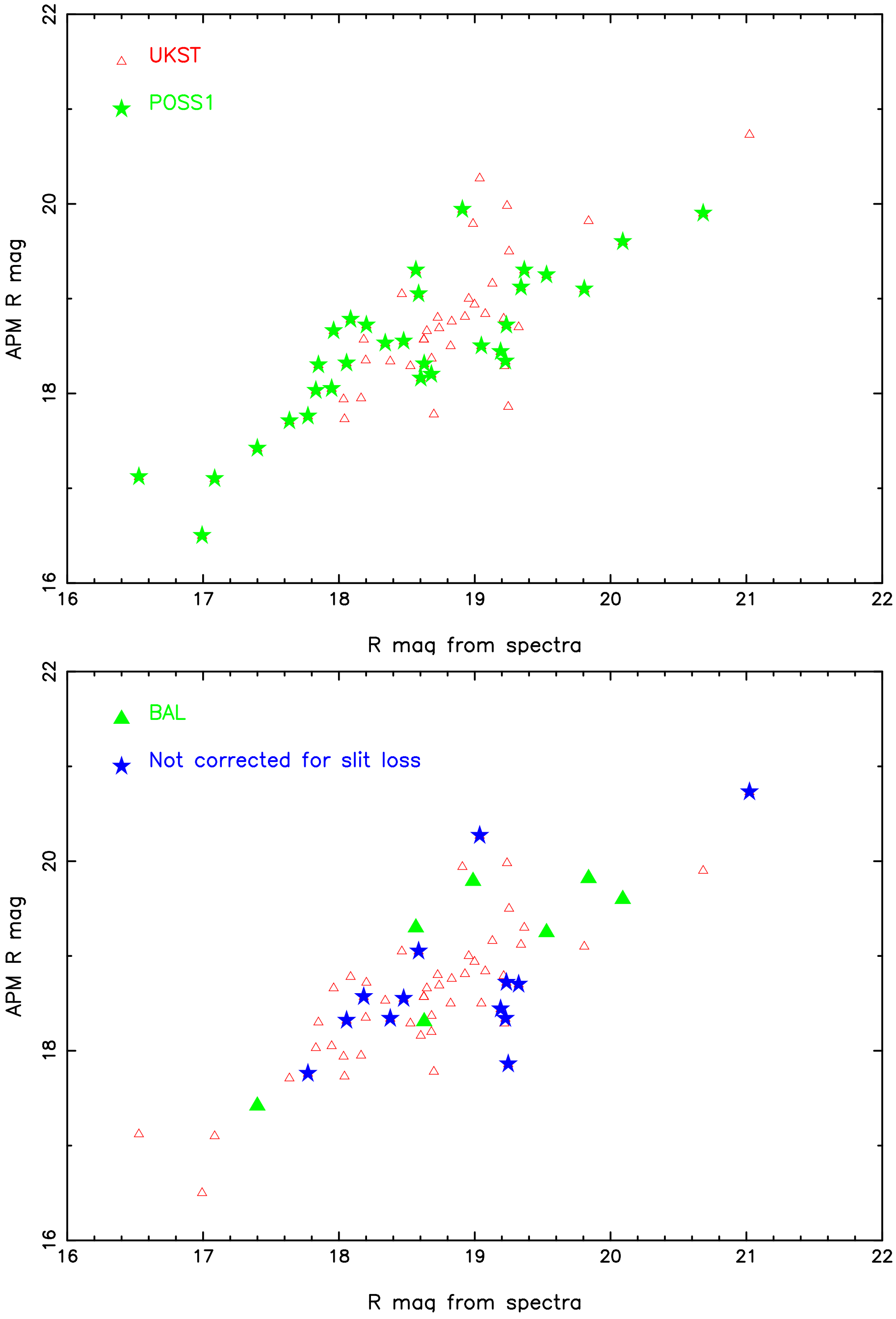

Fig. 6.— APM versus spectral magnitudes. Top panel emphasizes the two different surveys while the bottom panel shows the BAL objects and spectra not corrected for slit lost.

7. Q J0054−2742 (z=4.464): This quasar exhibits broad absorption lines. The spectrum is not used in our absorption line survey.

8. PSS J0106+2601 (z=4.309): This quasar has a strong candidate damped absorber at z=3.96 with associated metal lines.

9. PSS J0131+0633 (z=4.417): This quasar has two very weak candidate damped absorbers at z=3.17 and 3.69. CIV is also detected at z=3.69.

10. PSS J0133+0400 (z=4.154): This spectrum has four candidate damped absorbers. The absorbers at z=3.69 and 3.77 have estimated column densities above the formal definition of DLA ($N_{HI} \geq 10^{20.3}$ atoms cm^{-2}) and the absorbers at z=3.08 and 4.00 are below that threshold. Associated metal lines are detected for all of the candidate DLAs.

11. PSS J0134+3307 (z=4.532): The quasar has a DLA at z=3.76 with associated metal lines.

12. PSS J0137+2837 (z=4.258): This quasar exhibits broad absorption lines. The spectrum is not used in our absorption line survey.

13. PSS J0152+0735 (z=4.051): This quasar has an excellent DLA candidate at z=3.84 with associated metal lines, which is also detected as a Lyman limit system.

14. PSS J0207+0940 (z=4.136): This quasar exhibits strong intrinsic absorption features. The spectrum is not used in our absorption line survey.

15. PSS J0209+0517 (z=4.174): This quasar has weak emission lines but exhibits two DLA candidates at z=3.66 and 3.86. Both have associated metal absorption features.

16. SDSS J0211−0009 (z=4.874): We detect one weak candidate DLA in this quasar at z=4.64. SiII is also detected at that redshift.

17. BR J0234−1806 (z=4.301): This quasar shows one weak absorption candidate at z=3.69 with associated metal lines.

18. PSS J0248+1802 (z=4.422): This spectrum shows no DLA candidates.

19. BR J0301−5537 (z=4.133): This quasar shows three DLA candidates at z=3.22, 3.38, and 3.71. All have associated metal lines but the two higher redshift candidates have estimated column densities below 2×10^{20} atoms cm^{-2}.

20. BR J0307−4945 (z=4.728): The spectrum shows the highest redshift damped absorber currently known at z=4.46 with an estimated column density of log $N_{\rm HI}$ = 20.8. Associated metal lines of SiII, OI, CII, SiIV, CIV, FeII, and AlII are also detected at this redshift. The spectrum is shown in Figure 7. This object has been observed at high-resolution with the UV-Visual Echelle Spectrograph on VLT-2

and the metallicity of the DLA is derived (Dessauges-Zavadsky et al., 2001). The high metallicity , $\sim 1/90$ solar, sjows that this very young absorber(≤ 1.3 Gyr) has already experienced a significant metal enrichment. The [O/Si] ratio is nearly solar suggesting a limited amount of dust, the relative [Si, O/Fe] abundance ratios show a similar enhancement as observed in the Milky Way stars with comparable metallicities, and the [N/O] ratio is very low. All these results point to an enrichment pattern dominated by Tupe II supernovae which suggests a Milky Way tupe evolutionary model.

21. SDSS J0310−0014 (z=4.658): This quasar shows two candidate DLAs at z=3.42 and 4.34. The lower redshift system has an estimated column density above the DLA threshold. An associated Al II line is detected at z=3.424 but no metal lines associated with the higher redshift candidate are detected .

22. BR J0311−1722 (z=4.039): This quasar has a weak DLA candidate at z=3.73 which is also detected as a Lyman-limit system. Associated metal lines are also detected.

23. PSS J0320+0208 (z=3.840): This quasar exhibits broad absorption lines. The spectrum is not used in our absorption line survey.

24. BR J0324−2918 (z=4.622): No DLA candidates are detected in this spectrum.

25. BR J0334−1612 (z=4.363): A DLA candidate at z=3.56 with associated SiII is detected in this quasar. This candidate has previously been detected (Storrie-Lombardi & Wolfe 2000) with a lower estimated column density (log $N_{\rm HI}$=20.6) than we measure .

26. SDSS J0338+0021 (z=5.010): This quasar has one DLA candidate at z=4.06 with associated metals detected.

27. BR J0355−3811 (z=4.545): No DLA candidates are detected in this spectrum. There is a Mg II absorber at z=2.228.

28. BR J0403−1703 (z=4.227): No DLA candidates are detected. No metal lines could be identified in this spectrum.

29. BR J0415−4357 (z=4.070): A weak DLA candidate with associated metal lines is detected at z=3.81.

30. BR J0419−5716 (z=4.461): Three weak DLA candidates are detected just above the Lyman-limit edge in this spectrum at z=2.82, 2.90, and 2.98. One associated metal line is detected from each of the two lower redshift systems.

31. BR J0426−2202 (z=4.320): A very high column density candidate (log $N_{\rm HI}$=21.1) is detected at z=2.98 with associated Al II.

32. PMN J0525−3343 (z=4.383): No DLA candidates are detected in this spectrum. Two Mg II absorbers are detected at z=1.570 and 2.006.

33. BR J0529−3526 (z=4.413): A weak DLA candidate with associated metal lines is detected at z=3.57.

34. BR J0529−3552 (z=4.172): A 'doublet' of weak DLA candidates is detected at z=3.68 and 3.70. No associated metals are detected at these redshifts.

35. BR J0714−6455 (z=4.462): No DLA candidates are detected in this spectrum.

36. PSS J0747+4434 (z=4.430): Two DLA candidates are detected at z=3.76 and 4.02. The higher redshift system also has associated metal lines.

37. RX J1028−0844 (z=4.276): Two weak DLA candidates with associated metals are detected at z=3.42 and 4.05.

38. PSS J1048+4407 (z=4.381): This quasar exhibits broad absorption lines. The spectrum is not used in our absorption line survey.

39. PSS J1057+4555 (z=4.116): Three DLA candidates are detected at z=2.90, 3.05, and 3.32. The candidate absorber at z=3.32 has been confirmed as damped in a higher resolution spectrum. It has a redshift of z=3.3172 and a column density log $N_{\rm HI}$=20.34 (Lu, Sargent & Barlow 1998). The estimated column density (log $N_{\rm HI}$=20.3) for the z=3.05 is identical to the estimate reported in Storrie-Lombardi & Wolfe (2000).

40. PSS J1159+1337 (z=4.073): This quasar has a DLA candidate at z=3.72 with several associated metal lines.

41. PSS J1253−0228 (z=4.007): This quasar has two candidate damped absorbers. One absorber at z=2.78 has a very high estimated column density (log $N_{\rm HI}$=21.4) and an associated Al II line is detected. This is the highest column density absorber in our survey. Another absorber at z=3.60 is highly unlikely to be damped, with an estimated column density of log $N_{\rm HI}$=19.7, but does have several associated metal lines.

42. BR J1310−1740 (z=4.185): This quasar has a weak damped candidate at z=3.43. Associated metal lines are also detected at this redshift.

43. BR J1330−2522 (z=3.949): This quasar has two weak DLA candidates at z=2.91 and 3.08. The higher redshift system has associated metal lines.

44. FIRST J1410+3409 (z=4.351): There is a weak candidate damped absorber at z=3.43 with no associated metal lines. In this spectrum the redshift path surveyed for damped absorbers is not continuous due to a large noise spike in the forest at z≈3.59.

45. PSS J1438+2538 (z=4.234): This quasar exhibits broad absorption lines. The spectrum is not used in our absorption line survey.

46. PSS J1456+2007 (z=4.249): There are two weak DLA candidates at z= 3.22 and 4.16. The lower redshift system also has associated metal lines.

47. BR J1603+0721 (z=4.385): No DLA candidates are detected in this spectrum.

48. PSS J1618+4125 (z=4.213): There is a DLA candidate at z=3.92 with associated metal lines.

49. PSS J1633+1411 (z=4.351): There is a weak DLA candidate at z=3.90 with associated metal lines.

50. PSS J1646+5514 (z=4.037): No DLA candidates are detected in this spectrum.

51. PSS J1721+3256 (z=4.031): No DLA candidates are detected in this spectrum.

52. RX J1759+6638 (z=4.320): There is a DLA candidate at z=3.40 with associated metal lines.

53. PSS J1802+5616 (z=4.158): There are four damped absorber candidates detected in this spectrum at z=3.39, 3.56, 3.76, and 3.80. Only the absorber at z=3.76 has an estimated column density above the formal definition of DLA ($N_{HI} \geq 10^{20.3}$ atoms cm^{-2}). Associated metal lines are detected for the z=3.39 and 3.80 absorbers.

54. BR J2017−4019 (z=4.131): This quasar exhibits strong intrinsic absorption at the quasar emission redshift. The CIV and SiIV emission lines are completely absorbed. The spectrum is not used in our absorption line survey.

55. PSS J2122−0014 (z=4.114): This spectrum shows two DLA candidates at z=3.20 and 4.00. We estimate the column density of the lower redshift system to be log $N_{\rm HI}$=20.3, but this may be an overestimating as the Lyα line at z=3.20 is at the same position as the Lyβ line at z=4.00. Associated metal lines are detected for both absorption systems.

56. BR J2131−4429 (z=3.834): This quasar exhibits broad absorption lines. The spectrum is not used in our absorption line survey.

57. PMN J2134−0419 (z=4.334): This quasar has one weak DLA candidate at z=3.27 with associated metal lines.

58. PSS J2154+0335 (z=4.363): This quasar has two DLA candidates at z=3.61 and 3.79. Metal lines are detected for both, but only the lower redshift system has an estimated column density above 2×10^{20} atoms cm^{-2}.

59. PSS J2155+1358 (z=4.256): This quasar has a very high column density (log $N_{\rm HI}$ = 21.1) DLA candidate at z=3.32. Associated metal lines are also detected at this redshift.

60. BR J2216−6714 (z=4.469): This quasar has three weak DLA candidates at z=3.27, 4.28, and 4.32. At least one associated metal line has been detected for each.

61. PSS J2241+1352 (z=4.441): This quasar has two DLA candidates at z=3.65 and 4.28. The lower redshift system has an estimated column density below the formal definition of DLA ($N_{HI} \geq 10^{20.3}$ atoms cm^{-2}). Both have associated metal lines.

62. DMS B2247−0209 (z=4.335): This quasar exhibits broad absorption lines. The spectrum is not used in our absorption line survey.

63. PSS J2315+0921 (z=4.412): This quasar exhibits strong intrinsic absorption at the quasar emission redshift. The CIV and SiIV emission lines are almost completely absorbed. It is similar in character to the spectrum of BR J2017−4019. The spectrum is not used in our absorption line survey.

64. BR J2317−4345 (z=3.943): This quasar has a strong DLA candidate at z=3.49 with associated metal lines.

65. BR J2328−4513 (z=4.359): There is a weak DLA candidate at z=3.04. SiII is detected at this redshift but may be blended with CIV at z=3.719.

66. PSS J2344+0342 (z=4.239): There are two very high column density DLA candidates at z=2.68 and 3.21. Both have associated metal lines.

67. BR J2349−3712 (z=4.208): There is a weak DLA candidate at z=3.69 with associated SiII.

2.6 Summary

In this Chapter, we have presented the spectra of sixty-six $z \gtrsim 4$ bright quasars with ~ 5 Å resolution (FWHM) and signal-to-noise ratio ranging from 10 to 30. We emphasize the observational set up and data reduction processes for the whole sample. The fluxed spectra are presented as well as redshift and observed magnitude measurements for individual objects. We also provide a detailed description of the characteristics of the each quasar studied.

These observations form the basis for the analysis in subsequent chapters. The next Chapter concentrates on the properties of the quasars themselves. We will then search for and analyse the statistical properties of the Lyman-limit systems (Chapter 4) and the Damped Lyα absorbers (Chapter 5). The space density and column density evolution of these systems will be computed and the high-column density systems will also be used to measure the neutral hydrogen content of the Universe over a large redshift range, thus probing the formation epoch of these objects and tracing the gas from which stars form (Chapter 6). Analysed in conjunction with previous studies, our new survey provide enough data to help draw statistically significant conclusions on these issues at high redshift.

Chapter 3

Quasar Continua

'Les miroirs feraient bien de réfléchir davantage'
Jean Cocteau

In the first part, this Chapter describes the fitting of the continua of the quasars presented in Chapter 2. The grounds for using a power-law fit are introduced in Section 3.1.1. Following the Storrie-Lombardi (1994) methodology, a technique for the determination of the spectral indices of quasars is described (Section 3.1.2). The first step consists of building a quasar composite spectrum characterising a given survey. Such a composite spectrum is constructed for the quasar sample presented in Chapter 2 and the resulting median composite spectrum is compared with those from other large quasar surveys. The second step of the fitting technique is then detailed and measurement of continuum slopes are listed in Section 3.1.3. Section 3.1.4 presents the analysis of our measurements together with further comparisons with previous work.

In the second part of this Chapter (Section 3.2), the slope indices previously measured are correlated with the presence of an absorber in the quasar spectrum with the aim to detect dust in high column density quasar absorbers (see Chapter 5).

In the last part of this Chapter (Section 3.3), the continuum depression parameter are introduced. Measurements are undertaken on the sample of quasars presented in Chapter 2 (Section 3.3.3) and a detailed analysis is provided. Again, our results are compared with previous surveys as well as theoretical predictions from various models.

3.1 Quasar Continuum Fitting

3.1.1 Introduction

The quasar/AGN continuum has been observed from at least $\sim 10^8$ Hz in the radio region to $\sim 10^{27}$ Hz, the latter corresponding to extremely high energy γ-ray photons. This vast range spans many different physical processes but still the quasar continuum can be reasonably well represented by a simple power law over limited frequency ranges.

It is customary to determine the quasars' continua interactively by fitting a power law. This fit can be interchangeably expressed in frequency, ν (in Hertz) or in wavelength λ (in Angstroms):

$$F(\nu) \propto \nu^{-\alpha} \tag{3.1}$$

where the slope, α, is a constant typically lying in the range 0–1 (Francis, 1993b). Since ν can be directly related to λ using:

$$\lambda\, \nu = c \tag{3.2}$$

and hence:

$$\frac{d\lambda}{d\nu} = \frac{-c}{\nu^2} \tag{3.3}$$

Because:

$$F(\nu) = F(\lambda) \left| \frac{d\lambda}{d\nu} \right| \tag{3.4}$$

then:

$$F(\lambda) \propto \nu^{2-\alpha} \propto \lambda^{\alpha-2} \tag{3.5}$$

and

$$F(\nu) \propto \nu^{-\alpha} \propto \lambda^{\alpha} \tag{3.6}$$

Since $\alpha \sim 1$ in quasars, $F(\lambda)$ versus λ generally shows a slightly decreasing continuum with increasing wavelength while $F(\nu)$ versus λ shows a increasing continuum with increasing wavelength. For the $z \gtrsim 4$ quasar spectra presented in this thesis, $F(\lambda)$ versus λ is typically of the order of 10^{-16} ergs cm^{-2} s^{-1} Å^{-1}, while $F(\nu)$ versus λ is of the order of 10^{-27} ergs cm^{-2} s^{-1} Hz^{-1} and the power law slope, α, is typically ~ 0.60.

In addition to the observed power law, the polarisation found at some wavelengths and the compact sizes of the emitting regions deduced from the observed variability, are in favour of the argument for the continuum radiation originating in non-thermal processes such as synchrotron radiation and Compton scattering. Nevertheless, more detailed observations seem to indicate that the physical processes involved are complex and vary from one quasar type to another.

3.1.2 Methodology

In order to fit the quasar continuum of our spectra, we used a method developed by Storrie-Lombardi (1994). The first step of this technique consists in building a composite spectrum representative of a given quasar survey. Then a differential fitting technique is applied. We also compare our results with other large quasar surveys thus allowing for the characterisation of the general properties of each sample.

Building a Composite Spectrum

Several quasar survey composite spectra have been produced in the past. Composite spectra provide a valuable reference particularly for the detection of weak emission lines which would not been detected otherwise, for the calculation of k-corrections for use in studies of the evolution of the quasar population, and as in the present case, for the derivation of the form of the underlying continuum.

In addition, composite spectra provide the first step in the modelling and classification of quasar spectra. For example, Francis et al. (1992) have developed a model-fitting approach to the analysis of the individual quasar spectra in order to extract the parameters describing the rest-frame ultraviolet and optical spectra of the sample. They show these can be extracted in an automated, well-defined and homogeneous fashion and applied the statistical technique of principal component analysis (hereafter PCA) directly to a sample of quasar ultraviolet spectra taken from the Large Bright Quasar Survey. Interestingly, Francis et al. (1992) find that the first three principal components obtained from the PCA account for $\sim 75\%$ of the quasar sample intrinsic variance. They also observe a strong correlation between the continum of the quasar and the equivalent widths of the emission lines in their quasar sample (Francis, 1993a), the so-called "Baldwin-effect" (Baldwin, 1977).

Here, the median composite quasar spectrum of our survey is constructed following the method detailed by Francis & Koratkar (1995): each non-BAL spectrum, with enough wavelength coverage, was corrected to its rest-frame and scaled such that the median of the flux in a region free from emission lines (1420-1470 Å) is unity. The spectra were then rebinned into fixed 0.5 Å bins (i.e. similar to the resolution in the observed frame) and the median of the flux in each bin was calculated to produce the spectrum in Figure 1. Figure 2 shows the same composite spectrum but with all individual points plotted, showing the range of spectral variation.

Comparison with Other Surveys

A composite spectrum emphasises the characeristics of a given survey. For comparison, this section presents composite spectra from several large surveys. Figure 3 shows the composite spectra from the Large Bright Quasar Survey [LBQS] (Francis et al., 1991), the radio FIRST Bright Quasar Survey [FBQS] (Brotherton et al., 2001) and from the most recent Sloan Digital Sky Survey [SDSS] (Vanden Berk et al., 2001). The strength of the Lyman-α line and some of the narrow emission lines in the FBQS composite are stronger than for the other composites. The difference is probably due to the fact that the FBQS sample is entirely radio selected, and there is a correlation between line strengths and radio loudness. Otherwise, the relative fluxes are similar for the lines in common among the various composites.

The continuum slope changes abruptly near 5000 Å and becomes steeper with an index of $\alpha = 2.45$, which is a good fit up to the red end of the spectrum (8555 Å). This change is also evident in the FBQS composite. An upturn in the spectral energy

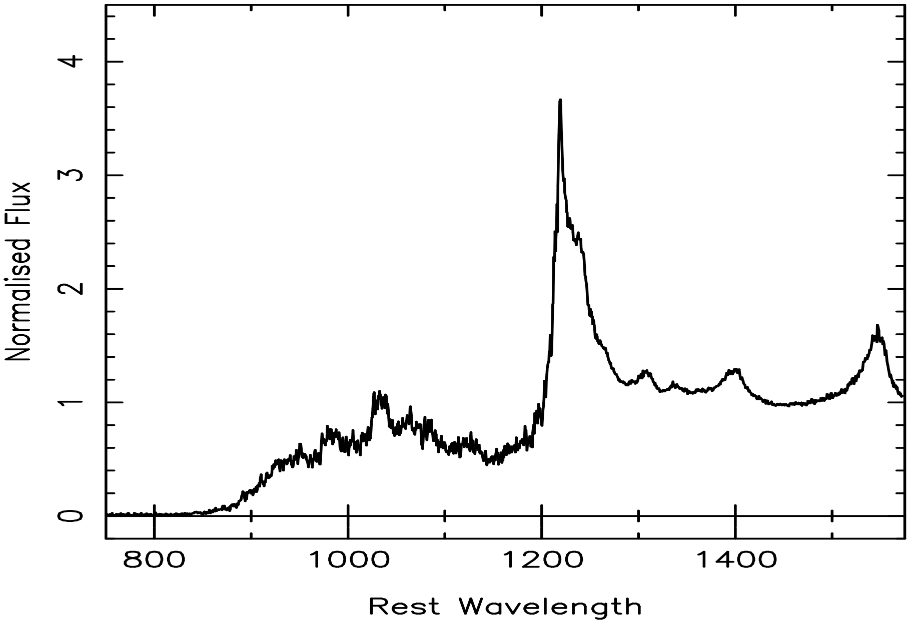

Fig. 1.— $F(\nu)$ median composite spectrum constructed by correcting each of the non-BAL spectra with enough wavelength coverage to rest frame and normalizing the flux over a region free of emission features (1420-1470 Å).

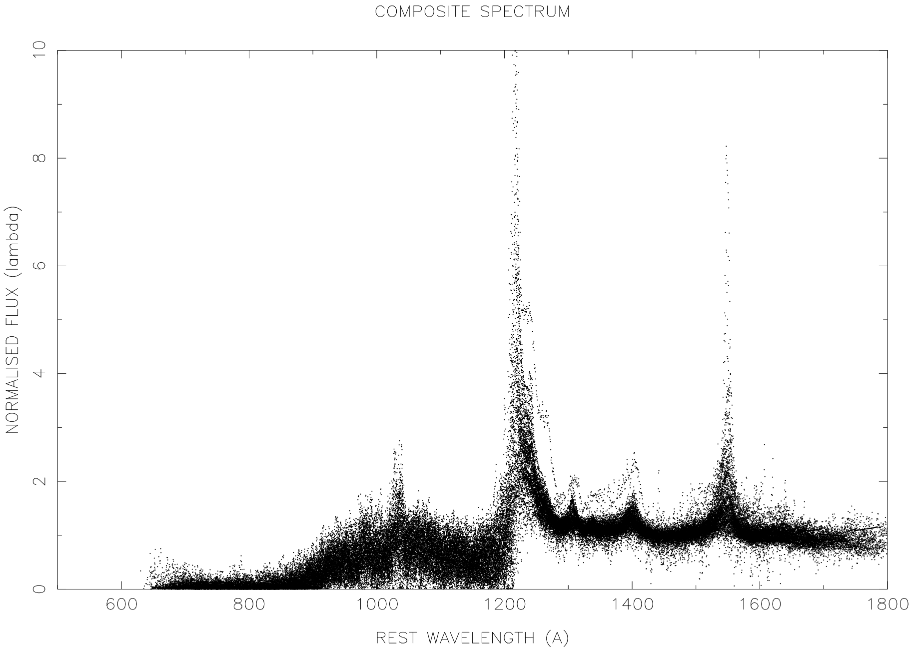

Fig. 2.— $F(\lambda)$ composite spectrum where all individual points are plotted, showing the range of spectral variation. As in Figure 1, this is constructed by correcting each of the non-BAL spectra with enough wavelength coverage to rest frame and normalizing the flux over a region free of emission features (1420-1470 Å).

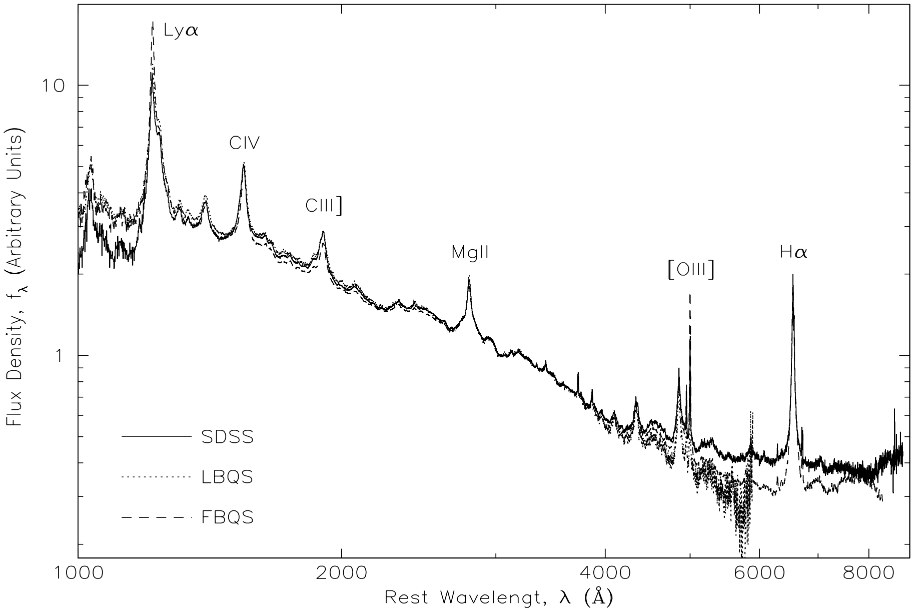

Fig. 3.— Comparison of the SDSS median quasar composite spectrum (solid) with the LBQS (dotted) and FBQS (dashed) composites. The spectra are scaled to the same average flux density between 3020 and 3100Å. Several major emission lines are labeled for reference (Francis et al., 1991; Brotherton et al., 2001; Vanden Berk et al., 2001).

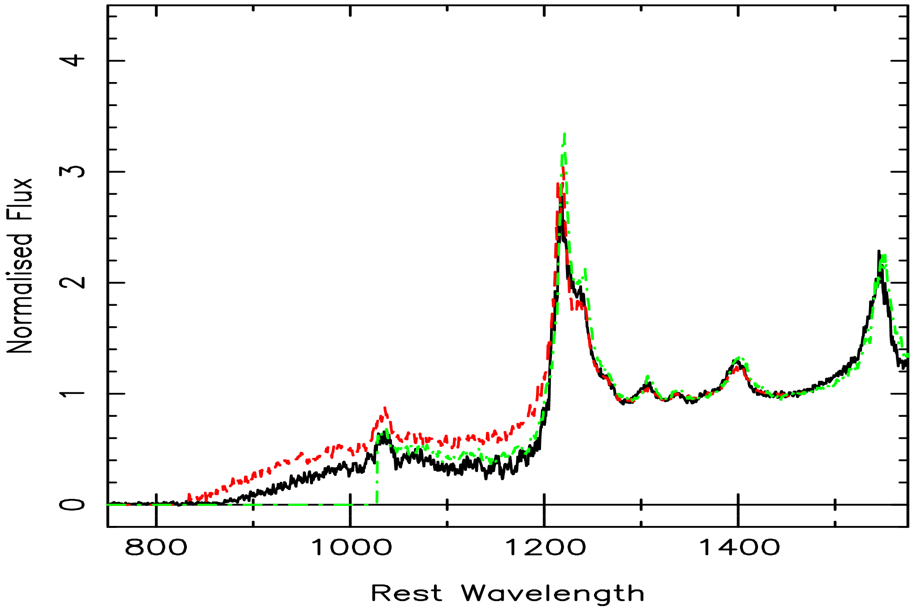

Fig. 4.— Median composite spectrum for various surveys. This is constructed as in Figure 1. The 1^{st} APM survey is shown with a solid line (black line), the SSB data set is the dashed line (top line) and SSG is dashed-dot-dashed (grey line).

distribution of quasars – the so-called near-infrared inflection, presumably caused by emission from hot dust – has been seen starting between 0.7 and 1.5μm. This may be in part what we are seeing at wavelengths beyond $\approx$ 5000Å, but it is unlikely that the sublimation temperature of dust would be high enough for the emission to extend to wavelengths below 6000Å.

Another possible contributor to the long wavelength steepening is contamination from the host galaxies. The best evidence for the contribution of host galaxy light is the presence of stellar absorption lines in the composite spectra. The lines become stronger as the redshift, and equivalently, luminosity, distributions of the quasar sample are lowered. The trend of a greater contribution from starlight with increasing wavelength is expected because the least luminous quasars, in which the relative host galaxy light is presumably most important, contribute the majority of spectra to the composite at longer wavelengths. It thus seem that both stellar light from the host galaxies and a real change in the quasar continuum cause the steepening of the spectral index beyond 5000Å.

Figure 4 displays the composite spectra of three different optical surveys. The 1^{st} APM survey (whose technique and selection criteria are similar to the sample presented in this thesis) was performed by Storrie-Lombardi et al. (1996c). It is composed of 31 quasars with $z \geq 4$, five of which exhibit Broad Absorption Lines (BAL). Sargent et al. (1989) (hereafter SSB) observed 59 quasars within in the redshift range $2.75 \leq z \leq 4.11$ but the spectra only cover the wavelength range 3150-7000 Å, therefore some of the highest redshift objects in the sample are neglected as they do not have sufficient red wavelength coverage. This makes up a total sample of 46 non-BAL quasar covering the redshift range $2.7 \leq z \leq 3.7$. The other survey was undertaken by Schneider et al. (1991) (hereafter SSG) making up a sample of 31 non-BAL quasars in the redshift range $3 \leq z \leq 5$. It can be seen on Figure 4 that the absorption across the Lyman-α forest is more pronounced in the composite spectra of the 1^{st} APM and SSG surveys which are composed from higher redshift quasars than in the SSB sample.

Differential Continuum Slope Fitting

In order to fit the quasar continuum of our spectra, we use the method developed by Storrie-Lombardi (1994): a fit was done for the quasar survey median spectrum and then the individual differences from this reference spectrum were measured for each object. In addition, Storrie-Lombardi (1994) noted that different flux units ($F(\nu)$ versus $F(\lambda)$, see §3.1.1) emphasise different part of the continuum. We thus choose to fit the spectra in log-log space so as not to be affected by this phenomenon.

Individual quasar spectrum with continuum slope α_i are corrected to rest-frame and logarithmically substracted from the sample composite spectrum with slope α_{ref} using IRAF task SARITH. Power laws are interactively fitted to the resulting "difference" spectra with slope α_{diff} using the CONTINUUM task in IRAF. The slope of the "difference" continuum fit is calculated and added to the slope of the reference spectrum for the given quasar sample. The value of slope of the original spectrum α_i is then recovered:

$$F_i(\nu) \propto \nu^{-\alpha_i} \propto \lambda^{\alpha_i} \tag{3.7}$$

and:

$$F_{ref}(\nu) \propto \nu^{-\alpha_{ref}} \propto \lambda^{\alpha_{ref}} \tag{3.8}$$

The "difference" spectrum can be written as:

$$F_{diff(\nu)} = \frac{F_i(\nu)}{F_{ref}(\nu)} \tag{3.9}$$

and hence:

$$\log F_{diff}(\nu) = \alpha_{diff} \log \lambda = (\alpha_i - \alpha_{ref}) \times \log \lambda \tag{3.10}$$

and thus:

$$\alpha_i = \alpha_{diff} + \alpha_{ref} \tag{3.11}$$

Comparison of the results from directly fitting the quasar spectra and undertaking this "difference fitting" Storrie-Lombardi (1994) demonstrated that the later technique is more robust, leading to a smaller scatter in the measured individual α slopes.

3.1.3 Measurements

Following the technique described above, we have undertaken measurement of the quasar continuum slopes of the objects presented in Chapter 1. Table 3.1.3 lists the "difference continuum slopes" α_{diff} and continuum slopes α_i measured for all the non-BAL quasars with enough red continuum. This makes up a sample of 52 objects with $z_{em} \gtrsim 4$. At first, quasar spectra were divided into two categories according to their emission line strengths and independant composite spectra were built, but as noted in Storrie-Lombardi (1994), we found very little difference in the two sub-groups and thus only the measurements based on one general composite quasar spectrum are reported here.

We found that the reference spectrum for our sample (shown in Figure 1) has a slope $\alpha_{ref} = 0.56$. The mean value of slopes measured is $\alpha = 0.81$ with a scatter, $\sigma = 0.48$, with values of α_i ranging from 0.00 to 1.93. The difference between the "median" template and the average slope might arises because obviously the reference spectrum cannot be fitted using our "difference" method and those the spectral index measurement is less robust.

3.1.4 Analysis

Table 1: Continuum slope (α) measurements of the quasar sample presented in Chapter 2.

Quasar	z_{em}	α_{diff}	α	DLA?
reference	...	...	0.56	
PSS J0003+2730	4.240	-0.36	0.20	no
BR J0006−6208	4.455	0.17	0.73	yes
BR J0030−5129	4.174	-0.15	0.41	yes
PSS J0034+1639	4.293	-0.05	0.51	no
SDSS J0035+0040	4.747	1.37	1.93	no
PSS J0106+2601	4.309	-0.19	0.37	yes
PSS J0131+0633	4.417	-0.06	0.50	no
PSS J0133+0400	4.154	-0.14	0.42	yes
PSS J0152+0735	4.051	0.14	0.70	yes
PSS J0209+0517	4.174	-0.02	0.54	yes
SDSS J0211−0009	4.874	1.00	1.56	no
BR J0234−1806	4.301	0.28	0.84	no
PSS J0248+1802	4.422	-0.06	0.50	no
BR J0301−5537	4.133	0.10	0.66	yes
BR J0307−4945	4.728	0.39	0.95	yes
SDSS J0310−0014	4.658	1.05	1.61	yes
BR J0311−1722	4.039	-0.37	0.19	no
BR J0324−2918	4.622	0.47	1.03	no
BR J0334−1612	4.363	0.31	0.87	yes
BR J0355−3811	4.545	0.30	0.86	no
BR J0403−1703	4.227	0.88	1.44	no
BR J0415−4357	4.070	0.59	1.15	no
BR J0419−5716	4.461	0.15	0.71	no
BR J0426−2202	4.320	0.15	0.71	yes
PMN J0525−3343	4.383	0.22	0.78	no
BR J0529−3526	4.413	0.21	0.77	no
BR J0529−3552	4.172	-0.18	0.38	no
BR J0714−6455	4.462	0.64	1.20	no
PSS J0747+4434	4.430	-0.02	0.54	yes
RX J1028−0844	4.276	0.31	0.87	no
PSS J1057+4555	4.116	-0.06	0.50	yes
PSS J1159+1337	4.073	0.67	1.23	yes
PSS J1253−0228	4.007	0.61	1.17	yes

BR J1310−1740	4.185	1.20	1.76	no
BR J1330−2522	3.949	1.13	1.69	no
FIRST J1410+3409	4.351	0.41	0.97	no
PSS J1456+2007	4.249	-0.51	0.05	no
BR J1603+0721	4.385	0.66	1.22	no
PSS J1618+4125	4.213	0.69	1.25	yes
PSS J1633+1411	4.351	0.40	0.96	no
PSS J1646+5514	4.037	-0.42	0.14	no
PSS J1721+3256	4.031	0.00	0.56	no
RX J1759+6638	4.320	0.06	0.62	yes
PSS J2122−0014	4.114	1.35	1.91	yes
PMN J2134−0419	4.334	-0.30	0.26	yes
PSS J2155+1358	4.256	0.60	1.16	no
BR J2216−6714	4.469	0.16	0.72	no
PSS J2241+1352	4.441	0.12	0.68	yes
BR J2317−4345	3.943	-0.15	0.41	yes
BR J2328−4513	4.359	0.32	0.88	no
PSS J2344+0342	4.239	-0.56	0.00	yes
BR J2349−3712	4.208	-0.34	0.22	no
mean	...	...	0.81	
sigma	...	...	0.48	
min	...	...	0.00	
max	...	...	1.93	

Results

The model from Francis (1993b) predicts that the mean continuum slopes of quasars should be harder when observed at shorter wavelengths, and that the numbers of quasars predicted from a sample observed at a particular wavelength using a single power-law luminosity function in the k-corrections is an underestimate of what should actually be observed.

Indeed, we have assumed in the previous measurements of slope indices that α are intrinsic to the quasar. If however there exists a significant amount of dust along the line of sight to the quasar nucleus, this could introduce a range of continuum slopes, and decrease all the power-law indices, reddening the spectra (see also Section 3.2). It is indeed possible that dust has an effect on measured continuum slopes. It is not however likely that all the difference in slopes between the spectra with the hardest and softest continua can be due to dust.

The spectral indices versus redshifts is plotted in Figure 5 for the quasars presented in this thesis, for the quasars issued from the 1^{st} APM survey and for objects from the SDSS (Fan et al., 2001a, the later measurements are tabulated in Table 2). No correlations are apparent as reflected by the correlation coefficients of each survey: r=0.26, r=–0.18 and r=0.11 (respectively). This result indicates no apparent correlation between α and redshift, suggesting no dust bias in our measurements of the spectral indices as a function of redshift.

Comparison with the 1^{st} APM survey

In order to test the reliability of quasar continuum measurements, the slopes of the quasars from the 1^{st} APM survey have been independently derived and are compared with previous measurements from Storrie-Lombardi (1994). The results for the 25 non-BAL quasars are listed in Table 3. We derive a $\alpha_{ref} = 0.61$ compared with $\alpha_{ref} = 0.70$ in Storrie-Lombardi (1994). This discrepancy is small but illustrates the lack of impartiality in measuring continuum slopes. Also the scatter in our measurements is larger, $\sigma = 0.35$ compared with $\sigma = 0.26$ in Storrie-Lombardi (1994), ranging from 0.19 to 1.57, compared with 0.31 to 1.15 in Storrie-Lombardi (1994). Figure 6 illustrates the difference between the two measurements: the scatter extends to ~ 1.

Ultimately and in the light of the large numbers of quasar spectra to be acquired thanks to large scale surveys (such as 2dF, Sloan Digital Sky Survey, etc), the fitting of the quasar continua should be automated so as to allow quick impartial the fitting of quasar absorbers. This is a challenging task, especially at high redshifts where absorption lines are more numerous and quasars are fainter (and hence the signal-to-noise ratio of their spectra is lower).

3.2 Detecting Dust in Quasar Absorbers

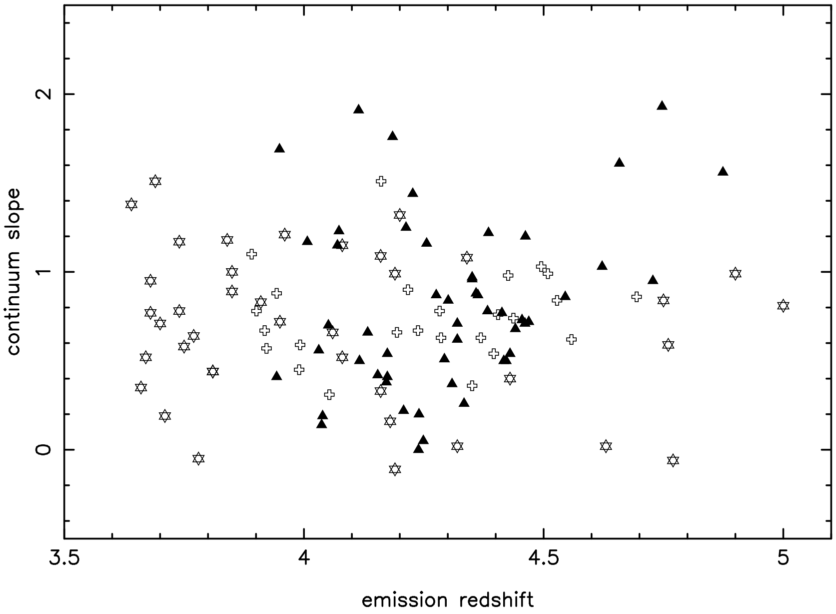

Fig. 5.— Continuum slope α as a function of the quasar emission redshift. The filled triangles are measurements from the quasar presented in this thesis, the open crosses are from the 1st APM survey (Storrie-Lombardi, 1994) and the open stars are from the SDSS (Fan et al., 2001a). No correlations are apparent as reflected by the correlation coefficients of each survey: r=0.26, r=–0.18 and r=0.11 (respectively).

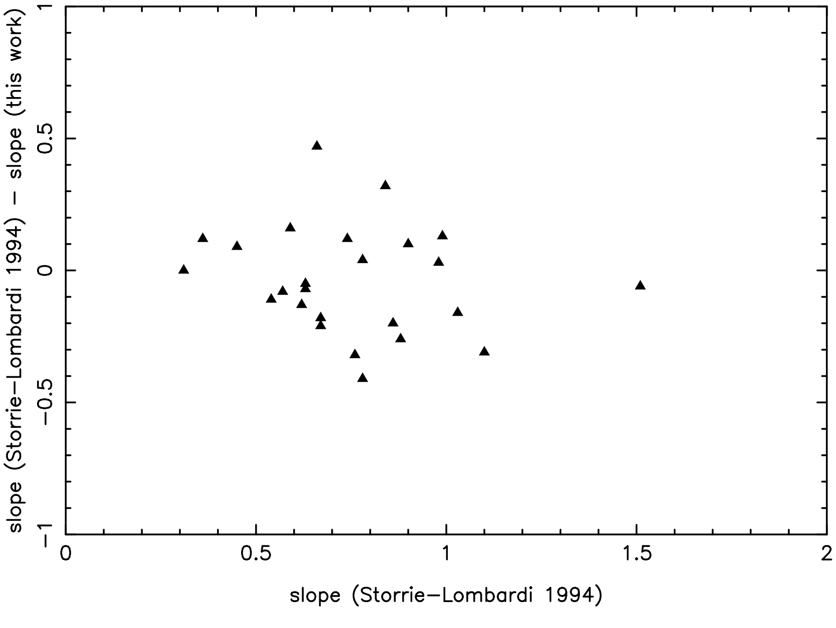

Fig. 6.— Storrie-Lombardi (1994) measurements minus our measurements of the continuum slope α on the 1st APM survey versus the Storrie-Lombardi (1994) measurements. The scatter extends to ~ 1.

Table 2: SDSS continuum slope (α) measurements (Fan et al., 2001a)

Quasar	z_{em}	α
SDSS J0019-0040	4.32	0.02
SDSS J0035+0040	4.75	0.84
SDSS J0059+0003	4.16	1.09
SDSS J0106+0048	4.43	0.40
SDSS J0108+0011	3.71	0.19
SDSS J0120+0007	4.08	0.52
SDSS J0124+0044	3.81	0.44
SDSS J0126+0116	3.66	0.35
SDSS J0127-0045	4.06	0.66
SDSS J0131+0052	4.19	-0.11
SDSS J0150+0041	3.67	0.52
SDSS J0153-0011	4.20	1.32
SDSS J0204-0112	3.91	0.83
SDSS J0207+0103	3.85	1.00
SDSS J0210-0018	4.77	-0.06
SDSS J0211-0009	4.90	0.99
SDSS J0232-0000	3.81	0.44
SDSS J0239-0021	3.74	0.78
SDSS J0244-0108	3.96	1.21
SDSS J0250+0046	4.76	0.59
SDSS J0251-0052	3.78	-0.05
SDSS J0300+0032	4.19	0.99
SDSS J0307-0016	3.70	0.71
SDSS J0310+0055	3.77	0.64
SDSS J0310-0014	4.63	0.02
SDSS J0326-0033	4.16	0.33
SDSS J0338+0021	5.00	0.81
SDSS J0339-0030	3.74	1.17
SDSS J0352-0019	4.18	0.16
SDSS J2254-0001	3.68	0.95
SDSS J2254+0048	3.69	1.51
SDSS J2255-0034	4.08	1.15
SDSS J2257+0016	3.75	0.58
SDSS J2303+0016	3.68	0.77
SDSS J2306+0108	3.64	1.38
SDSS J2309-0031	3.95	0.72
SDSS J2322-0052	3.84	1.18
SDSS J2350-0048	3.85	0.89
SDSS J2357+0043	4.34	1.08
mean	...	0.69
sigma	...	0.42
min	...	-0.11
max	...	1.51

Table 3: Continuum slope (α) measurements of the 1^{st} APM survey: comparing our measurements with those from Storrie-Lombardi (1994).

Quasar	z_{em}	α^1	α^2_{diff}	α^2	DLA?
reference	...	0.70	...	0.61	
BR 0019-1522	4.528	0.84	-0.09	0.52	yes
BR 0103+0032	4.437	0.74	0.01	0.62	no
BRI0151-0025	4.194	0.66	-.42	0.19	no
BRI0241-0146	4.053	0.31	-0.30	0.31	no
BR 0245-0608	4.238	0.67	0.24	0.85	no
BR 0351-1034	4.351	0.36	-0.37	0.24	no
BR 0951-0450	4.369	0.63	0.09	0.70	yes
BRI0952-0115	4.426	0.98	0.34	0.95	yes
BRI1013+0035	4.405	0.76	0.47	1.08	yes
BR 1033-0327	4.509	0.99	0.25	0.86	no
BRI1050-0000	4.286	0.63	0.07	0.68	no
BRI1108-0747	3.922	0.57	0.04	0.65	yes
BRI1110+0106	3.918	0.67	0.27	0.88	no
BRI1114-0822	4.495	1.03	0.58	1.19	yes
BR 1202-0725	4.694	0.86	0.45	1.06	yes
BRI1328-0433	4.217	0.90	0.19	0.80	no
BRI1335-0417	4.396	0.54	0.04	0.65	no
BRI1346-0322	3.992	0.59	-0.18	0.43	yes
BRI1500+0824	3.943	0.88	0.53	1.14	yes
GB 1508+5714	4.283	0.78	0.58	1.19	no
GB 1557+0313	3.891	1.10	0.80	1.41	no
GB 1745+6227	3.901	0.78	0.13	0.74	no
BR 2212-1626	3.990	0.45	-0.25	0.36	no
BR 2237-0607	4.558	0.62	0.14	0.75	yes
BR 2248-1242	4.161	1.51	0.96	1.57	no
mean	...	0.75	...	0.79	
sigma	...	0.26	...	0.35	
min	...	0.31	...	0.19	
max	...	1.51	...	1.57	

[1] measurements from Storrie-Lombardi (1994).

[2] this work.

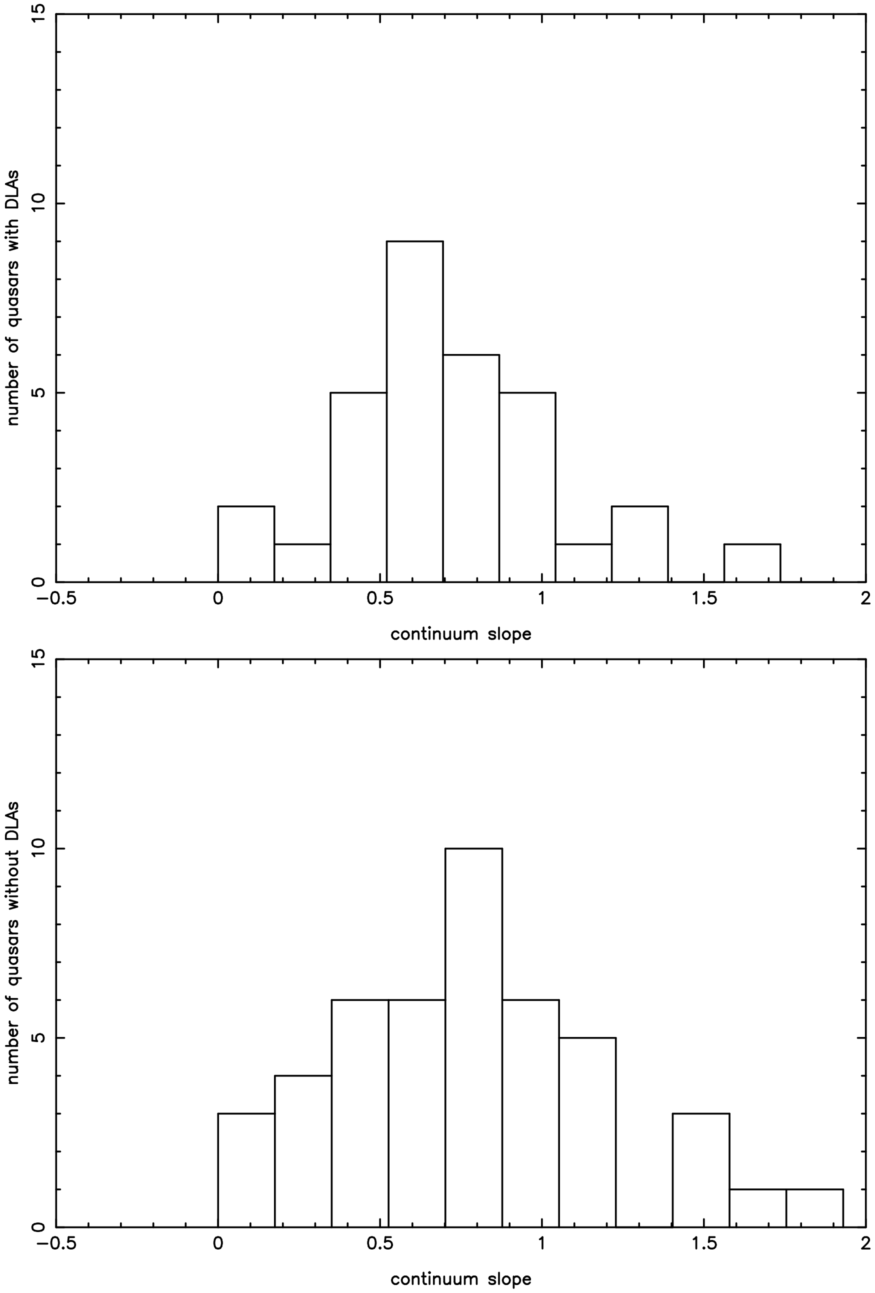

Fig. 7.— Number of quasars with or without DLAs as a function of continuum slope. The peak of the distribution of the number of quasars with absorbers (top panel) is *not* shifted towards higher values of α as one would expect in the case where significant amounts of dust were present in DLAs.

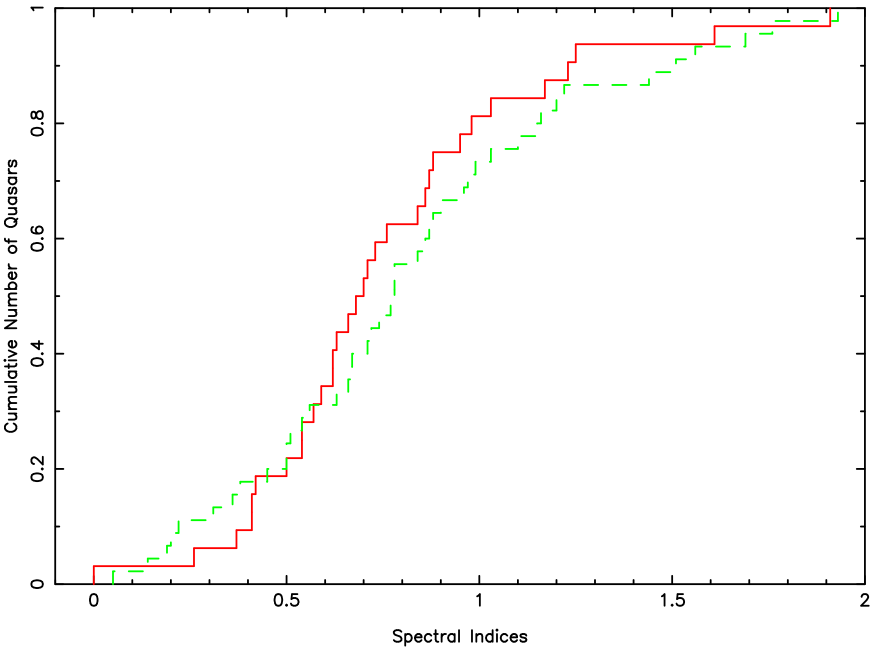

Fig. 8.— The distribution of slopes of quasar with (solid line) and without (dashed line) absorbers. A Kolmogorov-Smirnov (KS) test shows that the two distributions are consistent at a 0.75 level of probability.

If important amounts of dust were present in DLAs, one would expect that quasars with absorbers in the foreground would appear redder than those without absorbers in the foreground (Fall et al., 1989). Following Barkhouse & Hall (2001), we define dust *obscuration* to refer to the combined effects of dust *extinction*, the reduction in observed flux from an object screened by dust, and dust *reddening*, which arises from typical extinction that is stronger at bluer wavelengths. Extinction can thus occur without reddening, but reddening cannot occur without extinction. Therefore, the continuum slope measured in the above section provide a measurement of the amount of reddening in each quasar.

In an attempt to detect dust in DLAs, we compare the colour of the quasars presented in this thesis together with these from the 1^{st} APM survey in the presence or absence of DLA absorbers in their spectra. The selection techniques used to find DLAs in our quasars are detailed in Chapter 5 (see also Appendices C & D), and here we just use the results of that study which are summarised in the last column of Table 3.1.3 and Table 3 for the two different surveys. There are a total of 32 quasars with one or more DLA along their line-of-sight and a "control sample" of 45 quasars without DLA in their spectra.

Figure 7 shows the distribution of the number of quasars with or without DLAs as a function of continuum slope. The peak of the distribution of the number of quasars with absorbers (top panel) is *not* shifted towards higher values of α as one would expect in the case where important amounts of dust were present in DLAs. The mean continuum slope of the sample of quasars with DLAs is 0.76 (compared with the mean of the "control sample" of 0.82), with slope indices ranging from α=0.00 to α=1.91. In the remaining quasars without DLA along their line-of-sight, continuum slopes vary from α=0.05 to α=1.93. A Kolmogorov-Smirnov (KS) test shows that the two distributions are consistent at a 0.75 level of probability (Figure 8).

Contrary to Fall et al. (1989) conclusions, our results suggest that the continua of quasars with absorbers in their spectra are not any redder than other quasars, thus suggesting that the sample of DLAs here are not significantly dusty systems. It still might be argue that heavily obscured quasars would not even be in our optically selected quasar sample, but recent work by Ellison et al. (2001c) on the properties of a radio-selected sample of quasars conclude to similar results as the one presented here (this issue is discussed in more details in Chapter 6). Finally, it would be of interest to extend our work to other classes of absorbers detected in our quasars, such as MgII or CIV doublets.

3.3 Continuum Depression

3.3.1 Introduction

In addition to providing information on the central engine of the quasar, the fitting of high-redshift quasar continua provides a method to quantify the mean absorption of the Ly-α forest blueward of the quasar Ly-α emission. Several methods exist to quantify the mean absorption of the Ly-α forest (see Rauch, 1998, for a detailed review). One approach is to count the discrete absorption features and measure their distribution in terms of equivalent width, W, and redshift, z. At higher-resolution, individual absorption lines can be fitted with a Voigt profile (see §1.3.2). This is probably a more physically meaningful approach than line counting but large uncertainties are associated with the fitting of the local continuum.

An alternative approach to these two methods is to measure the mean flux decrement, D_A, between the Lyman-α and the Lyβ emission lines and the decrement D_B between the Lyman-β emission line and the Lyman-limit (Oke & Korycansky, 1982). This allows us, amongst other things, to investigate the redshift evolution of the Lyα forest and can be done even on relatively low-resolution data. Several authors have applied, or variant of, this technique of continuum depression measurements, e.g. Oke & Korycansky (1982); Bechtold et al. (1984); O'Brien et al. (1988); Steidel & Sargent (1987); Giallongo & Cristiani (1990); Jenkins & Ostriker (1991); Dobrzycki & Bechtold (1991); Schneider et al. (1991); Press et al. (1993); Zuo & Lu (1993); Lu & Zuo (1994).

In addition, a comparison of the results from the two methods described above can be used to detect the Gunn-Peterson Effect (see 1.3.1 I) 3). Jenkins & Ostriker (1991) used data from SSG to make a detailed analysis of the Lyman-α cloud population. They find that at redshift $z \sim 3$, the data imply approximately 30% more opacity than in measurable lines (the so-called "D_A enhancement"), which could be due to lines of very small column density undetected at this resolution or due to true continuous absorption. At $z > 4$, they find that the total absorption is larger by 20% ± 10% than a simple extrapolation from lower redshift data. They interpret this phenomenon as a 15% reduction in the ionising background from $z = 3$ to $z = 4.5$.

3.3.2 Methodology

In an attempt to describe the mean statistical properties of the forest region absorption in very low resolution data, Oke & Korycansky (1982) introduced the concept of "continuum depression". This is defined as:

$$D_i = \left\langle 1 - \frac{F_{observed}(\nu)}{F_{continuum}(\nu)} \right\rangle = 1- < e^{-\tau} >= 1 - e^{-\tau_{\rm eff}} \tag{3.12}$$

with:

$$i = A, B \tag{3.13}$$

where $F_{observed}(\nu)$ is the observed flux, $F_{continuum}(\nu)$ the estimated flux of the unabsorbed continuum in ergs cm^{-2} s^{-1} Hz^{-1}, τ is the resonance line optical depth as a function of wavelength or redshift and τ_{eff} is an "average" of τ. The absorption is measured against the power-law continuum level fitted as in the previous section, extrapolated from the region redward of the Ly-α emission line into the Lyman-α forest region.

The fit of the continuum is usually the main source of uncertainty in the measurement of the continuum depression.

D_A and D_B differ solely in the ranges over which they are integrated. D_A is calculated over the rest wavelength range $\lambda_1 = 1050$Å to $\lambda_2 = 1170$Å in order to avoid the quasar Lyman-α ($\lambda_\alpha = 1216$Å) and Lyman-β ($\lambda_\beta = 1026$Å). The measurements start slightly blueward of the Lyman-α emission line in order to avoid bias due to the proximity effect (see 1.3.1 I) 3). As in previous work, D_B is calculated from slightly above the Lyman limit ($\lambda_1 = 920$Å) to Lyman-β ($\lambda_2 = 1050$Å).

3.3.3 Measurements

The D_A and D_B measurements of the quasars presented in Chapter 2 are tabulated in Table 3.3.3. We obtain mean values of 0.54 and 0.57 for D_A and D_B respectively, with a scatter, σ, of 0.07 and 0.10, respectively. Measurement made on the "reference" median composite spectrum for this sample leads to D_A=0.55 and D_B=0.61. The spread in values of D_B is larger than for D_A because of the lower signal-to-noise in this part of the quasar spectra (D_B ranging from 0.32 to 0.91 as oppose to D_A ranging from 0.39 to 0.67). Not surprisingly, D_A seems to be a more robust measurement than D_B.

3.3.4 Analysis

Results

In general, the higher the quasar redshift, the more difficult is the continuum fit and hence slope measurement, which in turn affects the continuum depression measurements. In order to look for bias in the continuum fit that might impact the D_A and D_B measurements, we have plotted these as a function of slope in Figure 9. This plots reveal no apparent correlation as reflected by the correlation coefficients: r=–0.03 and r=–0.28 for D_A by Storrie-Lombardi (1994) and this work, respectively and r=–0.39 and r=–0.22 for D_B, but once more we note that the scatter in D_B is notably larger than in D_A.

Comparison with the 1^{st} APM survey

As in Section 3.1.4, we have remade measurement on the 1^{st} APM quasar survey in order to compare our results with those from Storrie-Lombardi (1994). The parameters are all listed in Table 5. The two set of measurements are in good agreement as illustrated in the case of D_A by Figure 10. The scatter between the two sets of measurements is small, , 0.2. We derive a mean D_A of 0.54 while Storrie-Lombardi (1994) finds 0.55 (with σ=0.07 and 0.09, respectively). Our measurements have a slightly broader distribution, ranging from 0.34 to 0.66, as opposed to 0.40 to 0.65.

Table 4: Measurements of the continuum depression D_A and D_B for all the quasar presented in Chapter 2.

Quasar	z_{em}	D_A	D_B
reference	...	0.55	0.61
PSS J0003+2730	4.240	0.58	0.52
BR J0006−6208	4.455	0.60	0.66
BR J0030−5129	4.174	0.49	0.52
PSS J0034+1639	4.293	0.51	0.53
SDSS J0035+0040	4.747	0.52	0.41
PSS J0106+2601	4.309	0.58	0.49
PSS J0131+0633	4.417	0.56	0.55
PSS J0133+0400	4.154	0.61	0.56
PSS J0152+0735	4.051	0.50	0.46
PSS J0209+0517	4.174	0.56	0.52
SDSS J0211−0009	4.874	0.65	0.58
BR J0234−1806	4.301	0.61	0.54
PSS J0248+1802	4.422	0.58	0.53
BR J0301−5537	4.133	0.48	0.60
BR J0307−4945	4.728	0.65	0.73
SDSS J0310−0014	4.658	0.52	0.64
BR J0311−1722	4.039	0.59	0.67
BR J0324−2918	4.622	0.55	0.54
BR J0334−1612	4.363	0.67	0.91
BR J0355−3811	4.545	0.58	0.63
BR J0403−1703	4.227	0.61	0.69
BR J0415−4357	4.070	0.46	0.61
BR J0419−5716	4.461	0.54	0.57
BR J0426−2202	4.320	0.52	0.50
PMN J0525−3343	4.383	0.52	0.61
BR J0529−3526	4.413	0.48	0.56
BR J0529−3552	4.172	0.59	0.65
BR J0714−6455	4.462	0.45	0.44
PSS J0747+4434	4.430	0.62	0.50
RX J1028−0844	4.276	0.45	0.55
PSS J1057+4555	4.116	0.53	0.74
PSS J1159+1337	4.073	0.39	0.32
PSS J1253−0228	4.007	0.42	0.40

BR J1310−1740	4.185	0.52	0.51
BR J1330−2522	3.949	0.46	0.49
FIRST J1410+3409	4.351	0.52	0.68
PSS J1456+2007	4.249	0.64	0.57
BR J1603+0721	4.385	0.50	0.54
PSS J1618+4125	4.213	0.60	0.60
PSS J1633+1411	4.351	0.57	0.65
PSS J1646+5514	4.037	0.44	0.58
PSS J1721+3256	4.031	0.42	0.56
RX J1759+6638	4.320	0.57	0.66
PSS J2122−0014	4.114	0.41	0.54
PMN J2134−0419	4.334	0.57	0.60
PSS J2155+1358	4.256	0.48	0.57
BR J2216−6714	4.469	0.55	0.59
PSS J2241+1352	4.441	0.58	0.67
BR J2317−4345	3.943	0.53	0.52
BR J2328−4513	4.359	0.51	0.51
PSS J2344+0342	4.239	0.54	0.73
BR J2349−3712	4.208	0.60	0.62
mean	...	0.54	0.57
sigma	...	0.07	0.10
min	...	0.39	0.32
max	...	0.67	0.91

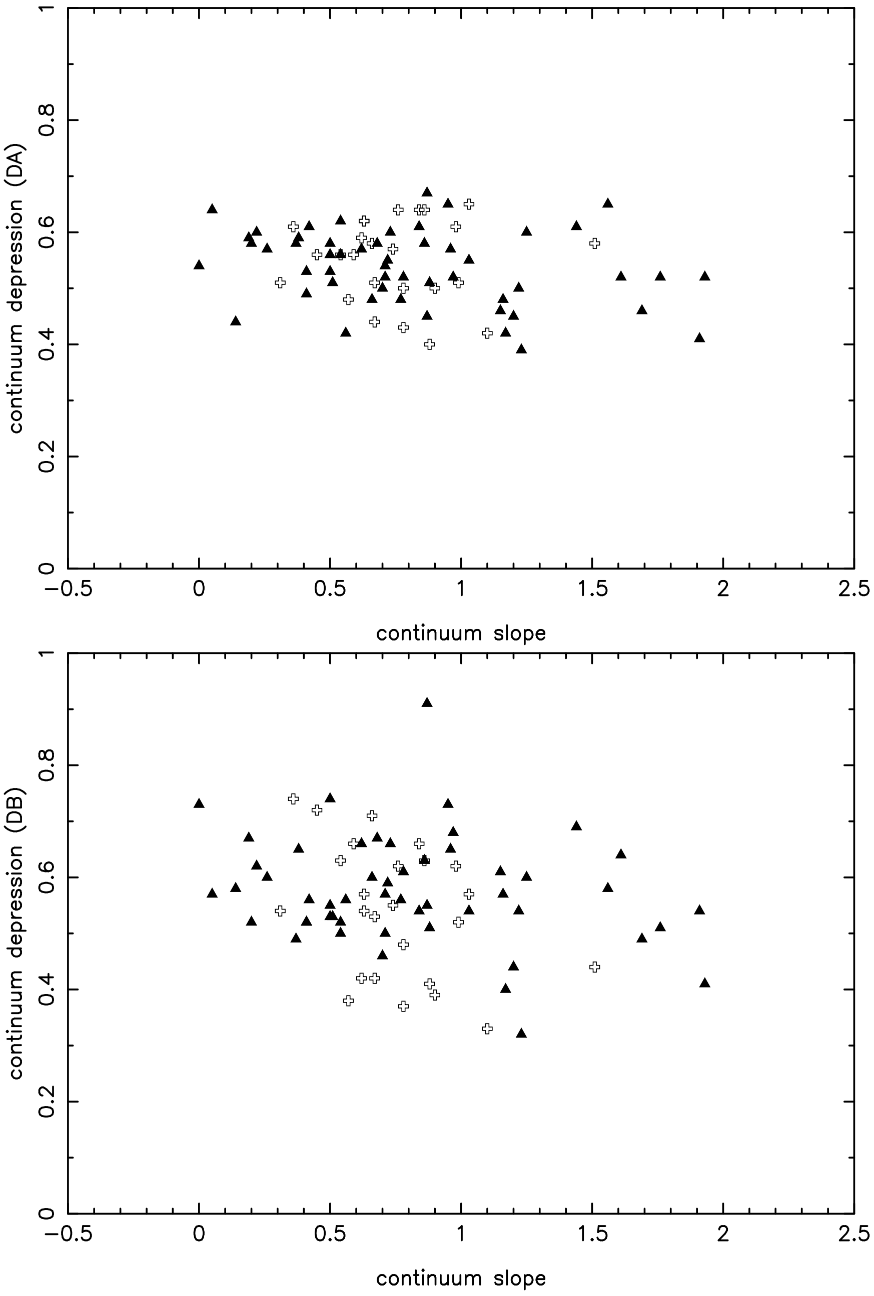

Fig. 9.— Continuum depression D_A versus the continuum slope α. The filled triangles are measurements from the quasar presented in this thesis and the open crosses are from the 1^{st} APM survey (Storrie-Lombardi, 1994). The bottom panel is for D_B. No correlations are apparent as suggested by the small correlation coefficients (r=–0.03 and r=–0.28 for D_A by Storrie-Lombardi (1994) and this work, respectively and r=–0.39 and r=–0.22 for D_B), suggesting no bias between these two measurements.

Table 5: Measurements of the continuum depression (D_A and D_B) of the 1st APM survey. In the case if D_A, mearsurements made by Storrie-Lombardi (1994) are provided for comparison.

Quasar	z_{em}	D_A^1	D_A^2	D_B^2
reference	...	...	0.57	0.58
BR 0019-1522	4.528	0.64	0.66	0.66
BR 0103+0032	4.437	0.57	0.59	0.55
BRI0151-0025	4.194	0.58	0.63	0.71
BRI0241-0146	4.053	0.51	0.50	0.54
BR 0245-0608	4.238	0.51	0.50	0.53
BR 0351-1034	4.351	0.61	0.62	0.74
BR 0951-0450	4.369	0.62	0.61	0.57
BRI0952-0115	4.426	0.61	0.64	0.62
BRI1013+0035	4.405	0.64	0.59	0.62
BR 1033-0327	4.509	0.51	0.55	0.52
BRI1050-0000	4.286	0.62	0.63	0.54
BRI1108-0747	3.922	0.48	0.45	0.38
BRI1110+0106	3.918	0.44	0.43	0.42
BRI1114-0822	4.495	0.65	0.62	0.57
BR 1202-0725	4.694	0.64	0.63	0.63
BRI1328-0433	4.217	0.50	0.48	0.39
BRI1335-0417	4.396	0.56	0.55	0.63
BRI1346-0322	3.992	0.56	0.62	0.66
BRI1500+0824	3.943	0.40	0.34	0.41
GB 1508+5714	4.283	0.50	0.43	0.37
GB 1557+0313	3.891	0.42	0.35	0.33
GB 1745+6227	3.901	0.43	0.45	0.48
BR 2212-1626	3.990	0.56	0.61	0.72
BR 2237-0607	4.558	0.59	0.58	0.42
BR 2248-1242	4.161	0.58	0.56	0.44
mean	...	0.55	0.54	0.54
sigma	...	0.07	0.09	0.12
min	...	0.40	0.34	0.33
max	...	0.65	0.66	0.74

[1] measurements from Storrie-Lombardi (1994).

[2] this work.

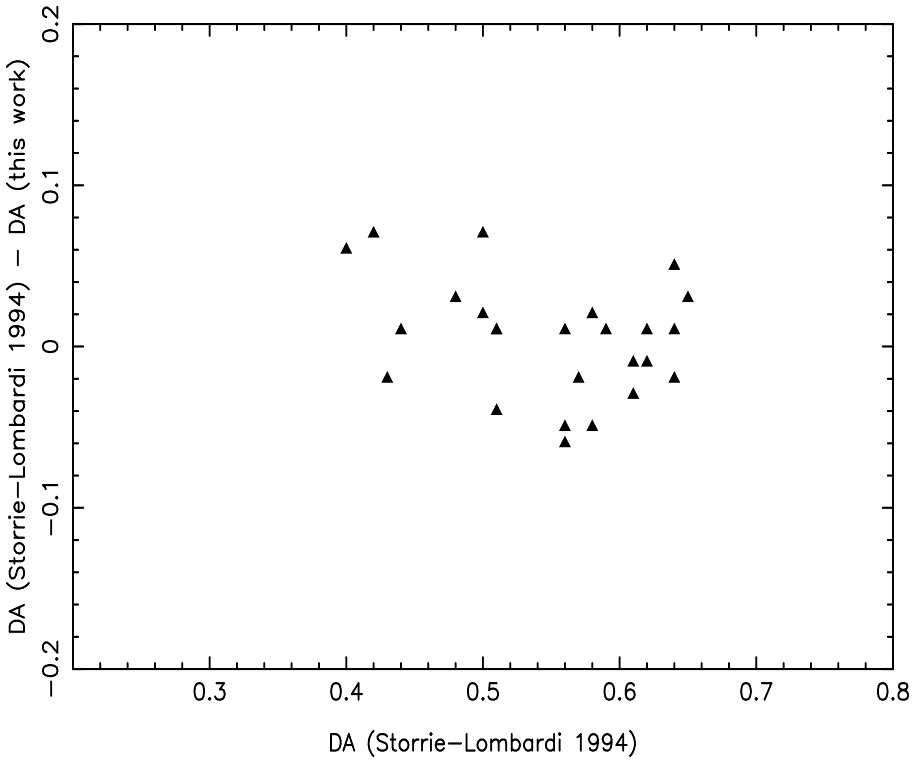

Fig. 10.— Storrie-Lombardi (1994) measurements minus our measurements of the continuum depression D_A on the 1^{st} APM survey versus the Storrie-Lombardi (1994) measurements. The scatter between the two sets of measurements is small, ,0.2.

Comparison with Other Surveys

Figure 11 displays D_A (top panel) and D_B (bottom panel) continuum depression evolution with redshift. It is evident that the amount of Lyman-α absorption increases rapidly with redshift, with $D_A > 0.9$ at $z_{em} > 5.0$. When available, data from over surveys are plotted for comparison, from the 1^{st} APM survey (Storrie-Lombardi, 1994), at low-redshift from Zuo & Lu (1993), the SSG measurements (Schneider et al., 1991), the SSB results (Sargent et al., 1989) and at high-redshift the SDSS measurements (Zheng et al., 2000; Fan et al., 2001b). The Sloan results agreed well with other high-redshift measurements: Songaila et al. (1999) measured D_A=0.75 in the SDDS J0338+0021 quasar ($z_{em} \sim 5$), Stern et al. (2000) measured D_A=0.90 and D_B=0.95 from the spectrum of the colour-selected quasar RD J0301+0020 ($z_{em} = 5.50$).

At low-redshift, the measurements are not straight forward either because the continuum depression value measured is small. Nevertheless, Zuo & Lu (1993) have used low-redshift D_A measurements together with SSB data to determine the intrinsic evolution of the Lyman-α forest lines. In particular, they explore how a simple Lyman-α cloud model in which all (baryonic) clouds are expanding and at the same time keeping roughly a r^{-2} density profile, combined with the evolution of the ionising background, can be used to understand the observed D_A evolution with redshift.

In a further study, Lu & Zuo (1994) used the fact that the true continuum in the Lyman$-\alpha$ forest can be estimated reliably at low-redshift, due to the much lower density of the Lyman-α forest lines, to make a comparison with the extrapolated continuum from redward of the Lyman-α emission line. They find that there is a systematic deviation between the two and thus propose a modification of the D_A method, namely to measure D_A locally using the continuum established in the Lyman-α forest. They also note that the fact that the extrapolated continuum from longward of Lyman-α emission often deviates systematically from the true continuum in the Lyman-α forest presents a major problem in the study of the Gunn-Peterson absorption (see Chapter 1).

Comparison with Models

Jenkins & Ostriker (1991) used the distribution of Lyman-α forest lines to predict the expected effective opacity, and hence continuum depression parameters at various emission redshift. Their results are overplotted on the top panel of Figure 11 as a dashed-dotted line. The model seems to represent well high-redshift measurements although it fails to reproduce the lower-redshift or the very high-redshift measurements.

In another approach, Meiksin & Madau (1993) computed the integrated UV background from observed quasars and use this to estimate the contribution of the Lyman-α forest to the continuum depression parameter D_A. Their model is also overplotted on the top panel of Figure 11 (dashed line).

Both the models presented here do not represent well the observed evolution of the continuum depression in the redshift range $2.5 < z < 5$ and are too steep outside this range. This suggests that the UV background used in these models differs from the

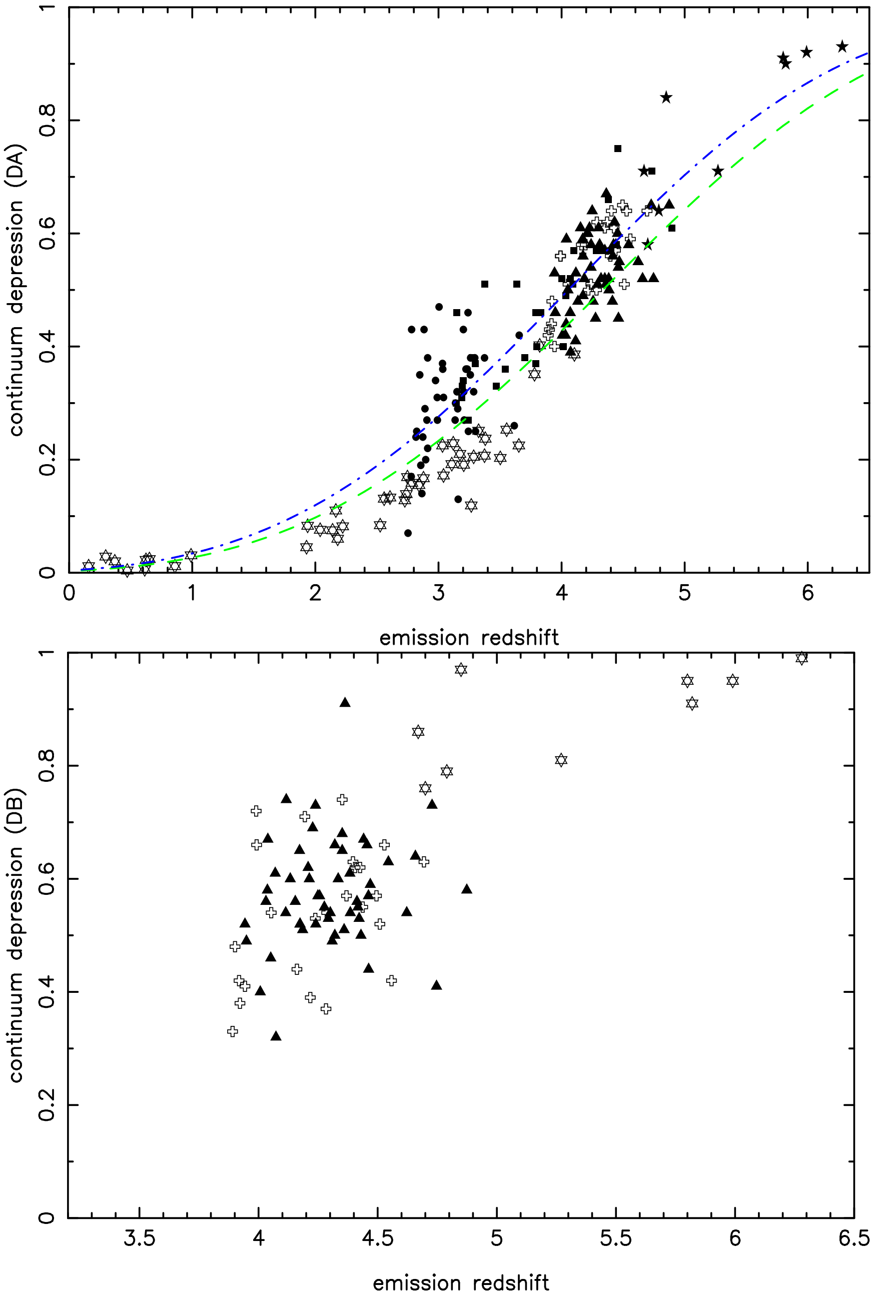

Fig. 11.— D_A parameter as a function of the quasar emission redshift. The filled triangles are measurements from the quasar presented in this thesis, the open crosses are from the 1^{st} APM survey (Storrie-Lombardi, 1994), the open stars are low-redshift measurements from (Zuo & Lu, 1993), the filled squares are from SSG (Schneider et al., 1991), the filled circles are from SSB (Sargent et al., 1989) and the filled stars are from SDSS (Zheng et al., 2000; Fan et al., 2001b). The dashed line represents the predictions from the Meiksin & Madau (1993) model ($\gamma = 2.40$) and the dashed-dotted line is for the Jenkins & Ostriker (1991) model ($\gamma = 2.33$). The bottom panel is D_B for our measurements (triangles), the 1^{st} APM survey (open crosses) and SDSS data (open stars).

one observed via D_A measurements.

3.4 Summary

In this Chapter, we have examined the properties of the quasars presented in Chapter 2. We have first introduced a technique developed by Storrie-Lombardi (1994) to measure the spectral indices of quasar power-law continua. The first step of this method consists in building a median composite spectrum which will be then used as a "reference" spectrum for a given quasar survey. We detailed the processes used to construct such composite and we compared our resulting "reference" spectrum with large quasar surveys' composite. This analysis revealed the characteristics of each sample and we discussed in details the differences between each. We explained the "differential fitting" method which allows for robust determination of the continuum slopes. Our measurements are tabulated and we have tested our technique by comparing our results with the ones from Storrie-Lombardi (1994).

We then investigate the amount of dust present in the high-column density quasar absorbers (DLAs, see Chapter5) by studying the correlation between the steepness of the continuum (reddening) of a quasar from our sample and from the 1^{st} APM survey with the presence of a quasar absorber along its line-of-sight. We find no direct evidence of dust in a sample of 32 quasars as compared with a "control sample" of 45 quasars.

In the third part of this Chapter, we measured the continuum depression across the Lyman-α forest by calculating the parameters D_A and D_B in the quasar sample. Again, the measurements were undertaken in the 1^{st} APM quasars as a check to the robustness of our technique. We found good agreements with previous results. We then analysed in details the evolution of the continuum depression parameter D_A with redshift and compared our results with low-redshift and recent high-redshift measurements. Finally, we confronted these observational results with various model predictions.

After analysing properties of the quasar themselves in this Chapter, the following Chapters will make use of the quasar spectra gathered together in this thesis to study the intervening systems present along the line-of-sight between the background quasar and the observern the so-called quasar absorbers.

Table 6: Measurements of the continuum depression (D_A and D_B) of SDSS quasars (Zheng et al., 2000; Fan et al., 2001b).

Quasar	z_{em}	D_A	D_B
SDSS J0836+0054[2]	5.82	0.90	0.91
SDSS J1021-0309[1]	4.70	0.58	0.76
SDSS J1030+0524[2]	6.28	0.93	0.99
SDSS J1044-0125[2]	5.80	0.91	0.95
SDSS J1122-0229[1]	4.79	0.64	0.79
SDSS J1129-0142[1]	4.85	0.84	0.97
SDSS J1208+0010[1]	5.27	0.71	0.81
SDSS J1306+0356[2]	5.99	0.92	0.95
SDSS J1451-0104[1]	4.67	0.71	0.86

[1] Zheng et al. (2000)

[2] Fan et al. (2001b)

Chapter 4

Lyman Limit Systems Analysis

'(...) ils me méprisaient: pire, ils m'ignoraient'
Simone de Beauvoir

This Chapter starts by defining (Section 4.1.1) Lyman Limit Systems (hereafter LLS) and summarising the previous surveys (Section 4.1.2) dedicated to these objects. A new sample of LLS detected in the sample of high-redshift quasars presented in Chapter 2 is introduced. Section 4.2.1 details the technique used to find these systems in the quasar spectra and Section 4.2.2 tabulates all the data used in the analysis. The number density of LLS is derived from a fit to the observations in Section 4.3.1 and the following Section 4.3.2 links these results with predictions from "mini-halo" models.

4.1 Introduction

4.1.1 Background

Lyman-limit systems (LLS) are absorption systems with hydrogen column densities N(HI)$\geq 1.6 \times 10^{17}$ atoms cm^{-2}, corresponding to systems optically thick to the Lyman ionising radiation (i.e. $\tau \geq 1$). They produce a sharp break (due to absorption of photons capable of ionizing HI) shortward of 912 Å. LLS are a lower column density superset of DLAs, which at $z < 1$ are probably associated with galactic halos (Steidel et al., 1994). At high redshift, LLS irrespective of their physical nature, are an important contributor to the UV opacity of the Universe since they essentially block all radiation shortward of 912 Å in the rest frame. See §1.3.1 I) for more background information of these systems. The present section details the properties of the LLS population and their evolution with redshift. Because the search for absorption systems in quasar spectra is not biased towards luminous intervening objects, our data constitute a complementary way to the more traditional emission observations to probe galaxy evolution.

4.1.2 Previous Samples

The redshift evolution of absorption lines is usually described by a power law of the form: $n(z)dz = n_0(1+z)^\gamma dz$, where $n(z)$ is the observed number density of absorbers. The observed number density of absorbers is the product of the space density and physical cross-section of the absorbers which are a function of the geometry of the Universe. For no evolution of the intrinsic properties of the individual absorbers in a $\Lambda = 0$ Universe this yields $\gamma = 1$ for $\Omega_M = 0$ and $\gamma = 0.5$ for $\Omega_M = 1$. Tytler (1982) was the first to study the statistical properties of LLS. He used ground-based data as well as International Ultraviolet Explorer (IUE) observations and found no evidence for significant evolution of the number density of LLS. Sargent et al. (1989) also found no evolution and fitted $n = n_o(1+z)^\gamma$ finding the parameter values $n_o = 0.76$ and $\gamma = 0.68 \pm 0.54$. At higher-redshift ($z > 3$), Lanzetta et al. (1991) were the first to detect strong evolution. Storrie-Lombardi et al. (1994) completed intermediate (Sargent et al., 1989; Lanzetta et al., 1991) and low (Bahcall et al., 1993) redshift studies, by adding data at $z > 4$. They found $n_o = 0.27^{+0.20}_{-0.13}$ and $\gamma = 1.55 \pm 0.45$ in the redshift range $0.40 < z < 4.69$. The new data added here show for the first time unambiguous evidence for intrinsic evolution in $n(z)$ for LLS at $z > 2.5$.

4.2 New High-Redshift LLS

Fifty-six of the $z \gtrsim 4$ quasar presented in Chapter 2 are used to search for LLS. The broad absorption lines (BAL) quasars are excluded from the studied sample since they are a class of quasar which shows absorption from predominantly highly ionised species believed to be intrinsic to the quasar.

4.2.1 LLS detection

We develop a method for automatically finding and measuring LLSs which follows the technique described in Schneider et al. (1993). The ratio $(f_{upperbin}/f_{lowerbin})$ is determined over 50 Å (rest frame) wide bins slid along the spectrum. $f_{upperbin}$ and $f_{lowerbin}$ correspond to the median of fluxes in bins either side of the wavelength studied. Significant minima in the ratio correspond to potential LLS detections and the redshift is calculated from the corresponding wavelength:

$$z_{LLS} = \frac{\lambda}{912} - 1 \tag{4.1}$$

Two examples of this technique are shown in Figure 1, one for a detection and the other for a non-detection. The optical depth is the logarithm of the ratio previously defined:

$$\tau_{LLS} = -\ln(f_{upperbin}/f_{lowerbin}) \tag{4.2}$$

The median flux in 50Å in the rest frame corresponds to approximately 250Å in the observed frame which provides a wide enough bin to get a good estimate of the continuum. The associated HI column density is:

$$N(HI) = 1.6 \times 10^{17} \left(\frac{912}{\lambda}\right)^{3} \tau(\lambda) \text{ atoms cm}^{-2} \tag{4.3}$$

In some cases, only a fraction of the radiation is absorbed forming a step in the quasar spectra which does not reach zero flux level. These so-called “grey” systems are only taken into account if they have an optical depth, $\tau > 1$, to be consistent with earlier samples.

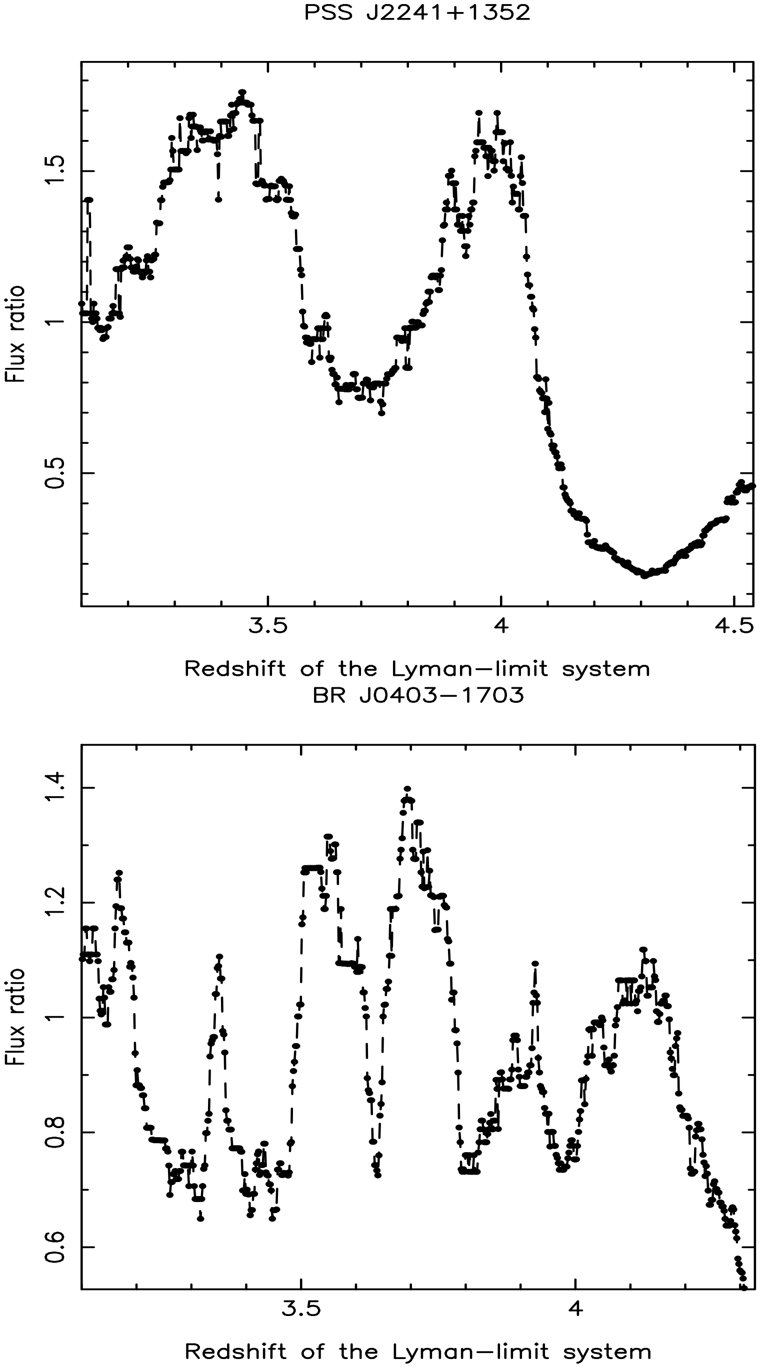

Fig. 1.— LLS detection/non-detection. Example of flux ratio above and below the putative Lyman-limit system redshift. The top panel indicates the presence of a LLS at redshift $z = 4.31$ in the quasar PSS J2241+1352 ($z_{em} = 4.44$). The bottom panel plot does not show the presence of a LLS in the spectrum of quasar BR J0403−1703 ($z_{em} = 4.23$).

Table 1: New survey for Lyman-limit Systems

Quasar	z_{em}	z^a_{min}	z^b_{max}	z_{lls}	τ
PSS J0003+2730	4.240	2.858	4.198	3.97	2.6
BR J0006−6208	4.455	3.079	4.400	4.14	1.8
BR J0030−5129	4.174	3.079	4.122	3.37	1.0
PSS J0034+1639	4.293	2.858	4.240	4.26	4.1
SDSS J0035+0040[c]	4.747	3.079	4.690	4.59	0.9
PSS J0106+2601[d]	4.309	2.858	4.256	4.05	2.3
				3.96	2.7
PSS J0131+0633	4.417	3.079	4.363	4.37	2.1
PSS J0133+0400[d]	4.154	3.079	4.102	4.02	1.5
				4.14	2.3
PSS J0134+3307	4.532	2.858	4.477	4.32	2.1
PSS J0152+0735[d]	4.051	2.858	4.000	3.97	2.5
				3.88	2.8
PSS J0209+0517	4.174	3.079	4.122	3.97	2.6
SDSS J0211−0009	4.874	3.079	4.815	4.81	1.2
BR J0234−1806	4.301	3.079	4.248	4.27	2.4
PSS J0248+1802	4.422	2.858	4.368	4.13	2.0
BR J0301−5537	4.133	3.079	4.082	4.10	2.5
BR J0307−4945	4.728	3.079	4.671	4.50	2.8
SDSS J0310−0014[e]	4.658	4.090	4.601	...	...
BR J0311−1722	4.039	3.079	3.989	3.76	2.0
BR J0324−2918	4.622	3.079	4.566	4.21	1.5
BR J0334−1612	4.363	2.858	4.309	4.24	1.4
SDSS J0338+0021	5.010	3.035	4.950	4.93	2.2
BR J0355−3811[d]	4.545	3.079	4.490	4.39	1.6
				4.43	2.0
BR J0403−1703[f]	4.227	4.175	4.175	...	...
BR J0415−4357	4.070	3.079	4.019	4.07	2.6
BR J0419−5716[d]	4.461	3.079	4.406	4.14	1.3
				4.33	1.1
BR J0426−2202[c]	4.320	3.079	4.267	3.97	0.8
PMN J0525−3343	4.383	3.079	4.329	4.09	2.3
BR J0529−3526	4.413	3.079	4.359	4.39	1.7
BR J0529−3552	4.172	3.079	4.120	4.10	2.8
BR J0714−6455	4.462	3.078	4.407	4.46	2.4
PSS J0747+4434	4.430	2.858	4.376	4.29	1.8
RX J1028−0844	4.276	2.857	4.223	3.62	3.0
PSS J1057+4555	4.116	2.857	4.065	3.90	4.4
PSS J1159+1337	4.073	2.857	4.022	3.77	4.0
PSS J1253−0228	4.007	2.857	3.957	3.65	3.5
BR J1310−1740	4.185	2.857	4.133	3.62	2.7

BR J1330−2522[d]	3.949	2.857	3.900	3.72	1.8
				3.82	2.0
FIRST J1410+3409	4.351	2.857	4.297	3.87	1.2
PSS J1456+2007	4.249	2.857	4.197	4.17	3.5
BR J1603+0721	4.385	2.857	4.331	4.38	2.5
PSS J1618+4125	4.213	2.857	4.161	3.94	2.0
PSS J1633+1411[d]	4.351	2.857	4.297	4.23	1.2
				4.33	1.4
PSS J1646+5514	4.037	2.858	3.987	4.03	5.3
PSS J1721+3256	4.031	2.858	3.981	4.03	2.5
RX J1759+6638[c]	4.320	2.856	4.267	4.20	0.9
PSS J1802+5616[e]	4.158	3.990	4.106	...	...
PSS J2122−0014	4.114	2.858	4.063	4.01	3.5
PMN J2134−0419	4.334	3.079	4.281	4.19	1.6
PSS J2154+0335[e]	4.363	3.990	4.309	...	...
PSS J2155+1358	4.256	3.079	4.203	4.23	2.9
BR J2216−6714	4.469	3.079	4.414	3.98	1.2
PSS J2241+1352	4.441	3.079	4.387	4.31	1.8
BR J2317−4345	3.943	3.079	3.894	3.93	1.4
BR J2328−4513	4.359	3.079	4.305	4.19	2.0
PSS J2344+0342	4.239	3.079	4.187	3.98	1.5
BR J2349−3712	4.208	3.079	4.156	4.17	2.5

[a] z_{min} corresponds to the shortest wavelength in the quasar spectrum.

[b] z_{max} is 3000 km s^{-1} blueward of the quasar emission redshift.

[c] Systems with optical depth, τ, < 1 are excluded from the total count of LLS because they do not conform to the formal definition of Lyman-limit Systems.

[d] In case where two breaks were detected, only the highest system is taken into account in the final count for LLS.

[e] No LLS have been detected over the specified redshift range.

[f] The signal-to-noise ratio of this spectrum is too low to enable reliable LLS detection.

The redshifts and optical depths of the LLS detected in our sample of quasars are summarized in Table 4.2.1, together with the minimum and maximum redshift over which a LLS *could* have been detected. The minimum redshift corresponds to the shortest wavelength in the spectrum and the maximum redshift is 3000 km s^{-1} blueward of the quasar emission redshift:

$$z_{max} = z_{em} - \left[\frac{3000 \text{ km s}^{-1}}{c} \times (1 + z_{em}) \right] \tag{4.4}$$

where c is the velocity of light ($c = 3 \times 10^5$ km s^{-1}). The actual redshift path surveyed is usually limited by the detection of the first Lyman-limit absorber, blueward of which there is either no residual flux or insufficient signal-to-noise to detect further LLSs. The observations result in the detection of 49 LLS, 15 of which are within 3000 km s^{-1} of z_{em}. The latter systems are not at first included in the analysis since they may not be typical intervening systems as they could be affected by the UV-radiation from the quasar or they could be associated with the quasar itself, i.e. intrinsic to the host galaxy, or clustered, with the quasar. Indeed, Pascarelle et al. (2001) claim the discovery of the *galaxy proximity effect* where galaxies in the vicinities of quasars do not exhibit the same incidence as galaxies far from the quasars. This effect appears to extend to velocity separations from the quasars of up to $\sim$ 3000 km s^{-1}. In addition, there are uncertainties in the systematic quasar emission redshifts, in that redshifts determined from high and low ionisation lines exhibit differences of up to 2000 km s^{-1} (see Chapter 2). Finally, the velocity 3000 km s^{-1} has been choosen so as to match the DLA analysis (see Chapter 5). Samples of LLS both including and excluding LLSs 3000 km s^{-1} away from z_{em} are analysed and we show that the results are relatively insensitive to this discrepancy.

In some cases, metal absorption features are also observed at the redshift of the LLS. In Appendix A, the quasar spectra are magnified in the wavelength range where a LLS is detected.

4.2.2 The Sample of LLS

In order to study the LLS population, we only use systems detected in quasars with $z > 4.2$ so as to minimise any colour selection bias. By this redshift the average intervening cosmological absorption due to the Lyman-α forest alone is sufficient to make the colour of the quasar red enough in $B_j - R$ to drive them well away from the main stellar locus (Irwin et al., 1991). Also, following their formal definition, only LLS with optical depth $\tau > 1$ are used. In addition, we combine our new high-redshift systems with data from the literature (Sargent et al., 1989; Bahcall et al., 1993; Bergeron et al., 1994; Storrie-Lombardi et al., 1994). Table 4.2.2 lists the characteristic of these LLSs as derived by Storrie-Lombardi (1994) from the quasar spectra.

Table 2: Lyman-limit Systems previously known

Quasar	z_{em}	z^{a}_{min}	z^{bc}_{lls}	τ^{d}
BR 0019−1522	4.52	2.51	4.27	5.8
BR 0103+0032	4.44	2.51	4.31	1.6
BRI0151−0025	4.20	2.51	4.05	3.7
BR 0245−0608*	4.24	2.51	4.23	3.9
BR 0951−0450	4.37	2.84	4.22	3.1
BRI0952−0115	4.43	2.84	4.25	2.1
BRI1013+0033	4.41	2.84	3.78	2.3
BR 1033−0327	4.51	2.84	4.19	3.5
BRI1050−0000	4.29	2.84	4.08	2.5
BRI1114−0822*	4.51	2.84	4.50	3.7
BR 1202−0725	4.69	2.84	4.52	3.0
BRI1328−0433	4.22	2.84	3.31	1.5
BRI1335−0417*	4.40	2.84	4.45	3.1
GB 1508+5714	4.30	2.84	3.88	4.6
BR 2237−0607	4.56	2.51	4.28	2.6
Q0000−263	4.111	2.51	3.412	>3.0
Q0001+087	3.243	2.51	3.007	>3.0
Q0004+171*	2.890	2.51	2.881	>3.0
Q0014+813	3.384	2.51	2.813	1.7
Q0029+073	3.259	2.51	3.059	>3.0
Q0045−036	3.135	2.51	2.830	>3.0
Q0054−284*	3.616	2.51	3.585	>3.0
Q0055−264	3.656	2.51	...	...
Q0101−304	3.150	2.51	2.907	>3.0
Q0102−190	3.035	2.51	2.940	>3.0
Q0112+029	2.823	2.51	...	...
Q0114−089	3.160	2.51	...	...
Q0132−198	3.130	2.51	2.484	>3.0
Q0143−015	3.138	2.51	...	...
Q0148−097	2.848	2.51	...	...
Q0153+045	2.991	2.51	...	...
Q0201+365	2.912	2.51	...	...
Q0207−003	2.856	2.51	2.531	>3.0
Q0216+080	2.993	2.51	...	...
Q0249−222	3.202	2.51	2.937	1.5
Q0249−184	3.205	2.51	2.665	>3.0
Q0256−000	3.374	2.51	3.090	2.1
Q0301−006	3.223	2.51	2.947	>3.0
Q0302−003	3.286	2.51	2.530	1.5
Q0308−193	2.752	2.51	...	...
Q0308+190	2.835	2.51	...	...
Q0316−203	2.865	2.51	...	...
Q0334−204	3.130	2.51	3.020	1.8

Q0352−275	2.819	2.51	...	...
Q0420+007	2.918	2.51	...	...
Q0449−134	3.093	2.51	2.963	2.4
Q0528−250	2.779	2.51	2.839	>3.0
Q0636+680	3.174	2.51	2.909	3.5
Q0642+449	3.406	2.51	3.295	2.1
Q0731+663	3.033	2.51	2.912	>3.0
Q0805+046	2.873	2.51	2.651	>3.0
Q0830+115	2.976	2.51	...	...
Q0941+261	2.906	2.51	...	...
Q0956+122	3.301	2.51	3.096	3.0
Q1017+109	3.156	2.51	3.048	2.2
Q1836+511*	2.827	2.51	2.861	1.6
Q2000−330	3.777	2.51	3.548	>3.0
Q2038−012	2.783	2.51	2.723	>3.0
Q2048+312	3.185	2.51	...	...
Q2126−158	3.261	2.51	2.973	2.3
Q2233+131	3.295	2.51	3.165	>3.0
Q2233+136	3.209	2.51	3.035	>3.0
Q2311−036	3.041	2.51	...	...
Q2348−011	3.005	2.51	2.949	>3.0
Q2359−022	2.817	2.51	...	...
Q2359+003	2.896	2.51	...	...
Q2359+068	3.234	2.51	...	...
NAB 0024+22	1.118	0.404	...	...
PKS 0044+030	0.624	0.404	...	...
Q0349−1438	0.614	0.404	...	...
Q0850+4400	0.513	0.404	...	...
Q0916+5118	0.553	0.404	...	...
Q1022+1927	0.828	0.404	0.546	1.42
Q1038+0625	1.270	0.404	0.456	1.15
Q1040+1219	1.028	0.404	...	...
PKS 1055+2007	1.110	0.404	1.036	2.68
Q1130+106Y	0.510	0.404	...	...
PKS 1136−13	0.554	0.404	...	...
PG 1206+459	1.158	0.404	...	...
MC 1215+113	1.230	0.404	...	...
B2 1244+32B	0.949	0.404	...	...
PKS 1252+11	0.870	0.404	...	...

PG 1259+593	0.472	0.404	...	...
Q1317+2743	1.022	0.404	0.649	4.43
PG 1333+176	0.554	0.404	...	...
PG 1338+416	1.219	0.404	...	...
B2 1340+29	0.905	0.404	...	...
Q 1347+5356	0.976	0.404	...	...
PG 1352+0106	1.121	0.404	0.677	6.70
PKS 1354+1919	0.720	0.404	0.470	1.70
PG 1407+265	0.944	0.404	...	...
MC 1415+172	0.821	0.404	...	...
PKS 1424−1150	0.805	0.404	0.666	2.20
Q 1618+1743	0.555	0.404	...	...
PKS 1656+053	0.879	0.404	...	...
Q 2251+1552	0.859	0.404	...	...

[a] z_{min} corresponds to the smallest wavelength in the quasar spectrum.

[b] In case where two breaks were detected, only the highest system is listed.

[c] '...' indicates that no LLS have been detected over the specified redshift range.

[d] Systems with optical depth, τ, < 1 are not included in this Table, because they do not conform to the formal definition of Lyman-limit Systems.

[*] z_{LLS} is within 3 000 km s^{-1} of z_{em}.

4.3 LLS Analysis

4.3.1 LLS Properties

LLS Number Density

The number density of quasar absorbers is the number of absorbers, n, per unit redshift dz, i.e., $dn/dz = n(z)$. If $l(z)$ is the mean distance in redshift from a lyman limit system to a quasar, then $n(z) = 1/l(z)$ is the number density per unit redshift along this line- of-sight. This is a directly observable quantity, although, its interpretation is dependent on the geometry of the Universe. Indeed, the evolution of the number density of absorbers with redshift is the intrinsic evolution of the true number of absorbers combined with effects due to the expansion of the Universe.

The LLS number density is traditionally modelled using a power law of the form:

$$n(z) = n_o(1+z)^\gamma \tag{4.5}$$

Figure 2 (top panel) shows the number density of LLS for our new high-redshift sample and for data from the literature overlaid with maximum likelihood fits to the observations. For a Poisson distribution of x absorbers detected in y quasars, the likelihood function can be written as the product of the probability density functions for each Lyman limit system detected and the probability of not detecting a Lyman limit system in the remaining quasars (Tytler, 1987):

$$\mathrm{L} = \prod_{\mathrm{i=1}}^{\mathrm{x}} \mathrm{n(z)e}^{-\int_{\mathrm{z^i_{LLS}}}^{\mathrm{z^i_{em}}} \mathrm{n(z)dz}} \prod_{\mathrm{j=x+1}}^{\mathrm{y}} \mathrm{e}^{-\int_{\mathrm{z^j_{min}}}^{\mathrm{z^j_{em}}} \mathrm{n(z)dz}} \tag{4.6}$$

where $n(z)$ is the number density per unit redshift, z_{em} is 3000 km s^{-1} from the quasar emission redshift, $z_{min} = z_{LLS}$ if a LLS is observed and the products over i and j are for systems in which a Lyman limit system was observed and not observed, respectively. The log-likelihood function is thus:

$$\ln \mathrm{L} = \sum_{\mathrm{i=1}}^{\mathrm{x}} \left[\ln \mathrm{n(z)} - \int_{\mathrm{z^i_{LLS}}}^{\mathrm{z^i_{em}}} \mathrm{n(z)dz} \right] - \sum_{\mathrm{j=x+1}}^{\mathrm{y}} \int_{\mathrm{z^j_{min}}}^{\mathrm{z^j_{em}}} \mathrm{n(z)dz} \tag{4.7}$$

In order to determine the redshift evolution of the Lyman limit systems, $n(z)$ in the log-likelihood function is replaced with the power law expression $n(z) = n_o(1+z)^\gamma$. Equation 4.7 becomes:

$$\ln \mathrm{L} = \sum_{\mathrm{i=1}}^{\mathrm{x}} \left[\ln \mathrm{n_o} + \gamma \ln\, (1+\mathrm{z_i}) - \mathrm{n_o} \int_{\mathrm{z^i_{LLS}}}^{\mathrm{z^i_{em}}} (1+\mathrm{z_i})^\gamma \mathrm{dz} \right] - \sum_{\mathrm{j=x+1}}^{\mathrm{y}} \mathrm{n_o} \int_{\mathrm{z^j_{min}}}^{\mathrm{z^j_{em}}} (1+\mathrm{z_j})^\gamma \mathrm{dz} \tag{4.8}$$

and thus:

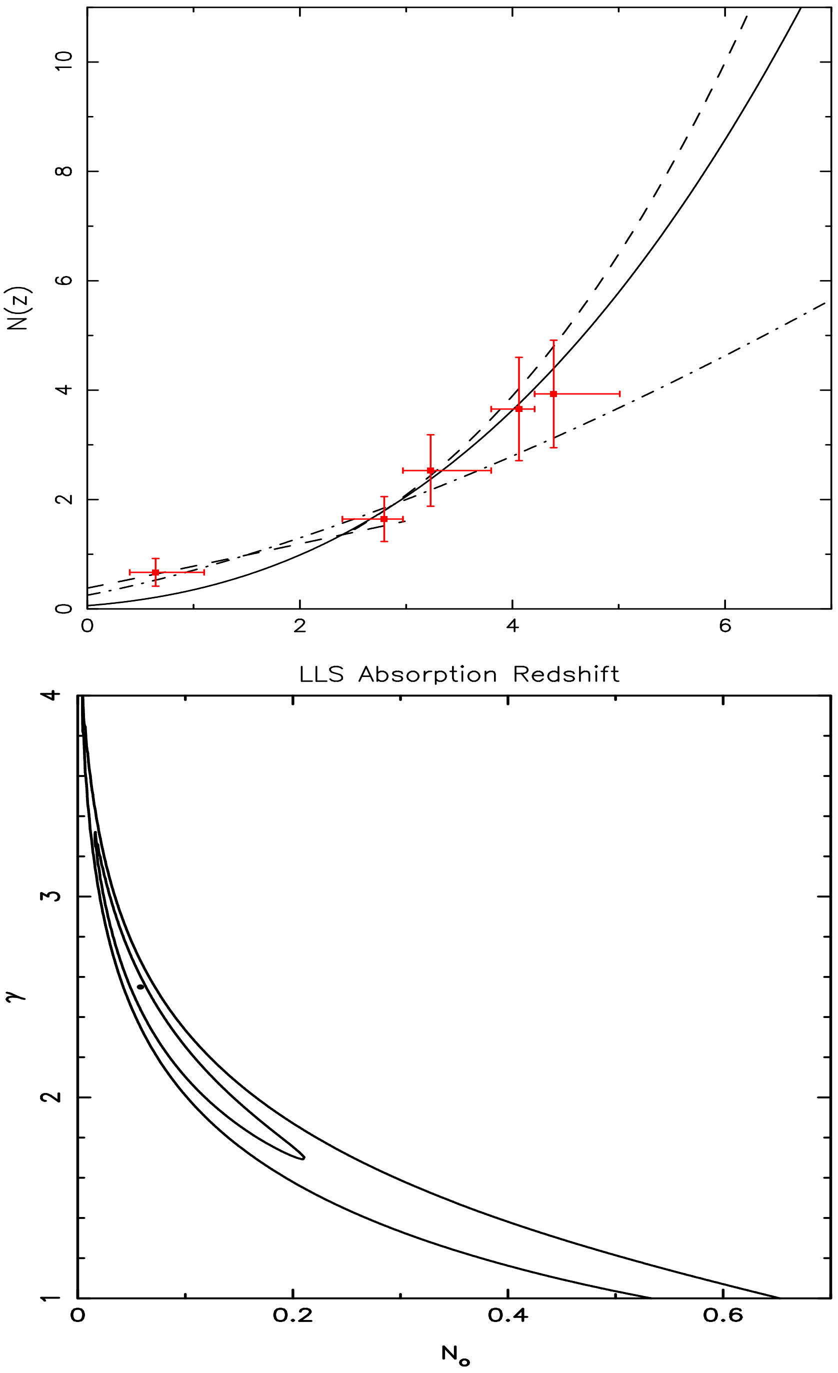

Fig. 2.— The top panel shows the number of lyman-limit systems per unit redshift. The solid line is our fit which only includes LLS with $z > 2.4$ because of the small number of systems known at low redshift. The dashed lines are double power law fit from Storrie-Lombardi et al. (1994) and the dashed-dot line is the fit from Stengler-Larrea et al. (1995). The horizontal error bars are the bin sizes and the vertical error bars are the 1-σ uncertainties. The observations indicate a strong evolution of the number of LLS with redshift. The data are binned for display purpose only. The bottom panel shows the logarithmic likelihood function. The 1 and 2-σ contours fit of the unbinned number of LLS per unit redshift are shown.

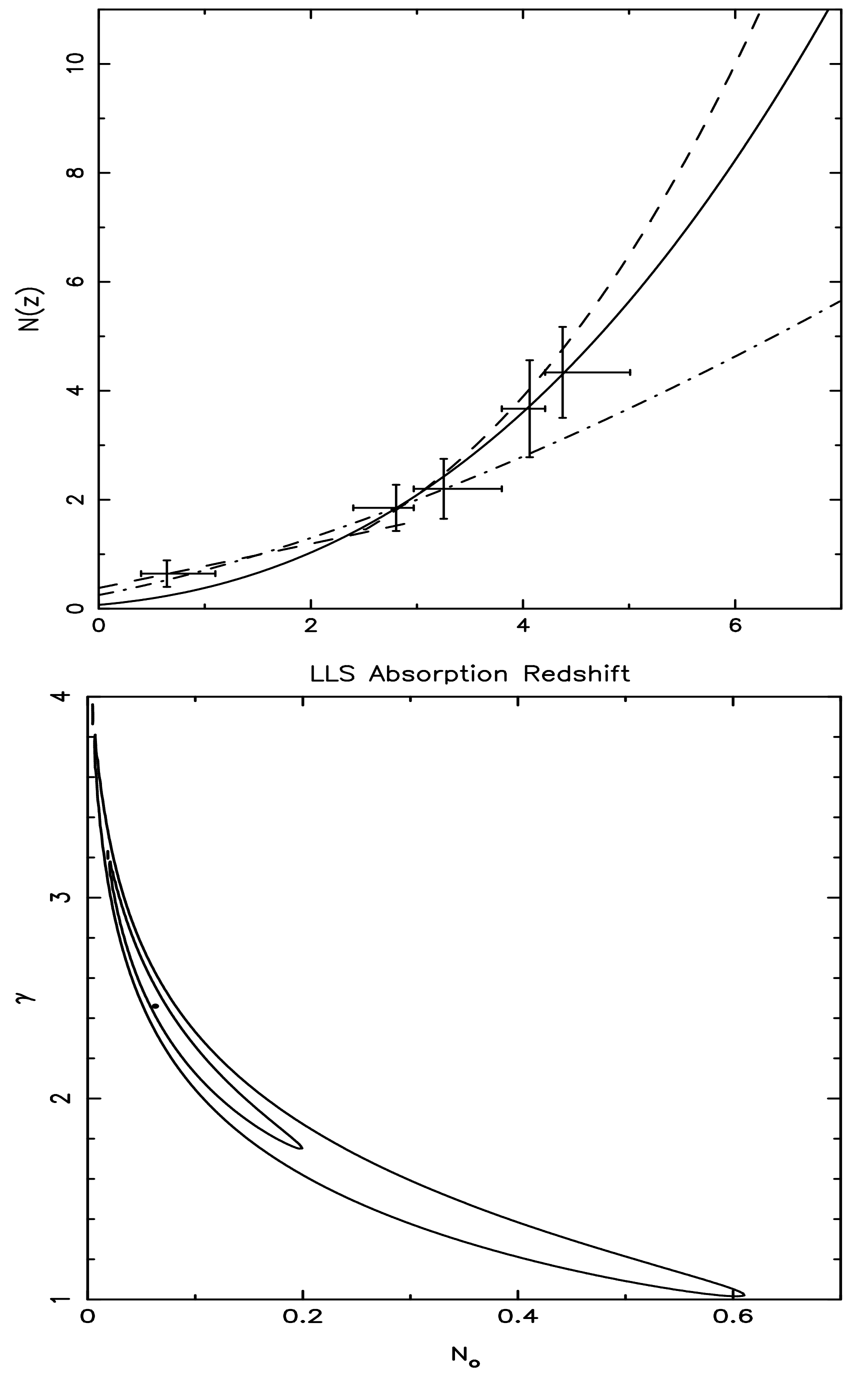

Fig. 3.— As in Figure 2 but also including systems within 3 000 $\mathrm{km\,s^{-1}}$ of the quasar emission redshift.

$$\ln \mathrm{L} = \mathrm{x} \ln \mathrm{n_o} + \gamma \sum_{\mathrm{i=1}}^{\mathrm{x}} \ln\,(1 + \mathrm{z}^{\mathrm{i}}_{\mathrm{LLS}}) - \left(\frac{\mathrm{n_o}}{1+\gamma}\right) \sum_{\mathrm{j=1}}^{\mathrm{y}} \left[(1 + \mathrm{z}^{\mathrm{j}}_{\mathrm{em}})^{\gamma+1} - (1 + \mathrm{z}^{\mathrm{j}}_{\mathrm{min}})^{\gamma+1}\right] \tag{4.9}$$

The bottom panel of Figure 2 displays the 1 and 2-σ confidence contours of the fit. The resulting likelihood function is highly asymmetrical because the normalisation, n_o, is strongly coupled to the power law index γ. Figure 3 is as Figure 2 but also includes systems within 3 000 $\mathrm{km\,s^{-1}}$ of the quasar emission redshift. The dashed lines are double power law fits from Storrie-Lombardi et al. (1994) and the dashed-dot line is the fit from Stengler-Larrea et al. (1995). The solid line is our fit which only includes LLS with $z > 2.4$ because of the very small number of LLSs known at low redshift ($0.4 \leq z \leq 2.4$), all of which are below $z = 1.1$.

Figure 4 shows the logarithm of the number density of LLS as a function of redshift. Interestingly the number density distribution in the Lyman-α forest shows a break at $z \sim 1.5$. Kim et al. (2001) used the high sensitivity of the Ultra-Violet Visual Echelle Spectrograph (UVES) mounted on VLT to study the Lyman-α forest in the range $1.5 < z < 4$ and determine γ at $z > 2.4$. They find $\gamma = 2.19 \pm 0.27$ while below the break, the distribution is flat (Weymann et al., 1998, $\gamma \sim 0.2$). Kim et al. (2001) also find the line counts as a function of the filling factor to be constant in the interval $1.5 < z < 4$, which suggests that the Hubble expansion is the main drive governing the forest evolution at $z > 1.5$ and that the metagalactic UV background changes more slowly than a quasar-dominated background at $z < 2$. The parameter values for our fit are $n_o = 0.06^{+0.15}_{-0.05}$ and $\gamma = 2.55^{+0.95}_{-0.85}$ (determined using a maximum likelihood analysis). If LLSs within 3 000 $\mathrm{km\,s^{-1}}$ of the quasar emission redshift are included the parameters are $n_o = 0.07^{+0.13}_{-0.04}$ and $\gamma = 2.45^{+0.75}_{-0.65}$. Surprisingly, the resulting difference is negligible, thus suggesting that the LLS within 3 000 $\mathrm{km\,s^{-1}}$ of the quasar emission redshift are not a diffrent class of absorbers than other LLSs. At high-redshift, the γ indexes are similar for both LLS and the Lyman-α forest. Storrie-Lombardi et al. (1994) had measured $\gamma = 1.55 \pm 0.45$ which is not significantly different from a non-evolving population in a $\Omega_M = 0$ Universe. But our new high-redshift data leading to $\gamma = 2.55^{+0.95}_{-0.85}$, unambiguously show the intrinsic evolution of number density of LLSs. All these results are listed in Table 3 together with the parameter fit of previous surveys.

Expected Number of LLS

The power law fit to the observed number of LLS per unit redshift is used to calculate the *expected number* of LLS systems:

$$LLS_{expected} = \sum_{i=1}^{n} \int_{z_{min}}^{z_{max}} n_o (1+z)^{\gamma} dz \tag{4.10}$$

where z_{min} and z_{max} is the redshift path along which quasar absorbers were searched for (see Tables 4.2.1 and 4.2.2). The LLS line profiles cannot be used to directly measure their column densities because in the range 1.6×10^{17} to 2×10^{20} atoms cm^{-2}

LSS sample	z range	γ	n_o
Lanzetta (1991)	0.36–2.50	0.3 ± 0.09	1.2
	2.50–3.61	5.7 ± 1.9	8.1×10^{-4}
Sargent et al. (1989)	0.67–3.58	0.68 ± 0.54	0.76
Storrie-Lombardi et al. (1994)	0.40–4.69	1.55 ± 0.45	$0.27^{+0.20}_{-0.13}$
including LLS within 3000 km s^{-1}		1.53 ± 0.42	0.25
this work	0.40–4.93	$2.55^{+0.95}_{-0.85}$	$0.06^{+0.15}_{-0.05}$
including LLS within 3000 km s^{-1}		$2.45^{+0.75}_{-0.65}$	$0.07^{+0.13}_{-0.04}$

Table 3: This tables summarises the LLS number density redshift evolution parameters for previous work and for the results presented here.

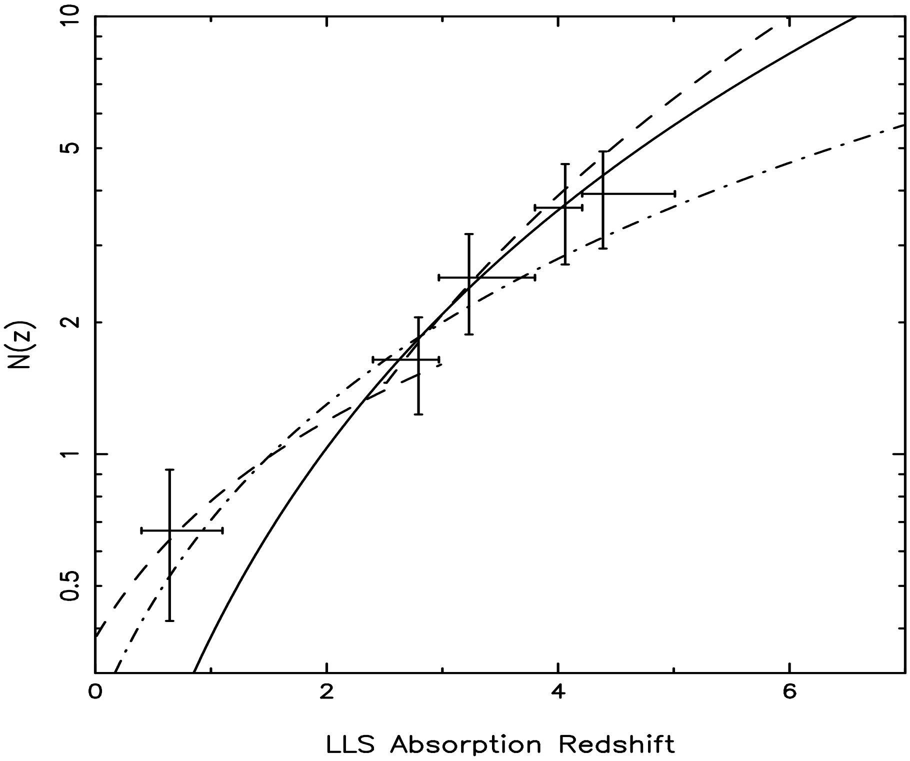

Fig. 4.— This Figure shows the logarithmic of the number density of LLS. Fits are as in Figure 3.

the curve of growth is degenerate. Nevertheless, the *expected number* of LLS provides a further constraint on the cumulative number of quasar absorbers (see Chapter 5). Figure 5 shows another way to present the number of LLS independently of binning for the sample studied. Our new high-redshift observations indicate a very strong evolution in the number density of LLS as a function of redshift. At $z = 4$, our observations indicate almost 4 LLS per unit redshift and our fit predicts 9 systems per dz at $z = 6$. This difference in number density with redshift might be due to the fact that LLS are *not* necessarily the same type of systems at high and at low-redshift.

4.3.2 Discussion

The results presented here show a strong evolution in the number density of LLS with redshift. Stengler-Larrea et al. (1995) combined data from several surveys and found a much shallower evolution (see dashed-dot line in Figure 4 and ligh grey bins in Figure 6). At $z \gtrsim 5$, the number density of Lyman-limit systems per unit redshift in our survey is $\sim$5, implying that these systems are a major source of UV opacity in the high redshift Universe.

Numerical simulations of LLSs are challenging because they contain both neutral and ionised gas. Gardner et al. (1997) extended existing numerical simulations in Cold Dark Matter models using a semi-analytical method. This allowed for the treatement of previously unresolved low-mass halos. Nevertheless, even with such corrections, the predicted number density of LLS is a factor of 3 below the observations. They interpret the deficit in the predicted number of LLS as either a failure of the Cold Dark Matter model or as an indication of the presence in the real Universe of an additional population of Lyman limit absorbers that are not resolved by simulations. Pushing this study further, Gardner et al. (2001a) investigate how the model predictions vary with various cosmological models. Standard simulations only resolve halos with circular velocity $v_c > 140$ km s^{-1} and thus underestimate the number density of LLS in all cosmological models. To estimate the absorption from lower mass halos, they fit a power-law to the relation between absorption area α and halo circular velocity v_c in the simulations and extrapolate using the Jenkins et al. (2001) halo mass function. The results from this extrapolation show that $n(z)$ LLS requires absorption in halos down to $v_c \sim 30 - 50$ km s^{-1}.

Abel & Mo (1998) propose an alternative solution to explain this discrepancy. They first note that the observed rate of incidence of LLS at $z \sim 4$ is about 30 times that expected from the local number density of galaxies. They propose to explain this difference by the presence at high-redshift of “mini-halos” which have formed prior to reionisation. They argue that the gas remains neutral until the UV background destroys the neutral hydrogen and the “mini-halos” merge into larger systems. This scenario is consistent with the observed number of LLS at high-redshift (Figure 6) even in a Cold Dark Matter model. Ultimately, such an approach could put constraints on the epoch of reionisation.

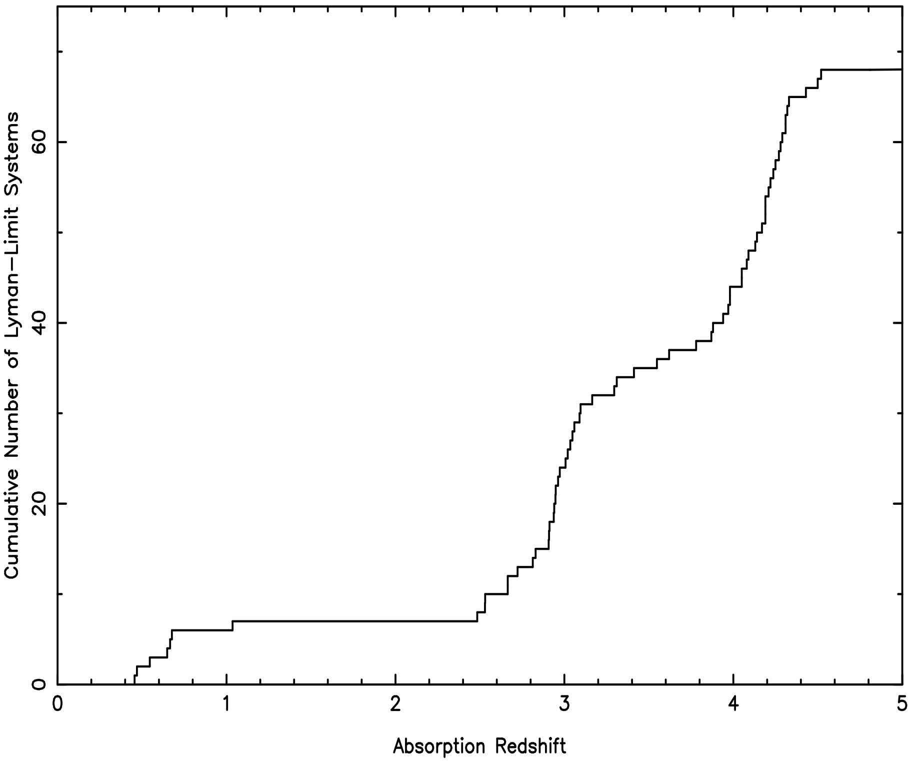

Fig. 5.— Cumulative number of Lyman-Limit Systems as a function of redshift for the whole LLS sample studied. This way of displaying the data is independent of binning.

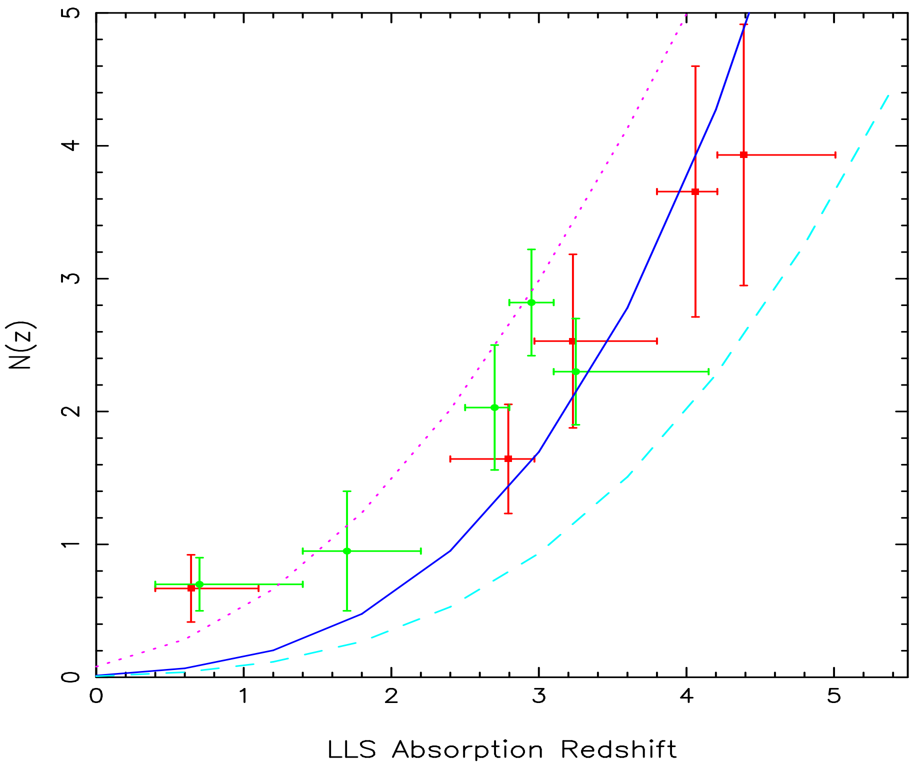

Fig. 6.— The number density of LLS from this work (dark bins) and from Stengler-Larrea et al. (1995) (light grey bins) are shown. "Mini-halo" models from Abel & Mo (1998) are overplotted: for velocities ranging 10-15 km s^{-1} (solid line), 15-20 km s^{-1} (dashed line), and 15-20 km s^{-1} with no merging (dotted line). The large difference between the model predictions illustrates its sensitivity to the input parameters.

4.4 Summary

In this Chapter we have made a statistical analysis of Lyman Limit Systems concentrating on the high-redshift range ($z \gtrsim 2.4$). By measuring the evolution with redshift of the number density of these absorbers, one can disentangle whether this population is truely evolving or whether $n(z)$ is changing solely due to the geometry of the Universe. First studies in this field, concentrating on the low redshift data available at the time, found no evolution of the intrinsic properties of the individual absorbers. Subsequent studies, acquiring more data at high redshift, started to find evolution in the case of a $\Lambda = 0$ Universe, $\Omega_M = 1$ cosmological model. Indeed the results presented here point to an apparent break at $z \sim 1.5$ that would partially explains the discrepancy between the low and high redshift results.

We use the high redshift quasar sample presented in Chapter 2 to build an homogeneous sample of LLS. We developed an automated algorithm to detect LLS and measure their redshift and optical depth, τ. We analyse this sample together with other data taken from the literature at high-redshift, $z_{em} > 4$ Storrie-Lombardi et al. (1994), intermediate redshift, $2.75 < z_{em} < 4.11$ (Sargent et al., 1989) and low redshift, $0.47 < z_{em} < 1.40$ (Bahcall et al., 1993; Bergeron et al., 1994). The number density was computed and for the first time, a strong intrinsic evolution was unambiguously detected. We used a maximum likelihood analysis to contrain the parameters of a power law fit, $n = n_o(1+z)^\gamma$ and found $n_o = 0.07^{+0.13}_{-0.04}$ and $\gamma = 2.45^{+0.75}_{-0.65}$. If there was no evolution of the intrinsic properties of the individual absorbers in a $\Lambda = 0$ Universe we would expect $\gamma = 1$ for $\Omega_M = 0$ and $\gamma = 0.5$ for $\Omega_M = 1$. An $\Omega_M = 0.3$ & $\Omega_\Lambda = 0.7$ cosmological model leads to very similar results as the $\Omega_M = 0.0$ & $\Omega_\Lambda = 0.0$ model. Clearly, our measurement of γ indicates evolution regardless of the geometry of the Universe. We further used this data set to calculate the expected number of absorbers which will allow us to put a additional constraint to the cumulative number of absorbers as a function of column density. The column density of LLS cannot be easily measure in medium resolution quasar spectra since the curve of growth (which relates the observed equivalent width to the column density) is degenerate in this column density range (see Chapter 1 for more details). We will show in Chapter 6 how we use the expected number of LLSs to overcome this particular problem and re-compute the column density distribution of quasar absorbers in a the LLS range. Finally, we have discussed our results in terms of consequences for the UV-opacity of the Universe and compare our measurements with recent models. We showed that further data are still necessary to differentiate between competing models.

Chapter 5

Damped Lyman-α Systems Analysis

> *'La conversation de Charles était plate comme un trottoir de rue,*
> *elle avait l'habit ordinaire des idées de tout le monde'*
> *Gustave Flaubert*

This Chapter starts by summarising the definition and rôle of Damped Lyman-α (hereafter DLA) systems (Section 5.1.1). Previous surveys (Section 5.1.2) and results (Section 5.1.3) are summarised. In section 5.2, our new survey for DLAs is introduced: the survey's sensitivity is defined and compared with previous surveys in Section 5.2.1. In the following section (5.2.2), the method used to select the DLA systems is detailed and the results are tabulated. Associate metal lines have also been studied (Section 5.3). In Section 5.4.1, the DLAs' properties are analysed and in section 5.4.2, their number density is calculated. Our results are compared with recent model predictions.

5.1 Introduction

5.1.1 Background

Damped Lyman-alpha systems have, by definition (Wolfe et al., 1986), a neutral hydrogen column density of $N_{HI} \geq 2 \times 10^{20}$ atoms cm^{-2} corresponding to a rest-frame equivalent width $W \geq 10$ Å. The true nature of the galaxies responsible for high-redshift damped systems is largely unconstrained. At present, there are two main competing scenario for the nature of DLAs.

One school of thought has DLAs being the (large) progenitors of massive *spiral discs* (e.g. Wolfe et al., 1986; Lanzetta et al., 1991). The gas discs would have formed at $z > 5$ through monolithic collapse, and this gas is converted to stars over a Hubble time. This picture is broadly supported by the kinematic work of Prochaska & Wolfe (1998) who used dynamical studies of the metal absorption lines associated the DLA systems to show that they are fully formed, large, rapidly rotating galactic discs with $v_{circ} \gtrsim 200$ km s^{-1}.

However, this "large disc" hypothesis runs counter to the currently-popular hierarchical structure formation models where present day galaxies are assembled from virialized sub-units over a large redshift range ($z \sim 1 - 5$). Recent hydrodynamic N-body simulations (Haehnelt et al., 1998; Maller et al., 2001) have shown that the velocity structure observed in the absorption lines can also be explained by infalling sub-galactic clumps in collapsing dark matter *halos* with small virial velocities of $\sim$ 100 km s^{-1}. This scenario has a remarkable resemblance to what has been observed already around quasars and radio galaxies over the redshift range 2–5 (e.g. Moller & Warren, 1998; Pascarelle et al., 1996; Hu & McMahon, 1996).

Intimately linked with this is one of the fundamental phenomena still poorly understood in cosmology, the detailed process relating to the origin of structure formation after the epoch of recombination. The basic dilemma is, that while the directly observable baryonic content of galaxies at the present epoch is concentrated in stars, in the past, logically, this must have been in the form of gas. Therefore the only way to obtain a self consistent and complete picture of the galaxy formation process is to combine studies of the star light and the star formation rate with studies of the gas content of the Universe to learn about the underlying metal production and gas consumption rates. Quasar absorbers provide a powerful observational means to study the early stages of galaxy formation independently of their intrinsic luminosity. The damped Lyman-α absorption lines are of particular importance since they contain the bulk of the neutral gas (and a large fraction of the baryonic content) in the Universe at high redshift and are the major directly observable baryonic component at these redshifts.

5.1.2 Previous Samples

Surveys for the highest column densities quasar absorbers are ambitious observational programs requiring extensive use of telescope time. The first search for high column density absorption lines was made in 1986 by Wolfe et al. who used 68 quasar spectra observed with the Lick Observatory and discovered 26 absorbers with (rest frame) equivalent width > 5Å in the redshift range $1.7 < z < 2.6$. One of the major results of this survey was that the incidence of DLAs was greater than expected if the absorption were arising in galaxies with the same cross section as present day spirals Wolfe (1988). A survey of similar size was conducted a few years later by Sargent et al. (1989). Combining their dataset with a similar number of quasars found in the literature, Lanzetta et al. (1991) selected DLA candidates from a sample of 101 quasars. In 1995, Lanzetta, Wolfe & Turnshek used published optical and International Ultraviolet Explorer observations to make a compilation of 260 quasars and found 16 DLAs candidates along a redshift path $\Delta(\mathrm{z}) = 202.8$ in the redshift range $0.1 \leq \mathrm{z} \leq 1.5$. A year later, Storrie-Lombardi, McMahon, Irwin & Hazard surveyed 2500 deg^2 of sky. They found 31 quasars with $\mathrm{z} \geq 4$ (at that time only around 50 $\mathrm{z} \geq 4$ were known) and probed a redshift path of $\Delta(\mathrm{z}) =$

239.4 leading to the discovery of 11 DLAs. More recently, Rao & Turnshek (2000), used a different method (based on the observations of Ly-α in 87 identified Mg II systems) and HST data to select 12 DLAs with z $\leq$ 1.65 in a redshift path Δ(z) = 104.6 redshift path. These systems are not included in the study presented in this Chapter because the work of this thesis concentrates on high-redshift data but are discussed later on in Chapter 6. Finally, Storrie-Lombardi & Wolfe (2000) made new spectroscopic observations of 30 quasars (11 new) at 0.008 $\leq$ z $\leq$ 4.494 resulting in 11 DLAs. They combine these with previous data to make a sample of 646 quasars and found 85 DLAs in a Δ(z) = 418.4 redshift path. Following this work, we undertook observations of a new sample based on a larger sky coverage in order to significantly improve the redshift path surveyed at high-redshift and hence make a statistically significant study of DLA properties as a function of redshift.

5.1.3 Previous Results

Lanzetta (1991) produced the first significant statistical analysis of DLA number density and the mass density of HI in DLAs. If the absorber population is not evolving, in a standard Friedmann cosmology with no Λ term, $n(z)$ is given by

$$n(z) = n_0(1+z)(1+2q_0z)^{-0.5} \tag{5.1}$$

where n_0 is the number of absorbers at $z = 0$.

For a non-evolving population, the index γ is equal to 1 for $q_0 = 0$ and 0.5 for $q_0 = 0.5$. The analysis of Lanzetta (1991) indicated $\gamma = 0.3 \pm 1.4$, consistent with a non-evolving population for either $\gamma = 1$ or 0.5.

A few years later, Lanzetta et al. (1995) extended their work to include DLAs at lower redshift by exploiting ultra-violet data obtained from the IUE satellite. The mean absorption redshift of the sample is $\langle z_{abs} \rangle \sim 0.64$ and the average DLA number density was found to be $n(z) = 0.08$. With the IUE data, an improved estimate of γ could be determined and was found to be 1.15±0.55. Given the reduction of the error bars on their determination of γ, it was concluded by Lanzetta et al. (1995) that the product of the absorption cross section and co-moving spatial number of DLAs has not evolved significantly from $z = 0.008$ to $z \sim 3.5$.

Finally, Wolfe et al. (1995) used the Large Bright Quasar Survey (Hewett et al., 1995, LBQS,) and references therein, to search for DLAs with 1.6 $\lesssim z_{abs} \lesssim$ 3.0. A total of 59 DLA candidates were pre-selected as having $W_0 \geq 5$ Å out of 228 spectra. In addition to the LBQS sample, they constructed a 'statistical sample' from the literature consisting of 80 DLAs from which they determined a value for γ identical (and with the same errors) as Lanzetta et al. (1995).

5.2 New DLA Sample

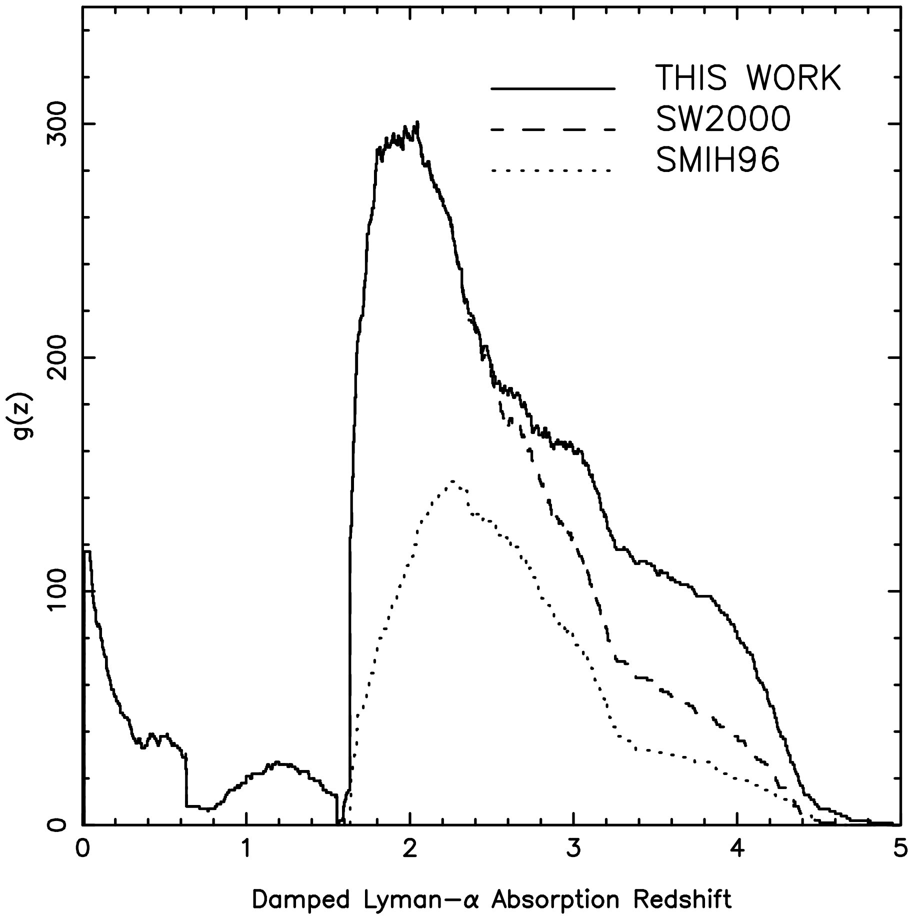

Fig. 1.— Survey sensitivity function. The g(z) function shows the cumulative number of lines of sight along which a DLA system could be detected if there was one. SW00 and SMIH96 are surveys undertaken by Storrie-Lombardi & Wolfe (2000) and Storrie-Lombardi et al. (1996a), respectively. Our new observations more than doubles the redshift path surveyed at $z \gtrsim 3.5$.

5.2.1 Survey's Sensitivity

DLAs are rare and to find them requires probing many quasar lines of sight. Figure 1 shows the cumulative number of lines of sight along which a DLA *could* have been detected at the 5σ confidence level for the previous major surveys. The survey sensitivity, $g(z)$, is defined by:

$$g(z) = \sum H(z_i^{max} - z)H(z_i^{min} - z) \tag{5.2}$$

where H is the Heaviside step function. The survey sensitivity, $g(z)$, is compared with those of previous DLA surveys in Figure 1 to show that our new observations more than double the redshift path searched for DLAs at z $\gtrsim$ 3.5. Although DLAs have a low number density per unit redshift compared with lower column density systems, they are still thought to contain most of the neutral hydrogen mass even at redshifts less than 3. Chapter 6 discusses how our new survey impacts upon measurement of the comoving mass density of neutral gas at high redshift, its implications for the formation epoch of DLA and for the rate of evolution of gas into stars. In the remainder of this Chapter, we discuss the selection techniques used to detect DLAs our survey and present an analysis of the statistical properties of these high column density systems.

5.2.2 DLA Detection

To select DLA candidates we have used the detection algorithm developed by Lanzetta et al. (1991), supplemented by a visual search. The algorithm computes the observed equivalent widths of all the absorption lines in the forest and plots these as a function of observed wavelengths. All absorptions with W greater the chosen threshold can thus clearly be picked up. Further investigations are necessary to check that the bottom of the corresponding absorption feature goes to zero flux level. It has previously been applied to other samples of z $>$ 4 quasars in Storrie-Lombardi et al. (1996c) and Storrie-Lombardi & Wolfe (2000). We have fitted the "local" quasar continua using IRAF SPLOT x-(j)x task (an example of which is displayed in Figure 6). These "local" continua follow, within the noise, the upper part of the flux in the forest: they do *not* include the continua depression (D_A and D_B, see Chapter 3) and thus lie well below the "true" quasar continua.

In order to find intervening quasar absorbers, the spectra were analysed from 3000 km s^{-1} blueward of the emission line (to avoid lines possibly associated with the quasar) towards shorter wavelengths. The analysis was stopped when the signal-to-noise ratio became too low to detect a Lyα line with rest equivalent width $\geq$ 5 Å at the 5σ level (corresponding to z_{min} in Table 5.2.2). This point was typically caused by the incidence of a Lyman limit system.

In the automated search, for each spectrum, we define an equivalent width spectrum (see Figure 4 and Figure 3 for usual spectra). We measured the equivalent widths of all the candidates with rest equivalent widths greater than 5 Å by fitting Gaussian

Quasar	Med Res N(HI)	z	High Res N(HI)	z	Δ N(HI)
BR 0019−1522	20.0	3.42	20.92	3.4370	+0.92
BR 0019−1522	20.5	3.98	<20.3	...	> −0.2
BR 0951−0450	21.0	3.84	20.6	3.8477	−0.40
BR 0951−0450	20.3	4.20	20.4	4.2028	+0.10
BRI 0952−0115	20.8	4.01	20.55	4.0238	−0.25
BRI 1013+0035	20.8	3.10	21.1	3.1031	+0.30
BRI 1108−0747	20.2	3.61	20.33	3.6070	+0.13
BRI 1114−0822	20.4	4.25	20.3	4.2576	−0.10
BR 1202−0725	20.5	4.38	20.49	4.3830	−0.01
BRI 1346−0322	20.3	3.73	20.72	3.7343	+0.42
BRI 1500+0824	20.4	2.80	20.8	2.7968	+0.40
BR 2237−0607	20.4	4.08	20.5	4.0691	+0.10
mean	20.46	3.7833	20.58	3.7693	+0.12
min value	30.0	2.80	<20.3	2.7968	−0.40
max value	21.0	4.38	21.1	4.3830	+0.92

Table 1: This table compiles the DLA column density and redshift estimates from 5Å (FWHM), signal-to-noise ratio per pixel ~ 20 (Storrie-Lombardi et al., 1996a) and 2Å, signal-to-noise ratio per pixel ~ 25 (Storrie-Lombardi & Wolfe, 2000) quasar spectra. This shows that our N(HI) estimates from 5 Å resolution quasar spectra are reliable. In particular, contrary to common believe, the column density derived from medium resolution data *are not* over-estimated.

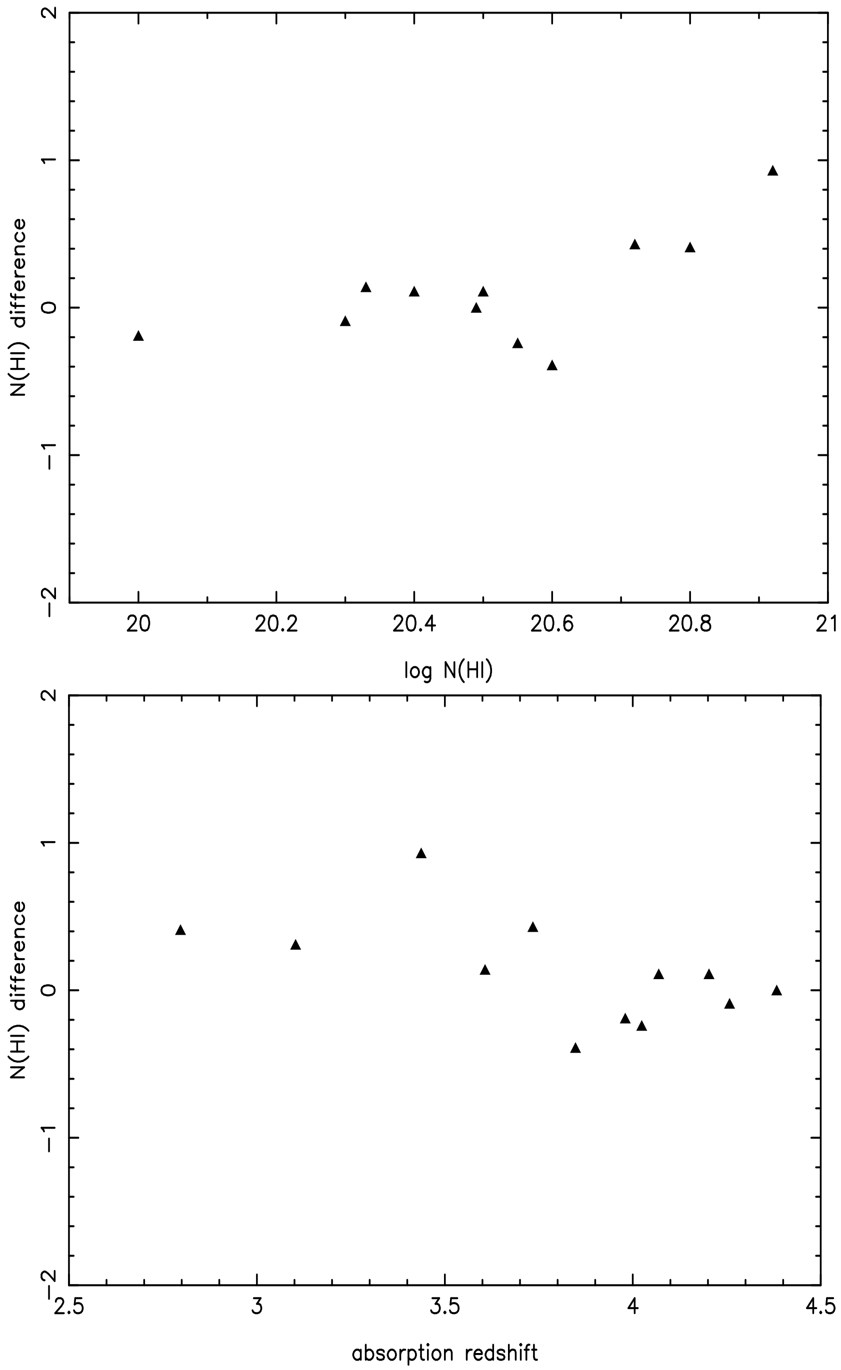

Fig. 2.— These figures illustrate the difference between the medium and high resolution DLA column density measurements as function of column density (top panel) and redshift (bottom panel). A trend in the top panel might be visible but the correlation parameter is low (r=0.62).

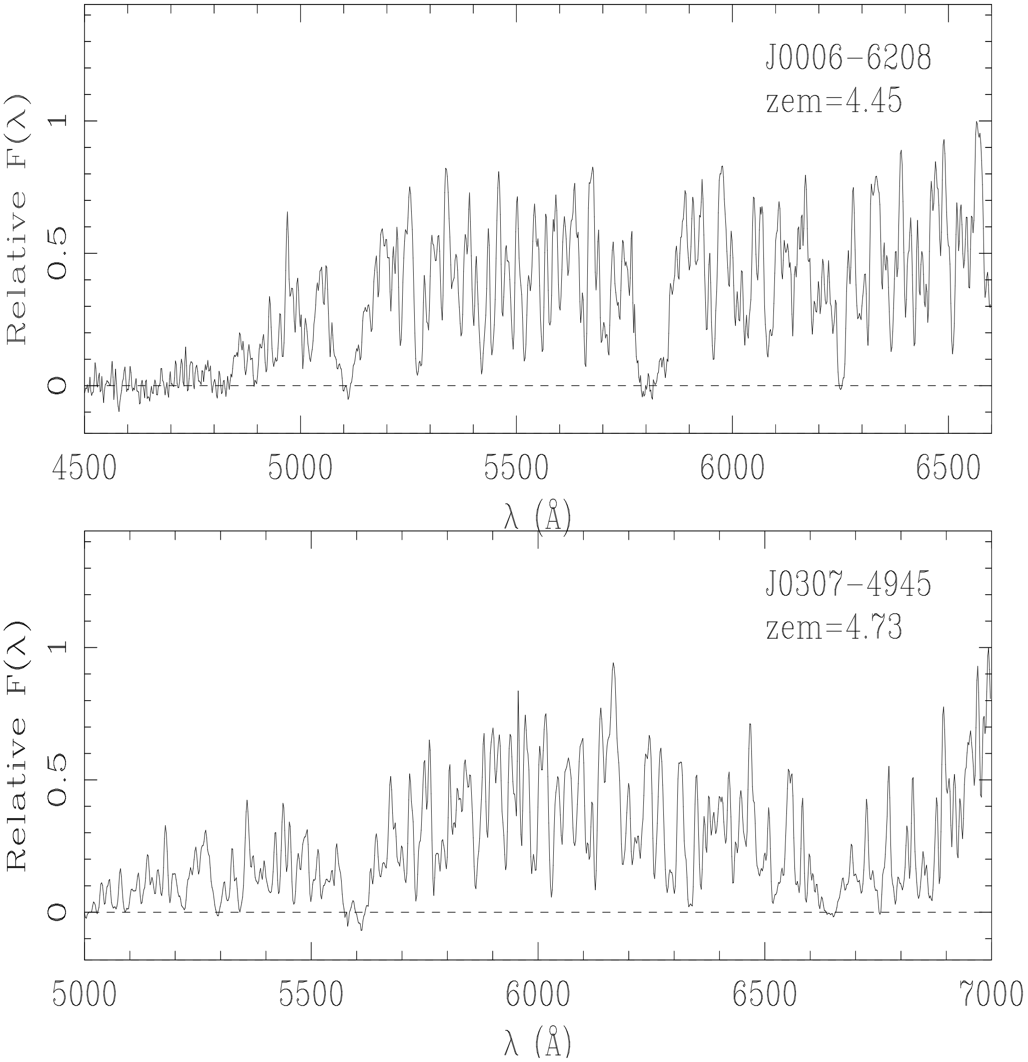

Fig. 3.— Spectra of quasars of the equivalent width analysis shown in next figure (Figure 4).

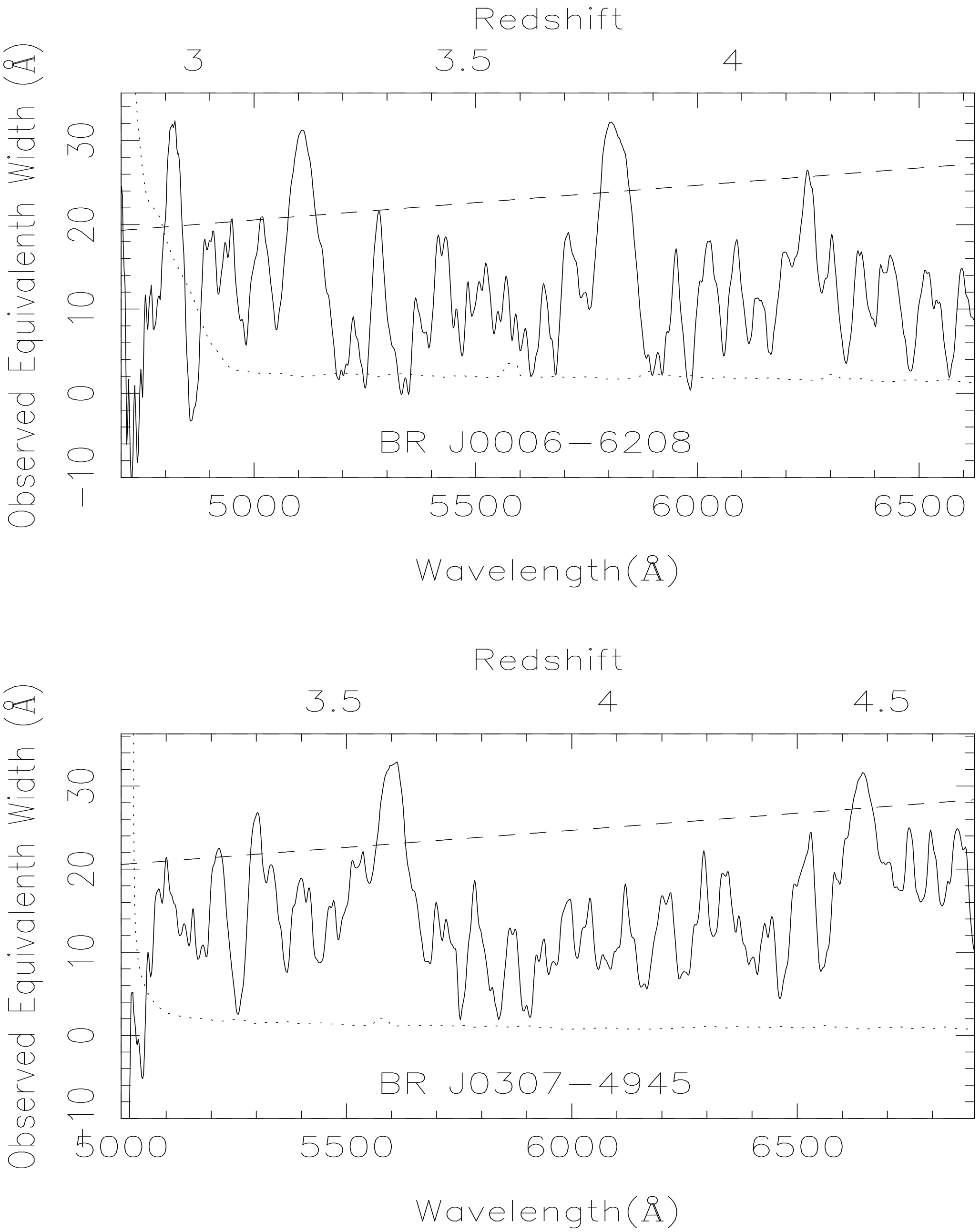

Fig. 4.— The figure shows two examples of the output from the algorithm that detects damped Lyα absorption candidates. The spectrum equivalent width bins are shown as a solid line, the error equivalent width are shown as a dotted line, and the dashed line shows the observed equivalent width of a 5 Å rest equivalent width line at the redshifts shown along the top axis. The lower axis shows the wavelength scale. The minimum redshift (z_{min} in table 5.2.2) to which we can survey for damped candidates is determined by the point where the error line (dotted) crosses the 5 Å rest equivalent width threshold (dashed line). The places where the spectrum array (solid line) goes above the dashed line threshold are the wavelengths at which we measure the equivalent width of the lines in the original spectrum. The upper panel shows four potential absorbers in BR J0006-6208 and the lower panel shows five potential absorbers in BR J0307-4945.

profiles in IRAF (SPLOT k-k task) against the "true" quasar continua. We then estimated their N (HI) column densities from the linear part of the curve of growth. Figure 5 shows the DLA feature in BR J0307−4945 on the medium resolution data (top panel) and the fit made with FITLYMAN (MIDAS package) on the high-resolution data (bottom panel). The column density estimates resulting from the two sets of data are in good agreement. Previous experience has shown that the column density estimates derived using this method are in good agreement with measurements done on higher resolution data as shown from a comparison of the results of Storrie-Lombardi et al. (1996a) [resolution 5Å (FWHM), signal-to-noise ratio per pixel $\sim$ 20] and Storrie-Lombardi & Wolfe (2000) [resolution 2Å, signal-to-noise ratio per pixel $\sim$ 25] (Table 1). The differences are illustrated by Figure 2 as function of column density (top panel) and redshift (bottom panel). A trend in the top panel might be visible but the correlation parameter is low (r=0.62). This shows that N(HI) estimates from 5 Å quasar spectra can be reliable. In particular, contrary to common believe, the column density derived from medium resolution data *are not* in general over-estimated.

In addition to the search described above, the spectra were surveyed interactively and the equivalent width and Full Width Half Maximum (FWHM) were measured as described above for any wide or saturated lines that looked like they might possibly be damped. Unfortunatly, the equivalent width is quite sensitive to the extrapolated continuum placement, particularly when trying to include possible damping wings. As pointed out earlier in Chapter 1, the equivalent width is traditionally used although measuring the FWHM of the line would be more appropriate as it is less depend on the exact continuum position since its sides are nearly parallel where it is measured.

These results were compared with the ones from the automated search to make up the list of DLAs shown in Table 5.2.2. The candidates with rest equivalent widths in the range 5 – 10 Å at z $\sim$ 4 are listed in the table for completion although many are unlikely to be damped. The sample of 66 $z \gtrsim 4$ quasar spectra has lead to the discovery of 26 new damped Lyα absorption candidates, 15 of which have $z > 3.5$.

For completeness, we also looked for quasar absorbers within 3000 km s^{-1} of the quasar emission line and thus possibly associated with the quasar. We found only one such system in PSS J0034+1639, at $z = 4.26$. The column density of this absorber is large: log N (HI) = 21.1 atoms cm^{-2}. The redshift path surveyed (between z_{em} and z_{em} − 3000 km s^{-1}) is $\Delta z = 2.9$, corresponding to $\Delta X = 12.1$ in a $\Omega_M = 0.3$, $\Omega_\Lambda = 0.7$ Universe ($\Delta X = 6.7$ in a $\Omega_M = 1.0$, $\Omega_\Lambda = 0.0$ Universe). It is interesting to note that in their survey for CORALS (Complete Optical and Radio Absorption Line Systems), Ellison et al. (2001c) observed 66 quasars with $z_{em} \geq 2.2$ and found 19 DLAs plus 3 systems with $z_{abs} \sim z_{em}$ [log N(HI) = 20.20 atoms cm^{-2}, $z_{abs} = 2.57$ in B0405–331; log N(HI) = 21.20 atoms cm^{-2}, $z_{abs} = 2.81$ in B0528–250; log N(HI) = 20.78 atoms cm^{-2}, $z_{abs} = 2.97$ in B1354–107] (Ellison et al., 2001b), i.e. more than us for a survey of comparable size. However, the poisson errors of a sample of three systems are large, and so these results do not necessarily show that radio-selected and optically-selected quasar samples are different.

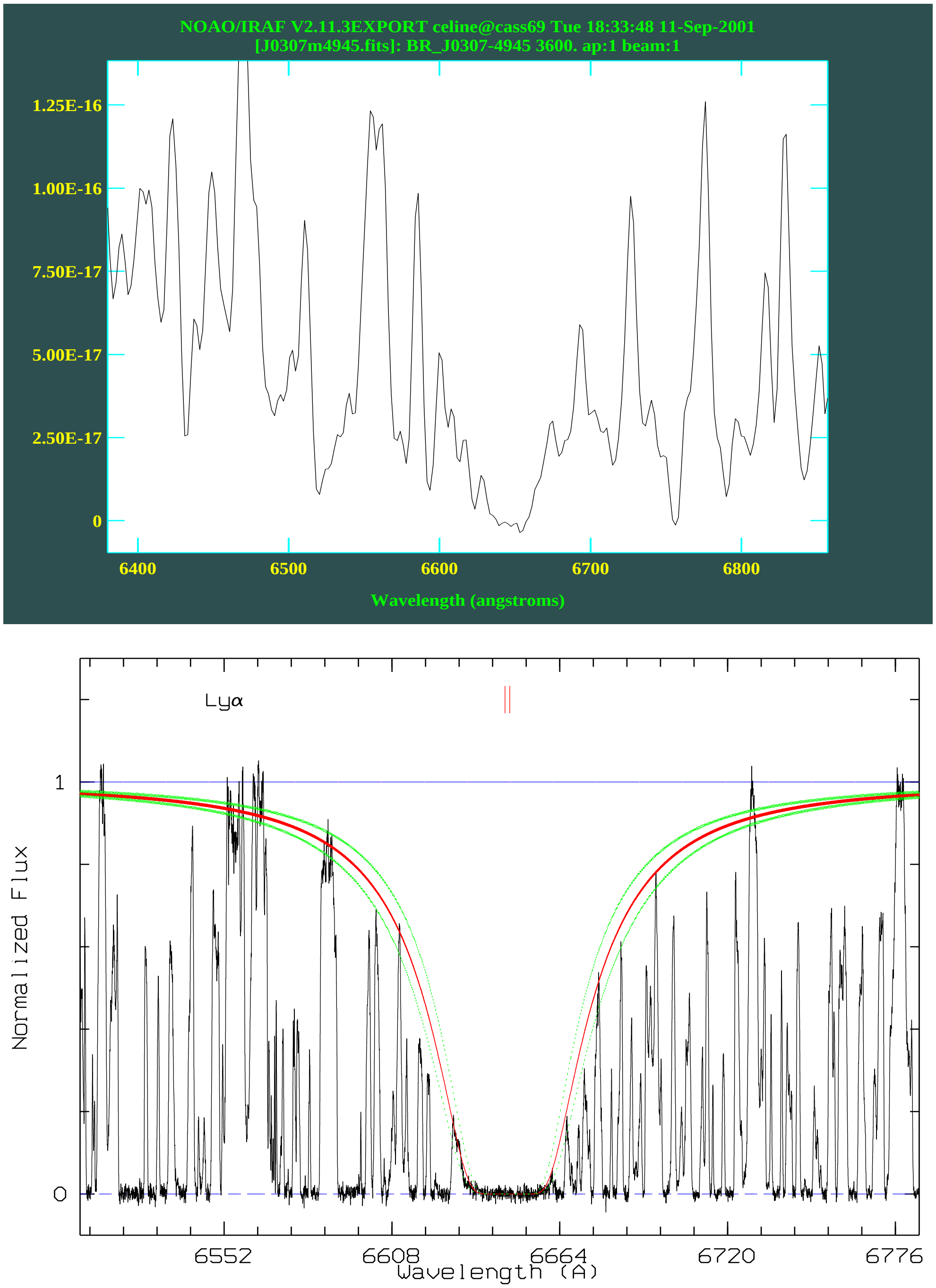

Fig. 5.— BR J0307−4945 DLA. The top panel shows the DLA feature on the medium resolution data and bottom panel shows the fit made with MIDAS's package FITLYMAN on the UVES high-resolution data. The two resulting column density estimates are in good agreement.

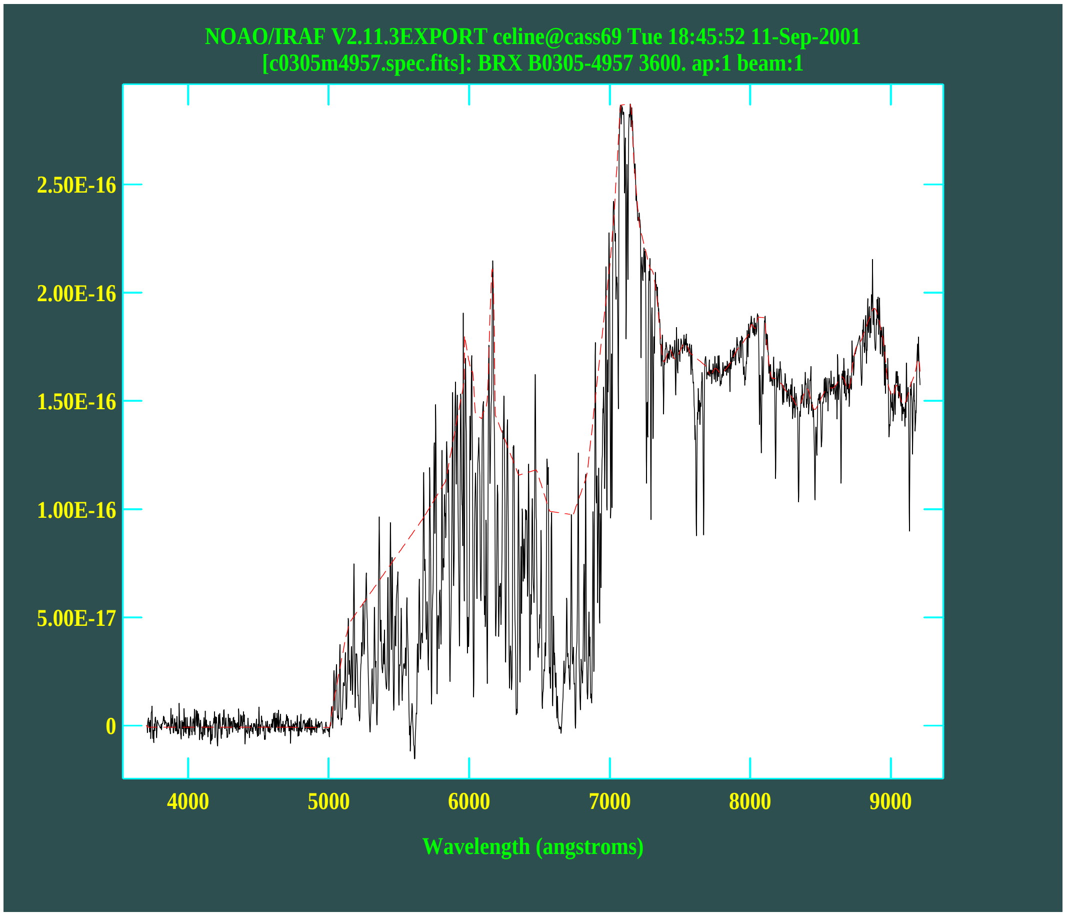

Fig. 6.— Example of medium resolution “local” continuum fit made with the “splot x-x” IRAF command for BR J0307−4945 quasar.

Table 2: Survey for Damped Lyman−α Absorption Systems

Quasar	z_{em}	z_{min}	z_{max}	z_{abs}	W (Å)	log $N_{\rm HI}$ (cm^{-2})	Metal Lines	$z_{\rm metal}$	Note
PSS J0003+2730	4.240	2.718	4.188	3.51	7.6	20.0	Si II 1527	3.513	
							Fe II 1608	3.510	
							Al II 1671	3.512	
				3.89	9.0	20.2	C II 1334	3.893	
							Si IV 1400	3.893	
							C IV 1549	3.893	
							Al II 1671	3.891	
BR J0006−6208	4.455	2.944	4.400	2.97	15.6	20.7	Si II 1808	2.965	
				3.20	21.6	20.9	Al II 1671	3.193	
				3.78	22.5	21.0	Si II 1527	3.776	
							Fe II 1608	3.780	a
				4.14	7.9	20.1	C II 1334	4.150	b
BR J0030−5129	4.174	2.304	4.122	2.45	18.1	20.8	Fe II 2261	2.449	
							Fe II 2344	2.452	
							Fe II 2383	2.451	
PSS J0034+1639	4.293	2.981	4.240	3.75	8.9	20.2	Si II 1527	3.752	
							C IV 1549	3.754	
				4.26	24.9	21.1	Si II 1260	4.252	b,c
							O I 1302	4.262	
							C II 1334	4.282	
							Si IV 1400	4.281	
							Si II 1527	4.282	
							C IV 1549	4.281	
							Fe II 1608	4.281	
SDSS J0035+0040	4.747	3.309	4.690	...	...	...	...	...	
PSS J0106+2601	4.309	2.764	4.256	3.96	13.5	20.5	Lyβ	3.96	b
							C II 1334	3.958	
							Si IV 1400	3.957	
							C IV 1549	3.959	
PSS J0131+0633	4.417	3.014	4.363	3.17	6.6	19.9	...	...	
				3.61	5.5	19.8	C IV 1549	3.609	
PSS J0133+0400	4.154	2.865	4.102	3.08	8.2	20.1	C IV 1549	3.083	
							Si II 1808	3.085	
				3.69	11.9	20.4	Si II 1527	3.691	
							Al II 1671	3.690	
				3.77	12.5	20.5	C II 1334	3.771	
							Si IV 1400	3.771	
							Si II 1527	3.771	
							Fe II 1608	3.770	
							Al II 1671	3.771	

				4.00	8.6	20.1	Si II 1260	3.993	
							O I 1302	3.994	
							Si IV 1400	3.996	
							Si II 1527	3.993	
PSS J0134+3307	4.532	2.562	4.477	3.76	14.8	20.6	Si II 1527	3.761	d
							C IV 1549	3.775	
							Al II 1671	3.780	
PSS J0152+0735	4.051	1.890	4.000	3.84	17.0	20.7	Lyβ	3.84	b
							O I 1302	3.841	
							C II 1334	3.842	
PSS J0209+0517	4.174	2.759	4.122	3.66	10.1	20.3	Al II 1671	3.664	
				3.86	15.2	20.6	Lyβ	3.86	
							Si II 1304	3.862	
							C II 1334	3.862	
SDSS J0211−0009	4.874	3.402	4.815	4.64	7.5	20.0	Si II 1527	4.645	
BR J0234−1806	4.301	2.971	4.248	3.69	8.7	20.2	Si IV 1400	3.694	
							Al II 1671	3.692	
PSS J0248+1802	4.422	2.810	4.368	...	...	...	...	...	
BR J0301−5537	4.133	2.825	4.082	3.22	10.4	20.3	Si II 1527	3.220	
				3.38	7.9	20.1	Si II 1527	3.377	
				3.71	7.0	20.0	C II 1334	3.705	
							C IV 1549	3.701	
BR J0307−4945	4.728	3.138	4.671	3.35	6.0	19.8	...	...	
				4.46	18.6	20.8	Lyβ	4.46	b
							O I 1302	4.465	
							Si II 1304	4.466	
							C II 1334	4.465	
							Si IV 1400	4.464	
							Si II 1527	4.466	
							C IV 1549	4.464	
							Fe II 1608	4.466	
							Al II 1671	4.466	
SDSS J0310−0014	4.658	3.087	4.601	3.42	13.2	20.5	Al II 1671	3.424	
				4.34	8.6	20.1	...	...	
BR J0311−1722	4.039	2.591	3.989	3.73	8.7	20.2	O I 1302	3.733	
							Si II 1304	3.733	
							C II 1334	3.733	
BR J0324−2918	4.622	2.900	4.566	...	...	...	...	...	
BR J0334−1612	4.363	3.080	4.309	3.56	24.5	21.0	Si II 1527	3.558	
SDSS J0338+0021	5.010	3.528	4.950	4.06	11.8	20.4	Si II 1527	4.059	
							Al II 1671	4.066	
BR J0355−3811	4.545	3.030	4.490	...	...	...	...	...	
BR J0403−1703	4.227	2.992	4.175	...	...	...	...	...	

BR J0415−4357	4.070	2.813	4.019	3.81	7.1	20.1	Lyβ	3.81	
							O I 1302	3.806	
							Si II 1304	3.806	
							C II 1334	3.806	
							Si II 1527	3.806	
BR J0419−5716	4.461	2.820	4.406	2.82	7.4	20.0	Fe II 2344	2.819	
				2.90	8.8	20.2	Fe II 2344	2.896	
				2.98	5.1	19.7	...	...	
BR J0426−2202	4.320	2.544	4.267	2.98	26.2	21.1	Al II 1671	2.982	
PMN J0525−3343	4.383	2.829	4.329	...	...	...	...	...	
BR J0529−3526	4.413	3.023	4.359	3.57	8.5	20.1	Fe II 1608	3.573	
							Al II 1671	3.571	
BR J0529−3552	4.172	2.821	4.120	3.68	7.6	20.0	...	...	
				3.70	7.6	20.0	...	...	
BR J0714−6455	4.462	3.050	4.407	...	...	...	...	...	
PSS J0747+4434	4.430	2.764	4.376	3.76	10.3	20.3	...	...	
				4.02	15.4	20.6	Lyβ	4.02	
							C II 1334	4.020	
							Al II 1671	4.017	
RX J1028−0844	4.276	2.533	4.223	3.42	8.0	20.1	Lyβ	3.422	
							Si II 1527	3.423	
							Al II 1671	3.422	
				4.05	5.0	19.7	Al II 1671	4.047	e
PSS J1057+4555	4.116	2.652	4.065	2.90	8.0	20.1	Al II 1671	2.910	
				3.05	10.0	20.3	Fe II 1608	3.061	
							Al II 1671	3.051	
							Si II 1808	3.049	
				3.32	8.9	20.2	Si II 1527	3.316	
							Al II 1671	3.317	
PSS J1159+1337	4.073	2.563	4.022	3.72	10.3	20.3	Lyβ	3.72	b,f
							C II 1334	3.723	
							Si IV 1400	3.723	
							Si II 1527	3.723	
							C IV 1549	3.724	
							Al II 1671	3.723	
PSS J1253−0228	4.007	2.498	3.957	2.78	38.5	21.4	Al II 1671	2.781	b
				3.60	5.2	19.7	C II 1334	3.602	
							Si IV 1400	3.603	
							C IV 1549	3.602	
							Fe II 1608	3.599	
BR J1310−1740	4.185	2.508	4.133	3.43	8.1	20.1	Si II 1527	3.435	
							C IV 1549	3.434	
							Al II 1671	3.433	

BR J1330−2522	3.949	2.578	3.900	2.91	7.5	20.0	...	...	
				3.08	5.7	19.8	Si II 1527	3.082	
							C IV 1549	3.081	
							Fe II 1608	3.080	
							Al II 1671	3.080	
FIRST J1410+3409	4.351	3.026	3.578	3.43	8.2	20.1	...	...	
		3.602	4.297	...	...	...	...	...	
PSS J1456+2007	4.249	2.878	4.197	3.22	5.6	19.8	Si II 1527	3.223	
							Si II 1808	3.221	
				4.16	6.8	19.9	...	...	b
BR J1603+0721	4.385	3.062	4.331	...	...	...	...	...	
PSS J1618+4125	4.213	2.820	4.161	3.92	12.9	20.5	Si IV 1400	3.920	b
							Si II 1527	3.914	
PSS J1633+1411	4.351	2.536	4.297	3.90	5.8	19.8	C IV 1549	3.895	
							Fe II 1608	3.906	
PSS J1646+5514	4.037	2.772	3.987	...	...	...	...	...	
PSS J1721+3256	4.031	2.791	3.981	...	...	...	...	...	
RX J1759+6638	4.320	2.804	4.267	3.40	12.4	20.4	Si II 1527	3.398	
							C IV 1549	3.397	
							Al II 1671	3.397	
PSS J1802+5616	4.158	2.891	4.106	3.39	8.3	20.1	Si II 1527	3.386	
							C IV 1549	3.389	
				3.56	9.7	20.2	...	...	
				3.76	11.2	20.4	...	...	
				3.80	8.5	20.1	C II 1334	3.807	
PSS J2122−0014	4.114	2.350	4.063	3.20	10.7	20.3	Si II 1527	3.206	g
							C IV 1549	3.206	
							Fe II 1608	3.205	
							Al II 1671	3.206	
				4.00	8.0	20.1	Si II 1260	3.999	b
							Si II 1527	4.001	
							C IV 1549	4.000	
PMN J2134−0419	4.334	2.903	4.281	3.27	7.0	20.0	C IV 1549	3.262	
							Fe II 1608	3.269	
PSS J2154+0335	4.363	2.979	4.309	3.61	11.3	20.4	Si II 1527	3.623	
				3.79	5.4	19.7	C IV 1549	3.778	
PSS J2155+1358	4.256	2.940	4.203	3.32	24.6	21.1	Si II 1527	3.316	h
							C IV 1549	3.313	
							Fe II 1608	3.316	
							Al II 1671	3.314	

BR J2216−6714	4.469	2.795	4.414	3.37	7.0	20.0	C IV 1549	3.369	
							Si II 1808	3.364	
				4.28	7.0	20.0	Lyβ	4.28	
							O I 1302	4.262	
				4.32	8.3	20.1	Si II 1304	4.323	
PSS J2241+1352	4.441	3.027	4.387	3.65	7.2	20.0	Si II 1808	3.647	
				4.28	17.1	20.7	Lyβ	4.28	
							O I 1302	4.282	
							Si II 1304	4.284	
							C II 1334	4.282	
							Si IV 1400	4.286	
							Si II 1527	4.283	
							Fe II 1608	4.284	
BR J2317−4345	3.943	2.448	3.894	3.49	20.2	20.9	Si IV 1400	3.483	
							C IV 1549	3.486	
							Fe II 1608	3.491	
BR J2328−4513	4.359	2.926	4.305	3.04	8.3	20.1	Si II 1808	3.041	i
PSS J2344+0342	4.239	2.696	4.187	2.68	23.0	21.0	Si II 1808	2.678	j
							Fe II 2260	2.684	
							Fe II 2367	2.678	
				3.21	21.1	20.9	C IV 1549	3.218	
							Fe II 1608	3.219	
							Al II 1671	3.219	
							Si II 1808	3.220	

BR J2349−3712	4.208	2.847	4.156	3.69	9.5	20.2	Si II 1527	3.691

[a] Fe II 1608 at z=3.780 is at the same position as Fe II 2600 at z=1.958.

[b] Also detected as a Lyman-limit system.

[c] This damped system is within 3000 km s^{-1} of the quasar emission redshift but we have included it in this table due to the fact that it is the first damped absorber detected at a redshift $z > 4$ with a column density log $N_{\rm HI} > 21$.

[d] Si II 1527 at z=3.761 is at the same position as C IV 1549 at z=3.686.

[e] Al II 1671 at z=4.047 is at the same position as Mg I 2853 at z=1.956.

[f] This damped absorption line has a very narrow core but strong damping wings are visible on both sides of the line.

[g] The Lyα line may be blended with Lyβ at z=4.00, therefore the column density may be overestimated. This quasar has an unusually rich absorption spectrum, with many C IV absorbers redward of the Lyα emission.

[h] Si II 1527 at z=3.316 is at the same position as Fe II 2260 at z=1.915.

[i] Si II 1808 at z=3.041 is blended with C IV 1549 at z=3.719.

[j] This damped absorption candidate is just below the minimum redshift determined with our detection algorithm. It is likely to be real but requires confirmation with a higher signal-to-noise spectrum.

Figure 4 shows two examples (BR J0006−6208 and BR J0307−4945) of the output of the algorithm we use to detect DLA candidates and Figure 3 for spectra of the corresponding quasars. One of the highest-redshift (z=4.46) DLA system currently known is detected in the spectrum of quasar BR J0307−4945 (Figure 7). It has many associated metal lines which have been studied in detail with higher-resolution observations undertaken with the UVES spectrograph on VLT (Dessauges-Zavadsky et al., 2001). This spectrograph is a unique facility perfectly suited to the study of quasar spectra thanks to its high sensitivity at extreme red and blue wavelengths (D'Odorico, 1997; D'Odorico et al., 2000). The spectrum shows complex low-ionisation and high-ionisation line profiles spanning ≈ 240 and 300 km s^{-1} in velocity space respectively. We derive accurate abundances for N, O, Al, Si and Fe, and place a lower limit on C and an upper limit on Ni: $[N/H] = -3.07 \pm 0.15$, $[O/H] = -1.63 \pm 0.19$, $[Al/H] = -1.79 \pm 0.11$, $[Si/H] = -1.54 \pm 0.11$, $[Fe/H] = -1.97 \pm 0.19$, $[C/H] > -1.63$ and $[Ni/H] < -2.35$. The derived metallicity, $\sim 1/90$ solar, shows that this very young absorber (≤ 1.3 Gyr) has already experienced a significant metal enrichment. The [O/Si] ratio is nearly solar suggesting a limited amount of dust, the relative [Si,O/Fe] abundance ratios show a similar enhancement as observed in the Milky Way stars with comparable metallicities, and the [N/O] ratio is very low. All these results point to an enrichment pattern dominated by Type II supernovae which suggests a Milky Way type evolutionary model.

5.2.3 Other Lines at the DLAs' Redshift

Absorption features redward of the Ly-α quasar emission line were selected using an automated algorithm[1] developed and made available for public use by Bob Carswell. The code systematically detects lines with equivalent width $W \geq 0.1$ Å. Gaussians were fitted to the lines in order to measure their redshifts and equivalent widths. Some of these lines were identified as low-ionization states of metals in association with DLA candidates. All the metal lines associated with DLA candidates are listed in Table 5.2.2.

In some cases Ly-β was observed blueward of the DLA candidate. Observing the Lyman series is useful because it permits a more detailed study and column density estimate of the DLA itself. As an example, the Ly-β associated with the z=4.46 DLA in BR J0006−6208 is clearly visible (see Figure 7). Even at medium resolution, it can be seen that the line resolves into two components.

5.3 Metal Systems

The observed equivalent width and wavelength of every absorption line detected redward of the quasar Lyman-α emission were measured using the algorithm described in section §5.2.3 above. The features which were not associated with a DLA or LLS were identified using the line list in Table 3. Most of the detected Mg II systems also show associated Fe II absorption. This survey resulted in the detection of 80 new C

---

[1] see the following URL for more details: http://www.ast.cam.ac.uk/~rfc/rdgen.html

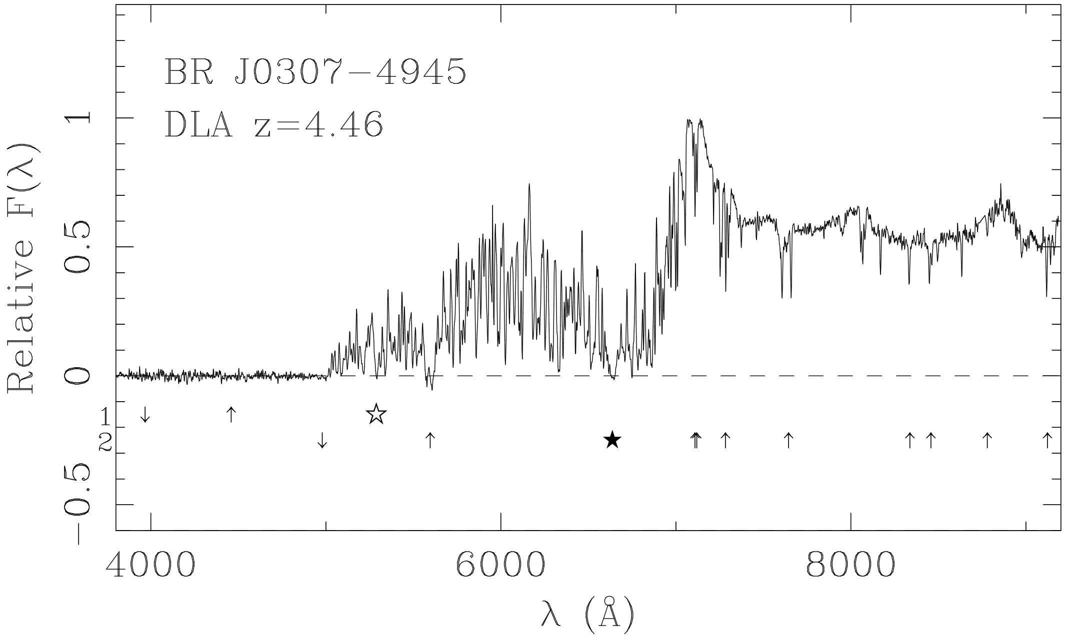

Fig. 7.— Example of DLA candidates. The spectrum of quasar BR J0307−4945 with DLA candidates marked at z=4.46 and z=3.35 is shown. The z=4.46 absorber is the highest redshift damped absorber currently detected. The notations are as in Figure 1. Many metal lines are observed at z=4.46 but no metals are detected at z=3.35. The higher redshift DLA has been studied in detail with higher-resolution observations undertaken with the UVES spectrograph on VLT (Dessauges-Zavadsky et al., 2001). The corresponding Ly-β clearly resolves into two components thus allowing a better estimate the DLA properties.

Table 3: Metal Lines Rest Wavelengths

Ion	λ (Å)	Ref.
N V	1238.821	1
N V	1242.804	1
Si II	1260.4221	1
Si II	1304.3702	1
C II	1334.5323	1
Si IV	1393.7550	1
Si IV	1402.7700	1
Si II	1526.7066	1
C IV	1548.1950	1
C IV	1550.7700	1
Fe II	1608.4511	1
Fe II	1611.2005	1
Al II	1670.7874	1
Si II	1808.0126	2
Fe II	2260.7805	1
Fe II	2344.2140	1
Fe II	2367.5910	3
Fe II	2374.4612	4
Fe II	2382.7650	4
Fe II	2586.6500	4
Fe II	2600.1729	4
Mg II	2796.3520	1
Mg II	2803.5310	1
Mg I	2852.9641	1

References:

(1) Morton 1991;

(2) Bergeson & Lawler 1993;

(3) Nussbaumer, Pettini & Storey 1982;

(4) Cardelli & Savage 1995

IV systems ($3.0 \lesssim z \lesssim 4.5$) and 48 new Mg II systems ($1.3 \lesssim z \lesssim 2.2$), see Chapter 1, Section 1.3.1 II) for more details. The results are summarized in Table B in Appendix B.

Metal production provides an indirect but powerful way to trace early stages of galaxy formation. CIV lines in particular probe galatic haloes and Mg II systems are known to be associated with the extended gaseous envelopes of bright galaxies which have been detected in emission at $z \sim 0.6$ (Bergeron & Boisse, 1991). Our data provide for the first time a sample of high-redshift CIV systems which will be studied in more details.

5.4 DLA Analysis

5.4.1 DLA Properties

Figure 8 (top panel) shows an overview of the distribution of column density with redshift. There appear to be less high column density systems at high-redshift ($z \gtrsim 3.5$). The other point to note is that in their sample, Rao & Turnshek (2000) have two distinct populations of absorbers: systems with high column density (log N(HI) > 21.3 atoms cm^{-2}), and systems with lower column density (log N(HI) < 20.7 atoms cm^{-2}). This is an important point because, when measuring the neutral gas from quasar absorbers, the high column density systems play a major role.

Figure 8 (bottom panel) shows the distribution of absorbers with column density. We do not observe systems with column density log N(HI) $\gtrsim 21.6$ atoms cm^{-2}, but it could be argued that at very high column density (i.e. log N (H I) $\gtrsim 23$ atoms cm^{-2}), the absorbers might prevent us finding the background quasar in the first place, because the damping wings would completely eat up the Ly-α emission line and flux redward of it, thus complicating the selection of the quasar via traditional colour-colour techniques. Indeed, smooth particle hydrodynamics simulations by Gardner et al. (2001a) *do* produce DLA systems with column density greater than the one observed and they even correct for this potential "observational limitation" to try and reproduce the observed column density distribution and neutral gas mass evolution with redshift. One should thus always keep in mind that we might be missing a population of extremely high column density quasar absorbers if such a population exists.

5.4.2 Number Density of DLAs

Figure 9 shows the number density of DLAs (top panel) and of sytems with log $N(HI) > 21.0$ atoms cm^{-2} (bottom panel). The number density of DLAs evolves strongly with redshift while very few systems with log $N(HI) > 21.0$ atoms cm^{-2} are observed, especially at high redshift. The quasar absorber sample presented in this thesis is large enough to provide a reliable contraint on the evolution of the high column density systems. These can be directly compared with results from hydrodynamical simulations,

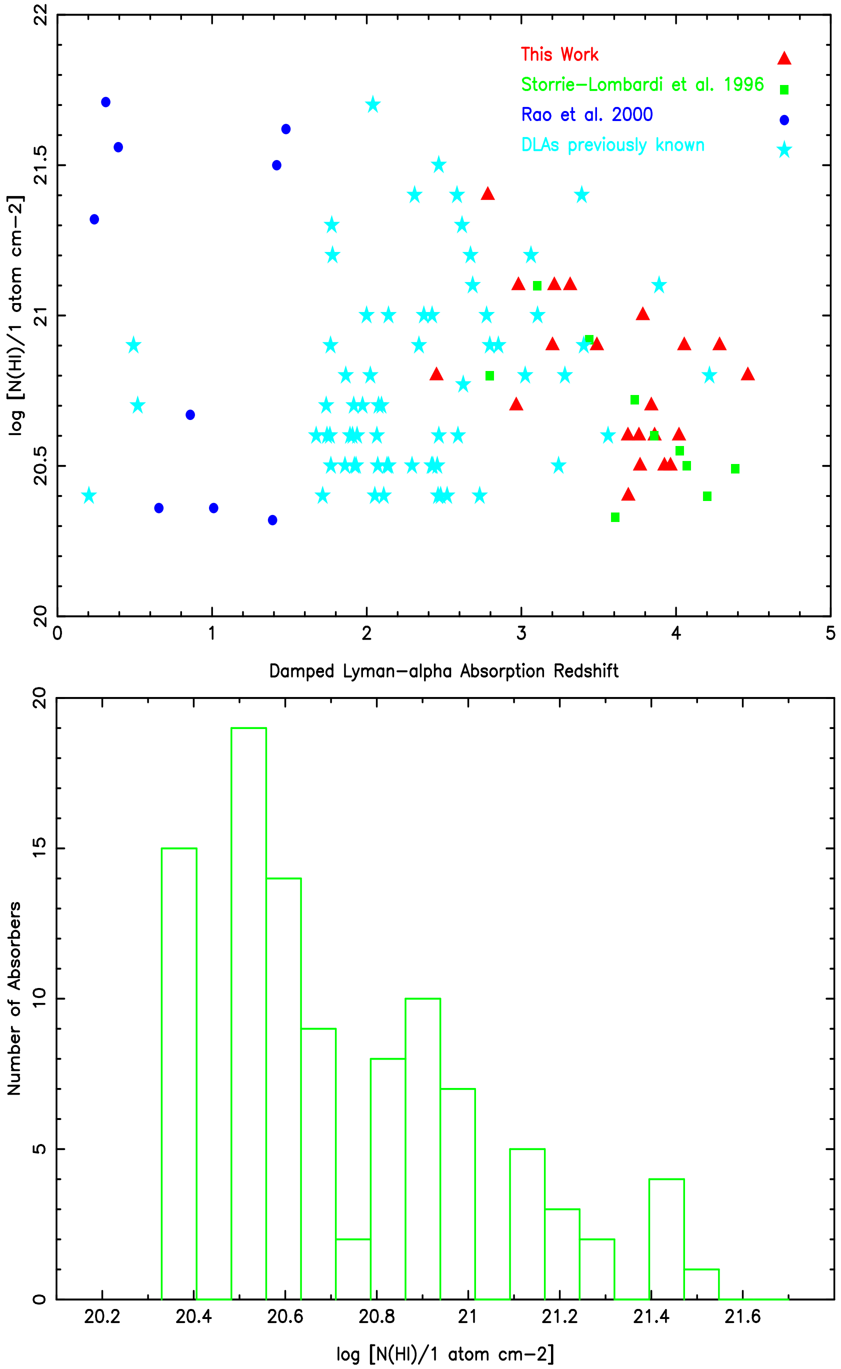

Fig. 8.— The top panel shows the column density distribution with redshift. The bottom panel shows the number of DLAs of a given column density N(HI).

although these are limited by their resolution. Gardner et al. (2001a) used the approach discussed in §4.3.2 to reproduce the observed number density of DLAs. Their results fall slightly below the observed values whatever the cosmological models used.

An alternative approach to reproduce the data has been proposed by Boissier & et al. (2001), who used a "backward" approach to the chemical evolution of disc galaxies, i.e. calibrate the models in the Milky Way and in local galaxies (Boissier et al., 2001) and compare the evolution they predict to the one observed in DLAs. In these models, a large variety of disc galaxies are included because a large range of rotational velocities are considered (80 to 360 km s^{-1}), as well as a large range of spin parameters, producing galaxies with various values of surface brightness (including a population of Low Surface brightness -LBS- galaxies).

The number density of DLA systems taken at face value suggests that present day disc galaxy precursors are a major component of DLAs up to redshift ~ 2. At higher redshifts, however, another component must be dominant (and increase with redshift). Various uncertainties might affect these resuts: if the galactic density is corrected by a factor 2, then all the DLAs up to redshift ~ 3 could be the present-day disc galaxy precursors. On the other hand, if the galactic density is corrected by a factor 1/2, then, even in the redshift range 0–2, disc galaxies would be responsible for only half of the DLAs and will be a minor component at higher redshift. At low redshifts one should note the importance of LSB galaxies. In the models, these come from the tail of the distribution of spin parameters, but observationally, there is still considerable debate over their actual number. Future work on these galaxies may be of great importance for the understanding of the nature of DLAs.

5.5 Summary

In this Chapter, we have used a new sample of high-redshift DLA systems issued from our quasar survey (see Chapter 2) to analyse the statistical properties of these absorbers. First, we briefly summarised the previous surveys with a particular emphasize to the sensitivity function $g(z)$ which characterises each samples. The redshift path probed for each individual quasar is computed and we show that we have more than double the redshift path surveyed at $z \gtrsim 3.5$. We then detailed the different techniques used to select the DLAs and discussed the possible sources of biases and the robustness of each method. Building on previous experience and several independent checks, we demonstrated that even in medium resolution spectra the DLAs can be reliably picked up. We listed all the systems we found down to a column density of log N(HI) = 19.0 atoms cm^{-2}, although absorbers below the traditional damped definition (log N (H I) < 20.3 atoms cm^{-2}) do not necessary make up a complete sample at this resolution. In addition, we have listed all the metal lines associated with the DLA and other metal systems detected redward of the Ly-α emission line. Possible interpretation are also provided. This resulted in the detection of 80 new CIV systems ($3.0 \lesssim z \lesssim 4.5$) and 48 new Mg II systems ($1.3 \lesssim z \lesssim 2.2$). We studied the several properties of the DLAs

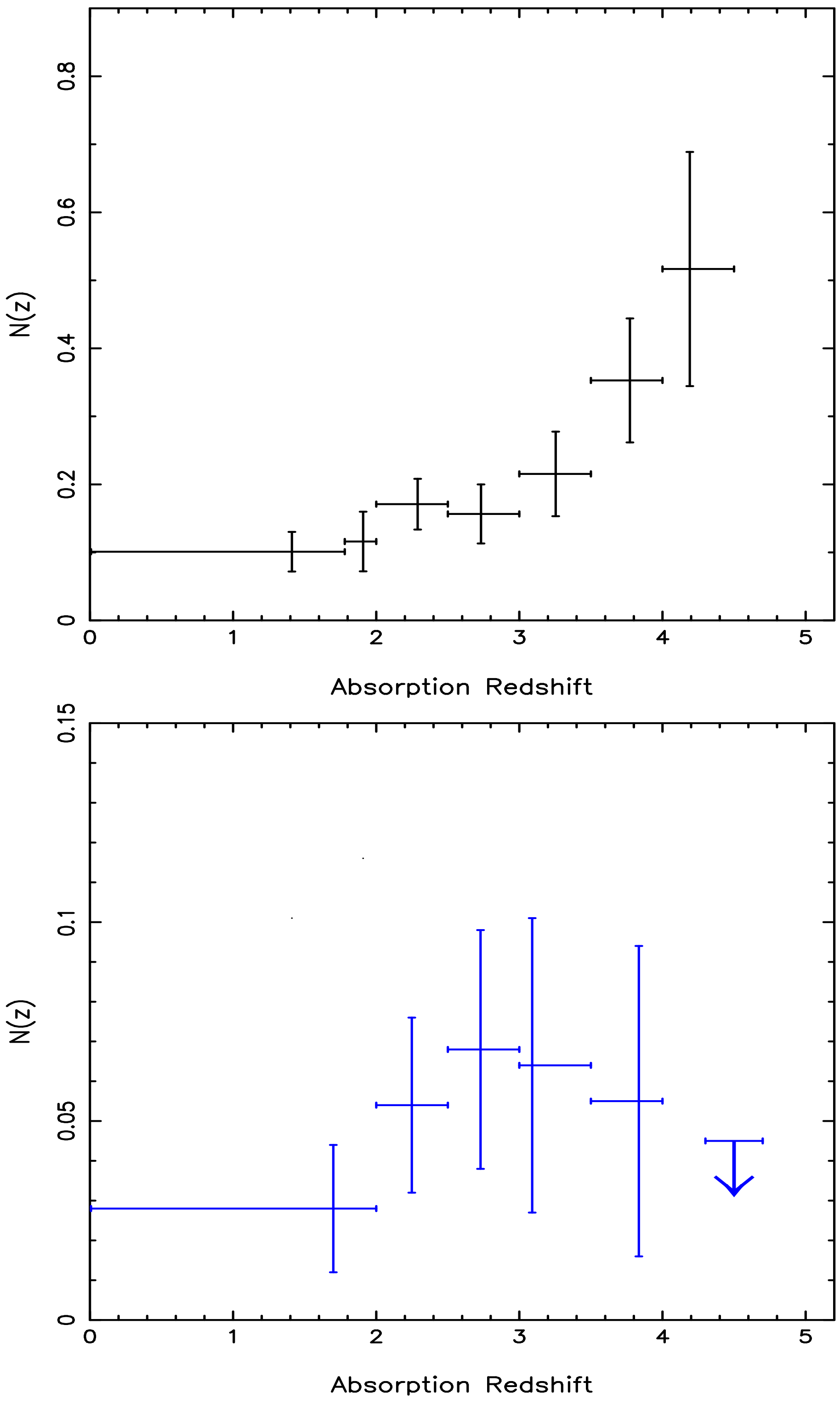

Fig. 9.— Number density of DLAs. The top panel shows the $n(z)$, the number of quasar absorbers per unit redshift for the DLAs from our new survey and data from the literature. The bottom panel only includes systems with N(HI) $\geq 10^{21.0}$ atoms cm^{-2}. No absorbers with $\log N(HI) > 21.0\ cm^{-2}$ are observed at $z > 4$ and the arrow indicates the 50% confidence upper limit.

presently known (number per column density range, column density at a given redshift) and compare results from various surveys. This analysis unreveals possible biases in the DLA samples at low-redshift ($z < 2$). Finally, we computed the number of quasar absorbers per unit redshift, $n(z)$, and presented different theoretical approaches to try and reproduce our observational results (namely smooth particle simulations and the "backward" model of the chemical evolution of disc galaxies).

Chapter 6

Quasar Absorbers: a Study of the History of the Universe

> *'Ce n'est pas assez de posséder le soleil, si nous ne sommes pas capables de le donner'*
> *Paul Claudel*

In this Chapter, I use the LLS and DLA samples presented in Chapter 4 and 5 together with data from the literature to derive the column density distribution of quasar absorbers (Section 6.1). Section 6.1.1 presents basic derivations of the distance interval for a non-zero Λ-Universe. I summarise previous works in Section 6.1.2. The results are discussed in Section 6.1.3 where a Γ-distribution fit is introduced and the evolution with redshift of $f(N,z)$ is presented. Section 6.1.4 compares the observational results with various types of models.

Section 6.2 presents mesurements of Ω_{DLA} from quasar absorbers. After summarising previous work (Section 6.2.2), I define a new class of absorber, the sub-DLAs, and discuss in details the cosmological evolution of Ω_{DLA} at all redshifts and the various biases which might affect these measurements. Once more, I compare our observational results with current models of structure formation (Section 6.2.4).

Section 6.3 puts these findings in the larger picture of galaxy formation and Section 6.4 presents a summary of the results.

6.1 Column Density Distribution

6.1.1 Introduction

The column density distribution describes the evolution of quasar absorbers as a function of column density. It is defined as:

$$f(N,z)dNdX = \frac{n}{\Delta N \sum_{i=1}^{m} \Delta X_i} dNdX \tag{6.1}$$

where n is the number of quasar absorbers observed in a column density bin $[N, N+\Delta N]$ obtained from the observation of m quasar spectra with total absorption distance coverage $\sum_{i=1}^{m} \Delta X_i$.

The distance interval, dX, is used to correct to co-moving coordinates and thus depends on the geometry of the Universe. Following the cosmological model currently favoured, we derive $X(z)$ for a non-zero Λ-Universe. Following Bahcall & Peebles (1969), we introduce the variable:

$$X(z) = \int_0^z (1+z)^2 \left[\frac{H_0}{H(z)}\right] dz \tag{6.2}$$

where

$$H(z) = \left(\frac{8}{3}\Pi G\rho(1+z)^2(z+\frac{1}{2q_0}) - \frac{\Lambda}{3}\left[\frac{(1+z)^2}{q_0} + z^2 + 2z\right]\right)^{1/2} \tag{6.3}$$

For convenience, we will define:

$$A = \frac{8}{3}\Pi G\rho \tag{6.4}$$

and remind the reader that:

$$\Omega_M = \frac{A}{H_o^2}; \qquad \Omega_\Lambda = \frac{\Lambda}{3H_o^2}; \qquad \Omega_k = 1 - \Omega_M - \Omega_\Lambda \tag{6.5}$$

In addition,

$$q_0 = \frac{1}{2}\Omega_M - \Omega_\Lambda \tag{6.6}$$

or

$$q_0 = \frac{1}{2}\frac{A}{H_o^2} - \frac{\Lambda}{3H_o^2} = \frac{1}{2H_o^2}(A - \frac{2\Lambda}{3}) \tag{6.7}$$

and thus

$$H(z) = \left[A(1+z)^2\left(z + \frac{H_o^2}{A-\frac{2\Lambda}{3}}\right) - \frac{\Lambda}{3}\left(\frac{(1+z)^2 2H_o^2}{A-\frac{2\Lambda}{3}} + z^2 + 2z\right)\right]^{1/2} \tag{6.8}$$

$$H(z) = \left[Az(1+z)^2 - \frac{\Lambda}{3}\left(z+(z+2)\right) + \frac{A(1+z)^2H_o^2}{A-\frac{2\Lambda}{3}} - \frac{\Lambda}{3}\frac{(1+z)^2H_o^2}{A-\frac{2\Lambda}{3}}\right]^{1/2} \tag{6.9}$$

$$H(z) = \left[Az(1+z)^2 - \frac{\Lambda}{3}\left(z+(z+2)\right) + H_o^2(1+z)^2\right]^{1/2} \tag{6.10}$$

$$H(z) = H_0\left[\Omega_M z(1+z)^2 - \Omega_\Lambda(z(z+2)) + (1+z)^2\right]^{1/2} \tag{6.11}$$

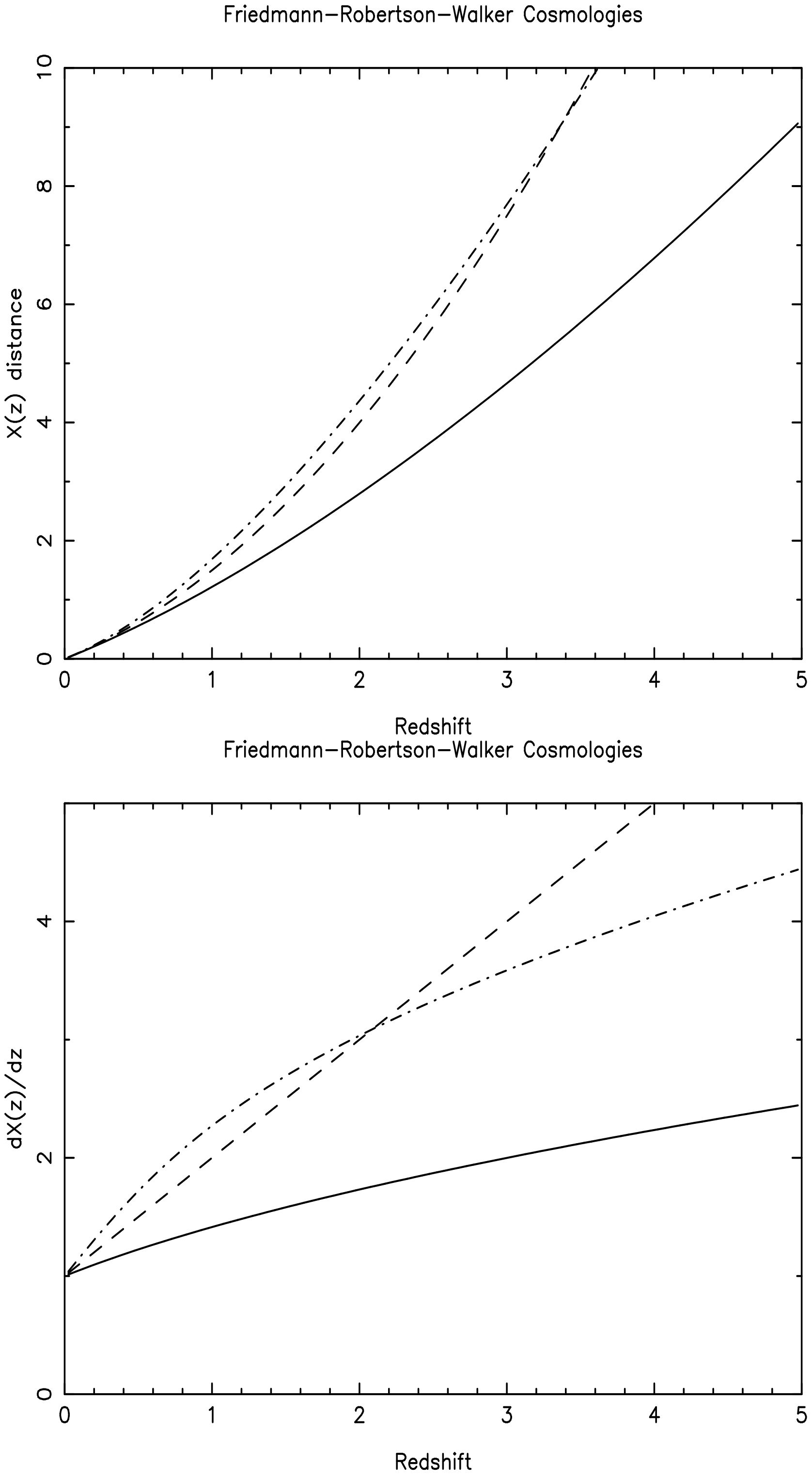

Fig. 1.— The top panel displays the distance interval, $X(z)$, and the bottom panel shows $dX(z)/dz$ as a function of redshift (see Equation 6.1.1). $\Omega_M = 1.0$ & $\Omega_\Lambda = 0.0$ (solid line), $\Omega_M = 0.0$ & $\Omega_\Lambda = 0.0$ (dashed line) and $\Omega_M = 0.3$ & $\Omega_\Lambda = 0.7$ (dashed-dotted line). These plots illustrate the similarity between $\Omega_M = 0.0$ & $\Omega_\Lambda = 0.0$ and $\Omega_M = 0.3$ & $\Omega_\Lambda = 0.7$ models.

$$H(z) = H_0\left[(1+z)^2(1+z\Omega_M) - z(2+z)\Omega_\Lambda\right]^{1/2} \tag{6.12}$$

Including this result in equation 6.2 leads to:

$$X(z) = \int_0^z (1+z)^2\left[(1+z)^2(1+z\Omega_M) - z(2+z)\Omega_\Lambda\right]^{-1/2} dz \tag{6.13}$$

This result can be used to recover the specific cases commonly used previously: if $\Lambda = 0$ and $q_0 = 0$:

$$X(z) = \int_0^z (1+z)^2(1+z)^{-1}dz = \int_0^z (1+z)dz = \frac{1}{2}\left[(1+z)^2 - 1\right] \tag{6.14}$$

and

$$\frac{dX(z)}{dz} = (1+z) \tag{6.15}$$

if $\Lambda = 0$ and $q_0 = 0.5$:

$$X(z) = \int_0^z (1+z)^2(1+z)^{-3/2}dz = \int_0^z (1+z)^{1/2}dz = \frac{2}{3}\left[(1+z)^{3/2} - 1\right] \tag{6.16}$$

and

$$\frac{dX(z)}{dz} = (1+z)^{1/2} \tag{6.17}$$

Figure 1 shows the evolution of $X(z)$ (top panel) and $dX(z)/dz$ (bottom panel) as a function of redshift for various cosmological models. These plots illustrate the similarity between $\Omega_M = 0.0$ & $\Omega_\Lambda = 0.0$ and $\Omega_M = 0.3$ & $\Omega_\Lambda = 0.7$ models.

6.1.2 Previous Work

The number of Lyα lines per unit column density decreases with increasing N(HI), with the smallest forest lines being far more numerous than the rare DLA systems. The column density distribution was first fitted by a power law over a large column density range N (H I) $10^{12} - 10^{21}$ atoms cm^{-2} (i.e. Carswell et al., 1984):

$$f(N) \propto N^{-\beta} \tag{6.18}$$

with $\beta \sim 1.5$ over the whole range of column densities. This was interpreted as the fact that all classes of absorbers arise from the same cloud population (Tytler, 1987). Assuming randomly distributed lines of sight through spherical isothermal halos, $f(N, z)$ was shown to be expected to have a power law of slope $\beta = 5/3$ (Rees, 1988)

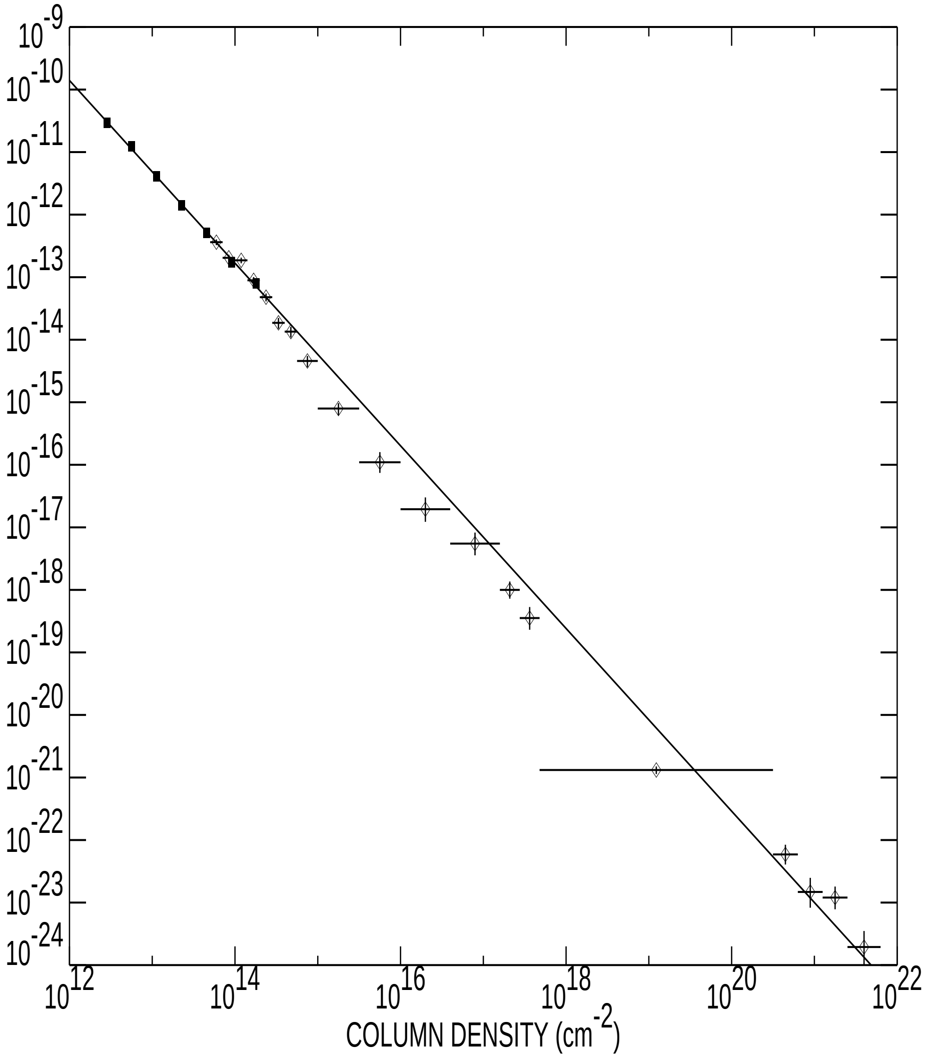

Fig. 2.— The column density distribution of quasar absorbers, $f(N, z)$, measured over 10 orders of magnitude at $< z > \sim 2.8$ and for a $\Omega_M = 0.0$ and $\Omega_\Lambda = 0.0$ cosmological model. The data are taken from Hu et al. (1995) and Petitjean et al. (1993) and are shown with a power law $\beta = 1.5$ ($f(N) \propto N^{-\beta}$). There is a deficit of lines at N(HI) $\sim 10^{15}$ atoms cm^{-2} and the data available at the time poorly constrained the column density distribution in the range N(HI) $10^{17.2} - 10^{20.3}$. The new sample of absorbers presented in this thesis is used together with data from the literature to determine $f(N, z)$ at high-column density (log N(HI) $\geq$ 17.2 atoms cm^{-2}) and study its evolution with redshift (Petitjean, 1998).

which agreed with the observational data within the errors. Nevertheless, as the quality of the data increased, deviations from a power law have been observed (Carswell et al., 1987; Petitjean et al., 1993). In particular Petitjean et al. (1993) observed a change in slope in the range N(HI) $10^{15} - 10^{17}$ and the data available at the time poorly constrain the column density distribution in the range N(HI) $10^{17.2} - 10^{20.3}$ (Figure 2). In this Chapter, we present for the first time a detailed study of the column density distribution in the range N(HI) $10^{17.2} - 10^{21.0}$. In addition, making use of the high-redshift data acquired as part of our survey, we make a detailed study of the evolution with redshift of the column density distribution of quasar absorbers.

6.1.3 Results

Cumulative Number of Absorbers

The cumulative number of absorbers per unit distance interval for two redshift ranges is presented in Figure 3 (top panel). The data with N(HI) $\geq 2 \times 10^{20}$ atoms cm^{-2} are DLAs taken from our high-redshift survey (our observations more than double the redshift path surveyed at $z \gtrsim 3.5$ – see Chapter 5) and from the literature. A summary of all quasars taken into account in this analysis is available in Appendix C & D (for quasars with DLA systems and without, respectively). The data from the literature are taken from Storrie-Lombardi & Wolfe (2000) with the following added modifications: Q 1329+4117 has no DLA at $z_{abs} = 0.5193$ (Jannuzi et al., 1998), Q 2112+059 has no DLA at $z_{abs} = 0.2039$ (Jannuzi et al., 1998; Fynbo et al., 2001) and Q 0302−223 has a DLA at $z_{abs} = 0.1014$ (Jannuzi et al., 1998).

The power law fit to the observed number of LLS per unit redshift:

$$f(N,z) \propto N^{-\beta}(1+z)^{\gamma} \tag{6.19}$$

is used to calculate the *expected number* of LLS systems (see Chapter 4):

$$LLS_{expected} = \sum_{i=1}^{n} \int_{z_{min}}^{z_{max}} N_o(1+z)^{\gamma} dz \tag{6.20}$$

where z_{min} and z_{max} is the redshift path along which quasar absorbers were searched for. The LLS line profiles cannot be used to directly measure their column densities because in the range 1.6×10^{17} to 2×10^{19} atoms cm^{-2} the curve of growth is degenerate. Nevertheless, the number of LLS provides a further constraint on the cumulative number of quasar absorbers and clear evidence that a simple power law does *not* represent well the observations over this column density range. For this reason, and because of the convergence of the integral used to derive the mass, we choose to fit the data with a Γ-distribution (a power law with an exponential turn-over, similar to Schechter (1976) function used in studies of the galaxy luminosity function) which was first introduced by Pei & Fall (1995) and used by Storrie-Lombardi et al. (1996a):

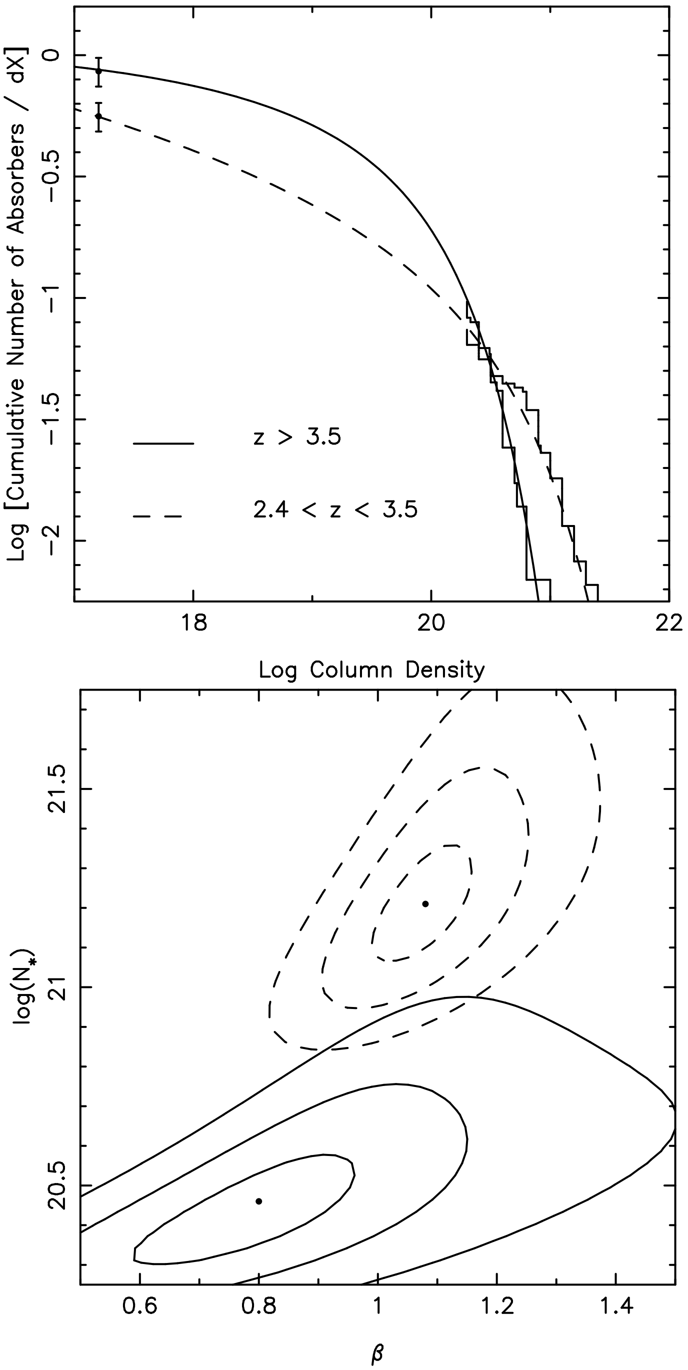

Fig. 3.— Cumulative number of absorbers per unit distance interval (top panel). The data are plotted for two different redshift ranges: $z < 3.5$ and $z > 3.5$. The data point at log $N(HI) = 17.2$ atoms cm^{-2} is the *expected number* of LLS derived from the observed number of LLS per unit redshift. The observations are fitted with a Γ-distribution of the form: $f(N,z) = (f_*/N_*)(N/N_*)^{-\beta}\exp(-N/N_*)$. The bottom panel shows the maximum likelihood estimator. 1, 2 and 3-σ confidence contours to the Γ-distribution fit of the observed number of absorbers in the redshift range $2.4 < z < 3.5$ (dashed line) and $z > 3.5$ (solid line).

$$f(N,z) = (f_*/N_*)(N/N_*)^{-\beta} e^{-N/N_*} \tag{6.21}$$

where N is the column density, N_* a characteristic column density and f_* a normalising constant. This functional form is identical to the Schechter luminosity function (Schechter, 1976). For $N << N_*$, the Γ-distribution tends to the same form as the single power law $f(N,z) \propto N^{-\beta}$, whilst for $N \gtrsim N_*$, the exponential term begins to dominate.

Table 1: Parameter fit to the column density distribution, $f(N,z)$, for absorbers with $\log N(HI) > 17.2$ atoms cm^{-2} (see equation 6.21). The number of quasar intervening in a given redshift bin, No. QSOs, the number of absorber, No. DLAs, and the distance interval, dX, are given for each redshift bin. Summing up the No. QSOs column does *not* reflect the total number of quasars used as a single object might intervene in several redshift bins. Incidently, the total number of quasars included in our study is 698 (113 DLAs).

z Range	β	f_* $\times 10^2$	log N_*	No. QSOs	No. DLAs	dX	Ω $\times 10^3$
0.0-2.0	0.74	8.70	20.76	537	22	362.8	0.64
2.0-2.7	1.08	3.25	21.27	380	34	522.3	1.04
2.7-3.5	1.10	4.06	21.18	251	28	414.9	0.98
2.4-3.5	1.08	4.29	21.21	314	46	608.2	1.13
> 3.5	0.80	25.1	20.46	112	29	290.2	0.71

A maximum likelihood analysis is used to derive the parameters in various redshift ranges (see Table 6.1.3). Using equation 6.19 for the column density distribution function, the damped Lyαabsorbers will be found randomly distributed according to this function along the quasar line-of-sight in $N - z$ space. If the space is divided into m cells each of volume δv, the expected number of points in cell i is given by

$$\phi_i = f(N,z)_i \delta v. \tag{6.22}$$

The probability of observing x_i points in cell i is

$$p(x_i) = e^{-\phi_i} \frac{\phi_i^{x_i}}{x_i!}. \tag{6.23}$$

The likelihood function for quasar j taking the product over all the cells is then

$$L_j = \prod_{i=1}^{m} p(x_i) = \prod_{i=1}^{m} e^{-\phi_i} \frac{\phi_i^{x_i}}{x_i!}. \tag{6.24}$$

If the volume of each cell δv becomes very small such that there is either 1 or 0 points in each cell,

$$x_i = \begin{cases} 1, & \text{if DLA detected;} \\ 0, & \text{if none detected,} \end{cases}$$

then the likelihood can be rewritten separating out the terms for full and empty cells. For $m = g$ empty cells + p full cells

$$L_j = \prod_{i=1}^{g} e^{-\phi_i} \prod_{j=1}^{p} e^{-\phi_j} \phi_j = \prod_{i=1}^{m} e^{-\phi_i} \prod_{j=1}^{p} \phi_j \tag{6.25}$$

Taking the log of the likelihood function gives

$$\begin{aligned} \log L_j &= \sum_{i=1}^{m} -\phi_i + \sum_{j=1}^{p} \ln \phi_j \\ &= \sum_{i=1}^{m} -f(N,z)_i \delta v + \sum_{j=1}^{p} \ln f(N,z)_j + p \ln \delta v \end{aligned} \tag{6.26}$$

(e.g. Schechter & Press, 1976). Ignoring the constant term, in the limit where $\delta v \to 0$ this becomes

$$\begin{aligned} \log L_j &= -\int_{z_{min}}^{z_{max}} \int_{N_{min}}^{N_{max}} f(N,z) dN dz + \sum_{j=1}^{p} \ln f(N,z)_j \\ &= -\int_{z_{min}}^{z_{max}} \int_{N_{min}}^{N_{max}} kN^{-\beta}(1+z)^{\gamma} dN dz + \sum_{j=1}^{p} \ln[kN^{-\beta}(1+z)^{\gamma}] \end{aligned} \tag{6.27}$$

To get the overall log likelihood for n quasars we evaluate the integrals in equation 6.27 and additively combine the log L's which for a power law simplifies to

$$\begin{aligned} \log L &= \sum_{i=1}^{n} \Big[\frac{kN_{min}^{1-\beta}}{(1-\beta)(1+\gamma)} \Big((1+z_{em}^{i})^{1+\gamma} - (1+z_{min}^{i})^{1+\gamma} \Big) + p \ln k \\ &+ \sum_{j=1}^{p_i} \Big(-\beta \ln N_j + \gamma \ln(1+z_{dla}^{j}) \Big) \Big] \end{aligned} \tag{6.28}$$

where p_i is the number of detected DLAs in quasar i and N_{min} is the minimum column density.

We note that the likelihood solution can be found over a two-dimensional grid of pairs of values of N_* and β, since the constant f_* can be directly computed using the integral constraint whatever the functional form of $f(N,z)$

$$m = \sum_{i=1}^{n} f_* \int_{N_{min}}^{N_{max}} \int_{z_{min}^{i}}^{z_{max}^{i}} f(N,z) dz dN \tag{6.29}$$

where m is the total number of observed systems. This is computationally much less intensive than doing a 3-D grid search. The 1, 2 and 3-σ confidence contours for a functional form $f(N,z) = f(N)$ only are shown in Figure 3 (bottom panel) for $z < 3.5$ and $z > 3.5$. The distributions are clearly different at the $\sim 3\sigma$ level and indicate that there are less high column density systems (N(HI) $> 10^{21}$ atoms cm^{-2}) at high-redshift, $z > 3.5$, compared with $2 < z < 3.5$ confirming the results from Storrie-Lombardi et al. (1996b) and Storrie-Lombardi & Wolfe (2000).

Column Density Distribution

Figure 4 shows the differential column density distribution of quasar absorbers for various redshift ranges. The points in the LLS range (N(HI) $= 1.6 \times 10^{17}$ to 2×10^{20} atoms cm^{-2}) are computed from the cumulative number of absorbers (top panel of Figure 3), assuming the Γ-distribution fit for the distribution of absorbers, in the range where column densities cannot be directly measured (see Chapter 4). The redshift evolution indicates that there are less high column density systems at high-redshift, and more at low redshift.

Figure 5 shows $f(N,z)$ over a large column density range at $z > 3.5$ (the data of the Lyman-α forest are from the CTIO 4m and Keck-HIRES spectra of BR 1033−0327 and Q0000−26, Williger et al. (1994) and Lu et al. (1996), respectively). The two $< z > \simeq 2.8$ power law fits (β=1.83 for log N(HI) $\lesssim$ 16 and β=1.32 for log N(HI) $\gtrsim$ 16) from Petitjean et al. (1993) corrected for the absorber number density evolution with redshift and for $\Omega_\Lambda = 0.7$, $\Omega_M = 0.3$ cosmology are overplotted. Their work had already shown that $f(N,z)$ cannot be well fitted by one (or two) power law(s).

6.1.4 Comparison with Models

Smooth Particle Hydrodynamics

In recent years, hydrodynamic simulations have been extremely sucessful in reproducing the observational properties of the Lyman-α forest (i.e. Petitjean et al., 1995). Using similar techniques to analyse both the data and the simulations, the column density distribution derived from models is in good agreement with observations (i.e. Theuns et al., 1998). But simulating high column density systems such as DLAs is still extremely challenging because of resolution limitations. However, Gardner et al. (1997) tried to overcome the problem by imposing the density profile of resolved halos onto unresolved ones. They predict the evolution with redshift of the column density distribution of absorbers (Figure 6). It is of interest to note that they predict a flattening of the distribution somewhere in the region log N (HI) 18.5 – 20.0 atoms cm^{-2}, which they attribute to the onset of self-shielding. More importantly, the theory predicts little change in the form of the column density distribution function over the redshift range 2 – 4. This seems counter to current observations since we have measured (Chapter 4) a strong evolution of the number density of LLS with redshift, implying a factor of 3 or more difference in the number of LLS between redshift 2 and redshift 4.

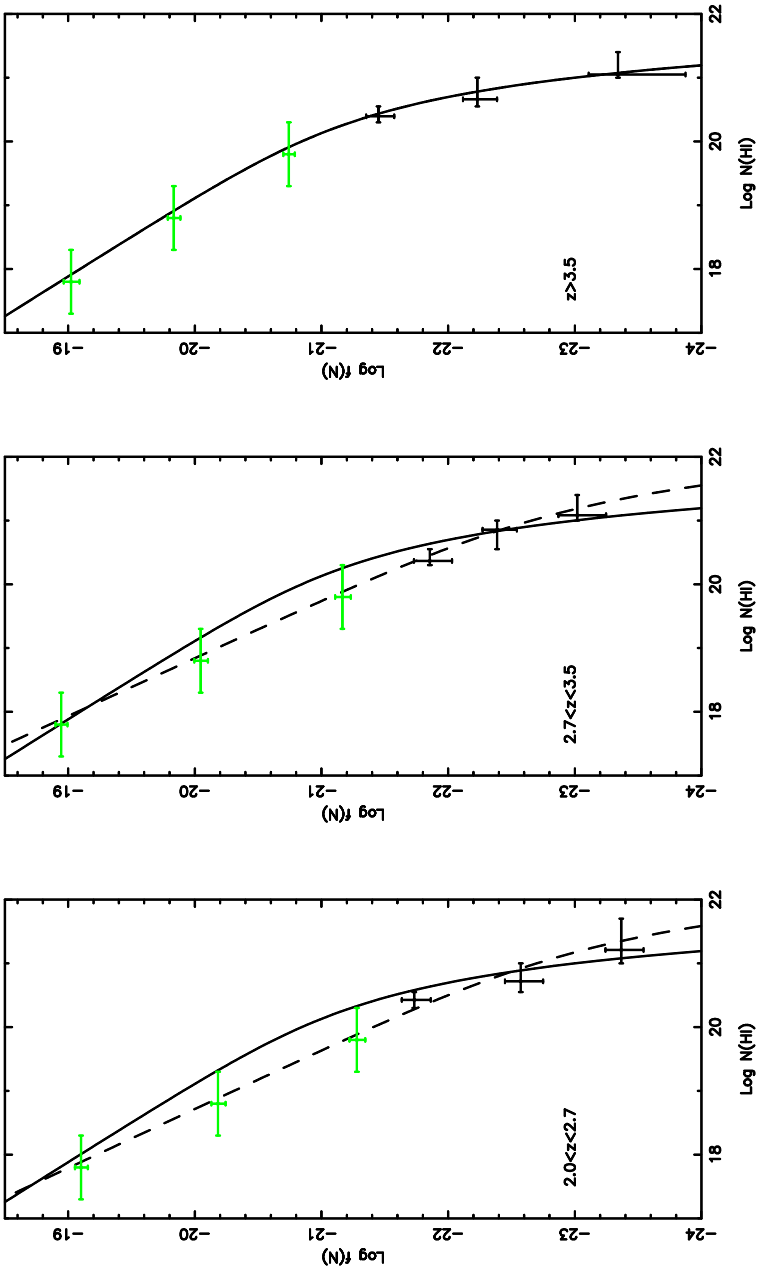

Fig. 4.— Column density distribution of quasar absorbers for various redshift ranges. $f(N,z)$ is the number of absorbers per column density range and per distance interval: $f(N,z) = n/(\Delta N \Delta X)$, where n is the number of absorbers. The redshift ranges are chosen to match the bins in the Ω_{DLA} plot (see Figure 10). The light grey bins (in the range $17.2 < \log N(HI) < 20.3$ atoms cm^{-2}) are deduced from the fit to the observed cumulative number of quasar absorbers. The solid line is the Γ-distribution fit for $z > 3.5$ and the dashed lines are the fits to the unbinned data in the relevant redshift range. [$\Omega_\Lambda = 0.7$, $\Omega_M = 0.3$ cosmology].

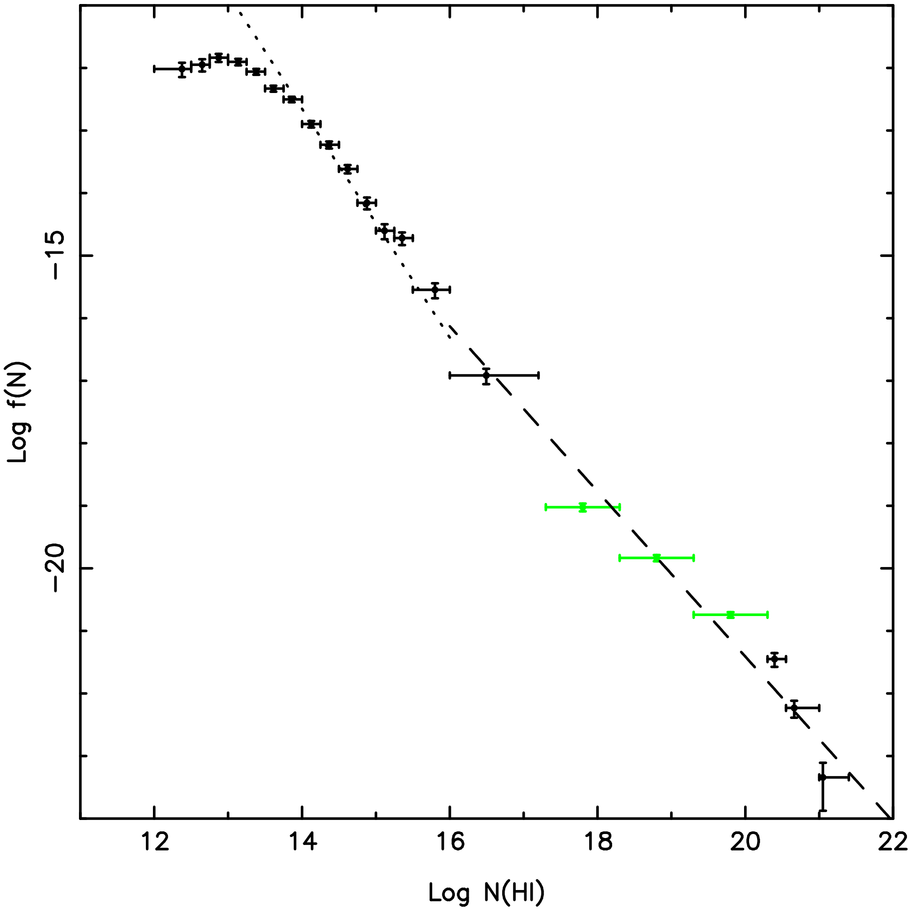

Fig. 5.— Differential column density distribution for $z > 3.5$. The low column density data are Keck-HIRES observations of the Lyman-α forest. The light grey bins (in the range $17.2 < \log N(HI) < 20.3$ atoms cm^{-2}) are deduced from the fit to the observed cumulative number of quasar absorbers. The turn-over at the low column density end is incompleteness due to a combination of spectral resolution and signal-to-noise. The dashed and dotted lines are the two $< z > \simeq 2.8$ power law fits (β=1.83 for log N(HI) $\lesssim$ 16 and β=1.32 for log N(HI) $\gtrsim$ 16) from Petitjean et al. (1993) corrected for the absorber number density evolution with redshift and for $\Omega_\Lambda = 0.7$, $\Omega_M = 0.3$ cosmology.

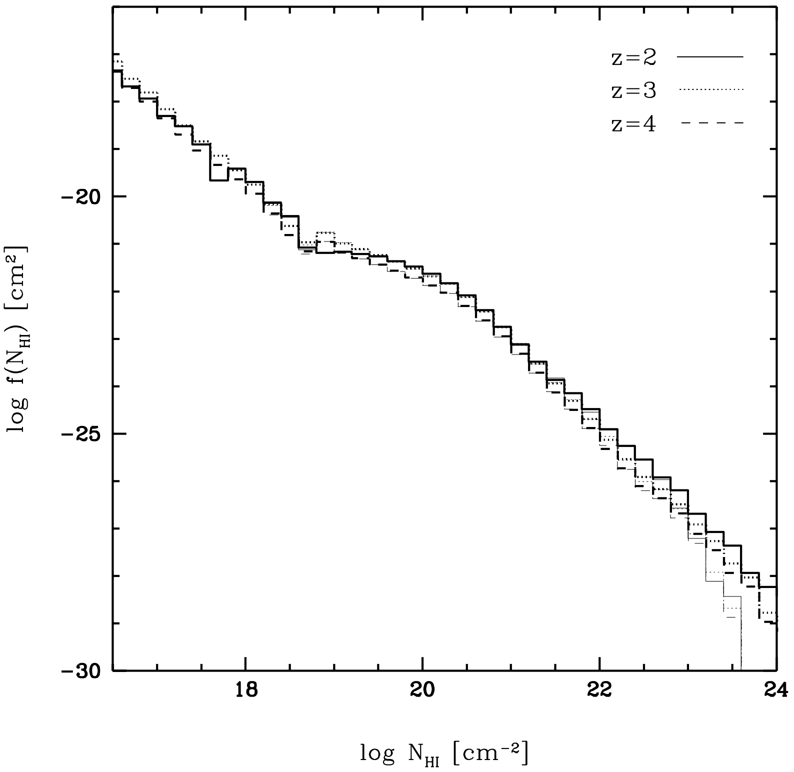

Fig. 6.— SPH simulations of the column density of absorbers for simulations with and without star formation. Histograms show the simulation results at $z = 2$ (solid), $z = 3$ (dotted), and $z = 4$ (dashed). Heavier lines represent the simulation without star formation and lighter lines the simulation with star formation (Gardner et al., 1997). The theory predicts little change in the form of the column density distribution function over the redshift range $2 - 4$, in contrast with current observations.

Semi-Analytical Models

Semi-Analytical Models provide a complementary approach to SPH simulations. They are not limited by the self-shielding problem and, by construction, they are in good agrement with many observed properties of galaxies. Kauffmann & Charlot (1994) used semi-analytical models of galaxy formation developed by Kauffmann et al. (1993) to reproduce the column density distribution of quasar absorbers and its evolution with redshift. They assume an exponential disc model in which the gas cooling in a halo collapses to form a planar disc and see a decrease of the number of high column density systems with decreasing redshift. Similarly, Maller et al. (2001) used semi-analytical models developed by the Santa Cruz group (Somerville et al., 2001), to reproduce the observed column density distribution of quasar absorbers. Their model falls short of reproducing the observed column density distribution, but further work is currently underway to try and reproduce the data presented in this thesis.

6.2 Cosmological Evolution of Neutral Gas Mass

6.2.1 Introduction

One of the fundamental cosmological parameters is the ratio of the baryonic density to the critical density of the Universe, Ω_b. On the one hand, this parameter is constrained by primordial nucleosynthesis theory and on the other hand it is bounded by observations which sum up the contribution of detected baryonic matter. The matter in stars today has been estimated by several authors (i.e. Gnedin & Ostriker, 1992; Persic & Salucci, 1992; Fukugita et al., 1998; Cole et al., 2001). It is expected that at high-redshift, at least part of the gas is in the inter-galactic medium. By integrating the observed column density distribution, one can calculate the contribution of quasar absorbers to the baryonic mass in units of the current critical mass density, ρ_{crit}, as:

$$\Omega_{DLA}(z) = \frac{H_o \mu m_H}{c \rho_{crit}} \int_{N_{min}}^{\infty} N f(N, z) dN \tag{6.30}$$

where μ is the mean molecular weight of the gas which is taken to be 1.3 (75% hydrogen and 25% helium by mass), m_H is the hydrogen mass and N_{min} is the low end of the HI column density range being investigated. With the limited samples currently available the variation with redshift has been investigated by partitioning the samples into redshift ranges and deriving $f(N)$ there, since there is evidence suggesting that $f(N, z) \neq g(N)h(z)$. If the fit to the column density distribution is made with a power law with index $\beta < 2$, most of the mass is in the highest column density systems (DLAs). Indeed, the integral diverges unless an artificial upper limit to the column density distribution, N_{max} is introduced, since

$$\mathrm{Mass}(HI) = \int_{N_{min}}^{N_{max}} N f(N) dN = \left[\frac{1}{2-\beta} N^{2-\beta}\right]_{N_{min}}^{N_{max}} = \frac{N_{max}^{2-\beta} - N_{min}^{2-\beta}}{2-\beta} \tag{6.31}$$

for $\beta < 2$.

For example, assuming $N_{max} = 21.5$ (i.e. the largest DLA observed so far) and $\beta = 1.5$ leads to:

$$\Big[\mathrm{Mass}(HI)\Big]_{20.3}^{21.5} = 8.41 \times 10^{10} \tag{6.32}$$

While the mass below the DLA definition is:

$$\Big[\mathrm{Mass}(HI)\Big]_{17.2}^{20.3} = 2.75 \times 10^{10} \tag{6.33}$$

Thus, DLA absorbers with N(HI) > $10^{20.3}$ atoms cm^{-2} contain at least 75% of the neutral hydrogen (HI) mass, but this result is strongly dependent on the chosen high-column density cut-off (i.e. assuming $N_{max} = 22.0$ will lead to a mass fraction of neutral hydrogen of 85% in the DLA range). In the following section, we will discuss the Γ-law alternative to the power law fit which both represents the data better and addresses the divergence problem of the power law form for the mass integral.

In the DLA region, it is common practice to estimate the total HI by summing up directly the individual column densities:

$$\int_{N_{min}}^{\infty} N f(N,z) dN = \frac{\sum N_i(HI)}{\Delta X} \tag{6.34}$$

where ΔX is the distance interval as defined in the previous section.

The errors in Ω_{DLA} are difficult to estimate accurately without knowing $f(N,z)$. Lanzetta et al. (1991) used the standard error in the distribution of N(HI) which yields zero error if all the column densities in a bin are the same. We have estimated the fractional variance in Ω_{DLA} by comparing the observed distribution of $f(N,z)$ with the equivalent Poisson sampling process. This gives

$$\Big(\frac{\Delta\Omega_{DLA}}{\Omega_{DLA}}\Big)^2 = \sum_{i=1}^{p} N_i^2 / \Big(\sum_{i=1}^{p} N_i\Big)^2 \tag{6.35}$$

and $1/\sqrt{p}$ fractional errors if all the column densities included in a bin are equal.

6.2.2 Previous Work

The first measurement of the cosmological mass density was made in 1991 by Lanzetta et al. who used a combination of their own spectra together with data from Sargent et al. (1989). It has since been the subject of many controversies. Lanzetta et al. (1995) derived a Ω_{DLA} at $z \sim 3.5$ twice the value at $z \sim 2$, implying a larger star formation rate than indicated by metallicity studies. This created the so-called "cosmic

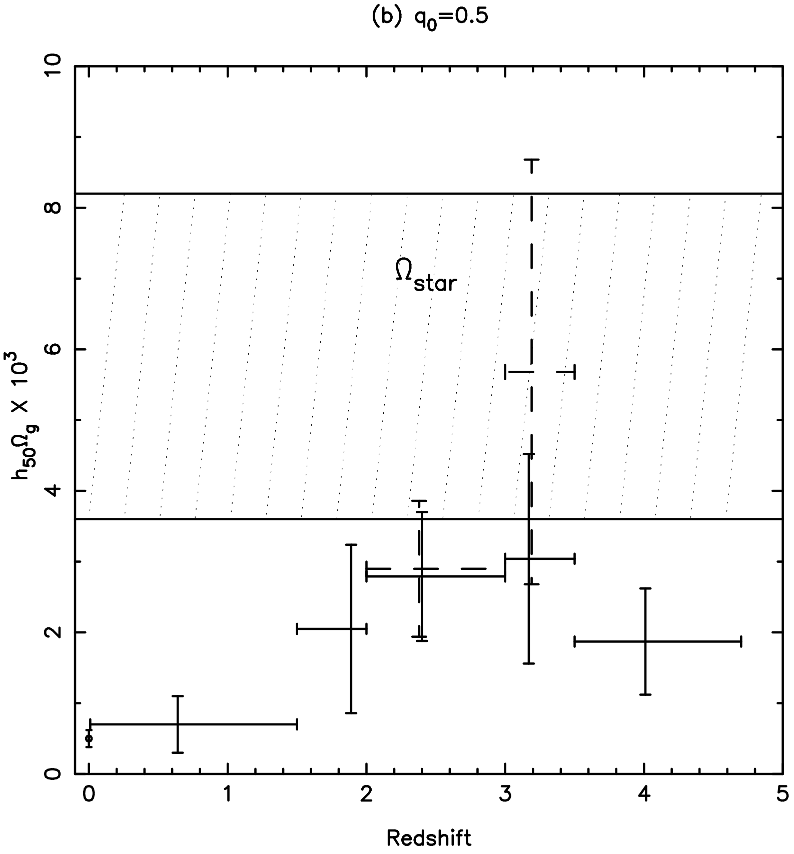

Fig. 7.— Evolution of neutral gas mass contained in quasar absorbers as a function of redshift as known in 1996 ($\Omega_M = 1.0$, $\Omega_\Lambda = 0.0$). Lanzetta et al. (1995) (dashed bins) found that Ω_{DLA} at $z \sim 3.5$ is twice the value at $z \sim 2$, implying a larger star formation rate than indicated by metallicity studies. This created the so-called "cosmic G-dwarf problem". Storrie-Lombardi et al. (1996b) used new data and improved statistical analysis to show that Ω_{DLA} appears to decrease at high-redshift (solid bins) thus solving the "cosmic G-dwarf problem". The hatched region corresponds to the mass density of stars in nearby galaxies as measured by Gnedin & Ostriker (1992). The point at $z = 0$ corresponds to the measurement inferred from the 21 cm observations of Rao & Briggs (1993).

G-dwarf problem". But Storrie-Lombardi et al. (1996b) later on showed that Lanzetta et al. (1995) error analysis lead to an underestimate of the error bars. They also used new data to derive Ω_{DLA} at high-redshift and thus solved the "cosmic G-dwarf problem" (see Figure 7). The work of Storrie-Lombardi & Wolfe (2000) confirmed such results by using a compilation of data gathered from the literature together with new spectroscopic observations. The situation of Ω_{DLA} at low-redshift ($z < 1.65$) is even more unsettled and the current situation will be reviewed in the following section.

6.2.3 Results

Introducing sub-DLAs

We have already explained that a power law fit to $f(N, z)$ is not an adequate representation of the observations since it both requires the introduction of an artificial cut-off at the high column density end because of the divergence of the integral and it also fails to describe the observed column density distribution. If instead a Γ-distribution (equation 6.21) is fitted to $f(N, z)$, this better describes the data and also removes the need to artificially truncate the high end column distribution, enabling it to be used to probe in more detail the neutral gas fraction as a function of column density and how this changes with redshift. We can thus integrate the Γ-distribution over the whole space of column densities for various redshift ranges, although we note that the Γ-distribution still does not address divergence in the numbers of systems at the faint end of the distribution.

Figure 8 shows the differential mass contribution (top panel) and the cumulative mass fraction (bottom panel), as a function of column density for $z > 3.5$ and $z < 3.5$ using the Γ-law fits from Section 6.1.3. This plot indicates that at $z \gtrsim 3.5$, up to 45% of the neutral gas is in systems with $10^{19.0} < N(HI) < 10^{20.3}$. We refer to these systems as *sub-DLAs*. As shown by the curve of growth relating the rest equivalent width of an absorber with its column density (Figure 13), any absorption system with a doppler parameter b <100 km s^{-1} and N(HI) > 10^{19} atoms cm^{-2} will exhibit damping wings. These are thus technically very similar to the traditional DLAs and can be easily picked out in quasar spectra thanks to their characteristic damping wings. Our work suggests that the traditional "low redshift" DLA definition needs to be extended at high redshift to include systems down to 10^{19} atoms cm^{-2}.

The sub-DLAs observed in our quasar survey are presented in Table 5.2.2, although this list is probably not complete due to resolution limitations. A systematic study of the kinematic and metallic properties of sub-DLA systems with z>3.5 and N(HI) above 10^{19} atoms cm^{-2} is an obvious program for the new generation of echelle spectographs on 8-m class telescopes (see Chapter 7). It will also be important to directly establish the N(HI) column density distribution function below 2×10^{20} atoms cm^{-2}. We are currently undertaking such a program using VLT UVES archival echelle data of high redshift quasars and preliminary results are presented in Chapter 7.

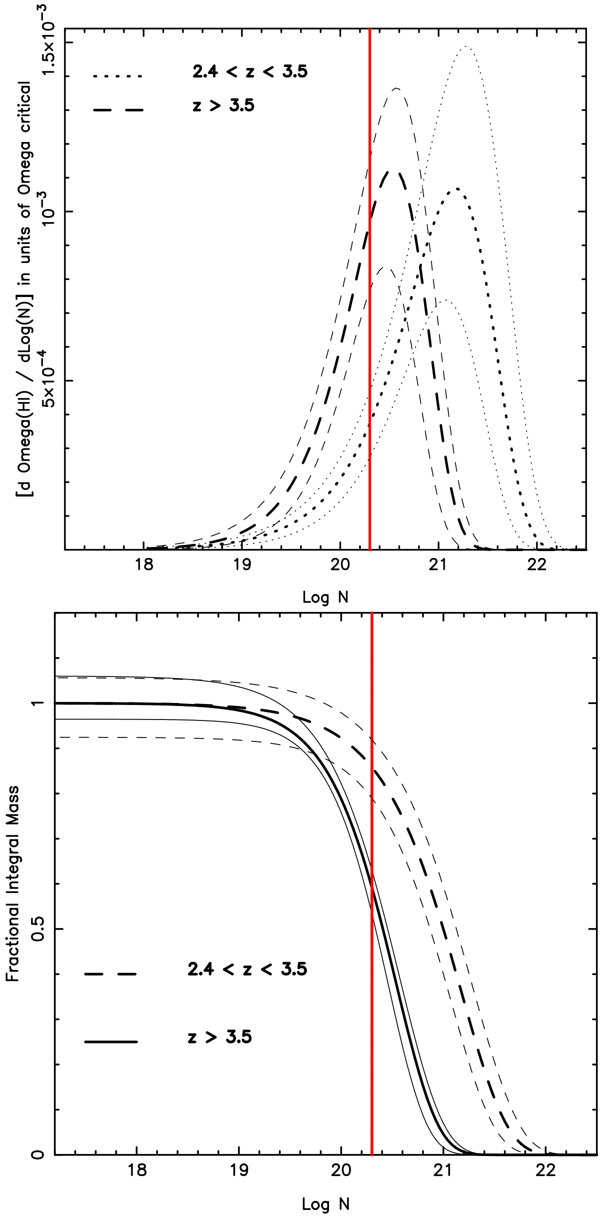

Fig. 8.— Differential mass contribution (upper panel) and integral mass function (lower panel) for two different redshift ranges ($z < 3.5$ and > 3.5). The fine lines represent the uncertainties in the model fit. The vertical solid line indicates the boundary of the DLA definition. This plot shows that at $2.4 < z < 3.5$ most of the mass is contained in DLA absorbers with $N(HI) \geq 2 \times 10^{20}$ atoms cm^{-2}, while at $z > 3.5$, $\sim 45\%$ of the mass is under this formal limit. The sub-DLAs, with $10^{19} < N(HI) < 2 \times 10^{20}$ atoms cm^{-2} contain the vast majority of the remaining mass.

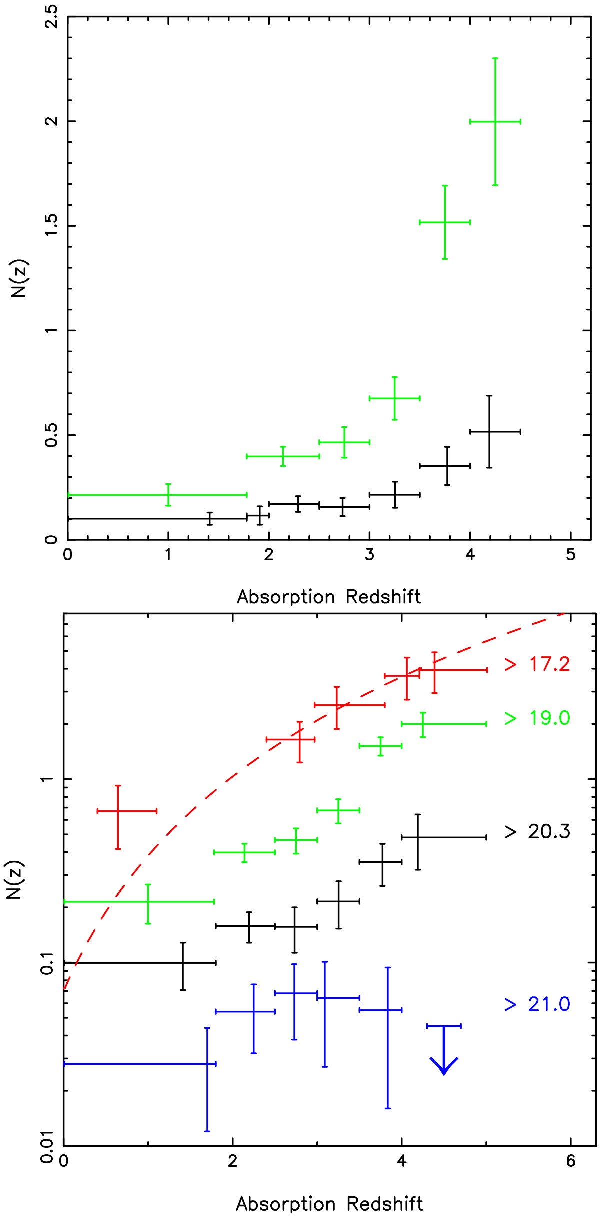

Fig. 9.— Number density of DLAs and sub-DLAs. On the top panel, the light grey bins corresponds to systems with $10^{19.0} < N(HI) < 10^{20.3}$, and the dark bins to the traditional DLAs. The $n(z)$ for sub-DLAs is *not* from direct observations but re-computed from the Γ-distribution fit to the column density distribution using the expected number of LLS as an additional datum. The bottom panel shows the number density of quasar absorbers with (from top to bottom) log $N(HI) > 17.2$, > 19.0, > 20.3 and > 21.0 atoms cm^{-2}. The dashed line is a power-law fit to the number density of LLS with $z_{abs} > 2.4$ (see Chapter 4). No absorbers with log $N(HI) > 21.0$ atoms cm^{-2} are observed at $z > 4$ and the arrow indicates the 50% confidence upper limit.

Using the expected number of LLS and the Γ-distribution fit, we can now probe the column density range of quasar absorbers in the region where the curve of growth is degenerate. Assuming that a Γ-law is a good representation of the data, we can, for the first time, re-compute the expected number of absorbers at a given column density and hence the number density in any column density range. Figure 9 (top panel) shows the $n(z)$ of DLAs and sub-DLAs. Our calculations predict that the number of sub-DLAs per unit redshift increases dramatically beyond $z = 3.5$. At $< z >\sim 2.5$, we expect about 0.3 sub-DLAs per unit redshift while at $< z >\sim 4.5$, this number is about 1.5 sub-DLAs per unit redshift. This implies that a quasar at $z > 4$ (with a typical redshift path for absorber of $\Delta z \sim 1$) will exhibit one sub-DLA or more. Figure 9 (bottom panel) shows the number density for absorbers of different column densities (log $N(HI) > 17.2$, > 19.0, > 20.3 and > 21.0 atoms cm^{-2}). All but the highest column density systems (log $N(HI) > 21.0$ atoms cm^{-2}), have their number density significantly increasing with redshift. No absorbers with log $N(HI) > 21.0$ atoms cm^{-2} are observed at $z > 4$ and the arrow indicates the 50% confidence upper limit.

Ω_{DLA} Evolution with Redshift

A) Ω_{DLA} at high redshift

Intervening absorption systems in the spectra of quasars provide a unique way to study early epochs and galaxy progenitors. In particular, they are not affected by the "redshift desert" from $1.3 \lesssim z \lesssim 2.5$, where spectral emission features in normal galaxies do not fall in optical passbands, yet where substantial galaxy formation is taking place. In addition, the absorbers are selected strictly by gas cross-section, regardless of luminosity, star formation rate, or morphology. Figure 10 displays Ω_{DLA} contained in DLAs (filled circles) and the total amount of neutral gas (DLAs plus sub-DLAs - grey stars) for a non-zero Λ-Universe ($\Omega_\Lambda = 0.7$, $\Omega_M = 0.3$ and $h = 0.65$). Vertical error bars correspond to 1-σ uncertainties and the horizontal error bars indicate bin sizes. These results are tabulated in Table 6.2.3.

The observations in the redshift range 2 to 5 show no evolution in the *total* amount of neutral gas in contrast to the earlier results of Lanzetta et al. (1995), who found that Ω_{DLA} ($z \sim 3$) was twice Ω_{DLA} ($z \sim 2$). Under simple assumptions of closed box evolution, this could be interpreted as indicating there is little gas consumption due to star formation in DLA systems in this redshift range. In addition, the fact that our observations are consistent with no evolution in the redshift range $z = 2$ to $z = 5$ and that an important fraction of neutral gas mass at $z > 3.5$ is in sub-DLAs, is strongly indicative that we are observing the assembly of high column density systems from lower column density units, and independently of the precise physical nature of damped Lyman-α systems, it shows that we are observing the epoch of their formation or initial collapse.

It can be seen in Figure 10 that Ω_{DLA} is significantly below the current estimates

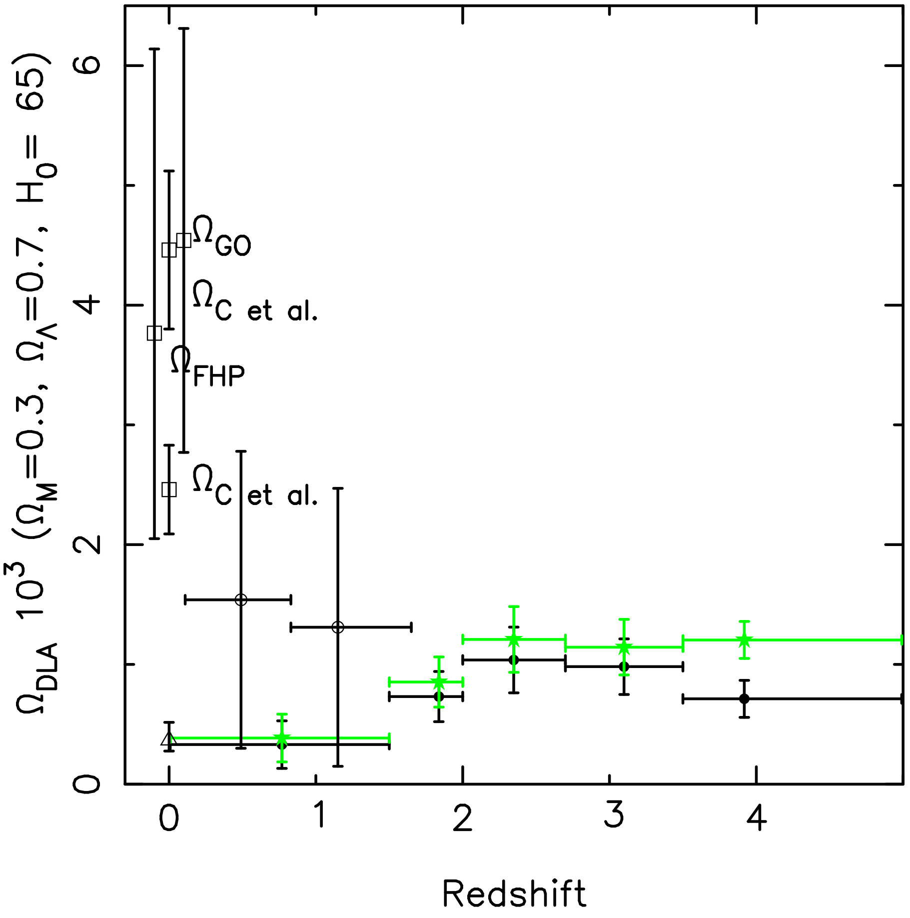

Fig. 10.— The circles show the neutral gas in damped lyman-α galaxies in a $\Omega_\Lambda = 0.7$, $\Omega_M = 0.3$ and $h = 0.65$ Universe. Vertical error bars correspond to 1-σ uncertainties and the horizontal error bars indicate bin sizes. The light grey stars are the total HI+HeII including a correction for the neutral gas not contained in DLAs. The open circles at low redshift are the measurements from Rao & Turnshek (2000), who used a method involving the observations of quasar spectra with known MgII systems. The triangle at $z = 0$ is the local HI mass measured by Natarajan & Pettini (1997) who used the most recent galaxy luminosity function to confirm results from Rao & Briggs (1993). The squares, Ω_{FHP}, Ω_{GO} and $\Omega_{Cetal.}$ (Fukugita et al., 1998; Gnedin & Ostriker, 1992; Cole et al., 2001, respectively) are $\Omega_{baryons}$ in local galaxies. The $\Omega_{Cetal.}$ error-bar plotted here does not include uncertainties in the galactic mass-to-light ratio.

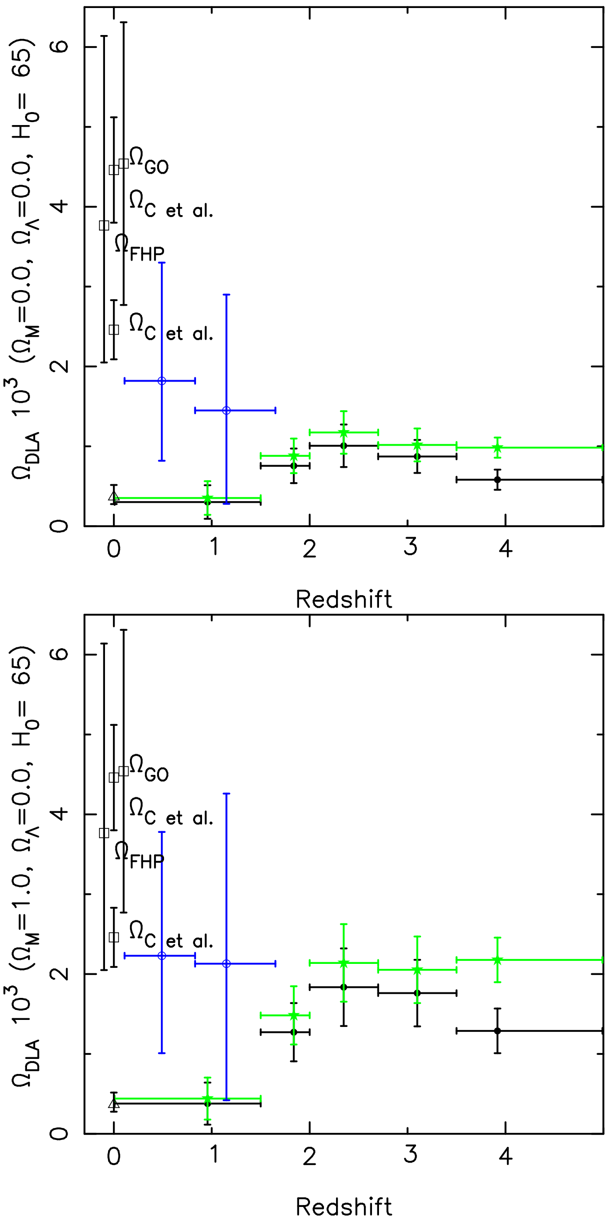

Fig. 11.— As in Figure 10 but for a $\Omega_M = 0$ (top panel) and $\Omega_M = 1$ (bottom panel) cosmology. This figure illustrates how the geometry of the Universe affects the absolute value of Ω_{DLA} with respect to the local $\Omega_{baryons}$.

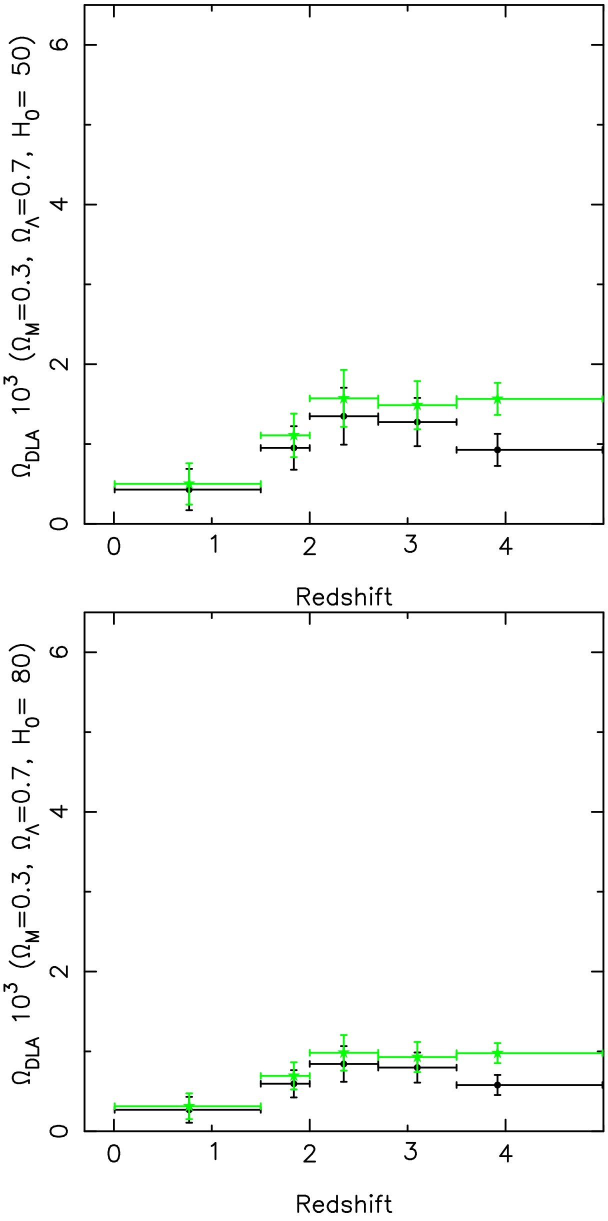

Fig. 12.— As in Figure 10 but for a $H_o = 50$ km s^{-1} Mpc^{-1} (top panel) and $H_o = 80$ km s^{-1} Mpc^{-1} (bottom panel) cosmology.

Table 2: Ω_{DLA} (top part) and $\Omega_{DLA+sub-DLA}$ (bottom part) values for a $\Omega_\Lambda = 0.7$, $\Omega_M = 0.3$ and $h = 0.65$ Universe (see Figure 10). Also available at http://www.ast.cam.ac.uk/~quasars.

z	z_{min}	z_{max}	Ω_{DLA} (10^{-3})	Ω_{min} (10^{-3})	Ω_{max} (10^{-3})
0.646175	0.008	1.5	0.391711	0.169076	0.614347
1.83780	1.5	2.0	0.731987	0.522307	0.941666
2.34807	2.0	2.7	1.03742	0.763106	1.31173
3.09909	2.7	3.5	0.981493	0.749395	1.21359
3.91833	3.5	4.99	0.713001	0.558581	0.867420
0.646175	0.008	1.5	0.456540	0.233905	0.679175
1.83780	1.5	2.0	0.853132	0.643452	1.06281
2.34807	2.0	2.7	1.20911	0.934800	1.48342
3.09909	2.7	3.5	1.14393	0.911833	1.37603
3.91833	3.5	4.99	1.20439	1.04997	1.35881

of $\Omega_{baryons}$ in stars in the nearby Universe. This is a significant change in the situation compared with previous work (see Figure 1b in Storrie-Lombardi et al., 1996b). The main reason for this change is that for the currently favoured Λ-dominated cosmology, the mass in HI at high redshift drops by a factor of ~ 50 % compared with an $\Omega_M = 1$ Universe. This is purely a geometric effect and mainly affects the relative normalisation between $z = 2$ and $z = 0$. Figure 11 displays Ω_{DLA} for different cosmologies: top panel is $\Omega_M = 0$, which leads to results very similar to those of Λ cosmological models and the bottom panel is $\Omega_M = 1$ cosmology. This illustrates how the geometry of the Universe affects the absolute value of Ω_{DLA} with respect to the local $\Omega_{baryons}$.

Similarly, the value of the Hubble constant, H_o, linearly affects Ω_{DLA} (see equation 6.2.1). The various methods used to measure H_o seem to be converging over the years (see Silk, 2001, for a recent review): the high value is now cited as 72 ± 8 km s^{-1} Mpc^{-1}, and the low value is 58.5 ± 6 km s^{-1} Mpc^{-1}. Both methods use Cepheid variable stars in nearby galaxies in conjunction with supernovae in distant galaxies. Direct determinations include the techniques of gravitational lensing of time-varying, multiply imaged quasars and the Sunyaev-Zeldovich effect in distant galaxy clusters. The latter approach favours a middle value: a recent study reports $H_o = 63 \pm 10$ km s^{-1} Mpc^{-1}. To illustrate the sensitivity toward H_o, figure 12 shows the evolution of the neutral gas mass with $H_o = 50$ km s^{-1} Mpc^{-1} (top panel) and $H_o = 80$ km s^{-1} Mpc^{-1} (bottom panel).

B) Ω_{DLA} at low redshift

Although the work presented in this thesis is concentrating on high redshift absorbers ($z > 2$), there have been recent developements at low redshift. Measurements of Ω_{DLA} at $z < 2$ are paradoxically more difficult for several reasons: the observed DLA wavelengths are shifted to the ultraviolet requiring Hubble Space Telescope observations and the geometry of the Universe combined with the paucity of DLA systems requires the observations of many quasar line of sights. Lanzetta et al. (1995) were the first to derive Ω_{DLA} at low redshift using space facilities (see the two lowest filled circles in Figure 10). Subsequent observations have shown that they were in error in identifying DLAs on two occasions, namely that the Q 1329+4117 $z_{abs} = 0.5193$ candidate absorber was not a DLA and that Q 0302−223 had an absorber at $z_{abs} = 1.010$ (Jannuzi et al., 1998; Rao & Turnshek, 2000). In addition, the absorber in Q 2112+059 was not confirmed (Fynbo et al., 2001). These modifications do not affect the derived Ω_{DLA} a lot as is shown by comparing Figure 7 and Figure 11 bottom panel. In any case, these measurements all suffer from small number statistics and future prospects for this approach are limited.

Recent work by Rao & Turnshek (2000) overcame these observational limitations by adopting an alternative technique to find low-redshift DLAs. Their method is based on observational evidence which indicates that DLAs are always associated with a MgII system (see Chapter 1), while the reverse is not true. They undertook Hubble Space Telescope observations of a sample of low-redshift quasars with known MgII systems, thus doubling the sample of MgII systems with available ultraviolet spectroscopic data. They then derived the impact on DLAs statistics by correcting for the observationally known incidence of MgII systems in a random quasar sample. Finally, they derive the mass of neutral gas as explained in the previous section using their “derived” sample of low-redshift DLAs as:

$$n_{DLA}(z = 1.15) = 0.10^{+0.10}_{-0.08} \tag{6.36}$$

and

$$n_{DLA}(z = 0.49) = 0.08^{+0.06}_{-0.04} \tag{6.37}$$

The Ω_{DLA} values they derive are presented in Figure 10 as open circles which show a surprisingly high value of Ω_{DLA} at $z \lesssim 1.65$. Their finding has been confirmed by recent work from Churchill (2001) who used 147 Hubble Space Telescope archival spectra to study Ω_{DLA} in the $0 \leq z \leq 0.15$ redshift range. He derives:

$$n_{DLA}(z \sim 0.05) = 0.08^{+0.09}_{-0.05} \tag{6.38}$$

which translates in a equivalently high value of Ω_{DLA} at $z \sim 0.05$.

These results are extremely difficult to reconcile with findings from 21 cm emission from local galaxies (Rao & Briggs, 1993; Natarajan & Pettini, 1997). One cannot explain such rapid decrease of Ω_{DLA} with the consumption of neutral gas due to star formation processes from what is currently known of the star formation rate at these redshift (see “Madau diagram” in the bottom panel of Figure 15). One possible loophole is that the gas cross-section could have increased at low redshift, i.e. due to the formation of “pancake” structures or disc-like structures as opposed to say spherical structures at higher redshift. In any case, it should be emphasized, as the authors themselves pointed out, that the analysis is based on a relatively small number of systems (Rao & Turnshek, 2000). As already noted in Chapter 5 (Figure 8 - top panel), the Rao & Turnshek (2000) sample is composed of two distinct populations of absorbers: 5 systems with high column density (log N(HI) $>$ 21.3 atoms cm^{-2}), and 4 systems with lower column density (log N(HI) $<$ 20.7 atoms cm^{-2}). If this sample is not a good representation of what DLAs at low-redshift really are, it might bias Ω_{DLA} in a significant way since it is the highest column density systems which most affect Ω_{DLA}. Another worry resides in the poorly known conversion rate from MgII systems to DLAs. Indeed, it can be argued that MgII systems point towards the highest column density quasar absorbers and that there is a need for a better understanding of the DLA/MgII conversion ratio. To summarise, the method pionered by Rao & Turnshek (2000) is promising for the measurements of Ω_{DLA} at low-redshift but might be biased in a way that we do not yet fully understand.

C) Uncertainties

Dust Bias: The study presented in this thesis is mainly based on optically selected quasars, so it is obvious that quasars that lie behind dusty DLA systems will be under-represented (if such systems exist). Pei & Fall (1995) have used self-consistent closed-box/inflow-outflow galactic chemical evolution models to show that the fraction of missing DLAs at $z = 3$ ranges from 23% to 38%. However, dust is less likely to be important at high-redshift because of the short time available for its production. Dust should have a larger effect at $z = 2$ compared with $z > 3$ and thus it is unlikely that it could cause the form of evolution in $f(N, z)$ that we observe.

As we have seen in Chapter 3, a way to address this issue is by checking whether quasars with damped Lyman-α systems in the foreground tend to appear redder than those without damped Lyman-α systems in the foreground (Fall et al., 1989). An alternative way to determine to what extent dust might be biasing DLA surveys is to look for quasar absorbers in the K-band. The near-infrared equivalent to the “UVX” method, the so-called “KX” method (Warren et al., 2000) provides a suitable way to select quasars unaffected by dust.

Another way is to use a radio-selected quasar sample. Ellison et al. (2001c) have put together a sample of flat spectrum radio sources from the Parkes Catalogue (Shaver et al., 1996) and observed in the optical all the quasar regardless of their apparent magnitude. The resulting sample is composed of 66 quasars with $z_{em} \geq 2.2$ which were subsequently searched for the DLAs they contain, the so-called CORALS (Complete Optical and Radio Absorption Line Systems). They found 19 DLAs along a redshift path of $\Delta z = 55.64$ and derive a Ω_{DLA} in good agreement with the results presented in this thesis (see the extra bin in Figure 13). This seems to indicate that the role of dust is not a major source of bias in deriving the neutral gas mass form quasar absorbers, although, once more, Ellison et al.'s results still suffer small number statistics. Interestingly, they also note that the number density of DLAs towards faint quasars (apparent B mag

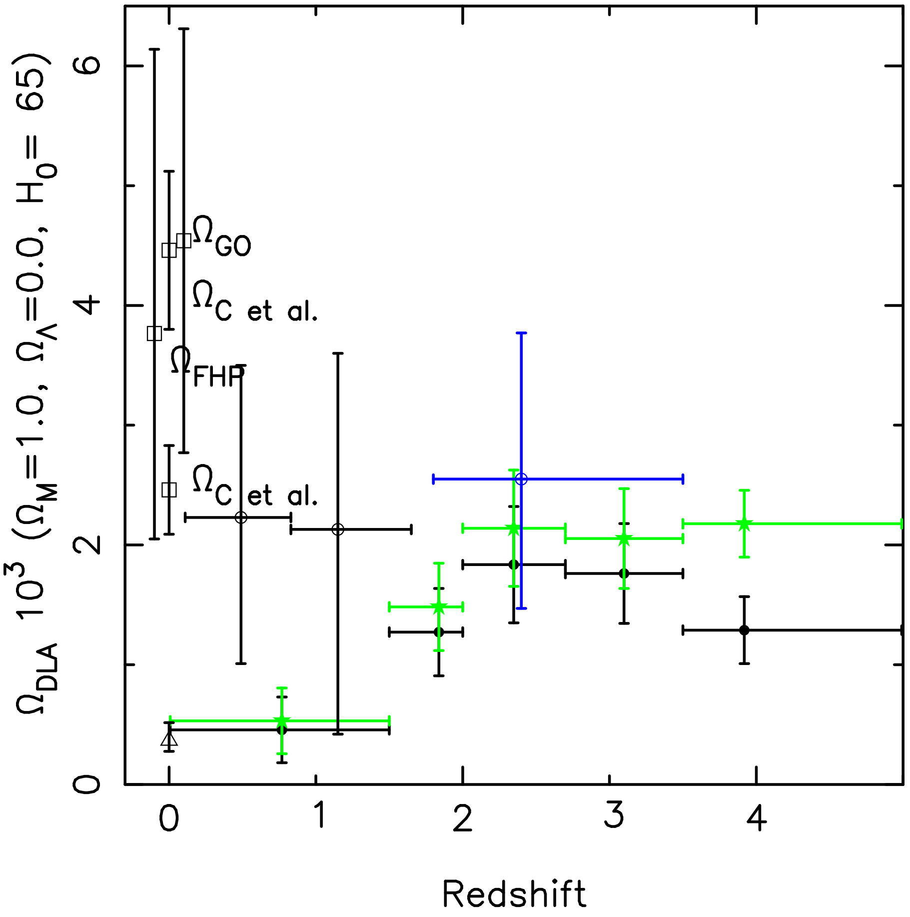

Fig. 13.— The light grey bin at $< z >\sim 2.4$ is Ω_{DLA} as derived from a sample of quasar absorbers found in radio-selected quasars (Ellison et al., 2001c). This Ω_{DLA} free from dust bias is in good agreement with the results presented in this thesis, but is based on a relatively small number of absorption systems as reflected by the large vertical error bar.

> 20) is twice that of DLAs towards brighter quasars (apparent B mag < 20). In addition, at $< z > \sim 2.4$, the $n(z)$ for the whole DLA sample is 50% larger than the value determined from optically selected quasar surveys, but again with the caveat of small number statistics.

Supernovae Feedback: It is also possible that the overall cosmological evolution of Ω_{DLA} is dominated by feedback processes rather than by gas consumption due to star formation. The observed mass of HI at any redshift may relate more to the recombination timescale for the ionized HII and the timescale for cooling collapse into molecular hydrogen (H_2) and thereafter into stars. In addition models from Efstathiou (2000) indicate that DLA systems might predominantly be due to the outer parts of galaxies which do not even participate in star formation, as one would expect from random quasar line-of-sight and the characteristic cross-sections of galaxies.

Ionisation Fraction: DLAs are mostly composed of neutral gas, but such a statement does not necessarily hold for sub-DLA classes of absorbers ($10^{19} < N(HI) < 2 \times 10^{20}$ atoms cm^{-2}). This is an important point because the Ω_{DLA} derived in this study only takes into account the neutral gas HI + He II. In order to link the cosmological evolution of Ω_{DLA} with the star formation in the Universe, one needs to assess the amount of neutral gas ionised solely because it is in its formation phase. We argue above that we are seeing the epoch of assembly of DLA systems from lower column density units at around $z \sim 3.5$. This is based on the assumption that the neutral fraction of hydrogen in sub-DLAs represents well their true total column density.

A way to assess this point is to use photo-ionisation models calculated using Ferland's CLOUDY program (Ferland et al., 1998), although results are extremely model dependent. Steidel (1990b) calculate the models in terms of the ionisation parameter:

$$\Gamma = \frac{n_\gamma}{n_H} \tag{6.39}$$

where n_γ is the number density of photons capable of ionising H incident on the face of the cloud, and n_H is the number density of hydrogen atoms in the gas. Γ is essentially just the ratio of the incident intensity of radiation at the Lyman limit J_{ν_o} to the particle density n_H in the cloud and thus n_H can be determined if the value of J_{ν_o} is known:

$$n_H = 6.3 \times 10^{-5} J_o/\Gamma \mathrm{cm}^{-3} \tag{6.40}$$

where $J_o = J_{\nu_o}/10^{-21}$ ergs s^{-1} cm^{-2} Hz^{-1} sr^{-1}. The most recent estimates of J_{ν_o} indicate $J_{\nu_o} = 1.4^{+1.1}_{-0.5} 10^{-21}$ ergs s^{-1} cm^{-2} Hz^{-1} sr^{-1} (Scott et al., 2000b). Estimates of the neutral fraction of absorbers with column density $10^{19} < N(HI) < 2 \times 10^{20}$ atoms cm^{-2} have never been done although studies have been undertaken at slightly lower N(HI) (Petitjean et al., 1992; Howk & Sembach, 1999). Further invertigations are planned in order to clarify this particular point.

Gravitational Lensing: Gravitational events might bias surveys for quasar absorbers by introducing in the quasar samples those objects which have an absorber along their line-of-sight and hence might have their apparent magnitude artificially boosted. Such effects tend to favour the selection of quasars containing absorbers in magnitude-limited sample and thus will increase the derived Ω_{DLA} with respect to its true value.

Le Brun et al. (2000) have shown that in a magnitude-limited quasar sample, 14 % of the quasars that contain a DLA in their spectrum, would have been observed because of gravitational lensing, although this number will vary with the brightness limit of the quasar survey. In addition, it is equally important to quantify how many quasars *without* DLA are lensed before concluding that there is a bias. Further computations by Bartelmann & Loeb (1996) have shown that the probability of gravitational lensing of quasars by their DLA is higher at low redshift.

Indeed, the probability of lensing is at the highest when the lens is half-way, in physical space, between the observer and the background quasar. But typically, at $z \gtrsim 3$, the absorber is physically close to the quasar because of the high number density of systems at high-redshift and because the redshift path surveyed in one given line-of-sight is limited to the presence of the LLS, which again at high-redshift, is typically close to z_{em}. Gravitational lensing might thus explain the high value of Ω_{DLA} derived by Rao & Turnshek (2000) at $z \lesssim 1.65$, although it does *not* explain the discrepancy between these results and previous low-redshift measurements made by Lanzetta et al. (1995).

6.2.4 Models

Smooth Particle Hydrodynamics

The observational cosmological evolution of Ω_{DLA} with redshift can be used to constrain various models of structure formation. Indeed, quasar absorbers are an un-biased way to probe galaxy formation over a large redshift range. In addition, as shown in Figures 11 and 12, the incidence of absorption is very sensitive to the cosmological models assumed. Gardner et al. (2001a) have used hydrodynamic cosmological simulations to compute Ω_{DLA} in various cold dark matter scenarios: COBE-normalized, cluster-normalized, and tilted ($n = 0.8$) $\Omega_M = 1$ models; and open and flat $\Omega_M = 0.4$ models. No DLA with N(HI) $> 10^{21.8}$ atoms cm^{-2} were observed in the quasar absorber sample they compare their simultations with (namely Storrie-Lombardi et al., 1996b), probably because high gas densities imply high star formation rates which in turns imply gas depletion and local ionisation. They thus computed an "observed" value, for which only gas in systems with N(HI) $< 10^{21.8}$ atoms cm^{-2} was taken into account. This "ob-

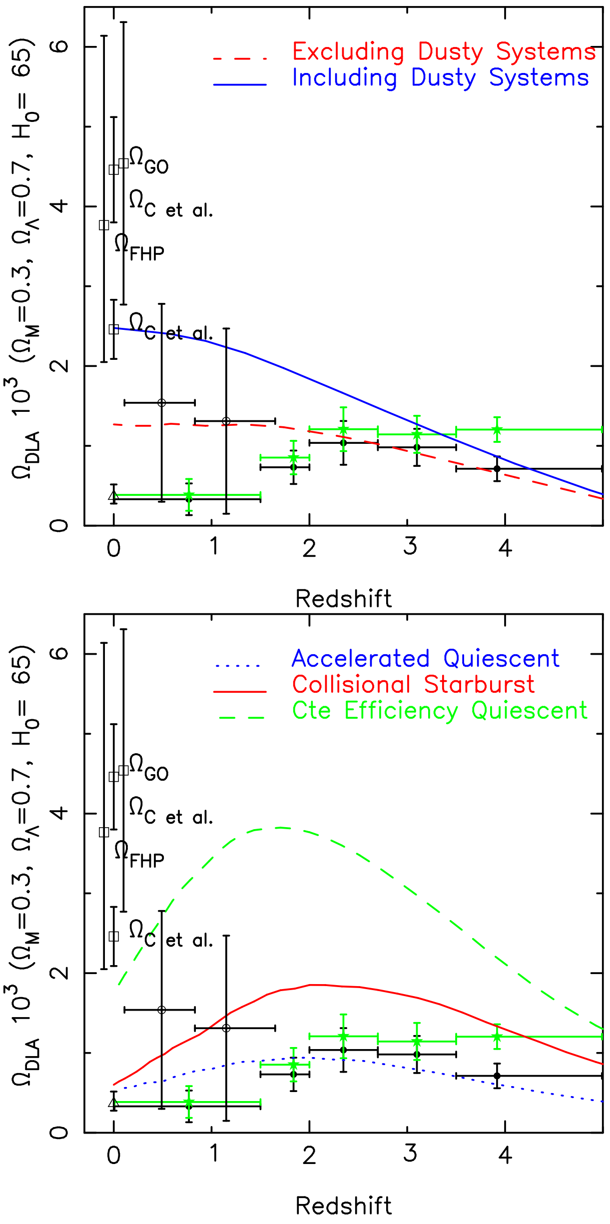

Fig. 14.— Comparison of observed Ω_{DLA} with models. The top panel shows a "backward" model of chemical evolution of disc galaxies including and excluding dusty sytems (as defined by Boisse et al., 1998; Hou et al., 2001). The bottom panel shows models by Somerville et al. (2001) which vary in their recipes for star formation (due to collisional starburst, constant efficiency quiescent star formation or accelerated quiescent star formation). The models take into account the "cold gas" which includes neutral as well as molecular gas.

served" value of Ω_{DLA} agrees best with Storrie-Lombardi et al.'s measurements in the case of a Λ-dominated Universe. In a more recent work (Gardner et al., 2001b), they run three hydrodynamic simulations that have identical initial conditions and cosmological parameters and differ only in the value of the baryon density Ω_b. On the whole, their results imply a fairly intuitive picture of the influence of Ω_b on high-redshift structure.

"Backward" Models

As described in Section 5.4.2, Boissier & et al. (2001) are using a "backward" model of the chemical evolution of disc galaxies (including low surface brightness galaxies) calibrated on the Milky Way and nearby galaxies and extrapolated towards higher redshift. Such models can be used to compute Ω_{DLA} and the results are shown in the top panel of Figure 14. The predicted evolution of neutral gas mass indicates an important contribution of disc galaxies at low redshift, and the possibility for another population appearing at high redshift. One should note that the model only takes into account systems with column density log $N(HI) > 20.3$ atoms cm^{-2}, while the data point go down to the sub-DLA limit. Thus, the observed value of Ω_{DLA} can not be due to disc galaxies according to the models. Finally, in order to better match the observational situation, dusty systems (as defined by Boisse et al., 1998; Hou et al., 2001) are excluded and the resulting predictions should be compared with results from Ellison et al. (2001c) discussed above (see Figure 13).

Semi-Analytical Models

Several groups (Kauffmann & Charlot, 1994; Kauffmann & Haehnelt, 2000; Somerville et al., 2001) have included more realistic physics in their simulations to construct semi-analytical models of galaxy formation which, among other things, predict the evolution of cold gas in the Universe. The models presented in the bottom panel of Figure 14 are from Somerville et al. (2001). They vary in their recipe for star formation: star formation is triggered by galaxy-galaxy mergers in the collisional starburst model, is constant with redshift in the constant efficiency model, and scales inversely with disc dynamical time in the accelerated efficiency model. These models compute the cold gas (molecular plus neutral) and thus should lie above the observations. Clearly, our observational results can be used to directly constrain theories of galaxy evolution.

6.3 Discussion

The observations in the redshift range 2 to 5 shows no evidence for significant evolution in the *total* amount of neutral gas. Under simple assumptions of closed box evolution, this could be interpreted as indicating there is little gas consumption due to star formation in DLA systems in this redshift range. Similarly, at z > 2, Prochaska et al. (2001) conclude that there is no evolution in the metallicity of DLA systems from column density-weighted Fe abundance measurements in DLAs. Since metallicity studies focus on the higher column density systems they may be giving a biased or incomplete view of global galactic chemical evolution at $z > 3$. These metallicity evolution results are still very much open to debate as another study by Savaglio & et al. (2000) shows that the metallicity content of DLAs and sub-DLAs *does* decrease with redshift when one excludes the highest column density systems (N (HI) $> 6 \times 10^{20}$) from the analysis. It is important to note that at $z > 3.5$, 90 % of the HI lies below this limit. Moreover, the current practice of using column density weighted metallicities neglects the fact that the metallicity observations are biased towards high HI column density systems and hence do not necessarily trace the global metallicity evolution.

Combining recent measurements of Ω_{DLA} together with 21 cm emission observations at $z = 0$ imply extremely efficient star formation in DLAs at very low redshift. These results suggest that quasar absorbers could be a specific phase in galaxy formation, thus explaining their lack of metallicity evolution and the difficulties encountered in detecting these systems in emission. Nevertheless, the high Ω_{DLA} derived by Rao & Turnshek (2000) at $z \lesssim 1.65$ and by Churchill (2001) at $< z > \sim 0.05$ may be affected by small number statistics, gravitational lensing or variability in the DLA/MgII conversion ratio. In any case, DLAs remain the most directly observable baryonic mass systems at high redshift.

Furthermore, as first pointed out by Storrie-Lombardi & Wolfe (2000), the higher redshift DLAs, here defined as $z > 3.5$, have a significantly different column density distribution to that of the lower redshift, $z < 3.5$, systems. At $z > 3.5$ there are no systems above N(HI)$= 10^{21}$ atoms cm^{-2} but there is a corresponding increase in the number of 'sub-DLA' systems with $10^{19} <$ N(HI) $< 2 \times 10^{20}$ atoms cm^{-2}. We interpret this change in properties as defining the epoch of formation of Damped Lyman-α absorption systems from lower column density units.

6.4 Summary

In this Chapter, we have used a new sample of high-redshift quasar absorbers together with data from the literature to probe in detail the column density distribution of quasar absorbers, i.e. the number of absorbers per distance interval per column density interval. For the first time, we have derived $f(N,z)$ for a non-zero Λ-cosmology. We use the expected number of LLS calculated from a fit to the observed number density of LLS to constrain $f(N,z)$ in the range where the curve of growth is degenerate. We also use our statistically significant sample of quasar absorbers to study the evolution of the column density distribution with redshift. Because it represents better the data and because it overcomes the divergent integral problem of the power law, we parameterise $f(N,z)$ with a Γ-distribution of the form $f(N,z) = (f_*/N_*)(N/N_*)^{-\beta}\exp(-N/N_*)$. In addition, we used the observed number of LLS as a function of redshift to help constrain the Γ-law fit. We found log $N_* = 21.21$, $\beta = 1.08$ and $f_* = 2.06 \times 10^{-2}$ at $z > 3.5$ and log $N_* = 20.46$, $\beta = 0.80$ and $f_* = 2.51 \times 10^{-2}$ at $z < 3.5$. Finally, we compare our observational results with most recent simulations and semi-analytical models.

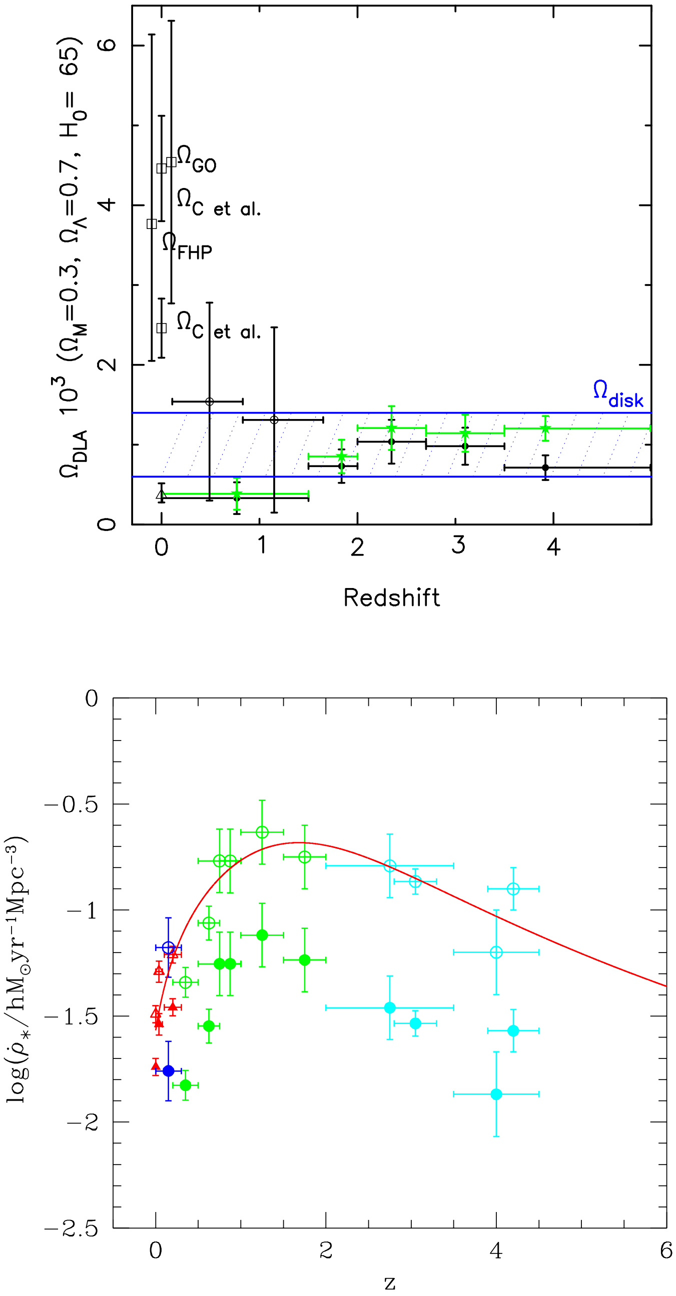

Fig. 15.— Ω_{DLA} and the star formation rate evolution with redshift. The top panel shoes Ω_{DLA} together with the gas contained in discs and the bottom panel is the star formation rate derived from the 2 degree Field (2dF) survey by Cole et al. (2001). The lack of evolution of Ω_{DLA} in the range $z = 5$ to $z = 2$ is in conflict with most recent derivations of the star formation history.

We then determine the neutral gas content of absorbers and find that, unlike previously though, at $z > 3.5$ up to 45% of HI+HeII is in sub-DLAs ($10^{19.0} <$ N(HI) $< 10^{20.3}$ atoms cm^{-2}). We thus define a new class of quasar absorbers which have column densities below the "classical" Wolfe et al. definition of DLAs. We make predictions on the number density of sub-DLAs from the Γ-distribution fit. We derive a total Ω_{DLA} consistent with no evolution over the range $2 < z < 5$. We show that the cosmology affects the total level of neutral gas contained in quasar absorbers with respect to the local $\Omega_{baryons}$ measurements. We summarise the latest results on the low redshift Ω_{DLA} and show that they are difficult to reconcile with local 21 cm observations. We thus review all the possible source of uncertainties which might bias measurements of Ω_{DLA} at both high and low redshifts. Finally, we show that our observations put direct constraints on both smooth particle hydrodynamic simulations and semi-analytical models.

To summarise, the cosmological evolution of the *total* neutral gas mass is a powerful way of tracing structure formation with redshift: it probes the epoch of assembly of high column density systems from lower column density units. We find that at z>3.5 the fraction of mass in DLAs is only 55% and that the remaining fraction of the neutral gas mass lies in systems below this limit, in the so-called "sub-DLAs" with column density $10^{19} <$ N(HI) $< 2 \times 10^{20}$ atoms cm^{-2}.

Chapter 7

Conclusions and Future Work

> *'Quel est donc cet arbre dont les fruits sont des oiseaux qui pleurent?'*
> *Erik Satie*

7.1 Conclusions

The aim of our new survey for quasar absorbers was to better understand the high-redshift end of the mass density of neutral hydrogen by significantly improving the statistics at $z \gtrsim 3.5$ and making a detailed study of the column density distribution function.

After briefly reviewing the context and current knowledge of quasar absorbers of all types, we have described the method used to find high-redshift quasars. We gave details on the various class of quasars absorbers and how they are used to study a wide range of astronomical problems. In addition, we have presented the theory of formation of absorption lines (Voigt profile) and the determination of the curve of growth which is used to determined the column density of damped Lyman-α systems from their observed equivalent widths, two milestones which constitute the main motivation of the project presented here.

A large set of data is presented in the form of the spectra of sixty-six $z \gtrsim 4$ bright quasars with ~ 5 Å resolution (FWHM) red continuum and signal-to-noise ratio ranging from 10 to 30. The observational set up and data reduction processes for the whole sample are emphasized.

The analysis started by concentrating on the properties of the quasars themselves, measuring the spectral indices of quasar power-law continua. We have also presented a median composite spectrum and the measurements of the continuum depression parameters which characterise the absorption across the Lyman-α forest. We used these results to investigate the amount of dust present in the high-column density quasar absorbers by studying the correlation between the steepness of the continuum (reddening) of a quasar from our sample with the presence of a significant quasar absorber along its line-of-sight. We find no direct evidence of the presence of dust in our sample of DLAs.

We then searched for and analysed the statistical properties of the Lyman-limit systems and the Damped Lyα absorbers. The space density and column density evolution of these systems have be studied. These high-column density systems have also been used to measure the neutral hydrogen content of the Universe over a large redshift range, thus probing the formation epoch of these objects and tracing the gas from which stars form. Analysed in conjunction with previous studies, our new survey provides enough data to help draw statistically more significant conclusions on these issues at high redshift.

We determined the neutral gas content of absorbers and find that, unlike previously thought, at $z > 3.5$ up to 45% of HI+HeII is in sub-DLAs ($10^{19.0} <$ N(HI) $< 10^{20.3}$ atoms cm^{-2}). We make predictions on the number density of sub-DLAs from the Γ-distribution fit and derive a total Ω_{DLA} consistent with no evolution over the range $2 < z < 5$.

7.2 Future Work

This thesis presented a unique sample of high-redshift $z \gtrsim 4$ quasars (and quasar absorbers) observed in a homogeneous manner. In addition to the studies described before, a series of further analyses is planned or already underway.

The cosmologically distributed absorption lines provide a cosmic clock following not only the traces of the local evolution of structure in the form of neutral hydrogen systems, but also revealing through the associated metal lines the products of stellar evolution as a function of look-back time. The sample of high-redshift absorption line systems presented in this thesis is ideally suited for the investigation of the metal content of (sub-)DLAs at high-redshift, and we are undertaking high-resolution observations with the state-of-the-art UVES spectrograph on the VLT to study chemical enrichment at high-redshift. This high-resolution spectrograph is a unique facility in the southern hemisphere and thanks to its high sensitivity at extreme red and blue wavelengths, is the perfect tool for such observations. A spectrum of PSS J0307 (a quasar from our sample) has already been taken during UVES comissioning and has led to the determination of the metal content of one of the farthest DLA currently known at $z = 4.466$ (Dessauges-Zavadsky et al., 2001). The results point to an enrichment pattern dominated by Type II supernovae which suggests a Milky Way type of evolutionary model.

The main scientific goals to be tackled with such observing programs are the following:

1. The primary aim of the project is study the metal content ofquasar absorbers at high redshift. The metallicity evolution with redshift is currently the subject of much debate. Prochaska et al. (2001) conclude that there is no evolution in the metallicity of DLA systems from column density-weighted Fe abundance measurements in DLAs (see Figure 7.2). This conflicts with virtually all chemical models but this work is based on a small number of measurements at high redshift.

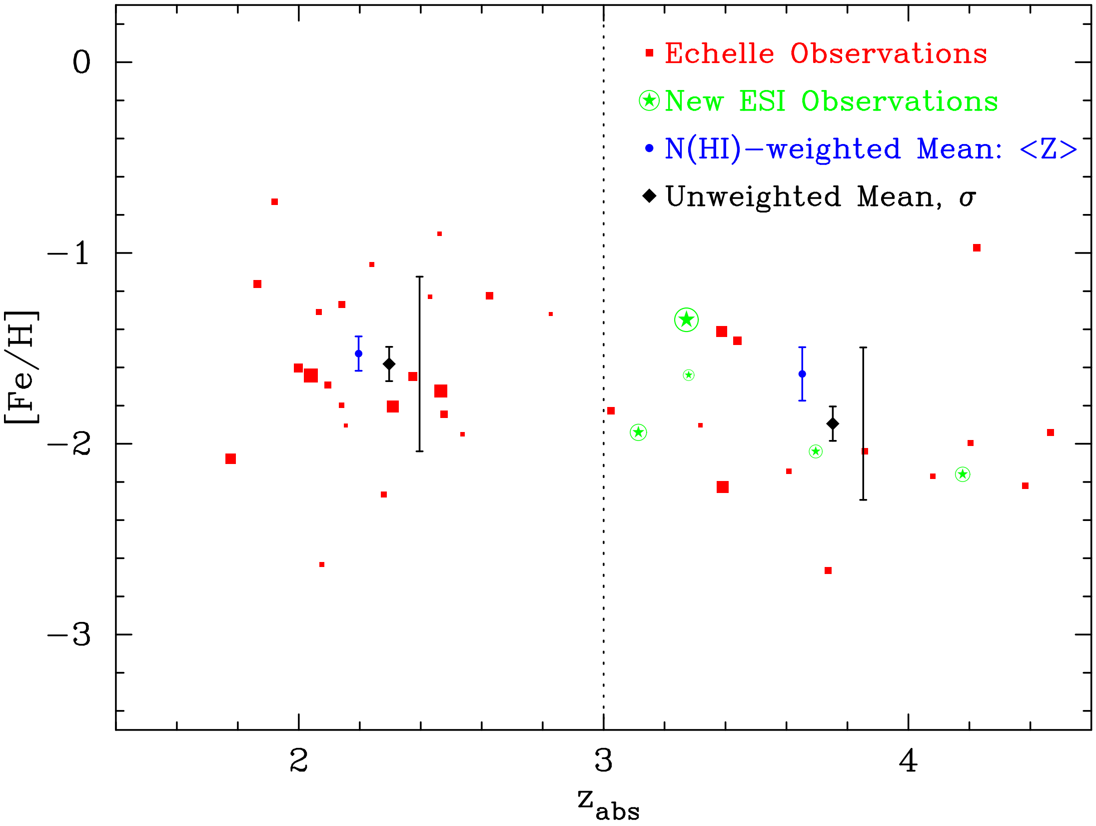

Fig. 1.— [Fe/H] evolution as compiled by Prochaska et al. (2001). The authors claim no evolution of the mean weighted Fe (filled circles) contained in DLAs, in contradiction with predictions from essentially all chemical evolution models. The small number statistics at high-redshift may explain this unexpected observational result and we propose to observe the high-redshift (sub-)DLA systems presented in this thesis with the UVES spectrograph on VLT to accurately determine the metallicity of quasar absorption systems at high redshift.

Futhermore the unweighted metallicity distribution shows evidence for a decrease of metallicity with increasing redshift suggesting that HI column densities weighted measurements solely based on conventional DLAs do not reveal the full picture. We propose to use the sample of high-redshift DLAs and sub-DLAs of this thesis to explore this problem and to better constrain the chemical evolution in the early Universe.

2. The content of DLAs in α-elements (O, Ar, S and Si) and iron peak elements (Zn, Fe, Cr and Ni) will be compared in order to distinguish between Type I and Type II supernovae chemical enrichment pattern. In some of the DLA, the dust content of individual absorbers will be estimated using measurements of undepleted metals (such as Zn whenever accessible) and their dust-free metallicity will then be derived.

3. Abundance of primordial elements can also be studied. The first synthesis of light elements (D, He and Li) took place in the early Universe and heavier elements have then been synthesised through stellar nucleosynthesis. High-resolution observations of quasar absorbers can be used to determinate the primordial abundances of elements formed in the Big Bang, which provide a fundamental tool for testing the Big Bang theory and a unique measure of the baryonic density of the Universe.

4. The molecular hydrogen content of DLAs have now been measured in few systems (Srianand & Petitjean, 1998; Levshakov et al., 2000; Petitjean et al., 2000). Such study will allow us to investigate the processes of dust formation as well as cooling and photodissociation from the first stars.

5. Finally the temperature of the Cosmological Background Radiation will be measured using the abundance ratio of excited states of CII. This puts a direct constraint on the Big Bang theory although only one measurement has been made so far (Srianand et al., 2000). We propose to use the new sample of high-redshift quasars to make further measurements of the Cosmological Background Radiation temperature.

In addition, the work presented in this thesis has shown that at $z > 3.5$, 45% of the neutral gas mass lies in systems below the traditional DLA definition, in "sub-DLAs" with column density $10^{19} < \mathrm{N(HI)} < 2 \times 10^{20}$ atoms cm^{-2}. This finding is based on indirect measurements of the column density distribution in this column density range. Nevetheless, any absorption system with a doppler parameter b <100 km/s and N(HI) $> 10^{19}$ atoms cm^{-2} will exhibit damping wings and thus a systematic study of the kinematic and metallicity properties of sub-DLA systems with z>3.5 and N(HI) above 10^{19} atom cm^{-2} is an obvious program for the new generation of echelle spectographs on 8 m class telescopes. It will also be important to directly establish the N(HI) column density distribution function below 2 $\times 10^{20}$ atom cm^{-2}. We are currently undertaking such a program.

Bibliography

Abel, T., Mo, H. J. 1998, ApJ, 494, L151

Bahcall, J. N., Bergeron, J., Boksenberg, A., Hartig, G. F., Jannuzi, B. T., Kirhakos, S., Sargent, W. L. W., Savage, B. D., Schneider, D. P., Turnshek, D. A., Weymann, R. J., Wolfe, A. M. 1993, ApJS, 87, 1

Bahcall, J. N., Jannuzi, B. T., Schneider, D. P., Hartig, G. F., Bohlin, R., Junkkarinen, V. 1991, ApJ, 377, L5

Bahcall, J. N., Peebles, P. J. 1969, ApJ, 156, L7+

Bajtlik, S., Duncan, R. C., Ostriker, J. P. 1988, ApJ, 327, 570

Baldwin, J., Burbidge, E., Burbidge, G., Hazard, C.nd Robinson, L., Wampler, E. 1974, ApJ, 193, 513

Baldwin, J. A. 1977, ApJ, 214, 679

Barkhouse, W. A., Hall, P. B. 2001, AJ, 121, 2843

Barlow, T. A., Hamann, F., Sargent, W. L. W. 1997, in ASP Conf. Ser. 128: Mass Ejection from Active Galactic Nuclei, p. 13+

Bartelmann, M., Loeb, A. 1996, ApJ, 457, 529+

Bechtold, J., Green, R. F., Weymann, R. J., Schmidt, M., Estabrook, F. B., Sherman, R. D., Wahlquist, H. D., Heckman, T. M. 1984, ApJ, 281, 76

Becker, R., Fan, X., White, R. L., Strauss, M. A., Haiman, Z., Schneider, D. P., Gregg, M. D., Gunn, J. E., Knapp, G. R., Lupton, R. H., Anderson, J. E., Anderson, S. F., Annis, J., Bahcall, N. A., Boroski, W. N., Brunner, R. J., Chen, B., Connolly, A. J., Csabai, I. ., Doi, M., Fukugita, M., Hennessy, G. S., Hindsley, R. B., Ichikawa, T., Ivezić, Z., Loveday, J., Meiksin, A., McKay, T. A., Munn, J. A., Newberg, H. J., Nichol, R., Okamura, S., Pier, J. R., Sekiguchi, M., Shimasaku, K., Stoughton, C., Szalay, A. S., Szokoly, G. P., Thakar, A. R., Vogeley, M. S., York, D. G. 2001, AJ

Becker, R. H., White, R. L., Gregg, M. D., Brotherton, M. S., Laurent-Muehleisen, S. A., Arav, N. 2000, ApJ, 538, 72

Bergeron, J., Boisse, P. 1991, A&A, 243, 344

Bergeron, J., Petitjean, P., Sargent, W. L. W., Bahcall, J. N., Boksenberg, A., Hartig, G. F., Jannuzi, B. T., Kirhakos, S., Savage, B. D., Schneider, D. P., Turnshek, D. A., Weymann, R. J., Wolfe, A. M. 1994, ApJ, 436, 33

Black, J. H., Chaffee, F. H., Foltz, C. B. 1987, ApJ, 317, 442

Boisse, P., Le Brun, V., Bergeron, J., Deharveng, J. 1998, A&A, 333, 841

Boissier, S., Boselli, A., Prantzos, N., Gavazzi, G. 2001, MNRAS, 321, 733

Boissier, S., et al. 2001, MNRAS

Boksenberg, A., Sargent, W. L. W. 1978, ApJ, 220, 42

Bowen, D. V., Tripp, T. M., Jenkins, E. B. 2001, AJ, 121, 1456

Briggs, F. H., Wolfe, A. M., Liszt, H. S., Davis, M. M., Turner, K. L. 1989, ApJ, 341, 650

Brotherton, M. S., Tran, H. D., Becker, R. H., Gregg, M. D., Laurent-Muehleisen, S. A., White, R. L. 2001, ApJ, 546, 775

Carswell, R. F., Morton, D. C., Smith, M. G., Stockton, A. N., Turnshek, D. A., Weymann, R. J. 1984, ApJ, 278, 486

Carswell, R. F., Rees, M. J. 1987, MNRAS, 224, 13P

Carswell, R. F., Webb, J. K., Baldwin, J. A., Atwood, B. 1987, ApJ, 319, 709

Carswell, R. F., Whelan, J. A. J., Smith, M. G., Boksenberg, A., Tytler, D. 1982, MNRAS, 198, 91

Charlton, J., Churchill, C. W. 2000, in Encyclopedia of Astronomy and Astrophysics (Mac Millan and the Institute of Physics Publishing)

Churchill, C. 2001, MNRAS

Churchill, C. W., Mellon, R. R., Charlton, J. C., Jannuzi, B. T., Kirhakos, S., Steidel, C. C., Schneider, D. P. 2000a, ApJS, 130, 91

Churchill, C. W., Mellon, R. R., Charlton, J. C., Jannuzi, B. T., Kirhakos, S., Steidel, C. C., Schneider, D. P. 2000b, ApJ, 543, 577

Cole, S., Norberg, P., Baugh, C. M., Frenk, C. S., Bland-Hawthorn, J., Bridges, T., Cannon, R., Colless, M., Collins, C., Couch, W., Cross, N., Dalton, G., De Propris, R., Driver, S. P., Efstathiou, G., Ellis, R. S., Glazebrook, K., Jackson, C., Lahav, O., Lewis, I., Lumsden, S., Maddox, S., Madgwick, D., Peacock, J. A., Peterson, B. A., Sutherland, W., Taylor, K., (The 2dFGRS Team) 2001, MNRAS, 326, 255+

Crotts, A. P. S., Burles, S., Tytler, D. 1997, ApJ, 489, L7

Dessauges-Zavadsky, M., D'Odorico, S., McMahon, R. G., Molaro, P., Ledoux, C., Péroux, C., Storrie-Lombardi, L. J. 2001, A&A, 370, 426

Djorgovski, S., Castro, S., Stern, D., Mahabal, A. A. 2001, AJ

Dobrzycki, A., Bechtold, J. 1991, ApJ, 377, L69

D'Odorico, S. 1997, in The Early Universe with the VLT., p. 54+

D'Odorico, S., Cristiani, S., Dekker, H., Hill, V., Kaufer, A., Kim, T., Primas, F. 2000, in Proc. SPIE Vol. 4005, p. 121-130, Discoveries and Research Prospects from 8- to 10-Meter-Class Telescopes, Jacqueline Bergeron; Ed., Vol. 4005, p. 121

D'Odorico, S., Dessauges-Zavadsky, M., Molaro, P. 2001, A&A, 368, L21

D'Odorico, V., Cristiani, S., D'Odorico, S., Fontana, A., Giallongo, E., Shaver, P. 1998, A&A, 339, 678

Efstathiou, G. 2000, MNRAS, 317, 697

Ellison, S. L., Ryan, S., Prochaska, J. 2001a, MNRAS

Ellison, S. L., Songaila, A., Schaye, J., Pettini, M. 2000, AJ, 120, 1175

Ellison, S. L., Yan, L., Hook, I., M., P., Wall, J. V., Shaver, P. 2001b, A&A

Ellison, S. L., Yan, L., Hook, I. M., Pettini, M., Wall, J. V., Shaver, P. 2001c, A&A, 379, 393

Fall, S. M., Pei, Y. C., McMahon, R. G. 1989, ApJ, 341, L5

Fan, X., Strauss, M. A., Richards, G. T., Newman, J. A., Becker, R. H., Schneider, D. P., Gunn, J. E., Davis, M., White, R. L., Lupton, R. H., Anderson, J. E., Annis, J., Bahcall, N. A., Brunner, R. J., Csabai, I. ., Doi, M., Fukugita, M., Hennessy, G. S., Hindsley, R. B., Ivezić, Ž., Knapp, G. R., McKay, T. A., Munn, J. A., Pier, J. R., Szalay, A. S., York, D. G. 2001a, AJ, 121, 31

Fan, X., Strauss, M. A., Schneider, D. P., Gunn, J. E., Lupton, R. H., Yanny, B., Anderson, S. F., Anderson, J. E., Annis, J., Bahcall, N. A., Bakken, J. A., Bastian, S., Berman, E., Boroski, W. N., Briegel, C., Briggs, J. W., Brinkmann, J., Carr, M. A., Colestock, P. L., Connolly, A. J., Crocker, J. H., Csabai, I. ., Czarapata, P. C., Davis, J. E., Doi, M., Elms, B. R., Evans, M. L., Federwitz, G. R., Frieman, J. A., Fukugita, M., Gurbani, V. K., Harris, F. H., Heckman, T. M., Hennessy, G. S., Hindsley, R. B., Holmgren, D. J., Hull, C., Ichikawa, S., Ichikawa, T., Ivezić , Z. E., Kent, S., Knapp, G. R., Kron, R. G., Lamb, D. Q., Leger, R. F., Limmongkol, S., Lindenmeyer, C., Long, D. C., Loveday, J., MacKinnon, B., Mannery, E. J., Mantsch, P. M., Margon, B., McKay, T. A., Munn, J. A., Nash, T., Newberg, H. J., Nichol, R. C., Nicinski, T., Okamura, S., Ostriker, J. P., Owen, R., Pauls, A. G., Peoples, J., Petravick, D., Pier, J. R., Pordes, R., Prosapio, A., Rechenmacher, R., Richards, G. T., Richmond, M. W., Rivetta, C. H., Rockosi, C. M., Sandford, D., Sergey, G., Sekiguchi, M., Shimasaku, K., Siegmund, W. A., Smith, J. A., Stoughton, C., Szalay, A. S., Szokoly, G. P., Tucker, D. L., Vogeley, M. S., Waddell, P., Wang, S., Weinberg, D. H., Yasuda, N., York, D. G. 1999, AJ, 118, 1

Fan, X., White, R. L., Davis, M., Becker, R. H., Strauss, M. A., Haiman, Z., Schneider, D. P., Gregg, M. D., Gunn, J. E., Knapp, G. R., Lupton, R. H., Anderson, J. E., Anderson, S. F., Annis, J., Bahcall, N. A., Boroski, W. N., Brunner, R. J., Chen, B., Connolly, A. J., Csabai, I. ., Doi, M., Fukugita, M., Hennessy, G. S., Hindsley, R. B., Ichikawa, T., Ivezić, Z., Loveday, J., Meiksin, A., McKay, T. A., Munn, J. A., Newberg, H. J., Nichol, R., Okamura, S., Pier, J. R., Sekiguchi, M., Shimasaku, K., Stoughton, C., Szalay, A. S., Szokoly, G. P., Thakar, A. R., Vogeley, M. S., York, D. G. 2001b, AJ

Ferland, G. J., Korista, K. T., Verner, D. A., Ferguson, J. W., Kingdon, J. B., Verner, E. M. 1998, PASP, 110, 761

Ferrara, A., Pettini, M., Shchekinov, Y. 2000, MNRAS, 319, 539

Francis, P. J. 1993a, ApJ, 405, 119

Francis, P. J. 1993b, ApJ, 407, 519

Francis, P. J., Hewett, P. C. 1993, AJ, 106, 2587+

Francis, P. J., Hewett, P. C., Foltz, C. B., Chaffee, F. H. 1992, ApJ, 398, 476

Francis, P. J., Hewett, P. C., Foltz, C. B., Chaffee, F. H., Weymann, R. J., Morris, S. L. 1991, ApJ, 373, 465

Francis, P. J., Koratkar, A. 1995, MNRAS, 274, 504

Fukugita, M., Hogan, C. J., Peebles, P. J. E. 1998, ApJ, 503, 518+

Fynbo, J. U., Möller, P., Thomsen, B. 2001, A&A, 368, 408

Fynbo, J. U., Moller, P., Warren, S. J. 1999, MNRAS, 305, 849

Ganguly, R., Eracleous, M., Charlton, J. C., Churchill, C. W. 1999, AJ, 117, 2594

Gardner, J. P., Katz, N., Hernquist, L., Weinberg, D. H. 1997, ApJ, 484, 31+

Gardner, J. P., Katz, N., Hernquist, L., Weinberg, D. H. 2001a, ApJ

Gardner, J. P., Katz, N., Hernquist, L., Weinberg, D. H. 2001b, ApJ

Giallongo, E., Cristiani, S. 1990, MNRAS, 247, 696

Gnedin, N. I., Ostriker, J. P. 1992, ApJ, 400, 1

Gunn, J. E., Peterson, B. A. 1965, ApJ, 142, 1633

Haehnelt, M. G., Steinmetz, M., Rauch, M. 1996, ApJ, 465, L95

Haehnelt, M. G., Steinmetz, M., Rauch, M. 1998, ApJ, 495, 647+

Hall, P. B., Osmer, P. S., Green, R. F., Porter, A. C., Warren, S. J. 1996, ApJ, 462, 614+

Hamann, F., Barlow, T. A., Beaver, E. A., Burbidge, E. M., Cohen, R. D., Junkkarinen, V., Lyons, R. 1995, ApJ, 443, 606

Hazard, C., Mackey, M. B., Shimmines, A. J. 1963, Nature, 1037

Henry, J. P., Gioia, I. M., Boehringer, H., Bower, R. G., Briel, U. G., Hasinger, G. H., Aragon-Salamanca, A., Castander, F. J., Ellis, R. S., Huchra, J. P., Burg, R., McLean, B. 1994, AJ, 107, 1270

Hewett, P. C., Foltz, C. B., Chaffee, F. H. 1995, AJ, 109, 1498

Hook, I. 1994, *Ph.D. thesis*, Cambridge University, UK

Hook, I. in preparation, MNRAS

Hook, I. M., McMahon, R. G., Boyle, B. J., Irwin, M. J. 1994, MNRAS, 268, 305+

Horne, K. 1986, PASP, 98, 609

Hou, J. L., Boissier, S., Prantzos, N. 2001, A&A, 370, 23

Howk, J. C., Sembach, K. R. 1999, ApJ, 523, L141

Hu, E. M., Kim, T., Cowie, L. L., Songaila, A., Rauch, M. 1995, AJ, 110, 1526+

Hu, E. M., McMahon, R. G. 1996, Nature, 382, 231

Irwin, M., McMahon, R. G., Hazard, C. 1991, in ASP Conf. Ser. 21: The Space Distribution of Quasars, p. 117

Jakobsen, P., Boksenberg, A., Deharveng, J. M., Greenfield, P., Jedrzejewski, R., Paresce, F. 1994, Nature, 370, 35

Jannuzi, B. T., Bahcall, J. N., Bergeron, J., Boksenberg, A., Hartig, G. F., Kirhakos, S., Sargent, W. L. W., Savage, B. D., Schneider, D. P., Turnshek, D. A., Weymann, R. J., Wolfe, A. M. 1998, ApJS, 118, 1

Jenkins, A., Frenk, C. S., White, S. D. M., Colberg, J. M., Cole, S., Evrard, A. E., Couchman, H. M. P., Yoshida, N. 2001, MNRAS, 321, 372

Jenkins, E. B., Ostriker, J. P. 1991, ApJ, 376, 33

Jimenez, R., Bowen, D. V., Matteucci, F. 1999, ApJ, 514, L83

Kauffmann, G., Charlot, S. 1994, ApJ, 430, L97

Kauffmann, G., Haehnelt, M. 2000, MNRAS, 311, 576

Kauffmann, G., White, S. D. M., Guiderdoni, B. 1993, MNRAS, 264, 201+

Kembhavi, A. K., Narlikar, J. V. (eds.) 1999, Quasars and active galactic nuclei : an introduction

Kennefick, J. D., de Carvalho, R. R., Djorgovski, S. G., Wilber, M. M., Dickson, E. S., Weir, N., Fayyad, U., Roden, J. 1995a, AJ, 110, 78+

Kennefick, J. D., Djorgovski, S. G., de Carvalho, R. R. 1995b, AJ, 110, 2553+

Kim, T., Cristiani, S., D'Odorico, S. 2001, A&A, 0, 0

Lanzetta, K. M. 1991, ApJ, 375, 1

Lanzetta, K. M., McMahon, R. G., Wolfe, A. M., Turnshek, D. A., Hazard, C., Lu, L. 1991, ApJS, 77, 1

Lanzetta, K. M., Wolfe, A. M., Turnshek, D. A. 1987, ApJ, 322, 739

Lanzetta, K. M., Wolfe, A. M., Turnshek, D. A. 1995, ApJ, 440, 435+

Le Brun, V., Bergeron, J., Boisse, P., Deharveng, J. M. 1997, A&A, 321, 733

Le Brun, V., Smette, A., Surdej, J., Claeskens, J.-F. 2000, A&A, 363, 837

Ledoux, C., Petitjean, P., Bergeron, J., Wampler, E. J., Srianand, R. 1998, A&A, 337, 51

Levshakov, S. A., Molaro, P., Centurión, M., D'Odorico, S., Bonifacio, P., Vladilo, G. 2000, A&A, 361, 803

Loeb, A. 1999, in ASP Conf. Ser. 193: The Hy-Redshift Universe: Galaxy Formation and Evolution at High Redshift, p. 586+

Loeb, A., Eisenstein, D. J. 1995, ApJ, 448, 17+

Lu, L., Sargent, W. L. W., Womble, D. S., Takada-Hidai, M. 1996, ApJ, 472, 509+

Lu, L., Wolfe, A. M. 1994, AJ, 108, 44

Lu, L., Wolfe, A. M., Turnshek, D. A., Lanzetta, K. M. 1993, ApJS, 84, 1

Lu, L., Zuo, L. 1994, ApJ, 426, 502

Lynds, B. T. 1970, in IAU Symp. 38: The Spiral Structure of our Galaxy, Vol. 38, p. 26+

Maller, A. H., Prochaska, J. X., Somerville, R. S., Primack, J. R. 2001, MNRAS, 326, 1475+

Maraschi, L., Grandi, P., Urry, C. M., Wehrle, A. E., Madejski, G. M., Fink, H. H., Ghisellini, G., Hartman, R. C., Koratkar, A. P., von Montigny, C., Pian, E., Thomas, H. C., Treves, A., Aller, M. F., Aller, H. D., Bailyn, C. D., Balonek, T. J., Bock, H., Collmar, W., Glass, I. S., Litchfield, S. J., McHardy, I. M., Mendez, R., Pesce, J., Reuter, H. P., Robson, E. I., Steppe, H., Stevens, J. A., Teraesranta, H., Wagner, S. J. 1994, ApJ, 435, L91

Matteucci, F., Molaro, P., Vladilo, G. 1997, A&A, 321, 45

Meiksin, A., Madau, P. 1993, ApJ, 412, 34

Meyer, D. M., Lanzetta, K. M., Wolfe, A. M. 1995, ApJ, 451, L13

Meyer, D. M., York, D. G. 1987, ApJ, 315, L5

Molaro, P., Bonifacio, P., Centurion, M., Vladilo, G. 1999, A&A, 349, L13

Moller, P., Warren, S. J. 1998, MNRAS, 299, 661

Natarajan, P., Pettini, M. 1997, MNRAS, 291, L28

O'Brien, P. T., Wilson, R., Gondhalekar, P. M. 1988, MNRAS, 233, 801

Oemler, A., Lynds, C. R. 1975, ApJ, 199, 558

Oke, J. B., Korycansky, D. G. 1982, ApJ, 255, 11

O'Meara, J. M., Tytler, D., Kirkman, D., Suzuki, N., Prochaska, J. X., Lubin, D., Wolfe, A. M. 2001, ApJ, 552, 718

O'Neil, K. 2001, in ASP Conf. Ser. : Extragalactic Gas at Low Redshift; Mulchaey J. and Stocke, J. (eds), 01

Outram, P. 1999, *Ph.D. thesis*, Cambridge University, UK

Pascarelle, C., Lanzetta, K., Chen, H.-W., Webb, J. 2001, in ASP Conf. Ser. : Extragalactic Gas at Low Redshift, p. astro

Pascarelle, S. M., Windhorst, R. A., Keel, W. C., Odewahn, S. C. 1996, Nature, 383, 45

Pei, Y. C., Fall, S. M. 1995, ApJ, 454, 69+

Persic, M., Salucci, P. 1992, MNRAS, 258, 14P

Petitjean, P. 1998, in in the proceedings of the Les Houches school "Formation and Evolution of galaxies"; O. Le Fevre and S. Charlot (eds.), Springer-VerlagScience

Petitjean, P. (ed.) 1999, Les Annales de Physique Vol. 24

Petitjean, P., Bergeron, J. 1990, A&A, 231, 309

Petitjean, P., Bergeron, J. 1994, A&A, 283, 759+

Petitjean, P., Bergeron, J., Puget, J. L. 1992, A&A, 265, 375

Petitjean, P., Mueket, J. P., Kates, R. E. 1995, A&A, 295, L9

Petitjean, P., Rauch, M., Carswell, R. F. 1994, A&A, 291, 29

Petitjean, P., Srianand, R., Ledoux, C. 2000, A&A, 364, L26

Petitjean, P., Surdej, J., Smette, A., Shaver, P., Muecket, J., Remy, M. 1998, A&A, 334, L45

Petitjean, P., Webb, J. K., Rauch, M., Carswell, R. F., Lanzetta, K. 1993, MNRAS, 262, 499

Pettini, M. (ed.) 1998, Graduate Lecture Notes (Cambridge University)

Pettini, M., Bowen, D. V. 2001, ApJ, 560, 41

Pettini, M., Smith, L. J., Hunstead, R. W., King, D. L. 1994, ApJ, 426, 79

Pettini, M., Smith, L. J., King, D. L., Hunstead, R. W. 1997, ApJ, 486, 665+

Press, W. H., Rybicki, G. B., Schneider, D. P. 1993, ApJ, 414, 64

Prochaska, J. X. 1999, ApJ, 511, L71

Prochaska, J. X., Gawiser, E., Wolfe, A. M. 2001, ApJ, 552, 99

Prochaska, J. X., Wolfe, A. M. 1997, ApJ, 487, 73+

Prochaska, J. X., Wolfe, A. M. 1998, ApJ, 507, 113

Quashnock, J. M., vanden Berk, D. E., York, D. G. 1996, ApJ, 472, L69

Rao, S., Briggs, F. 1993, ApJ, 419, 515+

Rao, S. M., Turnshek, D. A. 2000, ApJS, 130, 1

Rauch, M. 1998, ARA&A, 36, 267

Rauch, M., Carswell, R. F., Robertson, J. G., Shaver, P. A., Webb, J. K. 1990, MNRAS, 242, 698

Rauch, M., Sargent, W. L. W., Womble, D. S., Barlow, T. A. 1996, ApJ, 467, L5

Rees, M. J. 1988, in Proceedings of the QSO Absorption Line Meeting, p. 107

Reimers, D., Kohler, S., Wisotzki, L., Groote, D., Rodriguez-Pascual, P., Wamsteker, W. 1997, A&A, 327, 890

Sargent, W. L. W., Steidel, C. C., Boksenberg, A. 1988, ApJ, 334, 22

Sargent, W. L. W., Steidel, C. C., Boksenberg, A. 1989, ApJS, 69, 703

Sargent, W. L. W., Young, P. J., Boksenberg, A., Tytler, D. 1980, ApJS, 42, 41

Savaglio, S., D'Odorico, S., Moller, P. 1994, A&A, 281, 331

Savaglio, S., et al. 2000, in IAU Symposium, Vol. 204, p. E76

Schechter, P. 1976, ApJ, 203, 297

Schechter, P., Press, W. H. 1976, ApJ, 203, 557

Schmidt, M. 1963, Nature, 197, 1040

Schneider, D. P., Hartig, G. F., Jannuzi, B. T., Kirhakos, S., Saxe, D. H., Weymann, R. J., Bahcall, J. N., Bergeron, J., Boksenberg, A., Sargent, W. L. W., Savage, B. D., Turnshek, D. A., Wolfe, A. M. 1993, ApJS, 87, 45

Schneider, D. P., Schmidt, M., Gunn, J. E. 1991, AJ, 101, 2004

Scott, J., Bechtold, J., Dobrzycki, A. 2000a, ApJS, 130, 37

Scott, J., Bechtold, J., Dobrzycki, A., Kulkarni, V. P. 2000b, ApJS, 130, 67

Shaver, P. A., Robertson, J. G. 1983, ApJ, 268, L57

Shaver, P. A., Wall, J. V., Kellermann, K. I., Jackson, C. A., Hawkins, M. R. S. 1996, Nature, 384, 439

Shields, J. C., Hamann, F., Foltz, C. B., Chaffee, F. H. 1997, in ASP Conf. Ser. 113: IAU Colloq. 159: Emission Lines in Active Galaxies: New Methods and Techniques, p. 118+

Silk, J. 2001, Nuclear Physics B Proceedings Supplements, 95, 3

Somerville, R. S., Primack, J. R., Faber, S. M. 2001, MNRAS, 320, 504+

Songaila, A., Hu, E. M., Cowie, L. L., McMahon, R. G. 1999, ApJ, 525, L5

Srianand, R., Petitjean, P. 1998, A&A, 335, 33

Srianand, R., Petitjean, P., Ledoux, C. 2000, Nature, 408, 931

Steidel, C. C. 1990a, ApJS, 72, 1

Steidel, C. C. 1990b, ApJS, 74, 37

Steidel, C. C. 1993, in ASSL Vol. 188: The Environment and Evolution of Galaxies, p. 263+

Steidel, C. C., Bowen, D. V., Blades, J. C., Dickenson, M. 1995, ApJ, 440, L45

Steidel, C. C., Dickinson, M., Persson, S. E. 1994, ApJ, 437, L75

Steidel, C. C., Sargent, W. L. W. 1987, ApJ, 313, 171

Steidel, C. C., Sargent, W. L. W. 1992, ApJS, 80, 1

Stengler-Larrea, E. A., Boksenberg, A., Steidel, C. C., Sargent, W. L. W., Bahcall, J. N., Bergeron, J., Hartig, G. F., Jannuzi, B. T., Kirhakos, S., Savage, B. D., Schneider, D. P., Turnshek, D. A., Weymann, R. J. 1995, ApJ, 444, 64

Stern, D., Spinrad, H., Eisenhardt, P., Bunker, A. J., Dawson, S., Stanford, S. A., Elston, R. 2000, ApJ, 533, L75

Storrie-Lombardi, L. 1994, *Ph.D. thesis*, Cambridge University, UK

Storrie-Lombardi, L. J., Hook, I. M. 2000, ApJS

Storrie-Lombardi, L. J., Irwin, M. J., McMahon, R. G. 1996a, MNRAS, 282, 1330

Storrie-Lombardi, L. J., Irwin, M. J., McMahon, R. G., Hook, I. M. 2001, MNRAS, 322, 933+

Storrie-Lombardi, L. J., McMahon, R. G., Irwin, M. J. 1996b, MNRAS, 283, L79

Storrie-Lombardi, L. J., McMahon, R. G., Irwin, M. J., Hazard, C. 1994, ApJ, 427, L13

Storrie-Lombardi, L. J., McMahon, R. G., Irwin, M. J., Hazard, C. 1996c, ApJ, 468, 121+

Storrie-Lombardi, L. J., Wolfe, A. M. 2000, ApJ, 543, 552

Theuns, T., Leonard, A., Efstathiou, G., Pearce, F. R., Thomas, P. A. 1998, MNRAS, 301, 478

Turnshek, D. A., Wolfe, A. M., Lanzetta, K. M., Briggs, F. H., Cohen, R. D., Foltz, C. B., Smith, H. E., Wilkes, B. J. 1989, ApJ, 344, 567

Tytler, D. 1982, Nature, 298, 427

Tytler, D. 1987, ApJ, 321, 49

Tytler, D., O'Meara, J. M., Suzuki, N., Lubin, D. 2000, Physica Scripta Volume T, 85, 12

Vanden Berk, D. E., Richards, G. T., Bauer, A., Strauss, M. A., Schneider, D. P., Heckman, T. M., York, D. G., Hall, P. B., Fan, X., Knapp, G. R., Anderson, S. F., Annis, J., Bahcall, N. A., Bernardi, M., Briggs, J. W., Brinkmann, J., Brunner, R., Burles, S., Carey, L., Castander, F. J., Connolly, A. J., Crocker, J. H., Csabai, I. ., Doi, M., Finkbeiner, D., Friedman, S., Frieman, J. A., Fukugita, M., Gunn, J. E., Hennessy, G. S., Ivezić, Ž., Kent, S., Kunszt, P. Z., Lamb, D. Q., Leger, R. F., Long, D. C., Loveday, J., Lupton, R. H., Meiksin, A., Merelli, A., Munn, J. A., Newberg, H. J., Newcomb, M., Nichol, R. C., Owen, R., Pier, J. R., Pope, A., Rockosi, C. M., Schlegel, D. J., Siegmund, W. A., Smee, S., Snir, Y., Stoughton, C., Stubbs, C., SubbaRao, M., Szalay, A. S., Szokoly, G. P., Tremonti, C., Uomoto, A., Waddell, P., Yanny, B., Zheng, W. 2001, AJ, 122, 549

Vilkoviskij, E. Y., Irwin, M. J. 2001, MNRAS, 321, 4

Warren, S. J., Hewett, P. C., Foltz, C. B. 2000, MNRAS, 312, 827

Warren, S. J., Hewett, P. C., Osmer, P. S. 1991, ApJS, 76, 23

Warren, S. J., Hewett, P. C., Osmer, P. S. 1994, ApJ, 421, 412

Weymann, R. J., Jannuzi, B. T., Lu, L., Bahcall, J. N., Bergeron, J., Boksenberg, A., Hartig, G. F., Kirhakos, S., Sargent, W. L. W., Savage, B. D., Schneider, D. P., Turnshek, D. A., Wolfe, A. M. 1998, ApJ, 506, 1

Weymann, R. J., Morris, S. L., Foltz, C. B., Hewett, P. C. 1991, ApJ, 373, 23

Williger, G. M., Baldwin, J. A., Carswell, R. F., Cooke, A. J., Hazard, C., Irwin, M. J., McMahon, R. G., Storrie-Lombardi, L. J. 1994, ApJ, 428, 574

Wolfe, A. M. 1988, in Proceedings of the QSO Absorption Line Meeting, p. 297

Wolfe, A. M., Fan, X., Tytler, D., Vogt, S. S., Keane, M. J., Lanzetta, K. M. 1994, ApJ, 435, L101

Wolfe, A. M., Lanzetta, K. M., Foltz, C. B., Chaffee, F. H. 1995, ApJ, 454, 698+

Wolfe, A. M., Turnshek, D. A., Lanzetta, K. M., Lu, L. 1993, ApJ, 404, 480

Wolfe, A. M., Turnshek, D. A., Smith, H. E., Cohen, R. D. 1986, ApJS, 61, 249

Zheng, W., Tsvetanov, Z. I., Schneider, D. P., Fan, X., Becker, R. H., Davis, M., White, R. L., Strauss, M. A., Anderson, J. E., Annis, J., Bahcall, N. A., Connolly, A. J., Csabai, I. ., Davidsen, A. F., Fukugita, M., Gunn, J. E., Heckman, T. M., Hennessy, G. S., Ivezić, Ž., Knapp, G. R., Lupton, R. H., Peng, E., Szalay, A. S., Thakar, A. R., Yanny, B., York, D. G. 2000, AJ, 120, 1607

Zickgraf, F. ., Voges, W., Krautter, J., Thiering, I., Appenzeller, I., Mujica, R., Serrano, A. 1997, A&A, 323, L21

Zuo, L., Lu, L. 1993, ApJ, 418, 601+

Appendix A

Normalised Quasar Spectra

The following figure shows the normalised quasar spectra. The error arrays are plotted as dotted lines, offset below the spectra for clarity. In the upper left-hand corner, the blue region of the spectra are magnified to make the Lyman-limit systems and damped Lyα absorbers easier to see. Damped Lyα absorbers are marked below there positions as solid stars if they have estimated column densities $N_{\rm HI} \geq 2 \times 10^{20}$ atoms cm^{-2}, and as open stars if they have estimated column densities lower than this threshold, but greater than 5×10^{19} atoms cm^{-2}. To the right of the stars marking the DLA are the detected metal lines that are associated with this absorber. To the left of the stars are an upward arrow marking the position of Lyβ at the DLA redshift and a downward arrow marking the wavelength of the Lyman-limit that would be associated with this DLA.

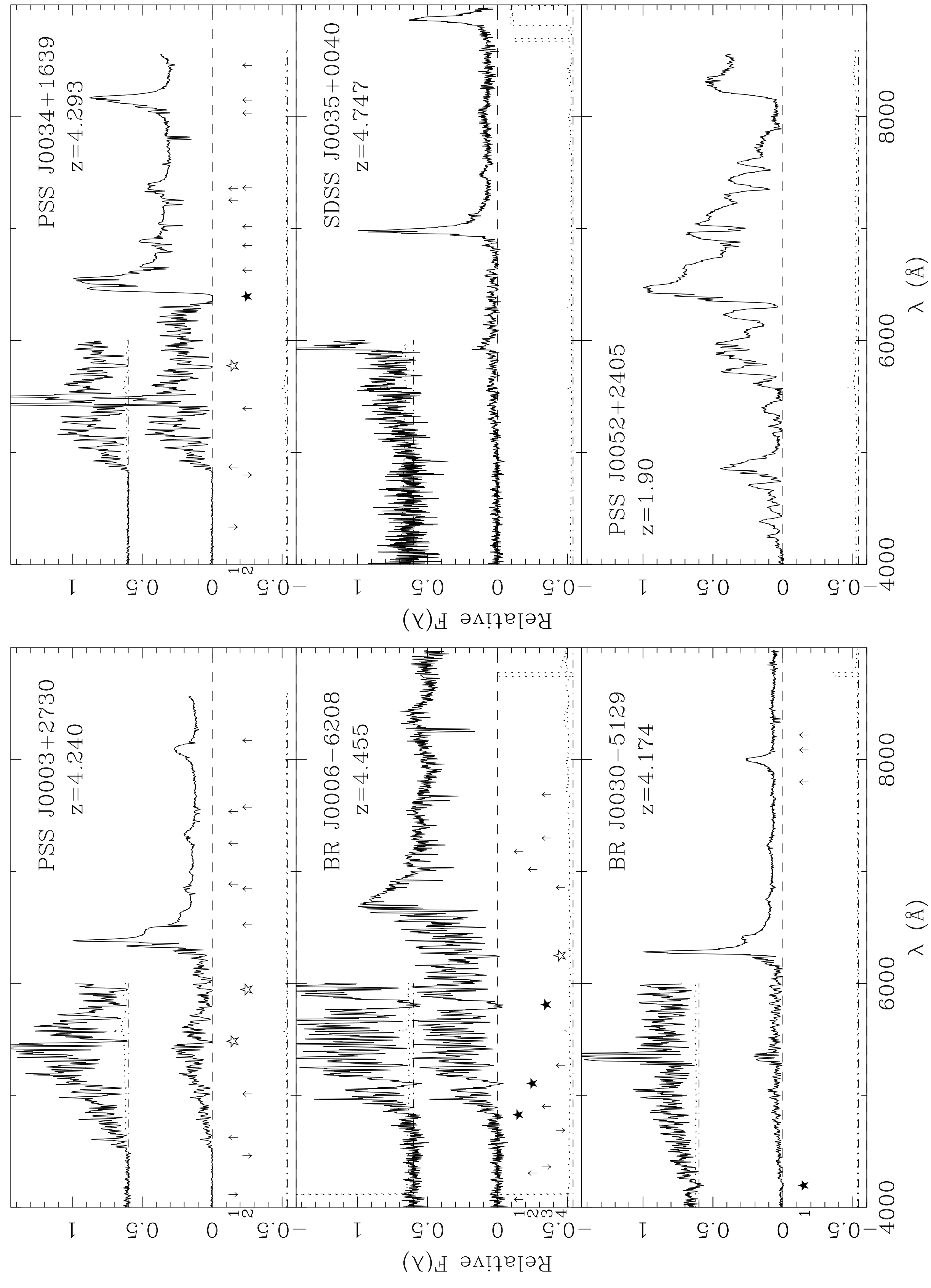

Fig. 1.— Normalised Quasar Spectra.

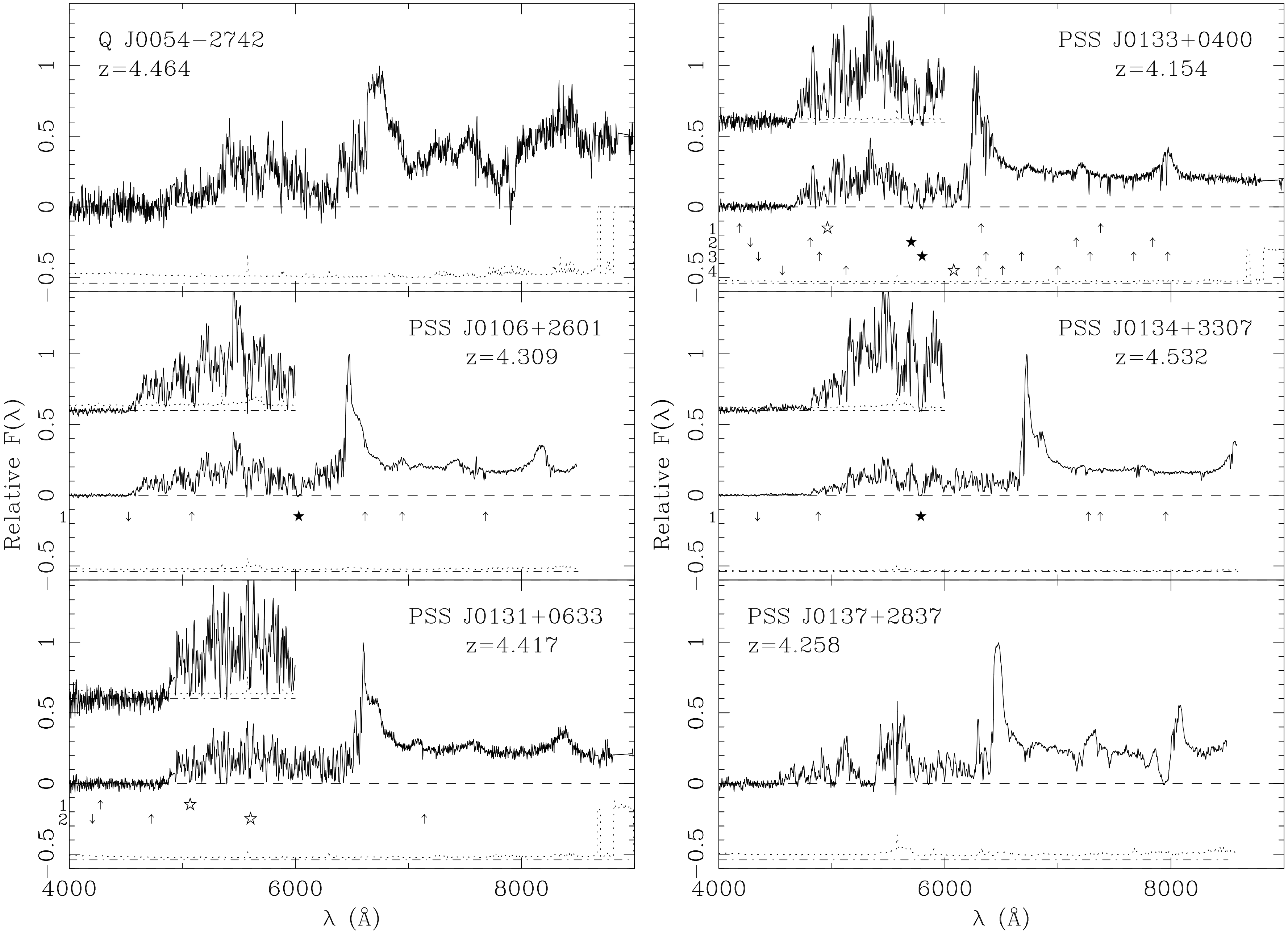

Fig. 1.— *continued*

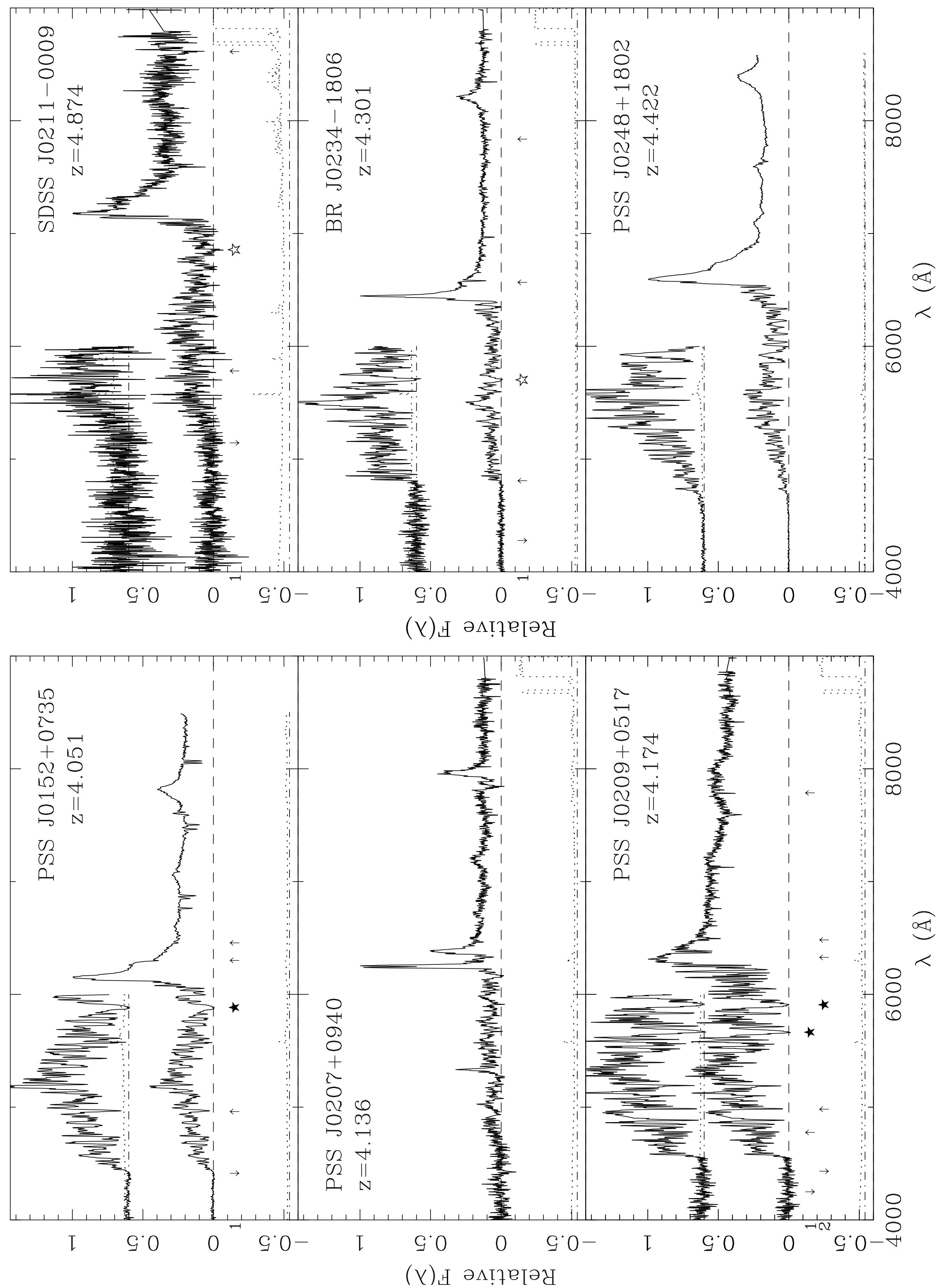

Fig. 1.— *continued*

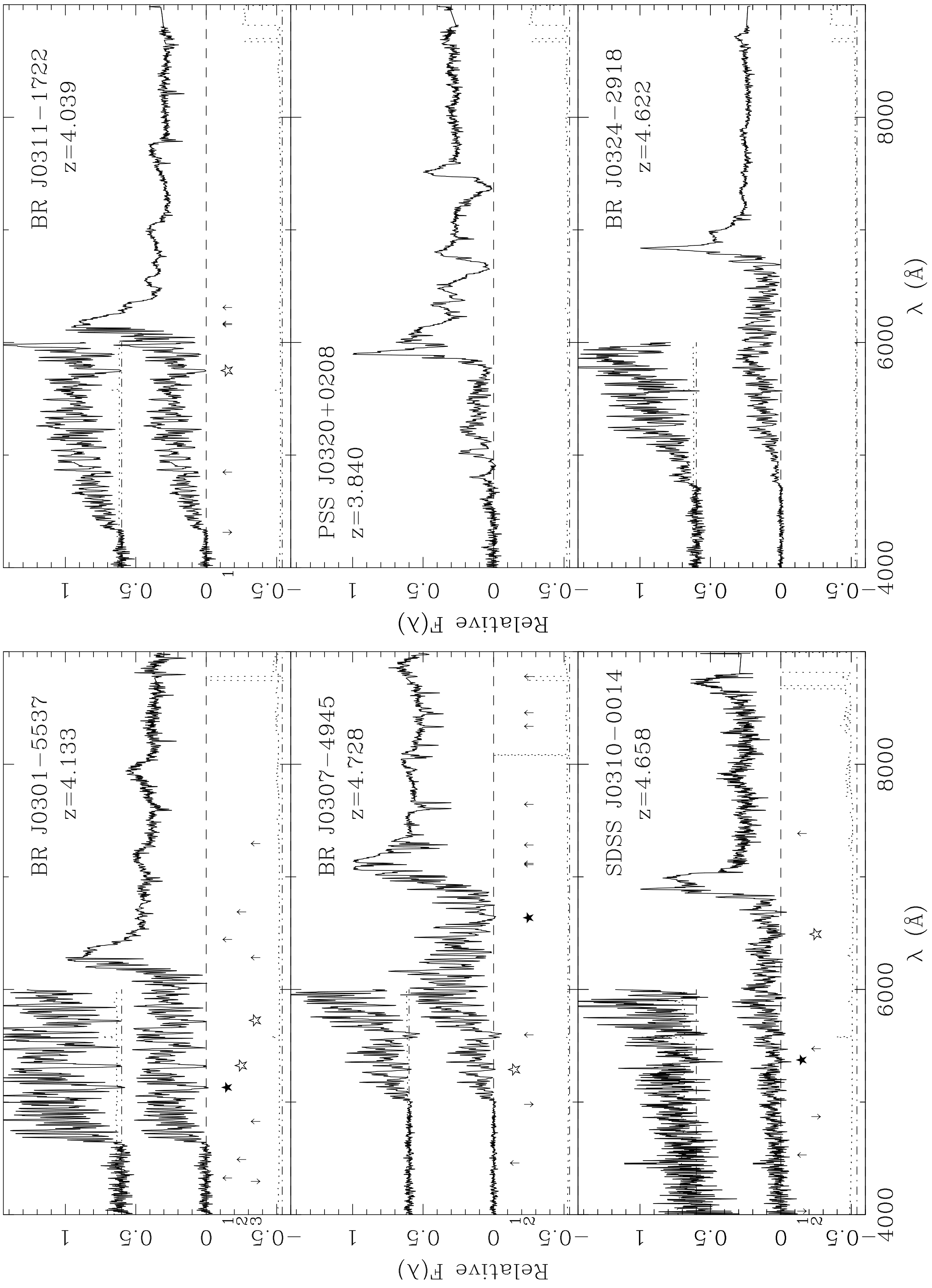

Fig. 1.— *continued*

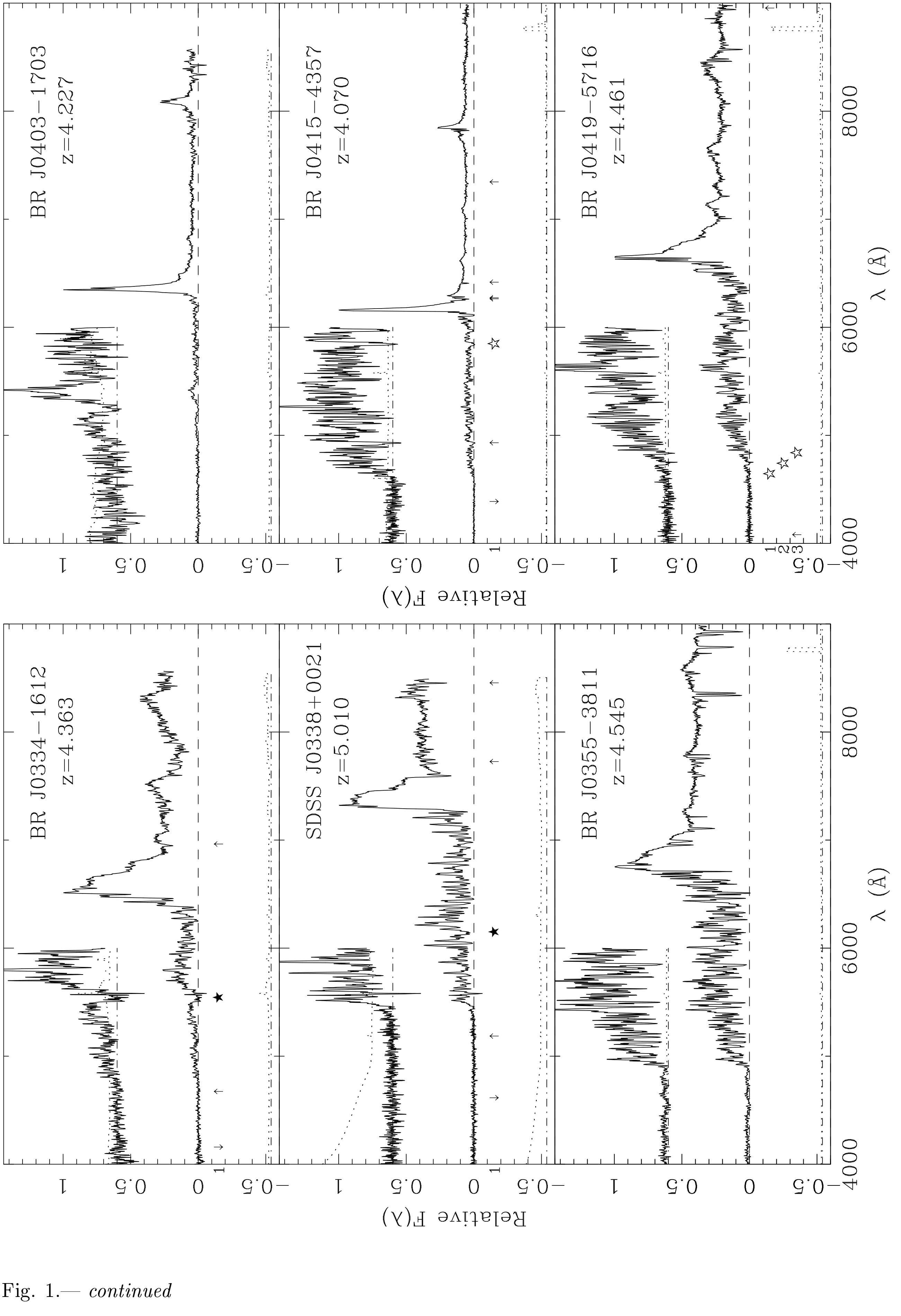

Fig. 1.— *continued*

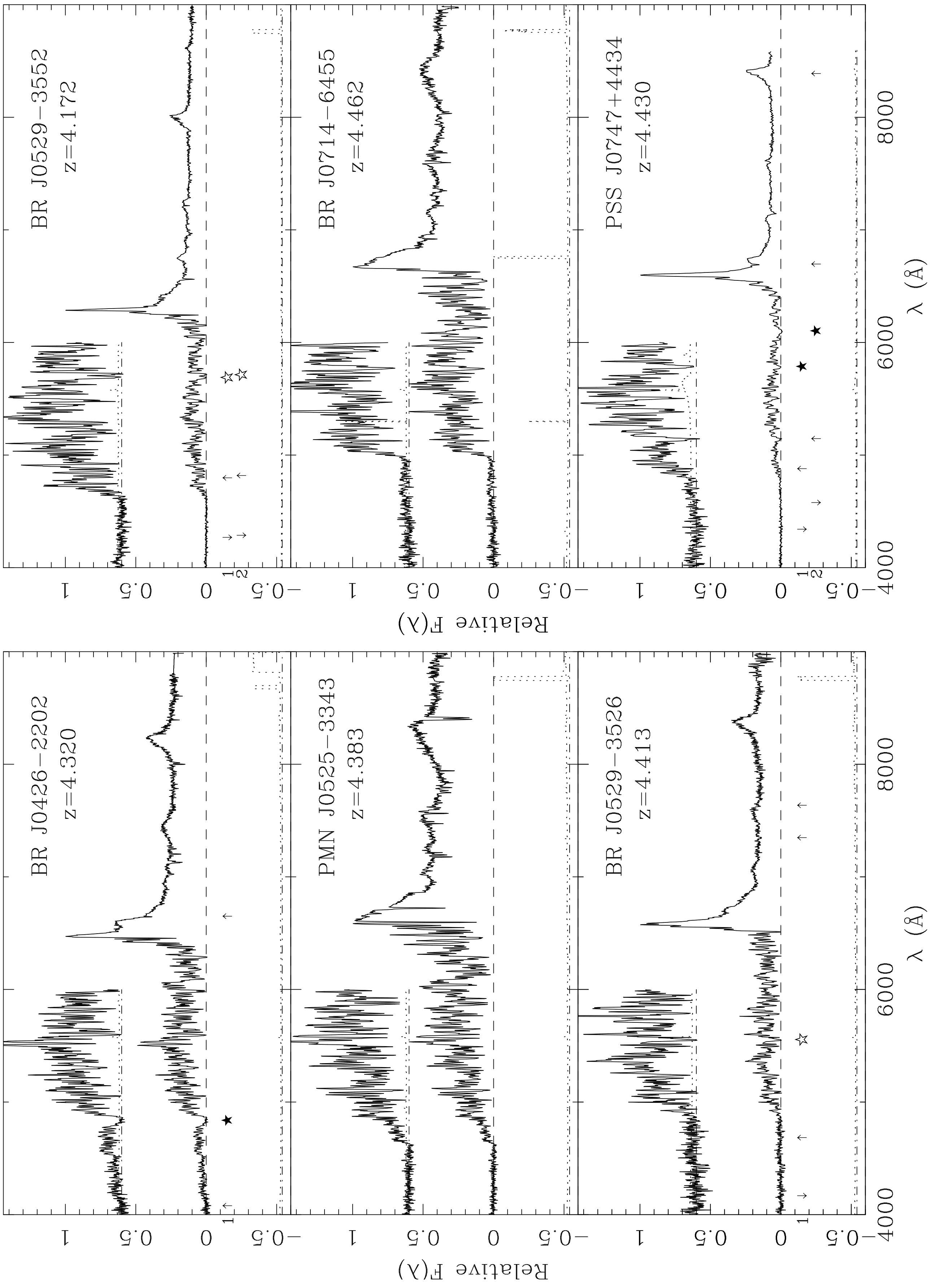

Fig. 1.— *continued*

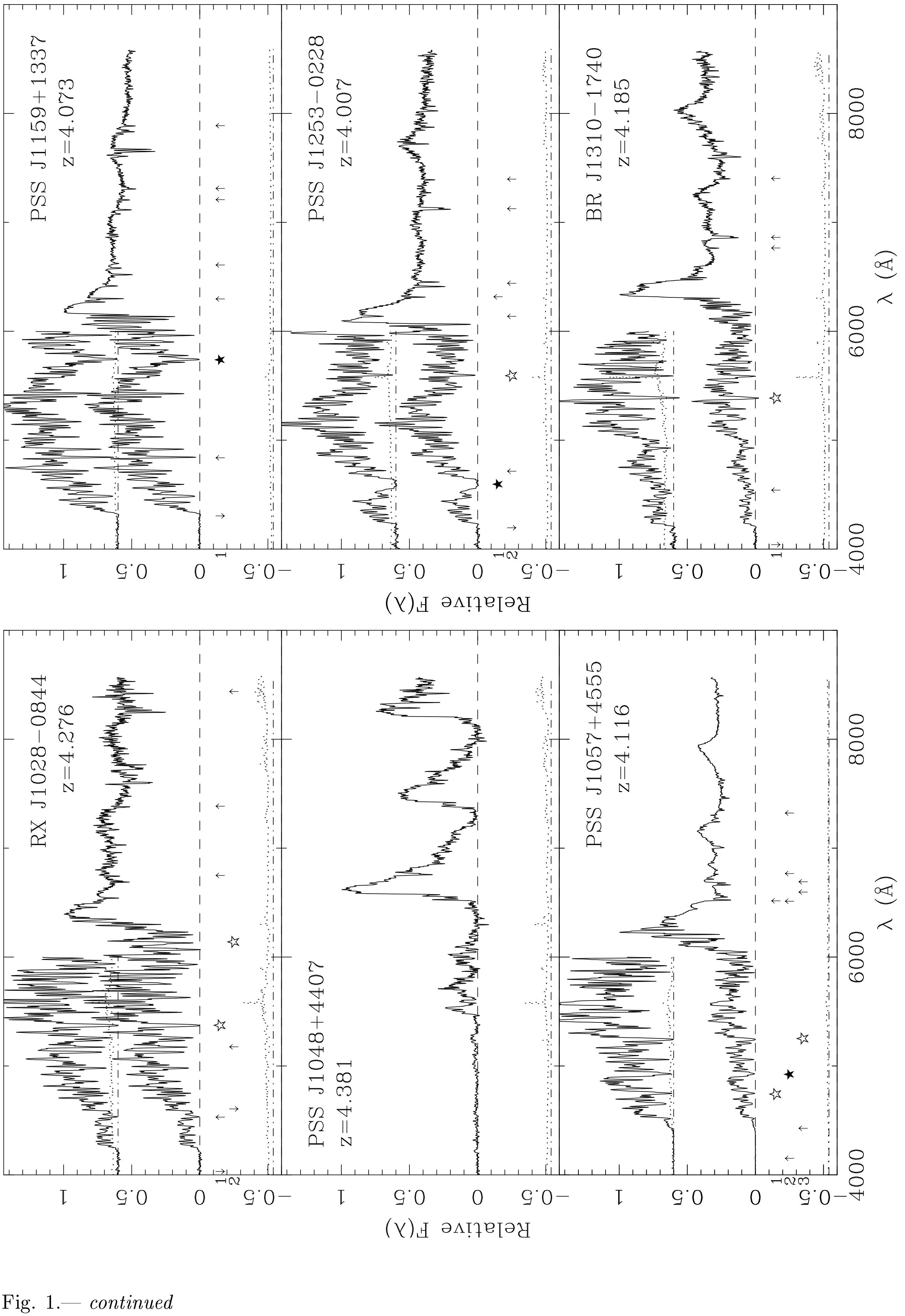

Fig. 1.— *continued*

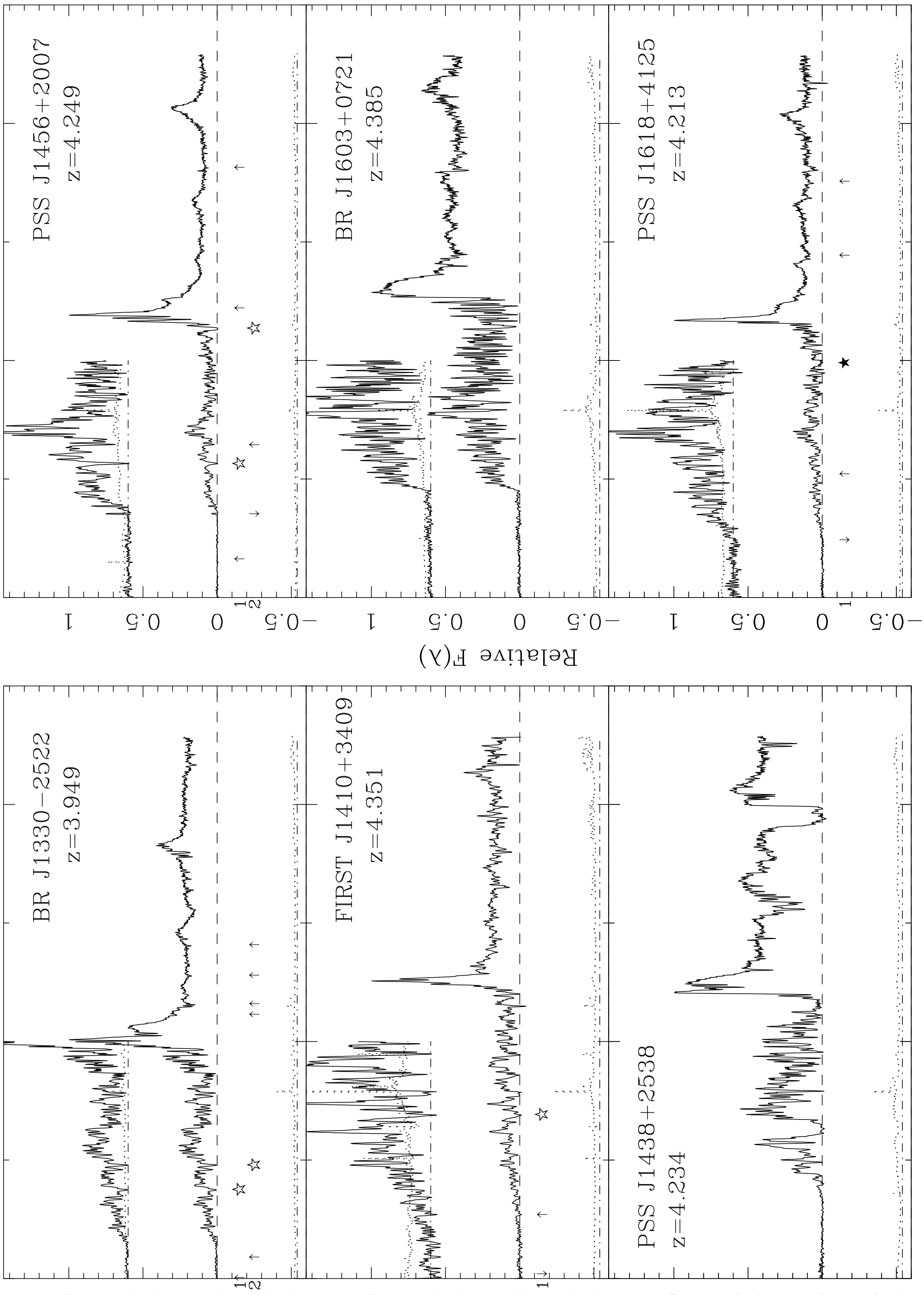

Fig. 1.— *continued*

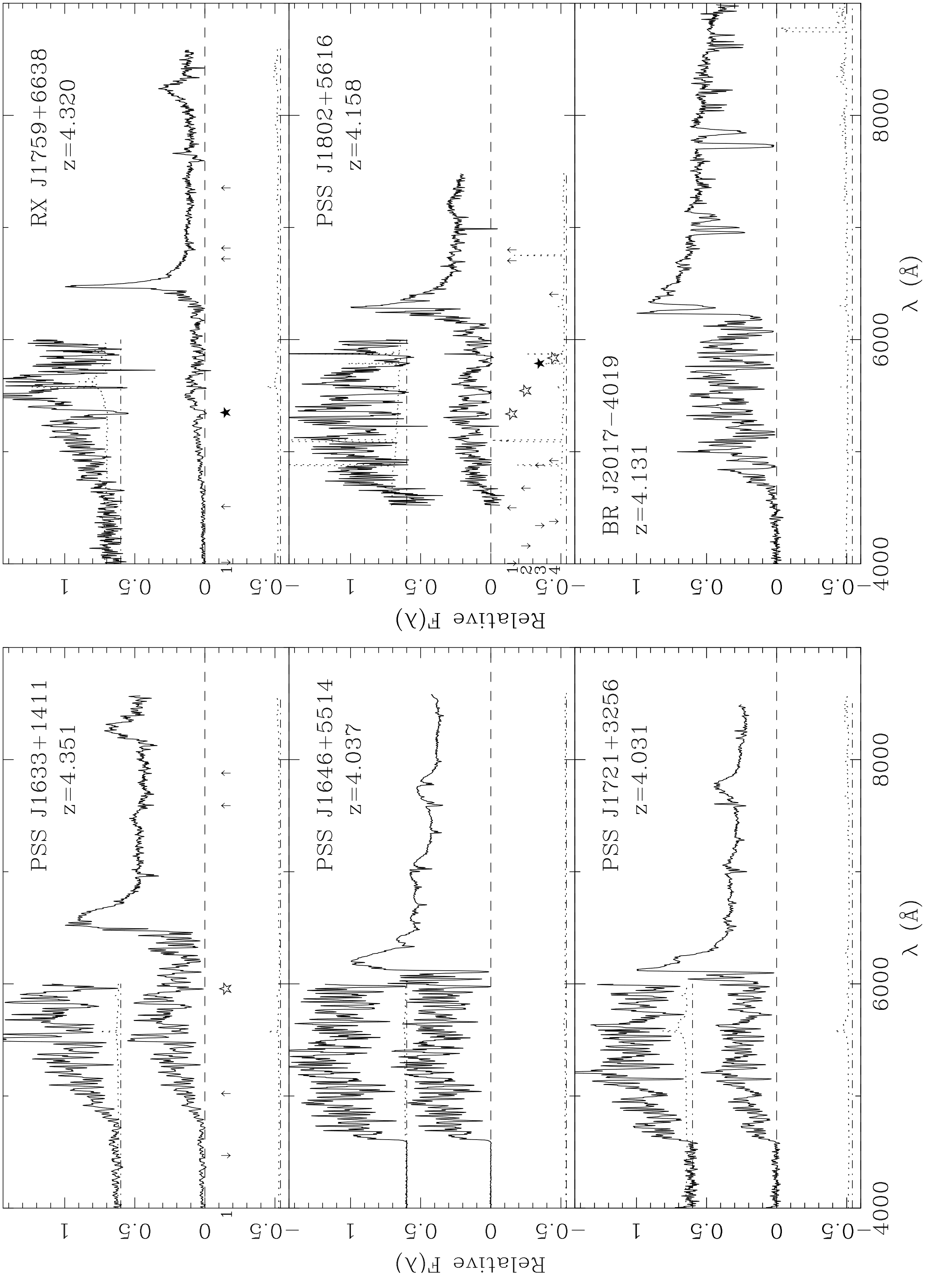

Fig. 1.— *continued*

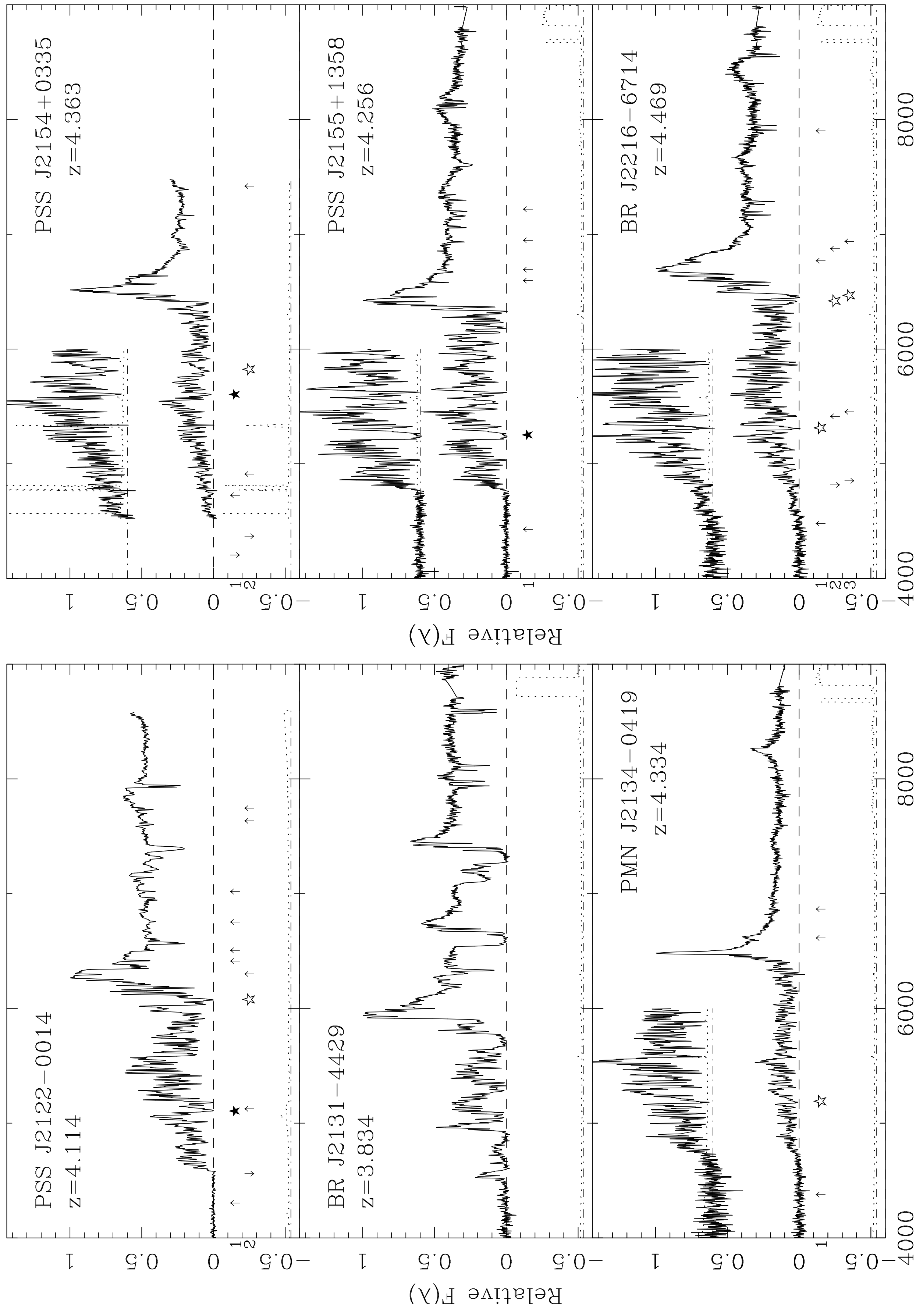

Fig. 1.— *continued*

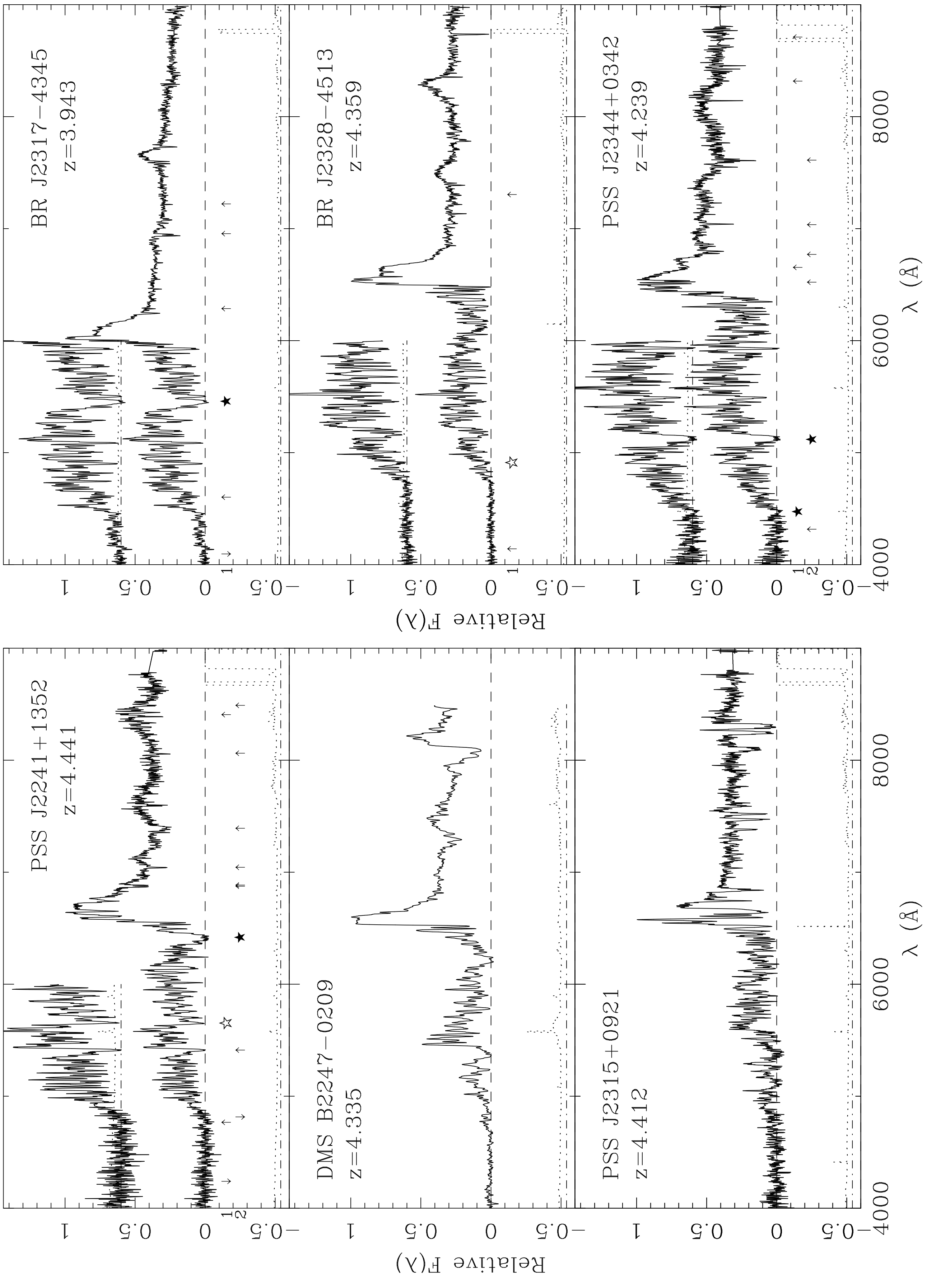

Fig. 1.— *continued*

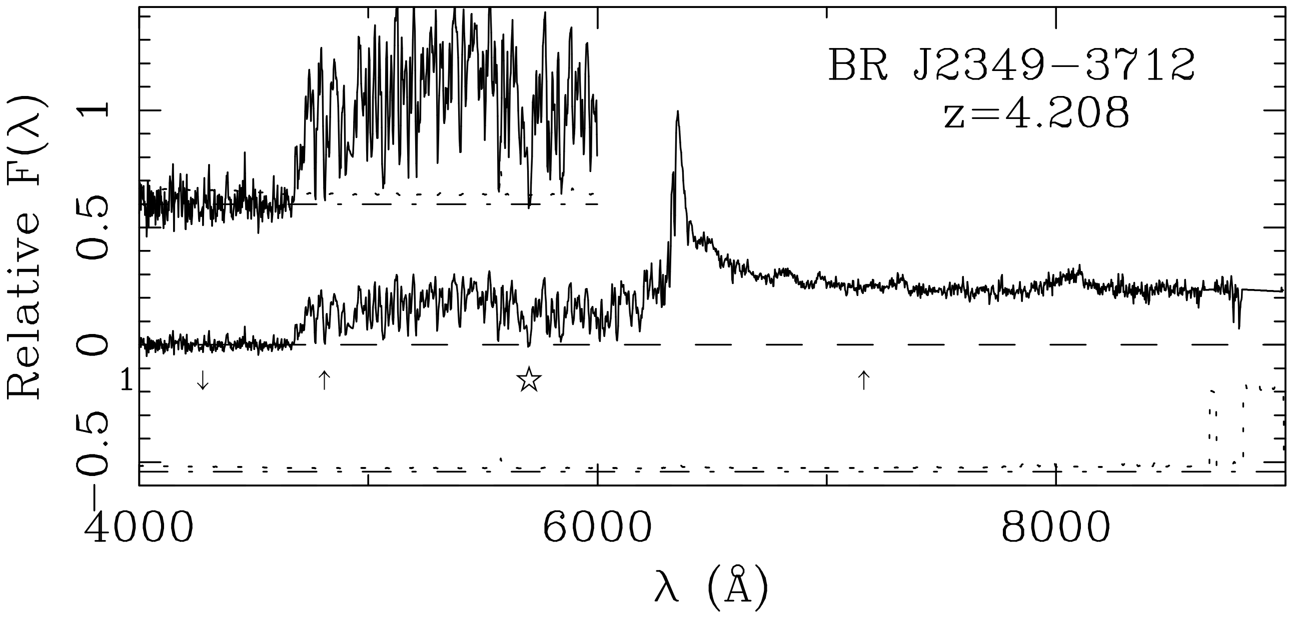

Fig. 1.— *continued*

Appendix B

Metal systems

This Table summarises the observed equivalent width and wavelength of every absorption line detected redward of the quasar Lyman-α emission and which were measured using the algorithm described in Chapter 5. The features which were not associated with a DLA or LLS were identified using the line list in Table 3. Most of the detected Mg II systems also show associated Fe II absorption. This survey resulted in the detection of 80 new C IV systems ($3.0 \lesssim z \lesssim 4.5$) and 48 new MgII systems ($1.3 \lesssim z \lesssim 2.2$).

TABLE 1—Identification of Metal Absorption Lines

Quasar	z_{em}	$\lambda_{\rm obs}$ (Å)	$W_{\rm obs}$ (Å)	Ion	$\lambda_{\rm rest}$ (Å)	z
PSS J0003+2730	4.240	6530.3	5.6	C II	1334	3.893
		6819.2	2.1	Si IV	1393	3.893
		6863.6	1.6	Si IV	1402	3.893
		6889.8	1.4	Si II	1527	3.513
		7254.7	1.7	Fe II	1608	3.510
		7320.6	1.3	C IV	1548	3.729
		7332.6	0.8	C IV	1551	3.728
		7468.7	3.3	Si II	1527	3.892
		7538.6	2.3	Al II	1671	3.512
		7574.3	3.9	C IV	1548	3.892
		7589.6	2.7	C IV	1551	3.894
		8042.5	0.9	C IV	1548	4.195
		8054.2	0.5	C IV	1551	4.194
		8078.6	0.4	···	···	···
		8172.2	3.6	Al II	1671	3.891
		8293.3	2.4	Mg II	2796	1.966
		8314.8	1.4	Mg II	2803	1.966
BR J0006-6208	4.455	6744.9	0.9	Al II	1608	3.193
		6872.2	0.6	C II	1334	4.150
		6903.8	0.9	···	···	···
		6933.6	2.4	Fe II	2344	1.958
		7022.1	2.5	Fe II	2374	1.957
		7033.3	2.0	···	···	···
		7048.1	4.7	Fe II	2383	1.958
		7105.9	1.6	···	···	···
		7168.6	1.3	Si II	1808	2.965
		7252.8	2.0	···	···	···
		7292.0	1.2	Si II	1527	3.776
		7428.1	0.7	···	···	···
		7650.6	2.6	Fe II	2586	1.958
		7689.2	4.3	Fe II	2600	1.957
		···	or	Fe II	1608	3.781
		8271.8	6.1	Mg II	2796	1.958
		8292.6	5.4	Mg II	2803	1.958
		8396.7	1.1	···	···	···
		8438.4	1.4	Mg I	2853	1.958

TABLE 1—*Continued*

Quasar	z_{em}	$\lambda_{\rm obs}$ (Å)	$W_{\rm obs}$ (Å)	Ion	$\lambda_{\rm rest}$ (Å)	z
BR J0030−5129	4.174	6743.6	2.3	···	···	···
		6869.0	2.6	C IV	1548	3.437
		6880.3	1.4	C IV	1551	3.437
		7165.8	1.3	···	···	···
		7224.4	1.2	···	···	···
		7658.7	1.7	C IV	1548	3.947
		7670.6	1.6	C IV	1551	3.946
		7798.2	1.2	Fe II	2261	2.449
		8091.6	2.7	Fe II	2344	2.452
		8223.0	1.8	Fe II	2383	2.451
		8355.1	5.0	···	···	···
		8384.6	3.7	···	···	···
		8987.4	2.9	···	···	···
		9002.7	3.8	···	···	···
PSS J0034+1639	4.293	6521.3	4.8	N V	1240	4.259
		6560.3	2.6	Fe II	2344	1.798
		6620.2	1.5	Si II	1260	4.252
		6645.1	1.4	Fe II	2374	1.799
		6657.1	3.0	C IV	1548	3.300
		6668.3	3.2	Fe II	2383	1.799
		···	or	C IV	1551	3.300
		6817.1	4.7	···	···	···
		6836.6	0.9	···	···	···
		6851.8	0.5	O I	1302	4.262
		6878.7	3.4	C IV	1548	3.443
		6890.6	2.2	C IV	1551	3.443
		6932.8	1.9	C IV	1548	3.478
		6945.6	1.3	C IV	1551	3.479
		7007.8	1.1	···	···	···
		7049.2	3.9	C II	1334	4.282
		7238.6	3.4	···	···	···
		7255.0	1.3	Si II	1527	3.752
		7279.9	4.8	Fe II	2600	1.800
		7318.9	0.6	···	···	···
		7330.5	1.1	···	···	···
		7361.5	2.2	Si IV	1393	4.281

TABLE 1—*Continued*

Quasar	z_{em}	$\lambda_{\rm obs}$ (Å)	$W_{\rm obs}$ (Å)	Ion	$\lambda_{\rm rest}$ (Å)	z
		···	or	C IV	1549	3.752
		7407.0	0.9	Si IV	1402	4.281
		7825.9	4.9	Mg II	2796	1.799
		7845.8	4.2	Mg II	2803	1.799
		7983.2	0.6	Mg I	2853	1.798
		8063.7	2.3	Si II	1527	4.282
		8089.6	4.2	C IV	1548	4.225
		8103.4	2.1	C IV	1551	4.225
		8131.5	1.4	···	···	···
		8176.1	1.2	C IV	1548	4.281
		8190.5	0.8	C IV	1551	4.282
		8495.0	1.5	Fe II	1608	4.281
SDSS J0035+0040	4.747	7132.3	2.4	N V	1240	4.752
		8736.1	2.5	···	···	···
		9002.2	5.1	···	···	···
PSS J0106+2601	4.309	6617.0	1.3	C II	1334	3.958
		6798.8	2.4	···	···	···
		6846.3	1.3	···	···	···
		6864.5	1.3	···	···	···
		6909.3	2.0	Si IV	1393	3.957
		6955.5	1.3	Si IV	1402	3.958
		7465.1	1.5	C IV	1548	3.822
		7477.5	0.7	C IV	1551	3.822
		7494.4	2.2	···	···	···
		7677.9	3.2	C IV	1548	3.959
		7690.2	2.0	C IV	1551	3.959
		8014.1	1.5	···	···	···
		8230.3	2.2	···	···	···
		8249.1	1.3	···	···	···
		8268.2	1.9	···	···	···
PSS J0131+0633	4.417	6770.6	1.0	···	···	···
		6792.0	1.3	···	···	···
		7135.7	1.5	C IV	1549	3.607
		7420.4	1.7	···	···	···
		9003.4	2.9	···	···	···
		9153.0	2.7	···	···	···

TABLE 1—*Continued*

Quasar	z_{em}	$\lambda_{\rm obs}$ (Å)	$W_{\rm obs}$ (Å)	Ion	$\lambda_{\rm rest}$ (Å)	z
PSS J0133+0400	4.154	6293.6	1.9	Si II	1260	3.993
		6320.8	5.6	C IV	1548	3.083
		6349.0	4.8	Fe II	2383	1.665
		6367.7	6.4	C II	1334	3.771
		6403.4	2.9	C IV	1548	3.136
		6414.0	1.4	C IV	1551	3.136
		6437.7	1.6	Si IV	1393	3.619
		6476.7	1.4	Si IV	1402	3.617
		6503.1	2.1	O I	1302	3.994
		6649.5	2.4	Si IV	1393	3.771
		6665.8	2.6	···	···	···
		6694.3	1.5	Si IV	1402	3.772
		6891.3	2.2	Fe II	2586	1.664
		6963.1	3.8	Si IV	1393	3.996
		7001.9	2.5	Si IV	1402	3.991
		7128.9	3.2	···	···	···
		7149.5	2.3	C IV	1548	3.618
		7162.3	1.9	C IV	1551	3.619
		···	or	Si II	1527	3.691
		7176.0	0.9	···	···	···
		7214.8	0.9	···	···	···
		7284.1	4.3	Si II	1527	3.771
		7385.7	3.5	Si II	1808	3.085
		7450.1	4.6	Mg II	2796	1.664
		7469.4	4.4	Mg II	2803	1.664
		7599.2	4.3	Mg I	2853	1.664
		7623.1	1.7	Si II	1527	3.993
		7672.9	3.7	Fe II	1608	3.770
		7836.7	0.9	Al II	1671	3.690
		7855.1	1.1	···	···	···
		7919.3	5.5	C IV	1548	4.115
		7933.0	3.1	C IV	1551	4.116
		7971.6	4.7	Al II	1671	3.771
		8070.1	0.9	···	···	···
		8085.7	2.3	···	···	···
		8105.5	1.4	···	···	···

TABLE 1—*Continued*

Quasar	z_{em}	λ_{obs} (Å)	W_{obs} (Å)	Ion	λ_{rest} (Å)	z
PSS J0134+3307	4.532	6744.5	1.9	···	···	···
		6834.8	2.2	···	···	···
		6856.5	1.4	···	···	···
		7129.4	1.2	Fe II	2586	1.756
		7166.4	2.3	Fe II	2600	1.756
		7255.3	2.9	C IV	1548	3.686
		7267.9	1.8	Si II	1527	3.761
		···	or	C IV	1551	3.686
		7391.9	1.8	C IV	1548	3.775
		7404.8	1.4	C IV	1551	3.775
		7689.0	1.4	Al II	1671	3.780
		7706.2	4.0	Mg II	2796	1.756
		7727.6	3.2	Mg II	2803	1.756
		7861.0	1.2	Mg I	2853	1.755
		8198.2	0.7	···	···	···
		8280.7	2.7	Mg II	2796	1.961
		8300.7	2.0	Mg II	2803	1.961
		8340.0	0.6	···	···	···
		8537.7	3.9	C IV	1548	4.515
		8552.5	3.3	C IV	1551	4.515
PSS J0152+0735	4.051	6304.2	2.5	O I	1302	3.841
		6462.3	0.5	C II	1334	3.842
		6770.3	2.9	Fe II	2344	1.888
		6858.9	3.5	Fe II	2374	1.888
		6882.4	4.6	Fe II	2383	1.888
		7093.9	1.3	···	···	···
		7445.3	2.4	···	···	···
		7473.3	4.4	Fe II	2586	1.888
		7512.8	3.8	Fe II	2600	1.888
		7685.4	0.8	···	···	···
		8061.1	5.3	Mg II	2796	1.883
		8080.0	5.3	Mg II	2803	1.882
		8208.5	0.8	···	···	···
PSS J0209+0517	4.174	6330.9	0.9	Si II	1304	3.854
		6377.3	3.7	Mg II	2796	1.281
		6393.0	2.6	Mg II	2803	1.280

TABLE 1—*Continued*

Quasar	z_{em}	$\lambda_{\rm obs}$ (Å)	$W_{\rm obs}$ (Å)	Ion	$\lambda_{\rm rest}$ (Å)	z
		6488.5	1.1	C II	1334	3.862
		6501.8	1.6	Mg I	2853	1.279
		6510.4	1.1	···	···	···
		6614.7	0.8	···	···	···
		6628.1	0.8	···	···	···
		6654.5	0.8	···	···	···
		6673.5	0.9	···	···	···
		6770.6	0.9	···	···	···
		6869.1	1.2	···	···	···
		7134.6	1.2	C IV	1548	3.608
		···	or	Si II	1527	3.673
		7145.9	0.7	C IV	1551	3.608
		7793.3	1.3	Al II	1671	3.664
		8123.6	1.9	···	···	···
SDSS J0211−0009	4.874	7199.9	1.3	C IV	1548	3.651
		7211.9	1.1	C IV	1551	3.651
		7227.4	4.3	···	···	···
		7262.9	2.2	···	···	···
		7411.0	2.4	···	···	···
		8122.3	4.2	···	···	···
		8618.6	0.0	Si II	1527	4.645
BR J0234−1806	4.301	6540.0	0.9	Si IV	1393	3.692
		6587.0	4.5	Si IV	1402	3.696
		6661.3	1.4	···	···	···
		6805.9	1.4	C IV	1548	3.396
		6818.3	1.5	C IV	1551	3.397
		6899.9	1.5	···	···	···
		6975.0	4.3	···	···	···
		7138.7	1.5	···	···	···
		7161.5	2.3	···	···	···
		7282.3	2.1	···	···	···
		7401.0	1.7	C IV	1548	3.780
		7413.2	1.2	C IV	1551	3.780
		7840.1	1.7	Al II	1671	3.692
		7956.1	2.0	···	···	···
		7980.3	2.1	···	···	···

TABLE 1—*Continued*

Quasar	z_{em}	$\lambda_{\rm obs}$ (Å)	$W_{\rm obs}$ (Å)	Ion	$\lambda_{\rm rest}$ (Å)	z
		8092.6	3.8	C IV	1548	4.227
		8107.9	1.8	C IV	1551	4.228
		8260.8	2.1	···	···	···
		8356.2	3.7	···	···	···
		8732.8	4.4	···	···	···
PSS J0248+1802	4.422	6682.8	0.3	···	···	···
		6865.3	0.4	Si IV	1393	3.926
		6885.0	0.8	Si IV	1393	3.939
		6910.3	0.6	Si IV	1402	3.926
		6928.5	0.8	Si IV	1402	3.939
		7184.1	0.4	···	···	···
		7646.1	2.8	C IV	1548	3.939
		7660.7	1.2	C IV	1551	3.940
		7788.9	1.1	···	···	···
BR J0301−5537	4.133	6278.7	3.2	C II	1334	3.705
		6357.7	1.0	···	···	···
		6409.2	0.8	···	···	···
		6421.9	0.9	···	···	···
		6442.2	0.9	Si II	1527	3.220
		6483.5	1.3	···	···	···
		6544.2	0.5	···	···	···
		6660.6	1.2	···	···	···
		6681.6	0.9	Si II	1527	3.377
		6970.3	2.2	···	···	···
		6999.3	1.3	···	···	···
		7219.3	0.5	···	···	···
		7281.2	1.7	C IV	1549	3.701
		7813.6	1.7	···	···	···
		8216.8	2.7	···	···	···
		8624.8	1.7	···	···	···
		8807.5	4.9	···	···	···
		8954.4	5.8	···	···	···
BR J0307−4945	4.728	7105.0	0.9	···	···	···
		7117.0	2.8	O I	1302	4.465
		7129.6	2.3	Si II	1304	4.466
		7224.0	1.2	C IV	1548	3.666

TABLE 1—*Continued*

Quasar	z_{em}	$\lambda_{\rm obs}$ (Å)	$W_{\rm obs}$ (Å)	Ion	$\lambda_{\rm rest}$ (Å)	z
		7235.6	0.8	C IV	1551	3.666
		7261.9	4.2	Si IV	1393	4.210
		7271.9	2.8	Si IV	1393	4.217
		7293.8	4.0	C II	1334	4.465
		7308.4	3.1	Si IV	1402	4.210
		7318.3	1.0	Si IV	1402	4.217
		7382.6	0.7	···	···	···
		7469.2	1.1	C IV	1548	3.824
		7482.4	0.7	C IV	1551	3.825
		7615.2	8.4	Si IV	1393	4.464
		7667.2	4.0	Si IV	1402	4.466
		7961.3	2.3	···	···	···
		8067.0	2.6	C IV	1548	4.210
		8077.9	3.6	C IV	1551	4.210
		···	and	C IV	1548	4.217
		8091.0	2.4	C IV	1551	4.217
		8180.1	2.0	···	···	···
		8345.0	2.8	Si II	1527	4.466
		8459.7	2.3	C IV	1548	4.464
		8473.2	1.2	C IV	1551	4.464
		8509.3	1.5	···	···	···
		8645.0	2.2	···	···	···
		8791.5	1.1	Fe II	1608	4.466
		8890.3	1.2	···	···	···
		8990.0	1.4	···	···	···
		9132.9	3.4	Al II	1671	4.466
		9155.4	1.7	···	···	···
		9175.6	1.9	···	···	···
SDSS J0310−0014	4.658	6921.0	7.1	Mg II	2796	1.475
		6939.6	4.1	Mg II	2803	1.475
		6955.3	4.6	O I	1302	4.341
		6976.8	3.2	···	···	···
		7049.2	3.6	···	···	···
		7126.0	1.6	C II	1334	4.340
		7391.4	3.5	Al II	1671	3.424
		7467.5	4.1	···	···	···

TABLE 1—*Continued*

Quasar	z_{em}	$\lambda_{\rm obs}$ (Å)	$W_{\rm obs}$ (Å)	Ion	$\lambda_{\rm rest}$ (Å)	z
		7706.3	0.0	···	···	···
		8229.9	3.6	···	···	···
		8655.0	0.0	···	···	···
		9086.7	6.9	···	···	···
BR J0311−1722	4.039	6163.0	0.6	O I	1302	3.733
		6173.3	0.8	Si II	1304	3.733
		6316.0	1.0	C II	1334	3.733
		6379.3	2.2	···	···	···
		6421.2	0.5	···	···	···
		6464.8	1.1	···	···	···
		6476.3	0.9	···	···	···
		6489.7	2.1	···	···	···
		6767.5	1.6	···	···	···
		7006.4	1.1	Fe II	2383	1.940
		7078.6	1.0	···	···	···
		7087.8	0.9	···	···	···
		7138.3	0.9	···	···	···
		7645.6	1.9	Fe II	2600	1.940
		7794.7	4.6	Mg II	2796	1.787
		7810.0	3.1	Mg II	2803	1.786
		8220.9	4.0	Mg II	2796	1.940
		8241.4	1.9	Mg II	2803	1.940
BR J0324−2918	4.622	6899.4	1.2	···	···	···
		6987.6	0.6	···	···	···
		7098.6	2.5	C IV	1548	3.585
		7110.7	1.4	C IV	1551	3.585
		7137.8	1.7	···	···	···
		7206.6	0.8	···	···	···
		7416.9	1.8	···	···	···
		7454.7	0.6	···	···	···
		7483.8	0.8	···	···	···
		7528.6	0.6	···	···	···
		7643.4	1.1	Fe II	2367	2.228
		7692.4	1.1	Fe II	2383	2.228
		7874.3	1.1	···	···	···
		8064.1	1.1	···	···	···

TABLE 1—*Continued*

Quasar	z_{em}	$\lambda_{\rm obs}$ (Å)	$W_{\rm obs}$ (Å)	Ion	$\lambda_{\rm rest}$ (Å)	z
		8179.5	0.8	···	···	···
		8291.6	1.2	Si II	1808	3.586
		8349.7	1.1	Fe II	2586	2.228
		8391.9	1.5	Fe II	2600	2.227
		8542.8	1.0	···	···	···
		8624.3	3.4	···	···	···
		9026.9	2.6	Mg II	2796	2.228
		9050.4	1.4	Mg II	2803	2.228
		9062.7	1.2	···	···	···
		9131.6	1.2	···	···	···
BR J0334−1612	4.363	6560.8	1.4	···	···	···
		6957.9	4.9	Si II	1527	3.558
		7284.8	2.3	C IV	1548	3.705
		7295.2	2.5	C IV	1551	3.704
		7364.7	2.2	C IV	1548	3.757
		7375.2	2.4	C IV	1551	3.756
		7667.6	6.9	···	···	···
		7682.5	2.9	···	···	···
		7698.1	8.4	···	···	···
		7737.2	6.6	···	···	···
		7825.1	5.8	···	···	···
SDSS J0338+0021	5.010	7323.1	1.8	···	···	···
		7722.9	4.9	Si II	1527	4.059
		7756.8	3.5	···	···	···
		8352.1	3.9	···	···	···
		8466.5	5.5	Al II	1671	4.067
BR J0355−3811	4.545	6776.8	1.8	C IV	1548	3.377
		6787.0	1.4	C IV	1551	3.377
		6858.1	0.5	···	···	···
		6871.2	0.5	···	···	···
		6960.1	3.2	···	···	···
		6997.4	4.6	Fe II	2344	1.985
		7091.0	1.0	Fe II	2374	1.986
		7116.9	4.9	Fe II	2383	1.987
		7223.9	1.0	···	···	···
		7414.2	0.8	Si IV	1393	4.319

TABLE 1—*Continued*

Quasar	z_{em}	$\lambda_{\rm obs}$ (Å)	$W_{\rm obs}$ (Å)	Ion	$\lambda_{\rm rest}$ (Å)	z
		7464.1	1.2	Si IV	1402	4.321
		7695.6	1.3	···	···	···
		7723.5	2.1	Fe II	2586	1.986
		7746.1	0.6	···	···	···
		7765.5	4.1	Fe II	2600	1.987
		7799.3	1.6	···	···	···
		8237.6	1.3	C IV	1548	4.321
		8250.7	0.7	C IV	1551	4.320
		8296.7	1.5	C IV	1548	4.359
		8309.9	1.6	C IV	1551	4.359
		8350.7	10.5	Mg II	2796	1.986
		8372.4	8.9	Mg II	2803	1.986
		8488.1	0.5	···	···	···
		8519.4	1.1	Mg I	2853	1.986
		8552.6	2.2	C IV	1548	4.524
		8568.7	1.3	C IV	1551	4.525
		8739.8	1.1	···	···	···
		8797.4	9.4	···	···	···
		8911.2	5.0	···	···	···
		8941.6	10.8	···	···	···
BR J0403−1703	4.227	7897.6	10.4	···	···	···
		7932.8	10.6	···	···	···
		8112.9	2.3	···	···	···
		8303.2	10.2	···	···	···
BR J0415−4357	4.070	6236.6	2.1	···	···	···
		6257.8	5.1	O I	1302	3.806
		6268.4	6.5	Si II	1304	3.806
		6286.2	4.6	···	···	···
		6413.6	3.5	C II	1334	3.806
		7012.8	1.4	···	···	···
		7339.6	2.6	Si II	1527	3.808
		7782.0	1.4	···	···	···
		7793.9	3.4	···	···	···
		7831.6	5.8	C IV	1548	4.059
		7844.5	5.5	C IV	1551	4.058
BR J0419−5716	4.461	6728.3	0.5	···	···	···

TABLE 1—*Continued*

Quasar	z_{em}	$\lambda_{\rm obs}$ (Å)	$W_{\rm obs}$ (Å)	Ion	$\lambda_{\rm rest}$ (Å)	z
		6843.6	1.6	···	···	···
		7013.9	2.1	Mg II	2796	1.508
		7031.7	1.6	Mg II	2803	1.508
		7103.6	1.3	Fe II	2344	2.030
		7221.0	2.1	Fe II	2383	2.031
		7375.8	1.0	···	···	···
		7527.8	0.7	···	···	···
		7878.2	2.6	Fe II	2600	2.030
		8080.3	2.4	···	···	···
		8181.1	0.7	···	···	···
		8417.9	1.4	···	···	···
		8438.6	1.3	···	···	···
		8474.0	5.2	Mg II	2796	2.030
		8494.9	3.4	Mg II	2853	2.030
		8582.6	6.6	···	···	···
		8953.4	4.2	···	···	···
BR J0426−2202	4.320	6652.8	0.6	Al II	1671	2.982
		6767.4	1.1	···	···	···
		7031.4	1.8	···	···	···
		7134.9	4.1	C IV	1548	3.609
		7147.0	1.4	C IV	1551	3.609
		7210.9	2.1	Si IV	1393	4.174
		7257.3	1.2	Si IV	1402	4.174
		8010.9	2.5	C IV	1548	4.174
		8024.2	2.1	C IV	1551	4.174
		8278.1	1.8	···	···	···
		8291.4	1.0	···	···	···
		8405.5	0.9	···	···	···
		9001.4	1.4	Fe II	2260	2.982
		9024.2	1.3	···	···	···
PMN J0525−3343	4.383	6604.0	7.8	···	···	···
		6682.0	0.7	Fe II	2600	1.570
		6728.8	6.0	···	···	···
		7185.3	2.2	Mg II	2796	1.570
		7204.1	2.2	Mg II	2853	1.570
		7223.9	0.8	···	···	···

TABLE 1—*Continued*

Quasar	z_{em}	$\lambda_{\rm obs}$ (Å)	$W_{\rm obs}$ (Å)	Ion	$\lambda_{\rm rest}$ (Å)	z
		7470.2	0.5	···	···	···
		7482.4	1.5	···	···	···
		7500.1	0.7	···	···	···
		7529.2	0.3	···	···	···
		7572.5	2.8	···	···	···
		7667.8	1.0	···	···	···
		7759.3	1.8	···	···	···
		7776.4	0.0	Fe II	2586	2.006
		7803.2	1.5	···	···	···
		7845.6	0.9	···	···	···
		7952.3	1.5	···	···	···
		8409.7	7.1	Mg II	2796	2.007
		8425.0	6.3	Mg II	2796	2.005
BR J0529−3526	4.413	6685.9	0.5	···	···	···
		6952.1	1.2	···	···	···
		7355.6	1.8	Fe II	1608	3.573
		7637.5	2.4	Al II	1671	3.571
BR J0529−3552	4.172	6527.2	1.1	···	···	···
		6567.7	3.6	···	···	···
		6608.7	0.7	Si II	1304	4.067
		6856.2	0.7	···	···	···
		6962.2	1.3	C IV	1548	3.497
		6975.0	2.1	C IV	1551	3.498
		7060.3	0.8	Si IV	1393	4.066
		7106.0	1.1	Si IV	1402	4.066
		7224.0	1.1	···	···	···
		7290.1	2.1	···	···	···
		7432.6	0.9	Mg II	2796	1.658
		7450.4	1.2	Mg II	2803	1.658
		7501.0	0.7	···	···	···
		7890.2	3.7	Si II	1526	4.168
		7993.6	1.3	C IV	1548	4.163
		8003.7	1.4	C IV	1551	4.161
BR J0714−6455	4.462	6717.3	0.7	···	···	···
		6845.4	0.6	···	···	···
		6926.2	0.8	···	···	···

TABLE 1—*Continued*

Quasar	z_{em}	$\lambda_{\rm obs}$ (Å)	$W_{\rm obs}$ (Å)	Ion	$\lambda_{\rm rest}$ (Å)	z
		7222.3	0.4	···	···	···
		7346.6	0.6	C IV	1548	3.745
		7356.3	1.5	C IV	1551	3.744
		···	or	C IV	1548	3.752
		7367.8	0.9	C IV	1551	3.751
		7654.7	1.9	···	···	···
		7694.2	2.2	C IV	1548	3.970
		7707.5	1.7	C IV	1551	3.970
		8044.3	2.1	C IV	1548	4.196
		8060.1	1.8	C IV	1551	4.197
		8242.5	0.9	···	···	···
		8984.7	5.0	···	···	···
PSS J0747+4434	4.430	6698.9	2.5	C II	1334	4.020
		7024.8	0.8	···	···	···
		7151.3	7.0	···	···	···
		7166.6	3.8	···	···	···
		7636.8	2.4	···	···	···
		8288.5	1.8	···	···	···
		8382.5	1.1	Al II	1671	4.017
RX J1028−0844	4.276	6463.8	2.0	···	···	···
		6551.4	1.4	···	···	···
		6697.4	1.0	···	···	···
		6709.3	1.2	···	···	···
		6751.8	1.2	Si II	1527	3.423
		6967.4	1.3	···	···	···
		7040.3	1.4	Fe II	2383	1.955
		7179.9	2.2	···	···	···
		7227.2	0.5	···	···	···
		7235.8	0.6	···	···	···
		7388.0	1.4	Al II	1671	3.422
		7682.1	1.3	Fe II	2600	1.954
		7737.0	2.5	C IV	1548	3.997
		7749.1	3.4	C IV	1551	3.997
		7777.1	1.3	···	···	···
		8261.2	4.4	Mg II	2796	1.954
		8280.4	2.4	Mg II	2803	1.954

TABLE 1—*Continued*

Quasar	z_{em}	$\lambda_{\rm obs}$ (Å)	$W_{\rm obs}$ (Å)	Ion	$\lambda_{\rm rest}$ (Å)	z
		8432.9	3.0	Mg I	2853	1.956
		···	or	Al II	1671	4.047
PSS J1057+4555	4.116	6315.9	1.4	Si IV	1393	3.532
		6356.8	1.1	Si IV	1402	3.532
		6452.5	1.7	···	···	···
		6532.0	4.2	Fe II	1608	3.061
		6559.8	2.4	C IV	1548	3.237
		6571.1	1.3	C IV	1551	3.237
		6589.1	0.8	Si II	1527	3.316
		6672.6	4.0	Mg II	2796	1.386
		6688.5	3.8	Mg II	2803	1.386
		6724.3	1.3	···	···	···
		6768.5	0.5	Al II	1671	3.051
		6806.3	0.4	Mg I	2853	1.386
		6875.2	0.6	···	···	···
		7018.1	4.0	C IV	1549	3.531
		7180.3	0.6	···	···	···
		7197.5	0.2	···	···	···
		7212.1	0.3	Al II	1671	3.317
		7251.4	1.9	Si II	1526	3.750
		7283.7	1.0	Fe II	1608	3.529
		7320.6	0.3	Si II	1808	3.049
		7358.7	1.0	C IV	1548	3.753
		7371.1	0.5	C IV	1551	3.753
		7469.9	1.9	C IV	1548	3.825
		7482.2	0.8	C IV	1551	3.825
		7574.0	0.5	Al II	1671	3.533
		7635.5	1.6	C IV	1548	3.932
		7649.2	0.7	C IV	1551	3.933
		7699.2	0.4	···	···	···
		8414.7	1.7	···	···	···
PSS J1159+1337	4.073	6222.7	0.3	···	···	···
		6271.6	1.6	···	···	···
		6292.1	0.7	···	···	···
		6302.9	2.4	C II	1334	3.723
		6419.2	1.3	Fe II	2344	1.738

TABLE 1—*Continued*

Quasar	z_{em}	$\lambda_{\rm obs}$ (Å)	$W_{\rm obs}$ (Å)	Ion	$\lambda_{\rm rest}$ (Å)	z
		6524.0	1.9	Fe II	2383	1.738
		6584.6	1.7	Si IV	1393	3.724
		6625.1	0.9	Si IV	1402	3.723
		6877.2	1.2	Mg II	2796	1.459
		6893.6	0.6	Mg II	2803	1.459
		6956.8	0.4	···	···	···
		7082.6	1.0	Fe II	2586	1.738
		7120.0	1.5	Fe II	2600	1.738
		7211.2	0.7	Si II	1527	3.723
		7248.6	0.4	···	···	···
		7313.5	1.2	C IV	1548	3.724
		7325.4	0.6	C IV	1551	3.724
		7537.3	0.3	···	···	···
		7637.4	1.6	···	···	···
		7656.3	5.4	Mg II	2796	1.738
		7676.9	3.7	Mg II	2803	1.738
		7816.7	0.8	Mg I	2853	1.740
		7839.1	1.8	C IV	1548	4.063
		7853.3	1.0	C IV	1551	4.064
		7891.8	1.5	Al II	1671	3.723
		7904.7	0.3	···	···	···
		8142.6	0.4	···	···	···
		8232.7	0.4	···	···	···
		8259.0	0.3	···	···	···
PSS J1253+0228	4.007	6142.0	2.2	C II	1334	3.602
		6317.2	1.9	Al II	1671	2.781
		6415.0	4.8	Si IV	1402	3.603
		6455.0	3.8	Si IV	1527	3.602
		7125.4	5.5	C IV	1548	3.602
		7137.3	4.1	C IV	1551	3.602
		7277.8	1.0	···	···	···
		7396.5	1.4	Fe II	1608	3.599
		7725.6	3.5	C IV	1548	3.990
		7738.9	1.4	C IV	1551	3.990
		7854.3	1.2	···	···	···
		7880.5	2.5	···	···	···

TABLE 1—*Continued*

Quasar	z_{em}	$\lambda_{\rm obs}$ (Å)	$W_{\rm obs}$ (Å)	Ion	$\lambda_{\rm rest}$ (Å)	z
		7918.5	0.7	···	···	···
		8034.2	3.1	Fe II	1608	3.995
		8073.6	1.8	···	···	···
BR J1310−1740	4.185	6352.6	1.4	···	···	···
		6409.3	1.2	···	···	···
		6477.9	2.2	Mg II	2796	1.317
		6496.4	2.0	Mg II	2803	1.317
		6770.2	1.7	Si II	1527	3.435
		6864.3	5.7	C IV	1548	3.434
		6875.2	4.3	C IV	1551	3.433
		7189.0	1.2	···	···	···
		7279.6	0.9	···	···	···
		7406.9	3.2	Al II	1671	3.433
		7644.7	3.2	···	···	···
		7752.6	1.3	···	···	···
		7826.1	1.5	···	···	···
		7894.4	2.6	···	···	···
		7933.8	3.1	···	···	···
		7981.6	1.2	C IV	1548	4.155
		7995.4	1.2	C IV	1551	4.156
		8298.0	1.5	···	···	···
		8346.3	2.8	···	···	···
BR J1330−2522	3.949	6013.0	3.4	···	···	···
		6051.0	12.4	···	···	···
		6077.4	8.7	···	···	···
		6231.3	1.5	Si II	1527	3.082
		6303.3	3.3	···	···	···
		6317.6	3.7	C IV	1548	3.081
		6329.4	1.9	C IV	1551	3.081
		6393.7	1.9	···	···	···
		6561.7	1.1	Fe II	1608	3.080
		6816.8	1.0	Al II	1671	3.080
		6875.6	1.9	Si IV	1393	3.933
		6921.0	1.1	Si IV	1402	3.934
		7288.0	1.1	···	···	···
		7304.5	1.1	···	···	···

TABLE 1—*Continued*

Quasar	z_{em}	λ_{obs} (Å)	W_{obs} (Å)	Ion	λ_{rest} (Å)	z
		7381.5	1.7	C IV	1548	3.768
		7394.0	1.2	C IV	1551	3.768
		7438.9	1.4	···	···	···
		7459.1	1.4	···	···	···
		7568.6	3.7	C IV	1548	3.889
		7582.2	2.9	C IV	1551	3.889
		7656.1	1.0	···	···	···
		8348.0	1.6	···	···	···
		8435.9	1.6	···	···	···
FIRST J1410+3409	4.351	6528.0	3.5	···	···	···
		6577.6	8.2	···	···	···
		6873.8	5.4	···	···	···
		7311.7	7.3	···	···	···
		8347.1	9.4	···	···	···
PSS 1456+2007	4.249	6373.0	8.9	···	···	···
		6447.5	0.5	Si II	1527	3.223
		6928.9	2.1	Si IV	1393	3.971
		6972.2	1.8	Si IV	1402	3.970
		7150.8	1.8	···	···	···
		7232.5	2.4	···	···	···
		7273.7	2.6	···	···	···
		7449.2	1.7	···	···	···
		7465.7	1.9	···	···	···
		7631.4	1.4	Si II	1808	3.221
		7753.8	2.1	···	···	···
		7977.5	1.4	···	···	···
		8401.5	3.0	···	···	···
BR J1603+0721	4.385	6604.4	0.8	···	···	···
		6730.1	2.1	···	···	···
		6801.5	3.1	···	···	···
		6813.7	1.6	···	···	···
		6876.0	2.1	···	···	···
		6898.6	1.5	···	···	···
		7634.3	1.4	C IV	1548	3.931
		7645.5	0.7	C IV	1551	3.930
		7753.1	2.0	C IV	1548	4.008

TABLE 1—*Continued*

Quasar	z_{em}	$\lambda_{\rm obs}$ (Å)	$W_{\rm obs}$ (Å)	Ion	$\lambda_{\rm rest}$ (Å)	z
		7766.2	1.5	C IV	1551	4.008
		8233.0	1.8	C IV	1548	4.318
		8246.5	1.0	C IV	1551	4.317
PSS J1618+4125	4.213	6561.1	2.2	···	···	···
		6857.1	5.1	Si IV	1393	3.920
		7058.5	1.7	···	···	···
		7378.5	5.5	···	···	···
		7502.6	6.2	Si II	1527	3.914
		7522.2	3.1	···	···	···
		7855.7	3.0	···	···	···
		7986.1	3.7	···	···	···
		8027.3	1.6	···	···	···
		8186.1	4.7	···	···	···
PSS J1633+1411	4.351	6542.7	1.8	···	···	···
		6564.7	2.0	···	···	···
		6625.1	0.4	···	···	···
		6728.1	0.5	···	···	···
		6833.1	0.3	···	···	···
		6972.5	2.6	C IV	1548	3.504
		6983.7	1.7	C IV	1551	3.503
		7178.4	0.6	···	···	···
		7227.2	0.9	···	···	···
		7325.1	0.6	Si IV	1393	4.256
		7371.9	0.6	Si IV	1402	4.255
		7577.9	1.0	C IV	1548	3.895
		7591.0	0.5	C IV	1551	3.895
		7703.3	1.6	C IV	1548	3.976
		7717.1	0.7	C IV	1551	3.976
		7890.3	0.8	Fe II	1608	3.906
		7930.1	1.1	···	···	···
		8102.6	1.2	···	···	···
		8138.0	2.2	C IV	1548	4.256
		8148.9	1.7	C IV	1551	4.255
		8178.0	1.4	···	···	···
		8217.4	0.8	···	···	···
		8230.3	0.5	···	···	···

TABLE 1—*Continued*

Quasar	z_{em}	$\lambda_{\rm obs}$ (Å)	$W_{\rm obs}$ (Å)	Ion	$\lambda_{\rm rest}$ (Å)	z
		8299.6	3.4	···	···	···
PSS J1646+5514	4.037	6335.9	1.7	···	···	···
		6490.6	0.4	C IV	1548	3.192
		6502.1	0.2	C IV	1551	3.193
		6549.7	0.5	···	···	···
		6624.5	0.2	···	···	···
		6638.2	0.4	C IV	1548	3.288
		6649.1	0.2	C IV	1551	3.288
		6712.2	0.9	···	···	···
		6857.5	0.3	···	···	···
		6870.7	0.5	···	···	···
		6891.3	0.2	Si IV	1402	3.913
		7010.8	0.9	Si IV	1393	4.030
		7033.0	2.1	C IV	1548	3.543
		7044.9	1.3	C IV	1551	3.543
		7055.6	0.4	Si IV	1402	4.030
		7356.8	1.2	C IV	1548	3.752
		7368.2	0.7	C IV	1551	3.751
		7678.4	0.5	···	···	···
		7785.2	1.9	C IV	1548	4.029
		7799.2	1.6	C IV	1551	4.029
		7955.2	0.2	···	···	···
		7993.1	0.6	Mg II	2796	1.858
		8013.7	0.2	Mg II	2803	1.858
		8404.5	0.9	···	···	···
PSS J1721+3256	4.031	6486.1	1.2	Fe II	2586	1.508
		6518.9	1.5	Fe II	2600	1.507
		6568.3	1.5	···	···	···
		6727.6	1.6	C IV	1548	3.345
		6738.6	0.8	C IV	1551	3.345
		7008.2	5.3	Mg II	2796	1.506
		7026.4	1.7	Mg II	2803	1.506
		7291.9	1.8	C IV	1548	3.710
		7305.3	0.8	C IV	1551	3.711
RX J1759+6638	4.320	6561.7	2.5	Mg II	2796	1.347
		6579.2	1.7	Mg II	2803	1.347

TABLE 1—*Continued*

Quasar	z_{em}	$\lambda_{\rm obs}$ (Å)	$W_{\rm obs}$ (Å)	Ion	$\lambda_{\rm rest}$ (Å)	z
		6643.1	0.6	···	···	···
		6715.0	1.3	Si II	1527	3.398
		6808.7	2.5	C IV	1548	3.398
		6817.2	2.0	C IV	1551	3.396
		6870.5	4.4	···	···	···
		7319.6	2.6	···	···	···
		7345.7	2.7	Al II	1671	3.397
		7752.8	2.7	···	···	···
		8347.1	5.6	C IV	1548	4.391
		8359.9	3.1	C IV	1551	4.391
PSS J1802+5616	4.158	6336.2	6.2	···	···	···
		6414.8	0.8	C II	1334	3.807
		6454.1	1.2	···	···	···
		6619.4	2.1	···	···	···
		6696.2	3.9	Si II	1527	3.386
		6798.8	2.3	C IV	1549	3.389
		6868.9	2.7	···	···	···
		6945.7	2.9	···	···	···
		6980.0	1.5	···	···	···
		7096.2	2.2	···	···	···
PSS J2122−0014	4.114	6300.7	1.5	Si II	1260	3.999
		6353.1	4.1	C IV	1548	3.104
		6363.2	3.3	C IV	1551	3.103
		6373.8	3.7	C IV	1548	3.117
		6384.5	2.4	C IV	1551	3.117
		6421.4	2.5	Si II	1527	3.206
		6511.4	0.8	C IV	1548	3.206
		6522.6	0.5	C IV	1551	3.206
		6570.3	5.1	C IV	1548	3.244
		6581.8	4.1	C IV	1551	3.244
		6600.7	1.7	C IV	1548	3.264
		6611.8	1.0	C IV	1551	3.264
		6763.7	0.7	Fe II	1608	3.205
		6952.9	2.2	···	···	···
		6967.2	2.5	···	···	···
		7026.7	1.7	Al II	1671	3.206

TABLE 1—*Continued*

Quasar	z_{em}	$\lambda_{\rm obs}$ (Å)	$W_{\rm obs}$ (Å)	Ion	$\lambda_{\rm rest}$ (Å)	z
		7094.2	1.9	···	···	···
		7147.7	2.6	Si IV	1393	4.128
		7194.9	2.0	Si IV	1402	4.129
		7225.1	7.2	C IV	1549	3.664
		7321.5	7.6	C IV	1549	3.727
		7400.9	22.4	C IV	1549	3.778
		7634.9	1.3	Si II	1527	4.001
		7708.8	1.2	···	···	···
		7741.0	1.9	C IV	1548	4.000
		7754.9	1.1	C IV	1551	4.001
		7870.4	1.0	···	···	···
		7879.1	0.7	···	···	···
		7890.4	1.1	···	···	···
		7939.0	5.0	C IV	1548	4.128
		7952.0	5.9	C IV	1551	4.128
PMN J2134−0419	4.334	6599.0	1.5	C IV	1548	3.262
		6607.9	0.5	C IV	1551	3.261
		6646.6	2.1	···	···	···
		6770.2	0.8	···	···	···
		6849.4	2.2	···	···	···
		6865.4	2.4	Fe II	1608	3.269
		7873.0	2.6	···	···	···
		8083.7	2.4	···	···	···
		8227.1	1.8	···	···	···
PSS J2154+0335	4.363	6548.0	0.7	Fe II	2374	1.758
		6570.4	2.8	Fe II	2383	1.757
		6627.3	1.5	···	···	···
		6640.6	2.2	···	···	···
		6873.2	3.0	···	···	···
		6889.1	2.2	···	···	···
		6916.1	1.4	···	···	···
		7057.3	0.7	Si II	1527	3.623
		7133.6	1.9	Fe II	2586	1.758
		7170.3	2.8	Fe II	2600	1.758
		7397.1	3.9	C IV	1548	3.778
		7409.4	3.0	C IV	1551	3.778

TABLE 1—*Continued*

Quasar	z_{em}	$\lambda_{\rm obs}$ (Å)	$W_{\rm obs}$ (Å)	Ion	$\lambda_{\rm rest}$ (Å)	z
PSS J2155+1358	4.256	6457.8	4.3	···	···	···
		6541.2	1.3	N V	1240	4.275
		6566.6	0.7	···	···	···
		6589.2	2.1	Si II	1527	3.316
		···	or	Fe II	2260	1.915
		6678.1	3.7	C IV	1549	3.311
		6710.8	0.6	···	···	···
		6785.2	0.6	···	···	···
		6811.2	0.9	···	···	···
		6830.6	0.9	Fe II	2344	1.914
		6890.9	0.5	···	···	···
		6916.9	0.9	Fe II	2374	1.913
		6941.7	2.9	Fe II	1608	3.316
		7066.2	1.9	C IV	1548	3.564
		7078.1	1.1	C IV	1551	3.564
		7133.7	0.8	···	···	···
		7170.5	4.5	···	···	···
		7207.6	2.8	Al II	1671	3.314
		7307.0	2.6	Si IV	1393	4.243
		7354.1	1.9	Si IV	1402	4.243
		7564.6	1.0	···	···	···
		7577.9	1.7	Fe II	2600	1.914
		7877.8	1.6	···	···	···
		7892.2	1.2	···	···	···
		7939.0	1.3	···	···	···
		7952.1	1.2	···	···	···
		8115.1	2.8	C IV	1548	4.242
		8129.6	1.8	C IV	1551	4.242
		8147.0	3.2	Mg II	2796	1.913
		8169.3	4.6	Mg II	2853	1.914
		8187.1	0.9	···	···	···
		9064.7	2.2	···	···	···
		9127.7	0.6	···	···	···
BR J2216−6714	4.469	6744.0	1.1	···	···	···
		6764.7	2.1	C IV	1548	3.369
		6776.4	0.3	C IV	1551	3.370

TABLE 1—*Continued*

Quasar	z_{em}	$\lambda_{\rm obs}$ (Å)	$W_{\rm obs}$ (Å)	Ion	$\lambda_{\rm rest}$ (Å)	z
		6790.4	0.4	···	···	···
		6851.4	0.4	O I	1302	4.262
		6918.5	1.8	Fe II	2260	2.060
		6942.1	0.4	···	···	···
		7003.8	0.9	···	···	···
		7068.2	1.4	···	···	···
		7137.1	0.6	···	···	···
		7175.7	2.7	Fe II	2344	2.061
		7203.5	1.3	···	···	···
		7267.8	2.9	Fe II	2374	2.061
		7293.8	4.5	Fe II	2383	2.061
		7889.8	2.0	Si II	1808	3.364
		7918.1	2.4	Fe II	2586	2.061
		7958.5	3.4	Fe II	2600	2.061
		8327.1	1.9	···	···	···
		8559.1	3.6	Mg II	2796	2.061
		8582.1	3.4	Mg II	2803	2.061
		8731.0	1.5	Mg I	2853	2.060
		9094.6	1.8	···	···	···
PSS J2241+1352	4.441	6738.7	0.8	···	···	···
		6752.2	3.4	···	···	···
		6810.4	1.2	···	···	···
		6833.8	1.3	···	···	···
		6878.1	3.7	O I	1302	4.282
		6892.0	3.4	Si II	1304	4.284
		6951.5	1.4	···	···	···
		7049.6	3.7	C II	1334	4.282
		7135.2	1.3	···	···	···
		7230.4	1.5	···	···	···
		7267.6	1.6	···	···	···
		7363.2	1.9	···	···	···
		7400.3	15.3	Si IV	1400	4.286
		8066.2	2.8	Si II	1527	4.283
		8307.0	2.3	···	···	···
		8344.5	3.7	···	···	···
		8401.2	3.2	Si II	1808	3.647

TABLE 1—*Continued*

Quasar	z_{em}	$\lambda_{\rm obs}$ (Å)	$W_{\rm obs}$ (Å)	Ion	$\lambda_{\rm rest}$ (Å)	z
		8437.7	4.5	C IV	1549	4.447
		8499.1	3.8	Fe II	1608	4.284
		9210.7	4.7	···	···	···
BR J2317−4345	3.943	6049.4	1.3	···	···	···
		6136.0	0.5	Fe II	2260	1.714
		6248.8	3.6	Si IV	1393	3.483
		6290.6	0.5	Si IV	1402	3.484
		6362.4	0.6	Fe II	2344	1.714
		6466.9	1.4	Fe II	2382	1.714
		6553.4	0.7	···	···	···
		6702.1	0.9	···	···	···
		6809.5	0.8	···	···	···
		6944.6	3.8	C IV	1548	3.486
		6956.7	3.5	C IV	1551	3.486
		7057.8	1.5	Fe II	2600	1.714
		7084.1	2.7	C IV	1548	3.576
		7097.2	1.0	C IV	1551	3.577
		7224.3	0.8	Fe II	1608	3.491
		7590.2	2.6	Mg II	2796	1.714
		7609.1	2.8	Mg II	2803	1.714
		7719.5	0.9	···	···	···
		7739.8	3.3	Mg I	2853	1.713
		7853.8	1.7	···	···	···
BR J2328−4513	4.359	6573.7	2.5	N V	1240	4.301
		6619.8	1.0	···	···	···
		6856.2	0.9	···	···	···
		6877.1	1.9	Fe II	2600	1.645
		7019.3	1.7	···	···	···
		7140.6	2.8	···	···	···
		7225.5	2.1	···	···	···
		7306.6	2.2	Si II	1808	3.041
		···	or	C IV	1548	3.719
		7319.2	1.0	C IV	1551	3.720
		7396.4	2.7	Mg II	2796	1.645
		7415.0	1.3	Mg II	2803	1.645
		7792.3	4.5	C IV	1548	4.033

TABLE 1—*Continued*

Quasar	z$_{em}$	$\lambda_{\rm obs}$ (Å)	W$_{\rm obs}$ (Å)	Ion	$\lambda_{\rm rest}$ (Å)	z
		7804.9	2.2	C IV	1551	4.033
		8113.1	1.4	⋯	⋯	⋯
		8176.6	1.6	⋯	⋯	⋯
		8240.3	1.3	⋯	⋯	⋯
		8258.4	1.3	⋯	⋯	⋯
		8365.4	2.5	⋯	⋯	⋯
		8400.3	1.4	⋯	⋯	⋯
		8501.7	2.4	⋯	⋯	⋯
PSS J2344+0342	4.239	6515.2	2.9	⋯	⋯	⋯
		6531.4	2.8	C IV	1548	3.218
		6541.8	2.6	C IV	1551	3.218
		6650.1	0.9	Si II	1808	2.678
		6786.0	1.3	Fe II	1608	3.219
		6804.0	2.7	Si IV	1393	3.882
		6848.4	1.3	Si IV	1402	3.882
		6869.5	1.5	⋯	⋯	⋯
		7049.1	3.8	Al II	1671	3.219
		7200.8	1.2	⋯	⋯	⋯
		7236.8	2.0	⋯	⋯	⋯
		7326.9	1.5	Mg II	2796	1.620
		7347.3	2.2	Mg II	2803	1.621
		7453.1	0.7	Si II	1526	3.882
		7504.5	1.3	⋯	⋯	⋯
		7560.2	2.4	⋯	⋯	⋯
		7630.5	2.4	Si II	1808	3.220
		7775.9	0.8	⋯	⋯	⋯
		8153.9	2.9	⋯	⋯	⋯
		8329.9	1.7	Fe II	2260	2.684
		8436.2	3.1	⋯	⋯	⋯
		8466.4	4.5	⋯	⋯	⋯
		8707.9	1.8	Fe II	2367	2.678
BR J2349−3712	4.208	6423.7	0.8	N V	1240	4.169
		6398.2	1.2	⋯	⋯	⋯
		6437.5	1.8	⋯	⋯	⋯
		6477.0	0.9	⋯	⋯	⋯
		6592.6	1.3	⋯	⋯	⋯

TABLE 1—*Continued*

Quasar	z_{em}	$\lambda_{\rm obs}$ (Å)	$W_{\rm obs}$ (Å)	Ion	$\lambda_{\rm rest}$ (Å)	z
		6759.7	1.1	···	···	···
		6770.8	1.1	···	···	···
		7090.9	1.7	···	···	···
		7161.2	1.1	Si II	1527	3.691
		7305.6	1.4	···	···	···
		7371.5	1.3	···	···	···
		7716.3	1.3	···	···	···
		8784.6	3.0	···	···	···
		9122.6	2.8	···	···	···

Appendix C

Quasars with Damped Lyman-α Systems

These Tables summarise all the quasars containing one or more damped Lyman-α system used in our anaylsis. The first Table lists all the quasars issued from the sample presented in this thesis (see Chapter 5). The second Tables includes data from the literature (mainly Storrie-Lombardi & Wolfe (2000) with the following added modifications: Q 1329+4117 has no DLA at $z_{abs} = 0.5193$ (Jannuzi et al., 1998), Q 2112+059 has no DLA at $z_{abs} = 0.2039$ (Jannuzi et al., 1998; Fynbo et al., 2001) and Q 0302−223 has a DLA at $z_{abs} = 0.1014$ (Jannuzi et al., 1998). The minimum and maximum redshift along which a DLA *could* have detected if there was one are mentioned in all cases as well as the relevant references in the case of the second Table.

The references in Table 2 are as follow:

1 = Storrie-Lombardi & Wolfe (2000)
2 = Storrie-Lombardi & Hook (2000)
3 = Lanzetta et al. (1995)
4 = Wolfe et al. (1995)
5 = Sargent et al. (1989)
6 = Turnshek et al. (1989)
7 = Wolfe et al. (1993)
8 = Lu et al. (1993)
9 = Lu & Wolfe (1994)
10 = Virgilio et al. 1995
11 = Pettini et al. (1994)
12 = Francis & Hewett (1993)
13 = Savaglio et al. (1994)
14 = Sargent et al. (1988)
15 = Black et al. (1987)
16 = Wolfe et al. (1986)
17 = Wolfe et al. (1994)
18 = Rauch et al. (1990)
19 = Williger et al. 1989
20 = Meyer et al. (1995)
21 = Lanzetta et al. (1991)
22 = Storrie-Lombardi et al. (1996c)
23 = Storrie-Lombardi et al. (1996a)
24 = Jannuzi et al. (1998)

TABLE 1—Quasar With Damped Lyman-alpha Absorbers - this work

Quasar	z_{em}	z_{min}	z_{max}	z_{abs}	log N (H I) [cm^{-2}]
BR J0006-6208	4.455	2.944	4.400	2.97	20.7
···	···	···	···	3.20	20.9
···	···	···	···	3.78	21.0
BR J0030-5129	4.174	2.304	4.122	2.45	20.8
PSS J0106+2601	4.309	2.764	4.256	3.96	20.5
PSS J0133+0400	4.154	2.865	4.102	3.69	20.4
···	···	···	···	3.77	20.5
PSS J0134+3307	4.532	2.562	4.477	3.76	20.6
PSS J0152+0735	4.051	1.890	4.000	3.84	20.7
PSS J0209+0517	4.174	2.759	4.122	3.66	20.3
···	···	···	···	3.86	20.6
BR J0301-5537	4.133	2.825	4.082	3.22	20.3
BR J0307-4945	4.728	3.138	4.671	4.46	20.8
SDSS J0310-0014	4.658	3.087	4.601	3.42	20.5
BR J0334-1612	4.363	3.080	4.309	3.56	21.0
SDSS J0338+0021	5.010	3.528	4.950	4.06	20.4
BR J0426-2202	4.320	2.544	4.267	2.98	21.1
PSS J0747+4434	4.430	2.764	4.376	3.76	20.3
···	···	···	···	4.02	20.6
PSS J1057+4555	4.116	2.652	4.065	3.05	20.3
PSS J1159+1337	4.073	2.563	4.022	3.72	20.3
PSS J1253-0228	4.007	2.498	3.957	2.78	21.4
PSS J1618+4125	4.213	2.820	4.161	3.92	20.5
RX J1759+6638	4.320	2.804	4.267	3.40	20.4
PSS J1802+5616	4.158	2.891	4.106	3.76	20.4
PSS J2122-0014	4.114	2.350	4.063	3.20	20.3
PSS J2154+0335	4.363	2.979	4.309	3.61	20.4
PSS J2155+1358	4.256	2.940	4.203	3.32	21.1
PSS J2241+1352	4.441	3.027	4.387	4.28	20.7
BR J2317-4345	3.943	2.448	3.894	3.49	20.9
PSS J2344+0342	4.239	2.696	4.187	3.21	20.9

TABLE 2—Quasar With Damped Lyman-alpha Absorbers - data from the literature

Quasar	z_{em}	z_{min}	z_{max}	z_{abs}	log N (H I) [cm^{-2}]	References
Q 0000-2619	4.11	2.389	4.060	3.3901	21.4	5,13
Q 0010-0012	2.15	1.634	2.119	2.0233	20.8	4,10
Q 0013-0029	2.08	1.634	2.049	1.9730	20.7	4,11
BR B0019-1522	4.528	2.97	4.473	3.4370	20.92	22,1
Q 0027+0103	2.29	1.634	2.257	1.9375	20.6	4,10
Q 0042-2930	2.39	1.591	2.354	1.931	20.5	4
Q 0049-2820	2.26	1.638	2.223	2.0713	20.5	4,11
Q 0056+0125	3.16	2.197	3.119	2.7750	21.0	4,10
Q 0058-2914	3.07	1.778	3.052	2.6711	21.2	21
Q 0100-3105	2.64	1.687	2.605	2.131	20.5	4
Q 0100+1300	2.69	1.64	2.74	2.3093	21.4	16,15
Q 0102-1902	3.04	2.044	2.995	2.3693	21.0	5,8
Q 0102-0214	1.98	1.649	1.949	1.7431	20.6	4,10
BRI B0111-2819	4.30	2.709	4.247	3.1043	21.0	1
Q 0112-3041	2.99	1.881	2.945	2.4191	20.5	21,9
Q 0112-3041	2.99	1.881	2.945	2.7023	20.3	21,9
Q 0112+0300	2.81	1.813	2.785	2.4227	21.0	5,11
PSS J0132+1341	4.147	2.844	4.096	3.93	20.3	1
Q 0149+3335	2.43	1.64	2.43	2.1413	20.5	16,7
Q 0201+3634	2.49	1.632	2.879	2.4614	20.4	21,8
Q 0201+3634	2.49	1.632	2.879	1.768	20.5	21
Q 0216+0803	3.00	1.731	2.953	2.2930	20.5	5,9
Q 0302-223	1.4000	1.0077	1.3760	1.0104	20.36	24
BR B0331-1622	4.38	2.868	4.326	3.56	20.6	1
Q 0336-0142	3.20	2.109	3.155	3.0619	21.2	21,8
Q 0347-3819	3.23	2.044	3.186	3.0244	20.8	21,18
Q 0449-1330	3.097	2.006	3.056	2.052	20.4	21
Q 0458-0203	2.29	1.96	2.29	2.0399	21.7	16,7
Q 0528-2505	2.779	1.961	2.741	2.1404	21.0	5
Q 0834-2006	2.75	1.632	2.704	1.715	20.4	21
Q 0836+1122	2.70	1.74	2.67	2.4660	20.6	16,6
Q 0913+0715	2.78	1.866	2.739	2.6187	20.3	21,8
MG 0930+2858	3.41	2.173	3.366	3.24	20.5	2
Q 0935+4143	1.9800	1.0626	1.550	1.369	20.3	3
BR B0951-0450	4.369	2.93	4.315	3.8580	20.6	22,1
BR B0951-0450	4.369	2.93	4.315	4.2028	20.4	22,1

TABLE 2—*Continued*

Quasar	z_{em}	z_{min}	z_{max}	z_{abs}	log N (H I) [cm^{-2}]	References
BRI B0952-0115	4.426	2.99	4.372	4.0238	20.55	22,1
PC 0953+4749	4.457	3.010	4.004	3.403	20.9	1
PC 0953+4749	4.457	3.010	4.004	3.890	21.1	1
BRI B1013+0035	4.405	2.61	4.351	3.1031	21.1	22,1
Q 1032+0414	3.39	2.067	3.347	2.839	20.3	21
PSS J1057+4555	4.101	2.652	4.050	3.05	20.3	1
BRI B1108-0747	3.922	2.64	3.873	3.607	20.33	22,23
BRI B1114-0822	4.495	3.19	4.440	4.2576	20.3	22,1
Q 1151+0651	2.76	1.65	2.76	1.7737	21.3	16,6
Q 1159+0132	3.27	1.988	3.226	2.6846	21.1	21,8
BR B1202-0725	4.694	3.16	4.637	4.383	20.49	22,23
Q 1205+0918	2.08	1.634	2.046	1.673	20.6	4
Q 1209+0919	3.30	2.175	3.254	2.5835	21.4	21,8
Q 1210+1731	2.54	1.634	2.502	1.8920	20.6	4,10
Q 1215+3322	2.61	1.64	2.60	1.9989	21.0	16,7
Q 1223+1753	2.92	1.945	2.879	2.4658	21.5	4,11
Q 1232+0815	2.57	1.789	2.534	2.3376	20.9	4,10
Q 1240+1516	2.28	1.634	2.247	1.738	20.7	4
Q 1244+3443	2.48	1.64	2.50	1.8593	20.5	16,7
Q 1246-0217	2.11	1.634	2.075	1.779	21.2	4
Q 1308+0105	2.80	1.634	2.763	1.762	20.6	4
GB 1320+3927	2.98	1.968	2.940	2.11	20.4	2
Q 1337+1121	2.92	1.86	2.92	2.7957	20.9	16,6
BRI B1346-0322	3.992	2.65	3.942	3.7343	20.72	22,1
Q 1347+1116	2.70	1.92	2.71	2.4709	20.3	16,6
Q 1409+0930	2.86	1.979	2.800	2.4561	20.5	21,8
PSS J1443+2724	4.407	2.950	4.353	4.216	20.8	1
Q 1451+1223	3.26	2.158	3.207	2.478	20.4	16,21
BR BI1500+0824	3.943	2.39	3.894	2.7968	20.8	22,1
GB 1610+2806	3.54	2.021	3.498	2.59	20.6	2
MG 1614+0506	3.21	1.984	3.168	2.52	20.4	2
GB 1759+7539	3.05	1.955	3.010	2.624	20.77	2
PC 2047+0123	3.799	2.620	3.751	2.7299	20.4	1
Q 2132-4321	2.42	1.595	2.386	1.916	20.7	4
Q 2138-4427	3.17	2.107	3.128	2.851	20.9	4,12
Q 2206-1958	2.56	1.85	2.58	1.9205	20.5	16,14

TABLE 2—*Continued*

Quasar	z$_{em}$	z_{min}	z_{max}	z_{abs}	log N (H I) [cm^{-2}]	References
Q 2206-1958	2.56	1.85	2.58	2.0763	20.7	16,17
Q 2223-0512	1.4040	0.4159	0.6310	0.4925	20.9	3
Q 2223-0512	1.4040	0.9259	1.3800	···	···	3
Q 2230+0232	2.15	1.634	2.119	1.8642	20.8	4,10,11
Q 2231-0015	3.015	1.749	2.980	2.0657	20.6	4,9
BR B2237-0607	4.558	2.96	4.502	4.0691	20.5	22,1
Q 2239-3836	3.55	2.389	3.508	3.2810	20.8	21,9
Q 2248+0127	2.56	1.634	2.524	1.9080	20.6	4,10
Q 2348-0108	3.01	2.044	2.965	2.4272	20.5	16,6
Q 2348-0108	3.01	2.044	2.965	2.6161	21.3	21,6
Q 2351+0217	2.03	1.634	2.000	1.766	20.9	4,10
Q 2359-0216	2.31	1.747	2.779	2.0951	20.7	16,7
Q 2359-0216	2.31	1.747	2.779	2.1537	20.3	16,7

Appendix D

Quasars Without Damped Lyman-α Systems

These Tables summarise all the quasars *not* containing damped Lyman-α system. The first Table lists all the quasars issued from the sample presented in this thesis (see Chapter 2). The second Tables includes data from the literature (mainly Storrie-Lombardi & Wolfe (2000) with the following added modifications: Q 1329+4117 has no DLA at $z_{abs} = 0.5193$ (Jannuzi et al., 1998), Q 2112+059 has no DLA at $z_{abs} = 0.2039$ (Jannuzi et al., 1998; Fynbo et al., 2001) and Q 0302−223 has a DLA at $z_{abs} = 0.1014$ (Jannuzi et al., 1998). The minimum and maximum redshift along which a DLA *could* have detected if there was one are mentioned in all cases as well as the relevant references in the case of the second Table.

The references in Table 2 are as follow:

1 = Storrie-Lombardi & Wolfe (2000)
2 = Storrie-Lombardi & Hook (2000)
3 = Lanzetta et al. (1995)
4 = Wolfe et al. (1995)
5 = Sargent et al. (1989)
6 = Turnshek et al. (1989)
7 = Wolfe et al. (1993)
8 = Lu et al. (1993)
9 = Lu & Wolfe (1994)
10 = Virgilio et al. 1995
11 = Pettini et al. (1994)
12 = Francis & Hewett (1993)
13 = Savaglio et al. (1994)
14 = Sargent et al. (1988)
15 = Black et al. (1987)
16 = Wolfe et al. (1986)
17 = Wolfe et al. (1994)
18 = Rauch et al. (1990)
19 = Williger et al. 1989
20 = Meyer et al. (1995)
21 = Lanzetta et al. (1991)
22 = Storrie-Lombardi et al. (1996c)
23 = Storrie-Lombardi et al. (1996a)
24 = Jannuzi et al. (1998)
25 = Fynbo et al. (2001)

TABLE 1—QUASAR WITHOUT DAMPED LYMAN-ALPHA ABSORBERS - THIS WORK

Quasar	z_{em}	z_{min}	z_{max}
PSS J0003+2730	4.240	2.718	4.188
PSS J0034+1639	4.293	2.981	4.240
SDSS J0035+0040	4.747	3.309	4.690
PSS J0131+0633	4.417	3.014	4.363
SDSS J0211-0009	4.874	3.402	4.815
BR J0234-1806	4.301	2.971	4.248
PSS J0248+1802	4.422	2.810	4.368
BR J0311-1722	4.039	2.591	3.989
BR J0324-2918	4.622	2.900	4.566
BR J0355-3811	4.545	3.030	4.490
BR J0403-1703	4.227	2.992	4.175
BR J0415-4357	4.070	2.813	4.019
BR J0419-5716	4.461	2.820	4.406
BR J0426-2202	4.320	2.544	4.267
PMN J0525-3343	4.383	2.829	4.329
BR J0529-3526	4.413	3.023	4.359
BR J0529-3552	4.172	2.821	4.120
BR J0714-6455	4.462	3.050	4.407
RX J1028-0844	4.276	2.533	4.223
BR J1310-1740	4.185	2.508	4.133
FIRST J1410+3409	4.351	3.026	3.578
...	...	3.602	4.297
PSS J1456+2007	4.249	2.878	4.197
BR J1603+0721	4.385	3.062	4.331
PSS J1633+1411	4.351	2.536	4.297
PSS J1646+5514	4.037	2.772	3.987
PSS J1721+3256	4.031	2.791	3.981
PMN J2134-0419	4.334	2.903	4.281
BR J2216-6714	4.469	2.795	4.414
BR J2328-4513	4.359	2.926	4.305
BR J2349-3712	4.208	2.847	4.156

TABLE 2—Quasar Without Damped Lyman-alpha Absorbers - data from the literature

Quasar	z$_{em}$	z_{min}	z_{max}	References
Q 0001+0842	3.241	2.024	3.229	21
Q 0002+151	1.8990	0.4723	0.6034	3
Q 0002+151	1.8990	1.1198	1.5500	3
Q 0003+158	0.4500	0.0080	0.4355	3
MG 0004+1359	3.25	1.899	3.207	2
Q 0004+1711	2.898	2.002	2.851	21
Q 0006+0230	2.09	1.787	2.059	4
Q 0006+0200	2.35	1.634	2.317	4
Q 0007-0004	2.26	1.634	2.227	4
Q 0007-000	2.29	1.670	2.260	16
MG 0007+0141	2.90	1.882	2.861	2
Q 0007+106	0.0890	0.0080	0.0781	3
Q 0009-0138	1.99	1.634	1.960	4
Q 0009+0219	2.66	1.784	2.623	4
Q 0009-0215	2.11	1.634	2.079	4
Q 0014+8118	3.380	1.928	3.340	21
Q 0014-0256	1.85	1.729	1.821	4
Q 0015+0239	2.47	1.784	2.435	4
Q 0016+0045	2.31	1.651	2.277	4
Q 0018-0220	2.56	1.634	2.524	4
Q 0018+0047	1.83	1.655	1.802	4
Q 0020+0217	1.80	1.665	1.772	4
Q 0022+0150	2.77	1.791	2.732	4
Q 0023+0010	1.90	1.657	1.871	4
Q 0025-0151	2.08	1.634	2.049	4
Q 0026+0158	1.89	1.727	1.861	4
Q 0026+129	0.1420	0.0080	0.1306	3
Q 0027+0149	2.33	1.694	2.297	4
Q 0028+0236	2.00	1.634	1.970	4
Q 0028-0148	2.08	1.840	2.049	4
Q 0029+0017 2	.23 1	.725 2	.198 4	
Q 0029-0152	2.39	2.013	2.356	4
PSS J0030+1702	4.282	2.763	4.229	1
Q 0037-018	2.34	1.654	2.303	16
Q 0039-2630	1.81	1.634	1.782	4
Q 0040-2917	2.09	1.634	2.056	4

TABLE 2—*Continued*

Quasar	z_{em}	z_{min}	z_{max}	References
Q 0041-2638	3.045	1.657	3.029	21
Q 0041-2707	2.79	1.668	2.748	4
Q 0041-2607	2.79	1.634	2.470	4
Q 0041-2658	2.46	1.634	2.422	4
Q 0041-2859	2.13	1.589	2.103	4
Q 0042-3053	1.97	1.634	1.944	4
Q 0042-2627	3.298	2.113	3.253	21
Q 0042-2656	3.33	2.215	3.314	21
Q 0042-2657	2.90	2.226	2.859	4
Q 0043-2937	2.23	1.656	2.198	4
Q 0044+030	0.6240	0.3386	0.6078	3
Q 0045-3002	2.02	1.603	1.991	4
Q 0045-0341	3.138	1.961	3.094	21
Q 0045-013	2.53	1.784	2.493	16
Q 0046-293	4.014	2.882	3.964	1
BRI B0046-2458	4.15	2.575	4.099	1
Q 0047-2759	2.13	1.649	2.099	4
Q 0047-3050	2.97	1.930	2.933	4
Q 0047-2538	1.97	1.591	1.939	4
Q 0047-2326	3.422	2.291	3.378	21
Q 0048-0119	1.88	1.634	1.849	4
Q 0048-2545	2.08	1.634	2.051	4
Q 0049-0104	2.10	1.715	2.065	4
Q 0049-0012	1.95	1.634	1.916	4
Q 0049+007	2.27	1.644	2.238	16
Q 0049+014	2.31	1.681	2.276	16
Q 0049+171	0.0640	0.0080	0.0534	3
Q 0050+124	0.0611	0.0080	0.0505	3
Q 0050-2523	2.16	1.592	2.127	4
Q 0051-0226	2.53	1.634	2.491	4
Q 0052-0058	2.21	1.634	2.180	4
Q 0052+251	0.1550	0.0080	0.1435	3
Q 0053-0134	2.06	1.634	2.031	4
Q 0053-2824	3.616	2.454	3.576	21
Q 0054+0200	1.87	1.634	1.844	4
Q 0054+144	0.1710	0.0080	0.1593	3

TABLE 2—*Continued*

Quasar	z_{em}	z_{min}	z_{max}	References
Q 0054-006	2.76	1.854	2.724	16
Q 0055+0141	2.23	1.651	2.200	4
Q 0055-2744	2.20	1.567	2.163	4
Q 0055-2629	3.6560	1.920	3.609	21
Q 0055-0200	1.98	1.782	1.953	4
Q 0055+0025	1.91	1.634	1.885	4
Q 0056-0241	2.23	1.779	2.194	4
Q 0057-0225	2.01	1.715	1.979	4
Q 0057-274	3.52	2.603	3.475	1
Q 0058-2604	2.47	1.606	2.437	4
Q 0058-0227	2.23	1.712	2.194	4
Q 0058+0155	1.95	1.634	1.924	4
Q 0059-0207	2.29	1.653	2.257	4
Q 0059-2625	2.10	1.614	2.069	4
Q 0059+0035	2.55	1.673	2.510	4
PSS J0059+0003	4.16	2.750	4.108	1
Q 0100+0146	1.91	1.692	1.880	4
Q 0101-2548	1.97	1.596	1.943	4
Q 0101-3025	4.073	1.937	3.116	21
Q 0102-0240	1.84	1.731	1.818	4
BRI B0103+0032	4.437	2.87	4.383	22
Q 0103-0141	2.21	1.634	2.174	4
Q 0103-2901	2.87	1.922	2.831	4
Q 0104+0030	1.87	1.667	1.845	4
PC 0104+0215	4.171	2.881	4.119	1
Q 0105-2649	2.46	1.667	2.428	4
Q 0106-0230	2.28	1.634	2.246	4
Q 0106+0119	2.10	1.871	2.068	4
Q 0107+0022	1.97	1.634	1.938	4
Q 0108+0028	2.01	1.733	1.975	4
Q 0109+022	2.35	1.734	2.317	16
Q 0110-0107	1.89	1.643	1.860	4
Q 0112-2728	2.894	1.784	2.855	21
Q 0114-0856	3.163	1.838	3.118	21
Q 0115-3002	3.249	1.733	3.207	21
PSS J0117+1552	4.244	2.646	4.192	1

TABLE 2—*Continued*

Quasar	z_{em}	z_{min}	z_{max}	References
Q 0117+213	1.4930	0.9989	1.4681	3
Q 0119-286	0.1170	0.0080	0.1058	3
Q 0119-013	0.0540	0.0080	0.0435	3
Q 0123+257	2.37	1.644	2.338	16
PC 0131+0120	3.792	3.116	3.744	1
Q 0132-1947	3.130	1.714	3.089	21
Q 0134+329	0.3670	0.0080	0.1050	3
BRI B0135-4239	3.97	2.575	3.920	1
Q 0136+010	2.35	1.749	2.317	16
Q 0136+1737	2.73	1.632	2.679	21
Q 0143-0135	3.141	1.673	3.097	21
GB 0148+2502	3.10	1.825	3.059	2
Q 0148-0946	2.850	1.797	2.810	21
BRI B0151-0025	4.194	2.74	4.142	22
Q 0153+0430	2.993	1.673	2.951	21
Q 0157+001	0.1631	0.0080	0.1515	3
Q 0159+036	2.47	1.644	2.436	16
Q 0205+024	0.1564	0.0080	0.1448	3
Q 0207-0019	2.853	1.756	2.817	21
Q 0215+015	1.7150	0.9996	1.5500	3
Q 0219+428	0.4440	0.0080	0.4296	3
GB 0229+1309	2.07	1.767	2.039	2
Q 0232-042	1.4360	0.0080	0.6320	3
Q 0232-042	1.4360	0.8733	1.4116	3
Q 0237-233	2.2230	1.1593	1.5402	3
Q 0239-1527	2.786	1.928	2.744	21
BRI B0241-0146	4.053	2.86	4.002	22
BR B0245-0608	4.238	2.96	4.186	22
PSS J0248+1802	4.43	2.810	4.376	1
Q 0249-1826	3.210	1.871	3.163	21
Q 0249-2212	3.21	2.044	3.160	5,1
Q 0252+0136	2.47	1.634	2.430	4
Q 0254+0000	2.25	1.634	2.215	4
Q 0256-0000	3.377	2.241	3.330	21
Q 0256-0031	2.00	1.634	1.965	4
Q 0258+0210	2.52	1.634	2.489	4

TABLE 2—*Continued*

Quasar	z_{em}	z_{min}	z_{max}	References
Q 0301-0035	3.226	2.060	3.181	21
Q 0302-0019	3.290	1.739	3.243	21
Q 0305+0127	2.15	1.634	2.118	4
Q 0307-0058	2.11	1.634	2.075	4
Q 0308+0129	2.34	1.739	2.302	4
Q 0308+1902	2.839	1.673	2.797	21
Q 0308-1920	2.756	1.673	2.714	21
Q 0312-770	0.2230	0.0080	0.2108	3
Q 0316-2023	2.869	1.747	2.826	21
Q 0323+022	0.1470	0.0080	0.1295	3
Q 0329-2534	2.689	1.661	2.662	21
Q 0334-2029	3.132	2.057	3.089	21
PC 0345+0130	3.638	2.699	3.592	1
BR B0351-1034	4.351	3.09	4.297	22
Q 0351-3904	3.01	1.632	2.970	21
Q 0352-2732	2.823	1.673	2.781	21
BR B0401-1711	4.236	2.82	4.184	22
Q 0405-123	0.5740	0.0080	0.5583	3
Q 0414-060	0.7810	0.0080	0.7632	3
Q 0420+007	2.918	1.673	2.879	21
Q 0420-3851	3.1230	2.094	3.082	21
Q 0428-1342	3.244	1.965	3.200	21
Q 0454-220	0.5340	0.1199	0.5187	3
Q 0454+039	1.3450	0.9672	1.3216	3
Q 0457+024	2.38	1.645	2.346	16
MG 0504+0303	2.46	1.803	2.425	2
Q 0521-365	0.0566	0.0080	0.0460	3
Q 0537-441	0.8940	0.5139	0.6300	3
Q 0548-322	0.0690	0.0080	0.0583	3
Q 0552+398	2.36	1.644	2.325	16
Q 0558-504	0.1370	0.0080	0.1256	3
Q 0624+691	0.3700	0.0080	0.3563	3
Q 0636+6801	3.178	2.019	3.132	21
Q 0637-752	0.6560	0.0080	0.6251	3
Q 0642+4454	3.408	2.192	3.362	21
Q 0702+646	0.0795	0.0080	0.0687	3

TABLE 2—*Continued*

Quasar	z_{em}	z_{min}	z_{max}	References
Q 0731+6519	3.038	2.019	2.993	21
Q 0735+178	0.4240	0.0765	0.4098	3
Q 0736+017	0.1910	0.0080	0.1791	3
Q 0742+318	0.4620	0.0080	0.4474	3
Q 0743-673	1.5130	1.0302	1.4879	3
GB 0749+4239	3.59	2.185	3.544	2
PC 0751+5623	4.281	3.526	4.228	1
Q 0754+100	0.6700	0.0080	0.6257	3
Q 0754+394	0.0958	0.0080	0.0848	3
Q 0804+761	0.1000	0.0080	0.0890	3
Q 0805+0441	2.880	1.838	2.834	21
Q 0812+332	2.42	1.677	2.385	16
Q 0819-032	2.35	1.704	2.319	16
Q 0820+296	2.37	1.644	2.333	16
MG 0830+1009	3.75	2.040	3.703	2
Q 0830+1133	2.979	1.797	2.936	21
Q 0831+1238	2.748	1.961	2.706	21
Q 0837-120	0.1980	0.0080	0.1860	3
Q 0844+349	0.0640	0.0080	0.0534	3
Q 0846+152	2.64	1.831	2.599	16
MG 0848+1533	2.01	1.735	1.980	2
Q 0849+080	0.0620	0.0080	0.0514	3
Q 0851+202	0.3060	0.0080	0.2929	3
Q 0855+182	2.62	1.682	2.580	16
Q 0903+155	2.68	1.659	2.645	16
MG 0906+0406	3.20	1.811	3.158	2
Q 0906+484	0.1180	0.0080	0.1068	3
Q 0910+403	0.9360	0.0080	0.9166	3
Q 0914-621	0.0573	0.0080	0.0467	3
Q 0916+555	0.1235	0.0080	0.1123	3
Q 0932+3646	2.84	1.634	2.814	21
Q 0933+733	2.53	1.651	2.493	16
Q 0938+1159	3.19	1.634	3.149	21
Q 0941+2608	2.913	1.731	2.867	21
Q 0953+414	0.2390	0.0080	0.2266	3
Q 0955+326	0.5330	0.0080	0.5177	3

TABLE 2—*Continued*

Quasar	z_{em}	z_{min}	z_{max}	References
Q 0956+1217	3.306	2.159	3.263	21
Q 0957+561	1.4050	0.8179	1.3810	3
Q 0958+551	1.7324	1.1762	1.4513	3
Q 1001+291	0.3290	0.0080	0.3157	3
Q 1004+130	0.2410	0.0080	0.2286	3
Q 1004+1411	2.707	1.786	2.672	21
Q 1007+417	0.6110	0.0080	0.5949	3
Q 1009-0252	2.75	1.651	2.708	4
Q 1011-282	0.6110	0.0080	0.1310	3
Q 1011-0144	2.24	1.669	2.204	4
Q 1011+250	1.6310	0.9718	1.5500	3
Q 1012+008	0.1850	0.0080	0.1732	3
Q 1012-0206	2.14	1.634	2.104	4
GB 1013+2052	3.11	1.945	3.069	2
Q 1014+0023	2.29	1.634	2.591	4
Q 1016-0039	2.18	1.649	2.144	4
Q 1017+1055	3.158	2.114	3.127	21
Q 1017+280	1.9280	0.9971	1.4678	3
Q 1018-0005	2.60	1.789	2.560	4
Q 1020+0028	1.90	1.680	1.872	4
Q 1021-0037	2.547	1.887	2.513	21
Q 1024+0030	2.17	1.717	2.135	4
Q 1025-0030	2.87	1.885	2.833	4
Q 1028+313	0.1770	0.0080	0.1652	3
Q 1029-140	0.0860	0.0080	0.0751	3
Q 1033+1342	3.07	1.800	3.048	21
BR B1033-0327	4.509	2.91	4.454	22,2
3 Q 1038+528	2.30	1.677	2.262	16
GB 1041+3014	2.99	1.735	2.950	2
Q 1047+550	2.1650	1.3299	1.5159	3
BRI B1050-0000	4.286	2.83	4.233	22
Q 1100+772	0.3110	0.0080	0.2979	3
Q 1100-264	2.1450	1.1551	1.5500	3
MG 1101+0248	2.51	1.736	2.475	2
Q 1103-006	0.4260	0.0080	0.4117	3
BRI B1110+0106	3.918	2.58	3.869	22

TABLE 2—*Continued*

Quasar	z_{em}	z_{min}	z_{max}	References
Q 1115+080	1.7180	0.4066	0.6330	3
Q 1115+080	1.7180	0.9595	1.5500	3
Q 1116+215	0.1770	0.0080	0.1652	3
Q 1123+264	2.35	1.645	2.317	16
Q 1124+5706	2.890	1.762	2.851	21
Q 1127+078	2.66	1.644	2.621	16
Q 1128+105	2.65	2.040	2.610	16
Q 1131-0043	2.16	1.653	2.128	4
Q 1132-0054	2.76	1.717	2.718	4
Q 1135-0255	2.41	1.739	2.373	4
Q 1136-135	0.5570	0.0080	0.5414	3
Q 1136+122	2.90	1.781	2.862	16
Q 1137+660	0.6460	0.0080	0.6295	3
Q 1138-0107	2.76	1.953	2.718	4
Q 1139-0139	1.93	1.634	1.884	4
Q 1139-0037	1.91	1.634	1.896	4
Q 1142+0138	2.42	1.791	2.390	4
Q 1142+1015	3.152	2.127	3.109	21
Q 1143+0142	2.28	1.634	2.248	4
Q 1143+099	2.60	1.676	2.567	16
Q 1144+115	2.51	1.682	2.471	16
Q 1144+0140	2.59	1.667	2.551	4
Q 1145-0039	1.94	1.634	1.912	4
Q 1145+0121	2.08	1.721	2.045	4
Q 1146+0207	2.06	1.634	2.025	4
Q 1147+084	2.61	1.854	2.577	16
GB 1147+4348	3.02	2.035	2.980	2
Q 1148-0007	1.977	1.634	1.947	4
Q 1148+0055	1.89	1.667	1.858	4
Q 1148+549	0.9690	0.0080	0.9493	3
Q 1151+117	0.1760	0.0080	0.1642	3
Q 1156+295	0.7290	0.0080	0.7117	3
Q 1159+0039	2.586	1.671	2.550	21
Q 1202+281	0.1650	0.0080	0.1534	3
Q 1205-3014	3.036	2.045	2.996	21
Q 1206+1155	3.106	2.039	3.073	21

TABLE 2—*Continued*

Quasar	z_{em}	z_{min}	z_{max}	References
Q 1206+1500	2.60	1.793	2.568	4
Q 1206+1727	2.36	1.634	2.321	4
Q 1206+459	1.1580	0.4231	0.6300	3
Q 1206+459	1.1580	0.8426	1.1364	3
Q 1209+1046	2.20	1.634	2.163	4
Q 1209+1524	3.06	1.634	3.021	4
Q 1211+143	0.0850	0.0080	0.0742	3
Q 1212+1551	1.95	1.665	1.918	4
Q 1212+1045	1.95	1.634	1.922	4
Q 1212+0854	2.35	1.634	2.319	4
Q 1213+1015	2.52	1.634	2.482	4
Q 1213+0922	2.72	1.675	2.681	4
Q 1215+1244	2.08	1.634	2.048	4
Q 1215+1202	2.83	1.634	2.788	4
Q 1215+303	0.2370	0.0080	0.2246	3
Q 1216+069	0.3340	0.0080	0.3207	3
Q 1216+1517	1.83	1.723	1.802	4
Q 1216+1754	1.81	1.634	1.781	4
Q 1216+1656	2.83	1.659	2.791	4
Q 1216+0947	2.31	1.645	2.279	4
Q 1217+023	0.2400	0.0080	0.2276	3
Q 1218+304	0.1300	0.0080	0.1187	3
Q 1219+755	0.0700	0.0080	0.0593	3
Q 1219+1140	2.18	1.634	2.147	4
Q 1222+228	2.0400	0.4647	0.6316	3
Q 1222+1053	2.30	1.641	2.263	4
Q 1223+1059	2.32	1.643	2.288	4
Q 1223+1723	2.42	1.659	2.386	4
Q 1224+1244	2.14	1.634	2.110	4
Q 1225+1512	2.01	1.797	1.977	4
Q 1225+1610	2.23	1.663	2.200	4
Q 1225+317	2.2190	1.1263	1.5500	3
Q 1226+1035	2.32	1.634	2.287	4
Q 1226+1115	1.98	1.634	1.950	4
Q 1226+1639	2.25	1.634	2.216	4
Q 1226+023	0.1580	0.0080	0.1464	3

TABLE 2—*Continued*

Quasar	z_{em}	z_{min}	z_{max}	References
Q 1227+1215	2.17	1.624	2.138	4
Q 1228+1808	2.64	1.780	2.607	4
Q 1228+077	2.39	1.691	2.354	16
Q 1229+1414	2.90	1.764	2.862	4
Q 1229+1531	2.27	1.634	2.237	4
Q 1229-021	1.0380	0.4738	0.6320	3
Q 1229+204	0.0640	0.0080	0.0534	3
Q 1230+1042	2.43	1.634	2.396	4
Q 1230+1318	2.29	1.634	2.257	4
Q 1230+1627B	2.70	1.634	2.663	4
Q 1230+0941	1.84	1.641	1.812	4
Q 1232-0051	2.78	1.782	2.745	4
Q 1232+1139	2.87	1.848	2.831	4
Q 1234+0122	2.03	1.634	1.996	4
Q 1235+1807A	2.41	1.782	2.371	4
Q 1236-0043	1.84	1.690	1.815	4
Q 1236-0207	2.25	1.729	2.213	4
Q 1237+1515	2.04	1.634	2.009	4
Q 1237+0107	1.81	1.733	1.780	4
Q 1237+1508	2.07	1.634	2.035	4
Q 1237+1212	2.31	1.634	2.281	4
Q 1239+1435	1.93	1.634	1.900	4
Q 1239+0249	2.22	1.719	2.184	4
Q 1240+1504	1.85	1.634	1.823	4
Q 1241+176	1.2730	0.4066	0.6320	3
Q 1241+176	1.2730	0.7657	1.2503	3
Q 1242+0213	1.99	1.634	1.958	4
Q 1242+0006	2.08	1.634	2.045	4
Q 1242+1732	1.83	1.696	1.805	4
Q 1242+1737	1.86	1.634	1.828	4
Q 1244+1129	3.16	2.101	3.118	4
Q 1244+1642	2.87	1.848	2.826	4
Q 1246-0059	2.45	1.669	2.415	4
Q 1246+0032	2.31	1.651	2.273	4
Q 1247+267	2.0380	0.9211	1.5500	3
Q 1248+401	1.0300	0.3984	0.6028	3

TABLE 2—*Continued*

Quasar	z_{em}	z_{min}	z_{max}	References
Q 1248+401	1.0300	0.8919	1.0097	3
Q 1253-055	0.5380	0.0080	0.5226	3
Q 1259+593	0.4720	0.0080	0.4573	3
Q 1302-102	0.2860	0.0080	0.2731	3
Q 1307+085	0.1550	0.0080	0.1435	3
Q 1308+326	0.9960	0.4670	0.6310	3
Q 1308-0214	2.85	1.892	2.811	4
Q 1308-0104	2.59	1.634	2.549	4
Q 1309+355	0.1840	0.0080	0.1722	3
Q 1312+043	2.35	1.813	2.319	16
Q 1313+0107	2.39	1.647	2.359	4
PSS J1317+3531	4.365	2.978	4.311	1
Q 1317+277	1.0220	0.2503	1.0018	3
Q 1318+290B	0.5490	0.3757	0.5335	3
Q 1318-0150	2.01	1.651	1.980	4
Q 1318-113	2.3080	1.896	2.273	16
Q 1320+0048	1.96	1.655	1.925	4
Q 1323-0248	2.12	1.661	2.090	4
Q 1324-0212	1.89	1.634	1.857	4
Q 1327-206	1.1690	1.1243	1.1473	3
Q 1328+0223	2.15	1.937	2.122	4
BRI B1328-0433	4.217	2.24	4.165	22
Q 1329+0231	2.43	1.663	2.400	4
Q 1329+0018	2.35	1.661	2.318	4
Q 1329+4117	1.9350	0.4853	0.6318	3
Q 1331+170	2.0840	1.2621	1.5500	3
Q 1333+176	0.5540	0.3902	0.5385	3
Q 1334+246	0.1070	0.0080	0.0959	3
Q 1334-0033	2.78	1.634	2.745	4
Q 1334+0212	2.38	1.634	2.350	4
BRI B1335-0417	4.396	3.08	4.342	22
Q 1336+0210	1.96	1.634	1.932	4
GB 1338+3809	3.10	1.737	3.059	2
Q 1338+101	2.45	1.724	2.412	16
Q 1338+416	1.2190	0.4066	0.6324	3
Q 1338+416	1.2190	0.8684	1.1968	3

TABLE 2—*Continued*

Quasar	z_{em}	z_{min}	z_{max}	References
Q 1340+0959	2.942	1.894	2.897	21
Q 1344+0137	1.92	1.634	1.886	4
Q 1345-0137	1.93	1.634	1.900	4
Q 1345-0120	2.95	1.926	2.906	4
Q 1346+0121A	1.93	1.634	1.901	4
Q 1346-036	2.36	1.653	2.327	16
Q 1351+640	0.0880	0.0080	0.0771	3
Q 1352+183	0.1520	0.0080	0.1405	3
Q 1352+108	3.18	1.928	3.137	16
Q 1353+186	0.0505	0.0080	0.0400	3
Q 1354+195	0.7200	0.3593	0.6330	3
Q 1355-416	0.3130	0.0080	0.2999	3
Q 1356+581	1.3710	0.5218	0.6310	3
Q 1358+115	2.59	1.677	2.550	16
Q 1358+3908	3.3	2.221	3.237	21
Q 1400+0935	2.980	2.022	2.930	21
Q 1402-012	2.52	1.789	2.479	16
Q 1402+044	3.20	2.340	3.160	16
Q 1406+123	2.94	2.018	2.903	16
Q 1407+265	0.9440	0.0080	0.9246	3
Q 1410+096	3.21	2.099	3.169	16
Q 1411+442	0.0900	0.0080	0.0791	3
GB 1413+3720	2.36	1.735	2.326	2
Q 1415+451	0.1140	0.0080	0.1029	3
Q 1416-129	0.1290	0.0080	0.1177	3
Q 1418+546	0.1520	0.0080	0.1405	3
Q 1419+480	0.0720	0.0080	0.0613	3
Q 1421+330	1.9040	1.0311	1.5500	3
Q 1425+267	0.3620	0.2409	0.3484	3
Q 1426+015	0.0860	0.0080	0.0751	3
Q 1428+0202	2.11	1.634	2.075	4
Q 1429-0053	2.08	1.719	2.047	4
Q 1429+118	3.00	1.958	2.963	16
PSS J1430+2828	4.306	2.777	4.253	1
Q 1433+0223	2.14	1.634	2.111	4
Q 1433-0025	2.04	1.634	2.012	4

TABLE 2—*Continued*

Quasar	z_{em}	z_{min}	z_{max}	References
PSS J1435+3057	4.297	2.905	4.244	1
GB 1436+4431	2.10	1.769	2.069	2
Q 1439+0047	1.86	1.649	1.828	4
Q 1440-0024	1.81	1.634	1.786	4
Q 1440+356	0.0781	0.0080	0.0673	3
Q 1444+407	0.2670	0.0080	0.2543	3
Q 1444+0126	2.21	1.717	2.174	4
Q 1444-0112	2.15	1.651	2.121	4
Q 1451-375	0.3140	0.0080	0.3009	3
Q 1455+123	3.08	1.830	3.033	16
MG 1500+0431	3.67	2.606	3.623	1
Q 1503+118	2.78	1.957	2.740	16
GB 1508+5714	4.283	2.73	4.230	22
Q 1512+370	0.3710	0.0080	0.3573	3
MG 1519+1806	3.06	1.955	3.019	2
GB 1520+4347	2.18	1.775	2.148	2
Q 1522+101	1.3210	0.0080	0.6310	3
Q 1522+101	1.3210	0.8803	1.2978	3
Q 1525+227	0.2530	0.0080	0.2405	3
GB 1526+6701	3.02	1.955	2.980	2
Q 1526+285	0.4500	0.0080	0.2428	3
Q 1538+477	0.7700	0.3326	0.6326	3
Q 1545+210	0.2640	0.0080	0.2514	3
Q 1548+0917	2.749	1.874	2.707	21
PC 1548+4637	3.544	2.607	3.499	1
Q 1553+113	0.3600	0.0080	0.3464	3
Q 1556+273	0.0899	0.0080	0.0790	3
MG 1557+0313	3.891	2.66	3.842	22
MG 1559+1405	2.24	1.737	3.059	2
Q 1600+0729	4.38	3.062	4.326	1
Q 1607+1819	3.123	1.814	3.0918	21
Q 1612+261	0.1310	0.0080	0.1197	3
Q 1613+658	0.1290	0.0080	0.1177	3
Q 1623+268A	2.47	1.644	2.433	16
Q 1623+268B	2.54	1.644	2.502	16
Q 1630+377	1.4710	0.0080	0.6320	3

TABLE 2—*Continued*

Quasar	z_{em}	z_{min}	z_{max}	References
Q 1630+377	1.4710	0.8641	1.4463	3
Q 1631+3722	2.940	1.785	2.906	21
Q 1634+706	1.3340	0.5547	1.3107	3
Q 1641+399	0.5950	0.0080	0.5791	3
PC 1640+4628	3.700	2.604	3.653	1
Q 1704+608	0.3710	0.0080	0.3573	3
Q 1705+0152	2.576	1.669	2.537	21
Q 1715+535	1.9290	1.1009	1.5500	3
Q 1718+481	1.0840	0.0080	1.0632	3
Q 1721+343	0.2060	0.0080	0.1939	3
Q 1726+3425	2.429	1.669	2.393	21
Q 1727+502	0.0550	0.0080	0.0445	3
Q 1738+3502	3.240	2.093	3.197	21
GB 1745+6227	3.901	2.47	3.852	22
Q 1803+676	0.1360	0.0080	0.1246	3
Q 1807+698	0.0512	0.0080	0.0407	3
Q 1821+643	0.2970	0.0080	0.2840	3
Q 1831+731	0.1230	0.0080	0.1118	3
Q 1833+326	0.0590	0.0080	0.0484	3
Q 1836+5108	2.827	1.920	2.789	21
Q 1839-785	0.0743	0.0080	0.0636	3
Q 1845+797	0.0556	0.0080	0.0450	3
Q 1912-550	0.4020	0.1769	0.2041	3
Q 1928+738	0.3020	0.0080	0.2890	3
PKS 1937-101	3.787	2.442	3.739	21
Q 2000-3300	3.783	2.521	3.729	21
Q 2005-489	0.0710	0.0080	0.0603	3
Q 2038-0116	2.783	1.887	2.745	21
Q 2045-377	1.8000	1.0040	1.5500	3
Q 2048+3116	3.198	1.830	3.143	21
Q 2050-359	3.49	2.605	3.445	1
Q 2112+0555	0.4660	0.1105	0.4513	3,24
,25 Q 2113-4345	2.05	1.664	2.023	4
Q 2113-4534	2.54	1.969	2.506	4
Q 2114-4346	2.04	1.606	2.011	4
Q 2115-4434	2.16	1.755	2.128	4

TABLE 2—*Continued*

Quasar	z_{em}	z_{min}	z_{max}	References
Q 2117-4703	2.26	1.849	2.223	4
Q 2122-4231	2.27	1.550	2.233	4
Q 2126-1551	3.2660	2.011	3.218	21
Q 2126-4618	1.89	1.715	1.859	4
Q 2127-4528	2.71	2.018	2.676	4
Q 2128-123	0.5010	0.0940	0.4860	3
Q 2130+099	0.0610	0.0080	0.0504	3
Q 2131-4257	2.10	1.590	2.065	4
Q 2134-4239	1.80	1.590	1.776	4
Q 2134-147	0.2000	0.0080	0.1880	3
Q 2135-4632	2.21	1.879	2.182	4
Q 2136+141	2.43	1.784	2.390	16
Q 2139-4434	3.23	2.373	3.188	4
Q 2141+175	0.2130	0.0080	0.2009	3
Q 2145+067	0.9900	0.9426	0.9701	3
MG 2152+1420	2.56	1.800	2.524	2
Q 2153-2056	1.85	1.634	1.821	4
Q 2155-304	0.1170	0.0080	0.1058	3
Q 2159-2058	2.12	1.634	2.089	4
Q 2201+315	0.2970	0.0080	0.2840	3
Q 2203-2145	2.27	1.692	2.240	4
Q 2203-1833	2.73	1.849	2.691	4
Q 2205-2014	2.64	1.652	2.599	4
MG 2206+1753	3.14	1.769	3.099	2
Q 2209-1842	2.09	1.634	2.061	4
Q 2209+184	0.0700	0.0080	0.0593	3
Q 2211-1915	1.95	1.634	1.923	4
BR B2212-1626	3.990	2.69	3.940	22
Q 2214+139	0.0658	0.0080	0.0551	3
MG 2222+0511	2.32	1.800	2.287	2
GB 2223+2024	3.56	2.101	3.514	2
Q 2231+0125	1.90	1.634	1.871	4
Q 2231-0212	1.90	1.634	1.871	4
Q 2233+1341	3.209	2.216	3.167	21
Q 2233+1310	3.298	2.134	3.252	21
Q 2241+0014	2.14	1.657	2.099	4

TABLE 2—*Continued*

Quasar	z$_{em}$	z_{min}	z_{max}	References
Q 2243+0141	2.30	1.663	2.267	4
Q 2244-0234	1.97	1.787	1.940	4
Q 2244-0105	2.04	1.634	2.010	4
Q 2246-0006	2.05	1.651	2.019	4
BR B2248-1242	4.161	2.94	4.109	22
MG 2251+2429	2.33	2.019	2.297	2
Q 2251-178	0.0680	0.0080	0.0573	3
Q 2251+113	0.3230	0.1310	0.3098	3
MG 2254+0227	2.09	2.767	2.059	2
Q 2256+017	2.67	1.786	2.629	16
Q 2302+029	1.0440	0.3942	0.6290	3
Q 2302+029	1.0440	0.8060	1.0236	3
Q 2308+098	0.4320	0.0080	0.4177	3
Q 2311-0341	3.048	1.714	3.001	21
MG 2320+0755	2.09	1.780	2.059	2
Q 2326-477	1.2990	0.9164	1.2760	3
PC 2331+0216	4.093	3.115	4.042	1
Q 2334+1041	2.243	1.634	2.211	21
Q 2344+092	0.6720	0.0080	0.6288	3
Q 2351+1042	2.379	1.632	2.345	21
Q 2351+0120	2.07	1.634	2.039	4
Q 2351-1154	2.67	1.632	2.633	21
Q 2352+0205	2.19	1.634	2.158	4
Q 2354-0134	2.21	1.665	2.178	4
Q 2356+0139	2.07	1.661	2.039	4
Q 2356+0237	2.50	1.634	2.465	4
Q 2359+0653	3.238	1.632	3.203	21
Q 2359+0023	2.897	1.714	2.857	21

ACKNOWLEDGMENTS

First of all, my thanks go to Mike Irwin for his trust and patience and for doing science his way (with humour, modesty and much intelligence) and to Richard McMahon for his never-dying enthusiasm and creativity, two fantastic qualities for a supervisor! I am very grateful to Lisa Storrie-Lombardi for contributing hard work to the project presented here and for providing a model of efficiency. Thank you all for suggesting this exciting Ph.D. project. Warm thanks also to Max Pettini for his generosity, support and advice when most needed and for insightful scientific discussions, to Bob Carswell for expert and friendly help with VPFIT and to Ofer Lahav for introducing me to the wonders of cosmology in the first place.

I would like to thank Patrick Petitjean, R. Srianand and Bastien Aracil for sharing ideas and for welcoming me at the Institut d'Astrophysique de Paris on two occasions during my Ph.D. Thanks also to Sandro D'Odorico, Miroslava Dessauges-Zavadsky and TaeSun Kim for arranging for me to visit the European Southern Observatory and teaching me all I know about echelle data reduction.

I would like to thank the people I met in Cambridge. In DAMTP, Matt (for making me laugh so much), Toby and Thomas; in the IoA, I thank Andrea (for listening over all these years, thank you) & Ale & Irene, and all the students in my year: David (for shared madness and office), Andrew D., Andrew F., Chris, Steve Mo., Raquel, Jeremy (thanks so much for providing most professional help with computer related problems - and I had many!), Rob S., Mark, Lisa W. (thanks for organising about a billion social events). Thanks to Phil (sorry about the wallet...), Jarle & Anabela, Mike H., Sara & Jon, Alwyn, Meg, Felipe & Claudia, Manuela, Pascale, multi-talented Panayiotis, Joop, Robert P., Enrico, Rich M. (partner in far-east travelling, hiking, skiing, diving, squashing and much more), Melvyn, Steve Ma., Ian B. & Gigi, the French speaking club: Francine, Sylvie, Alex, Pierre-Alain & Carole, Suzanne, Oleg (thanks for showing me around Saint-Petersburg), Marcus, Rachel J., Rachel S., Simon (the f-man), Andy, Sam (thanks for brightening up my days with funny e-mails and never, never turning up), Ian P., Ben and Tom (thanks for all - the squash games, the Belgian chocolates, listening to my concerts... to name just a few). Thanks to all of you who rowed, that was fun.

Thanks to John and Elsie for seemingly permanent good moods, to Paul for help with financial matters, to the very competent helpdesk team (Sue, Peter, Andy & Hardip), to Richard S. for arty conversations, to Peter & Terry for tools and advice on fixing my bike and to Jim, Steve & the X-ray bun-club for many cakes and biscuits.

Thanks also to those I met while astro-travelling, TzuChing (I still do not understand how we made it home that night), Markus (more brightening e-mails, more hiking and skiing, and still listening to me) & his women, Ana, Eric, Didier, Isobel, Nikos, Valentina, Bastien (thanks for making sure that we see the most romantic part of Paris, with the best view of London while visiting Rome), Emmanuel, Thibaut, Brice, Cédric, Mirka & Luc (even more hiking and skiing), Johan, TaeSun (thank you so much for generously letting me stay in your flat while I was in Garching), Iskra and Ari.

I will make no attempt whatsoever to thank here my friends who are unrelated to astrophysics, although whether you are in Cambridge, Paris or elsewhere, you have been the best help to stop me from getting lost in my star gazing.

Finally, I would like to thank my family for support and in particular my father for providing (good) advice on what he knows nothing about and my mother for her constant attention.